



Structure of Confined Liquids studied by an X-ray Surface Force Apparatus

Henning Weiss
April 2018

Structure of Confined Liquids
studied by an
X-ray Surface Force Apparatus

Dissertation

zur Erlangung des Grades
"Doktor der Naturwissenschaften"
im Promotionsfach Chemie

Fachbereich Chemie, Pharmazie und Geowissenschaften
der Johannes Gutenberg-Universität
in Mainz

Henning Weiss
geb. in Bonn

Mainz, Februar 2018

Die vorliegende Arbeit wurde im Zeitraum von Oktober 2014 bis Februar 2018 am Max-Planck-Institut für Polymerforschung in Mainz unter der Anleitung von [n.a. in online version] in der Abteilung von [n.a. in online version] angefertigt.

This dissertation is the result of work carried out in the Physics at Interfaces Group at the Max Planck Institute for Polymer Research (MPI-P) from October 2014 until February 2018 under the supervision of [n.a. in online version] in the group of [n.a. in online version].

Tag der mündlichen Prüfung:	17.04.2018
Dekan: [n.a. in online version]	
Erster Berichterstatter:	[n.a. in online version]
Zweiter Berichterstatter:	[n.a. in online version]

Zusammenfassung

Wenn der Durchmesser flüssigkeitsgefüllter Poren molekulare Größenordnungen erreicht, ändert sich die Struktur der darin befindlichen Flüssigkeit und kann stark von der Gleichgewichtsstruktur innerhalb der Flüssigkeit abweichen. Die Strukturänderung kann die Moleküldynamik beeinflussen und somit die Eigenschaften der Flüssigkeit ändern. Die Struktur an einer Flüssig-Fest-Grenzfläche ist jedoch für eine Vielzahl technischer Prozesse bedeutsam. So hängt die Leistung von Batterien und Kondensatoren entscheidend von der Struktur der Flüssig-Fest-Grenzfläche ab. Auch katalytische Prozesse werden von der Molekülstruktur am Übergang von flüssig zu fest beeinflusst. Ein weiteres Beispiel für eine starke Abhängigkeit der molekularen Anordnung von der Spaltgröße zeigt sich in tribologischen Anwendungen. Die Erforschung der molekularen Struktur der Flüssig-Fest-Grenzfläche ist deshalb nicht nur aus wissenschaftlicher Sicht von Bedeutung, sondern kann auch einen Beitrag zu technischem Fortschritt leisten.

Die experimentelle Untersuchung der Flüssigkeitsstruktur in engen Spalten ist jedoch nicht so einfach möglich. Methoden wie Surface Force Apparatus, Colloidal Probe oder Atomic Force Microscopy messen Kräfte und schließen daraus auf die molekulare Anordnung. Eine direkte Untersuchung der Molekülstruktur findet nicht statt. Die Untersuchung eingeschlossener Flüssigkeit in einer Porenstruktur ist ebenfalls nicht zielführend, da die Krümmung der Porenwände die Eigenschaften der Flüssigkeit beeinflusst. Ein idealer Versuchsaufbau würde die Untersuchung der Flüssigkeit in einer Schlitzporengeometrie ermöglichen und signalgebende Methoden, welche direkt die Molekülstruktur untersuchen, verwenden.

Eine solcher Versuchsaufbau wurde mit dem in dieser Arbeit konstruierten Gerät realisiert. Das als X-ray Surface Force Apparatus bezeichnete Gerät verbindet die Methoden der Surface Force Apparatur mit Methoden der Röntgenstreuung. Die somit zugänglichen Informationen über die Struktur der Flüssigkeit ergänzen sich komplementär und ermöglichen neue wissenschaftliche Einblicke. Der Abstand zweier Oberflächen lässt sich mit diesem Gerät bis zu molekularen Größenordnungen kontrollieren. Die Flüssigkeitsstruktur lässt sich durch dynamische Auslenkung einer der beiden Spaltoberflächen in horizontaler und vertikaler Ausrichtung mikrorheologisch untersuchen. Anwendbare Röntgenmethoden umfassen Röntgenstreuung zur Untersuchung der horizontalen Flüssigkeitsstruktur, aber auch Röntgenreflektivitätsmessungen zur Untersuchung der Struktur vertikal zu den Spaltoberflächen.

In dieser Arbeit wurden zwei unterschiedliche Probensysteme anhand des X-ray Surface Force Apparats untersucht. Der smektische Flüssigkristall 4'-Octyl-4-Cyanobiphenyl wurde bei Spaltbreiten von 120 nm und 1700 nm untersucht. Streuexperimente ermittelten eine Ausrichtung der Moleküle senkrecht zu den Spaltoberflächen. Diese geschichtete Struktur wurde durch Kompressions/Dekompressions-Zyklen mechanisch belastet. Es zeigte sich, dass Kompression die Anisotropie der smektischen Schichten erhöht, während Dekompression zu einer Verringerung der Anisotropie der Flüssigkeitsmoleküle führt. Die Moleküle reagieren viskoelastisch auf Störung und zeigen eine Reorientierung zurück in den Ausgangszustand auf einer Zeitskala von 20 Sekunden. Ein Anisotropieniveau wie unter Kompression wird jedoch nicht wieder erreicht. Bei einer Spaltbreite von 120 nm wurde ein Absinken der Spaltbreite aufgrund der mechanischen Belastungszyklen gemessen. Vor dem Hintergrund einer konstanten Röntgenreflektivität wird dies durch die Induzierung von Fehlstellen im Flüssigkristall erklärt. Einzelne Fehlstellenmoleküle liegen desorientiert in den smektischen Lagen und ergeben sogenannte "Parking-lot-states".

Das zweite untersuchte Probensystem war die ionische Flüssigkeit 1-Decyl-3-Methylimidazolium Chlorid. Ionische Flüssigkeiten werden als erfolgversprechende Elektrolyte in Batterien und Kondensatoren gehandelt, in denen sie meist in einer Porenstruktur vorliegen. Da sich in der praktischen Anwendung der Kontakt mit Luftfeuchtigkeit kaum ausschließen lässt, wurde der Einfluss von Wasser auf die Struktur der ionischen Flüssigkeit untersucht. Dazu wurden Röntgenmessungen und rheologische Experimente durchgeführt, aber auch Untersuchungen in engen Spalten durch Einsatz des X-ray Surface Force Apparates. Dies ermöglicht einen Vergleich des Verhaltens in Poren im Gegensatz zur unbeeinträchtigten Flüssigkeit. Die Absorption von Wasser im Bereich von $10 \leq w_i \leq 60$ Gewichtsprozent induziert in 1-Decyl-3-Methylimidazolium Chlorid eine hoch geordnete flüssigkristalline Phase. Die mechanischen Eigenschaften ändern sich stark, die Viskosität steigt um fünf Größenordnungen. Eine Domänenstruktur aus hexagonal dichtgepackten Stäbchen bildet sich aus. Der Stäbchendurchmesser entspricht der Anordnung von zwei Decyl-Seitenketten und einer Imidazolium-Kopfgruppe. Diese Struktur wurde nun im X-ray Surface Force Apparat bei Spaltbreiten von 180 nm und 80 nm durch Scherversuche untersucht. Bei schrittweiser Auslenkung der Oberfläche zeigte sich eine viskoelastische Kraftrelaxation durch Kriechen. Da gleichzeitig eine konstante Röntgenreflektivität auf eine gleichbleibende Struktur hindeutet, wurde dies als ein Fließen der Stäbchenstruktur interpretiert. Oszillatorische Scherbelastung ergab, dass die Flüssigkristallstruktur durch Scherung ausgelenkt, aber nicht zerstört wird. Oberhalb einer Scherrate von $\dot{\gamma} \leq 0.401 \text{ s}^{-1}$ wird die Struktur beeinträchtigt. Die beobachtete mesoskopische Struktur in der Flüssigkeit, kann durch die Mobilität der Mesogene in der flüssigkristallinen Phase erklärt werden.

Die in dieser Thesis präsentierten Ergebnisse ermöglichen neue Einblicke in Flüssigkristalldynamiken in Poren. Die erzielten Resultate ermöglichen ein besseres Verständnis von Strukturen komplexer Flüssigkeiten in der Flüssig-Fest-Grenzschicht. Der Grundstein zu weiteren Versuchen auf dem Feld der Mikrorheologie wurde durch die erfolgreiche Konstruktion des X-ray Surface Force Apparat gelegt.

Abstract

When confinement approaches the molecular dimensions of a liquid, the structure of the liquid adjacent to the solid wall can differ significantly from bulk structure. These interfacial structures can strongly affect the dynamics of the confined system and thereby properties. Recent studies on the performance of batteries and capacitors showed that electrochemical processes at electrodes are highly sensitive to the molecular scale liquid structure adjacent to interfaces. In catalytic processes the molecular scale liquid structure adjacent to interfaces is important as well. Also liquids in lubrication applications rely on the structure in between two solid walls, as the properties of the lubricant have to meet performance expectations in the confinement gap. These examples demonstrate that many technical devices and applications rely on liquids under confined conditions. Thus, a detailed knowledge of the molecular scale structure of liquids in confinement is of great interest for scientific as well as for technical progress.

However, the elucidation of structures in confinement is intricate. Force measurements as performed by a Surface Force Apparatus, Colloidal Probe, or Atomic Force Microscopy, do not directly probe the molecular structure. Other techniques, such as the confinement of liquids in porous bulk-like materials, have the drawback that the curvature of the walls influences the confined structure. Hence, a slit-pore geometry would be ideal to investigate structures formed in confinement.

To tackle this problem, in this work a new set-up to probe liquids in slit-pore confinement was designed, constructed and operated. This device combines Surface Force Apparatus and X-ray techniques. Complementary structural information are obtained by X-ray techniques and simultaneous force measurements. Using white light interferometry, the X-ray Surface Force Apparatus can realize a controlled confinement in a slit-pore geometry with a gap thickness down to the molecular length scale. Forces between the apposing interfaces can be modulated to compress/decompress or shear the structure giving insight into the dynamics of confined liquids. X-ray techniques include X-ray reflectivity, investigating the profile perpendicular to the confining interfaces, and X-ray scattering, investigating the in-plane structure parallel to the slit-pore.

Results for two different complex liquid sample systems were obtained in this thesis. The smectic liquid crystal 4'-octyl-4-cyano-biphenyl was confined to gap widths of 120 nm as well as 1700 nm. Scattering patterns indicate that the smectic layers are preferably arranged with their long axis perpendicular to the solid/liquid interfaces. This layered structure was stressed by compression/decompression cycles. Compression stress enhances orientation within the smectic layers as well as in in-plane orien-

tation. Uptake of molecular orientation upon stress application occurs viscoelastic on a time scale of 20 seconds. Decompression results in misalignment. However, perpendicular molecule orientation recovers viscoelastic, again on a time scale of 20 seconds. Deflected from an orientation perpendicular to the surface due to the decompression, the molecules tilt back to perpendicular position, though not reaching their previous scale of anisotropy. Gap distance decrease is observed upon subsequent compression/decompression cycles. Corresponding to the observed X-ray signal behavior, this is interpreted by defect formation and relaxation processes. So called parking-lot-states are induced by the compression stress cycles. Here, liquid crystal molecules are lying in their smectic layers in a disordered way.

In the second example, experimental data on the structure of the confined ionic liquid 1-decyl-3-methyl-imidazolium chloride are presented. Confined ionic liquids play an important role in many technical applications and processes as they are candidates for future electrolytes in batteries and capacitors. In these applications, humidity is an ubiquitous pollutant. Answering to this, the structural response of the wet ionic liquid is probed by X-ray and rheology measurements in bulk, as well as in confinement using the X-ray Surface Force Apparatus. This enables a concise comparison between bulk and confinement behavior. Water absorption in 1-decyl-3-methyl-imidazolium chloride induces a transition from a liquid structure to a highly oriented liquid crystalline phase for water contents of $5 \leq w_i \leq 60$ weight percent. Mechanical properties change drastically and viscosity rises by five decades indicating gelation. Highly orientated pillars with dimensions of two times the molecule length scale are ordered in a hexagonally close packing. Different domains of orientation are formed. Time resolved X-ray Surface Force Apparatus measurements elucidate the structural behavior after shear stress application in 180 to 80 nm slit-pore confinement. Applying step-wise shear force the structure shows viscoelastic creeping above a shear strain threshold. This is interpreted as a structure flow as it is not answered by a structural change observed by X-ray reflectivity. Oscillatory shear measurements show that the liquid crystalline domain structure is deflected by shear below a certain shear strain, but not destroyed. Beyond a shear rate of $\dot{\gamma} \geq 0.401 \text{ s}^{-1}$ the liquid crystalline structure is perturbed. The observed mesoscopic orientation after oscillatory shear is explained by the anisotropic mobility of the mesogens in the lyotropic liquid crystalline phase.

The work presented provides novel insights into liquid (crystal) dynamics under molecular confinement. Results obtained can lead to a better understanding of structures formed by complex liquids and the resulting dynamics at the solid-liquid interface. The constructed X-ray Surface Force Apparatus can form the starting point for future research in several fields, such as lyotropic structure dynamics or confinement induced structure dynamics.

Contents

Zusammenfassung	i
Abstract	iii
I Introduction	1
II Theory and Background	5
1 Structure of Liquids	7
1.1 Intermolecular Forces	7
1.2 Distribution Functions	9
2 Small Angle Scattering	13
2.1 Small Angle Scattering	13
2.2 Probing Liquid Structure by Scattering Methods	17
3 X-ray Reflectivity	19
3.1 Reflectivity	19
3.2 Probing Structures by Reflectivity	22
4 Ionic Liquids	25
4.1 Hydrophilicity/Hydrophobicity of Ionic Liquids	27
4.2 Ionic Liquid Bulk Structure	28
5 Confined Liquids	31
5.1 Molecular Liquids at Interfaces	31
5.2 Ionic Liquids at Interfaces	33
III Bulk Ionic Liquids	39
6 Materials	41
6.1 Ionic Liquids for Bulk Structure Analysis	41

CONTENTS

7	Experimental	47
7.1	Small Angle Scattering	47
8	Data Analysis	53
8.1	Azimuthal Averaging	53
8.2	Teubner-Strey Model	53
8.3	Asymmetric Lorenz Model	56
8.4	Fitting	56
9	Results and Discussion	59
9.1	Hydrophobic Ionic Liquid Bulk Structure	59
9.1.1	Periodicity	59
9.1.2	Correlation Length	61
9.1.3	Temperature Effects	62
9.1.4	Anions and Cations	63
9.1.5	Entropy of Fusion	64
9.1.6	Conclusions	64
9.2	Hydrophilic Ionic Liquid Water Mixtures	66
9.2.1	1-methyl-3-octyl-imidazolium chloride	66
9.2.2	1-decyl-3-methyl-imidazolium chloride	69
IV	X-ray Surface Force Apparatus	73
10	Materials	75
10.1	Liquid Crystal 4'-octyl-4-cyano-biphenyl (8CB)	75
10.2	Hydrophilic Ionic Liquid 1-decyl-3-methyl-imidazolium chloride	76
11	Experimental Technique	79
11.1	Compendium on X-ray Surface Force Apparatus Concept	79
11.2	X-ray Surface Force Apparatus	82
11.3	Confining Surface Fabrication	84
11.4	Surface Positioning and Force Measurements	87
11.5	Light Microscopy and FECO	88
11.6	Sample Atmosphere Control	89
11.7	In-Situ X-Ray Scattering and Reflectivity	90
11.8	Instrument Characterization	91
12	Analysis	93
12.1	Mechanical Analysis	93
12.2	Analysis by X-ray Methods	94

13 Results and Discussion	97
13.1 Benchmark System 4'-octyl-4-cyano-biphenyl	97
13.1.1 Static Structure of 8CB in Confinement	97
13.1.2 Relaxation Dynamics	99
13.2 Ionic Liquid Crystal System 1-decyl-3-methyl -imidazolium chloride	105
13.2.1 Water induced IL structure under static confinement	105
13.2.2 Dynamic stress of water induced IL structure under confinement	110
 V Summary	 125
14 Summary and Conclusion	127
15 Outlook	131
A Abbreviations and Acronyms	135
B Symbols used in equations	137
C Appendix	141
C.0.3 Small-Angle X-ray Scattering Measurements of hydrophobic ILs used at different temperatures	141
C.0.4 Comparison of SAXS and SANS data at 90 degree Celsius . . .	144
 Danksagung	 171
Curriculum Vitae	173

Part I

Introduction

Introduction

Just as the number of people walking through a narrow alley at a busy Saturday afternoon changes how the casual shopper roams, the same applies at the molecular level. The close approach of two solid walls creates a spatial confinement. Spatial confinement influences structural order. Structure formation changes molecular mobility, interaction and hence the properties of the material in confinement. A process illustrated in Fig. 1. Especially liquid molecules are found frequently in confinement, as they exhibit a high mobility and enter small pores easily. When the distance between confining solid surfaces reaches the molecular dimensions of the liquid, the behavior of molecules at interfaces changes [45, 77, 95, 129]. Different regimes apply in molecular confinement than in bulk, governing structure formation at the interfaces.

Molecular confinement of liquids can be found in many technical applications. Batteries [8, 112], Fuel Cells [49, 164] and Capacitors [11, 24, 143, 144] are examples of electrochemical devices that rely on the chemical structure of a liquid adjacent to a solid interface. In catalysis, the chemical structure at liquid/solid interfaces is important as well [221, 255, 259]. Friction and lubrication [114, 161, 178] are examples from the field of tribology in which the confined liquid structure plays the key role, too. This shows how the problem of confined liquid structures branches to different fields of industry, making the structure on a molecular level of a liquid under confinement of fundamental interest. Of special interest are applied complex liquids such as liquid crystals (LCs) or complex electrolytes like Ionic Liquids (ILs). Liquid crystals find application in displays, where they are used in thin films, confined between electrodes [75, 125]. The large, anisotropically orientated, but still liquid molecules make a well behaved system for measurements and are often used to probe molecular orientation. Ionic Liquids (ILs) are molten salts as they consist entirely of ionic species [287]. They have melting points below 100° C. In contrast to that, melting temperatures of conventional salts are significantly higher, e.g. NaCl has a melting point of 800° C. Having unique properties, ILs see application in all aforementioned technical situations.

When trying to mimic a slit pore confinement as it can be found in powders, electrodes, membranes, foams, nano-tubes or other highly porous media, an immediate problem becomes obvious: How to probe the structure in confinement? The slit geometry requires two solid surfaces to be brought close together, leaving no space for the approach of a physical probe as in Atomic Force Microscopy (AFM). In contrast to that, the so called Surface Force Apparatus (SFA) approaches two surfaces and creates a controlled confinement, but can only measure forces exerted onto the solid surfaces

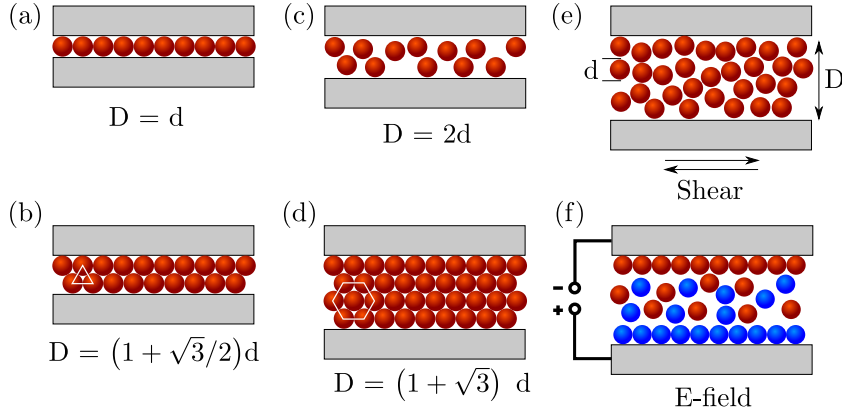


Figure 1: Change of structure, when the confinement dimension D reaches the molecular level d . The properties of the material can change drastically due to a change in structure, when in molecular confinement.

[109]. Structure on a molecular level in the liquid is not directly probed, but structure is interpreted from force measurements only. Probing the molecular structure directly is possible by X-ray techniques. They are sensitive to the chemical structure on molecular length scales of a liquid at a liquid/solid interface. Hence, the combination of both techniques into one device promises new insights into mechanisms and interactions of confined liquids.

To address the question on how confined liquids behave, the present work researches on confined liquid structures using SFA and X-ray methods in a newly constructed device that combines both methods to a so called X-ray Surface Force Apparatus (XSFA). A focus is especially laid on Ionic Liquid structures. Promised results contribute to the elucidation of IL structures in confinement and the properties of the structures formed at the solid-liquid interface.

The work is divided into four parts. The second part **THEORY AND BACKGROUND** gives an introduction into how structures in Ionic Liquids arise, which forces are acting and how liquid structures can be described and quantified in general. It also gives an overview on structures probed in confinement to date. The third part **BULK IONIC LIQUIDS** presents structures formed in neat and water infused bulk Ionic Liquids. This lays the ground work for a better understanding of structures observed in confined Ionic Liquids in the fourth part **X-RAY SURFACE FORCE APPARATUS**. Here, the device constructed and used throughout this work is introduced. Acquired data are presented and discussed. Part five **SUMMARY** recapitulates the results achieved in this work, puts them in context to each other and concludes with a focus on future research possible with the newly constructed device.

Part II

Theory and Background

Chapter 1

Structure of Liquids

Commonly chemists deal with three states of matter: solid, liquid and gaseous. In each state the principal constituent of the phase, the atom or molecule, does not change. It is the interactions between particles and with it the arrangement of particles relative to each other that is subject to transition. The mobility of the particles is described by the kinetic energy K_N , the interactions between particles by the potential energy of the system $|V_N|$ [84]. In a first approach, each specific phase of state is identified by a certain molecular arrangement of the particles. A distinction can be made as follows:

Solid: $\frac{K_N}{|V_N|} \ll 1$

Solid phases display a high potential energy of the particles, but low kinetic energy. Practically no relative motion of particles is observed, as the interactions between molecules are strong. A long and short range orientation of particles follows, for example a crystal lattice structure.

Liquid: $\frac{K_N}{|V_N|} \approx 1$

In liquids, the kinetic and potential energy of the system are of the same order. Liquid phases usually have no long range orientation, but a short range order as the interactions between molecules are only influencing close neighbors. Liquid structures exhibit close to zero compressibility as the particles are still densely packed.

Gaseous: $\frac{K_N}{|V_N|} \gg 1$

In gases the kinetic energy of the particles is high, whereas interactions between particles are low. Thus mobility of the particles is high, whereas the interactions, in comparison to the distances between particles, are weak, resulting in no long or short range order.

1.1 Intermolecular Forces

In this work we are concerned with structure determination in the liquid state, especially with the structures displayed by complex liquids, such as ionic liquids (ILs). Ionic liquids are molten salts, are solely made of ions and have melting temperatures below 100°C. The molecules in ILs display intricate interactions, due to their complex chemical structure. For liquids, the interparticle forces are in the same range as the par-

ticle distances. Two major contributions occur in the molecular interactions of ionic liquids[30, 225]: short and long range interactions. The interplay of short and long range interactions is well balanced between kinetic and potential energy. In an ionic liquid, the potential energy between two particles α and β is described by:

$$W_{\alpha\beta} = 4\epsilon_0 \left[\left(\frac{\sigma_{\alpha\beta}}{r_{\alpha\beta}} \right)^{12} - \left(\frac{\sigma_{\alpha\beta}}{r_{\alpha\beta}} \right)^6 \right] + \frac{1}{4\pi\epsilon_0} \frac{q_\alpha q_\beta e^2}{r_{\alpha\beta}} \quad (1.1)$$

In Eq. 1.1 the first term is associated with short range forces, the second term with long range forces. ϵ is the depth of the potential well, σ is the distance at which the inter-particle potential is zero, ϵ_0 is the dielectric constant of vacuum, q_α and q_β are the charges of particles, α and β , respectively, e is the elementary charge.

Short Range Forces

The first term of Eq. 1.1 describes the Lennard-Jones potential, contributing short ranged interactions [116]. They usually do not extend further than one particle dimension. Short range forces can be divided into repulsive forces originating in the Pauli-principle and attractive forces, such as van-der-Waals-forces C_{total} (vdW).

When bringing atoms or molecules in close contact to each other, orbitals start to overlap. Following the Pauli-principle, two electrons can not occupy the same state in an orbital. Hence, strong repulsive forces occur because the electrons have to switch to energetically higher orbitals when starting to overlap. Naturally, these repulsive forces are very short ranged and decay quickly with increasing distances between molecules showing an r^{-12} dependency with the radius r between particles.

The term van-der-Waals-forces C_{total} summarizes several attractive or repulsive forces originating in dipole-dipole interactions [26]: $C_{\text{total}} = C_{\text{orient}} + C_{\text{ind}} + C_{\text{disp}}$. Here, C_{orient} represents the interaction of freely rotating dipoles, often refereed to as Keesom interactions. Debye interactions between an induced dipole created by the influence of a permanent dipole are described by C_{ind} . London dispersion forces C_{disp} summarize the fluctuations of electron density in an atom or molecule, leading to induced dipoles in normally completely apolar particles. In this term, for normal simple molecules, London dispersion forces C_{disp} have the largest contribution. Van-der-Waals-forces are longer ranged and decay over an r^{-6} dependency.

Long Range Forces

A distinct difference of ionic liquids to simple liquids is the presence of discrete charges q_i within the molecule. Resulting in Coulomb interactions this is described by the second term of Eq. 1.1. Coulomb forces are long range forces with a decay over r^{-1} with attractive or repulsive interactions, depending on the sign of the two interacting particles. In classical molten salts, they dictate molecular behavior [142, 300]. In contrast to that, organic salts are liquids and display liquid structure around room-temperature,

despite the strong interactions. This can be attributed to the diminished coulombic interaction by ion pairing [186], an effect not observed in classical molten salts. However, a picture of a discrete association of ion pairs would be misleading. Ion species do screen each other, and are associated, though on short timescales and not permanently, as self diffusion coefficient measurements show [266, 289]. So interactions between pairs are observed, attributed to much weaker forces, such as hydrogen bonding, supporting the idea of screening of the Coulomb interactions [279, 284].

Another reason for the liquid behavior of ILs despite Coulombic interactions is the asymmetry and complexity of the IL molecules, rendering it difficult to crystallize and form short and long range order. IL cations usually show low molecular symmetry and good distribution of the electric charge throughout their electronic system [286]. When introducing long alkyl side-chains in the cation, even mesoscopic structure is observed, due to vdW-interactions in apolar parts of the molecule. IL anions are usually larger, branched molecules, also stabilized by a distribution of their negative charge.

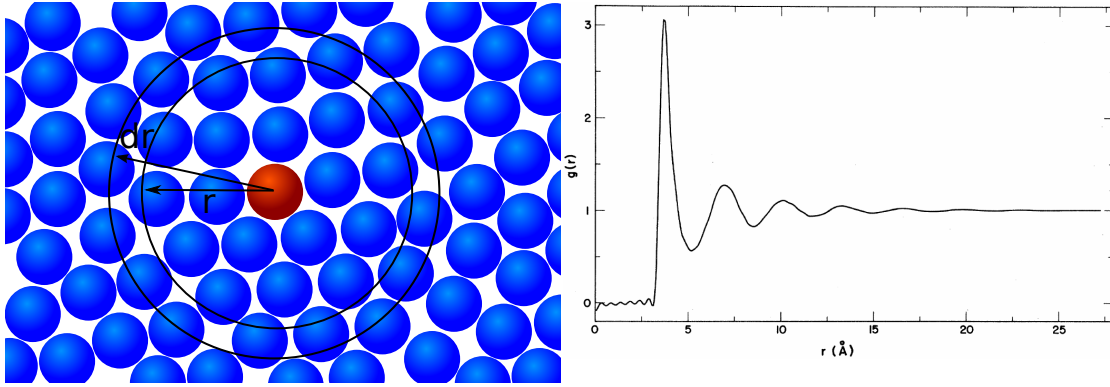
1.2 Distribution Functions

In liquids, the balanced interplay of intermolecular forces and molecular kinetics leads to a short range structure. The absolute particle position might not be fixed, however the relative position of particles to each other is not random, giving rise to a local atomic environment. Hence, a good parameter to describe the liquid structure is the interatomic distance $r_{\alpha\beta}$ between a particle α , forming the origin of coordinates, to a particle β . As we are usually not interested in the single pair distance, but in a statistical description of an average of interparticle distances, a pair distribution function (PDF) can be used to describe the distribution of interatomic distances. The PDF gives the probability of finding a particle β at a distance r of a particle α . As liquids are isotropic, the PDF is independent of orientation and is only a function of the separation distance $r_{\alpha\beta} = |r_\beta - r_\alpha|$. It is then called radial distribution function (RDF) $g_{\alpha\beta}(r)$ and is described by:

$$g_{\alpha\beta}(r) = \frac{1}{N_\alpha N_\beta} \sum_{\alpha=1}^{N_\alpha} \sum_{\beta=1}^{N_\beta} \langle \delta(|r_{\alpha\beta}| - r) \rangle \quad (1.2)$$

Here, N_α, N_β is the number of particles in a Volume V and δ is the Dirac delta. The sums are taken over all particles in the sample result in a histogram of distances between particles. When the distances $r_{\alpha\beta}$ become large, the interatomic potential gets weaker and finally vanishes. Particle α does not exert a strong influence on particle β anymore, they become uncorrelated, $g_{\alpha\beta}(r)$ approaches the ideal gas case for $r \rightarrow \infty$. In an ideal gas, the particles are totally uncorrelated and $g_{\alpha\beta}(r) \approx 1$. For $r \rightarrow 0$ the RDF approaches 0, because it is impossible to find a particle in the same position (c.f. Fig. 1.1b).

A more useful parameter is the reduced pair distribution function $h(r) = g(r) - 1$ (often pair correlation function $G(r)$), which fluctuates around 0 [53]. One advantage is that it is directly accessible from the scattering amplitude $S(q)$ acquired in scattering



- (a) 2-dimensional sketch of a liquid structure around a central particle. Area probed is indicated by radius r . When extending the radius by dr , the liquid structure loses correlation, as can be seen from the amount of particles fully lying within the area $A = \pi r dr$.
- (b) Oscillations in a pair correlation function of liquid Argon probed by Neutron Scattering describing inter-particle distances. Reproduced from J. Yarnell et al. [302]

Figure 1.1: Structure in bulk liquid

experiments via Fourier-Transformation, as we will show later. Due to this for $h(r)$, in contrast to $g(r)$, the random uncertainties are constants in r , making it easier to use when comparing calculated and measured distribution functions.

We can now describe the direct correlation between two particles by $h(r)$. In a many-body system this way of interaction is unrealistic and indirect correlations have to be taken into account as well. This relation is achieved by the Ornstein-Zernike-Equation (OZR) [192].

$$h(r_{\alpha\beta}) = c(r_{\alpha\beta}) + \delta \int c(r_{\alpha\beta}) h(r_{\alpha\beta}) dr_3 \quad (1.3)$$

Here, $c(r_{\alpha\beta})$ gives the direct correlation between particles, the second term gives the indirect correlations. This equation is valid for a single component fluid, but can be adapted to mixtures of different components, as in the case for ionic liquids, which compose of two different species. The OZR then reads:

$$h_{\alpha\beta}(r) = c_{\alpha\beta}(r) + \delta \sum_{\gamma} x_{\gamma} \int c_{\alpha\gamma}(|r - r'|) h_{\gamma\beta}(r') dr' \quad (1.4)$$

Here, the number concentration of species γ is given by $x_{\gamma} = N_{\gamma}/N$.

Solving Eq. 1.4 in Fourier space using the generalized mean spherical approximation (GMSA) it can be shown that two types of correlation decays are possible[147]: a monotonic exponential decay

$$r h_{\alpha\beta}(r) \propto A \exp\left(-\frac{r}{\gamma}\right) \quad (1.5)$$

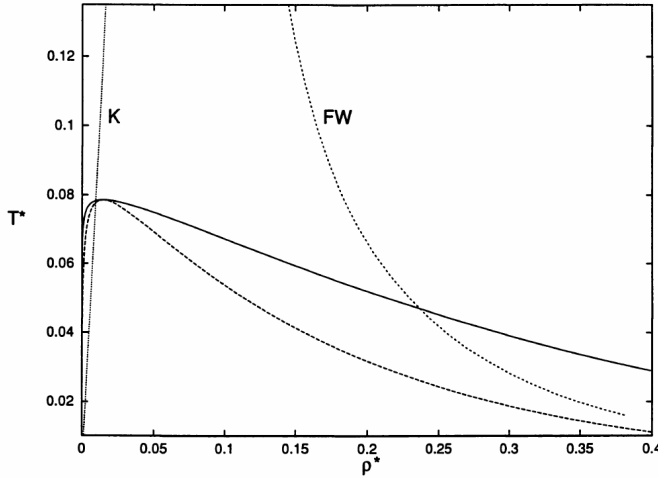


Figure 1.2: Cross-over lines for the RPM calculated using the GMSA. The short-dashed curve is the FW line where cross-over from monotone to damped oscillatory decay occurs for the total number density correlation function $h_s(r)$. Onset of charge oscillations, in $h_D(r)$, occurs on the dotted line K. The solid line is the liquid-vapor coexistence curve and the long-dashed line marks the accompanying spinodals. Reprinted (adapted) with permission from R. Evans and R.J.F. Leote de Carvalho [54]. Copyright 1996 American Chemical Society.

or an exponentially oscillatory decay.

$$r h_{\alpha\beta}(r) \propto A \exp \left(-\frac{r}{\gamma} \cos \left(\frac{2\pi r}{d} - \theta \right) \right) \quad (1.6)$$

The boundary condition of a restricted primitive model (RPM), which assumes charged hard spheres of equal diameter R , simplifies mathematical treatment. Here, γ is the correlation length, d is the periodicity and θ is a phase angle. A cross-over between the two states means a change in molecular environment. Two different parameters can change: The number of molecules in the volume around a particle can change, leading to number density oscillations. Also, the amount of charge in the volume around a particle can change, leading to charge oscillations. Number density oscillations were first observed by Fisher [60], charge oscillations were described by Kirkwood [124]. For the number density oscillations a cross-over between the two states is observed when $2\pi r/d = -1/\gamma$. The occurrence of a transition of the total correlation function $h_{\alpha\beta}(r)$ from an exponential decay to an oscillatory decay can be justified by the interplay of repulsive and attractive interactions. If repulsive interactions are the dominant interaction, a monotonic decay results. If attractive interactions contribute, an oscillatory decay can occur. As real liquids feature both interactions, thermodynamic states occur in which a transition between monotonic and oscillatory decay results. In a ρ - T -diagram this transition is marked by the so called Fisher-Widom line (see Fig.1.2). If long range interactions are present, as in the case of molten salts, the transition from exponential to oscillatory is represented by the Kirkwood line. In both cases, for charge as well as for number density oscillation, the decay length ξ and the periodicity d is the same.

Chapter 2

Small Angle Scattering

2.1 Small Angle Scattering

Small angle scattering (SAS) is an established method of diffraction to probe the structure of matter on length scales from Ångstrom up to one hundred Nanometer. An impinging wave is deflected by the molecular or mesoscopic structure of the sample into a solid angle, where it is recorded by a detector. The amplitude of scattering I_{SC} is determined by the scattering length b of the scattering source. Two different SAS techniques, Small Angle X-ray Scattering (SAXS) (photons) and Small Angle Neutron Scattering (SANS) (cold neutrons) were used in this work, whereas primary focus is laid on X-ray radiation. For both methods the principle of scattering is similar, whereas the radiation, and with it the center of scattering, is different. Several monographs can be found in literature giving excellent introduction into the topic [2, 41, 172, 242].

X-ray radiation, constituting of photons, is an electromagnetic wave and is scattered at electrons. The free, single electron is the basic center of scattering. A key feature for SAS techniques is that they consider scattering to be elastic. The wavelength λ' of the scattered particle is the same as the incident wavelength λ . No energy is transferred to the point at which the wave is scattered. The particle, having a wave vector $k = 2\pi/\lambda$, has a wave vector transfer $q = k - k'$ (see Fig. 2.1). The wave vector transfer q in a scattering experiment depends on the incident wavelength and the angle of scattering 2Θ and can be calculated following Eq. 2.1.

$$q = \frac{4\pi}{\lambda} \sin\left(\frac{2\Theta}{2}\right) \quad (2.1)$$

The incident wave is scattered at different particle positions. The subsequent electric field from each scattering event at the sample is superposed, leading to constructive or destructive interference, resulting in the observed scattering pattern recorded by the detector. The interaction with matter is assumed to be weak and multiple scattering effects are not considered (kinematical approximation).

In a SAS experiment the fundamental quantity determined is the differential scattering cross section (see Fig. 2.2), which is given in Eq. 2.2. The incident radiation with a

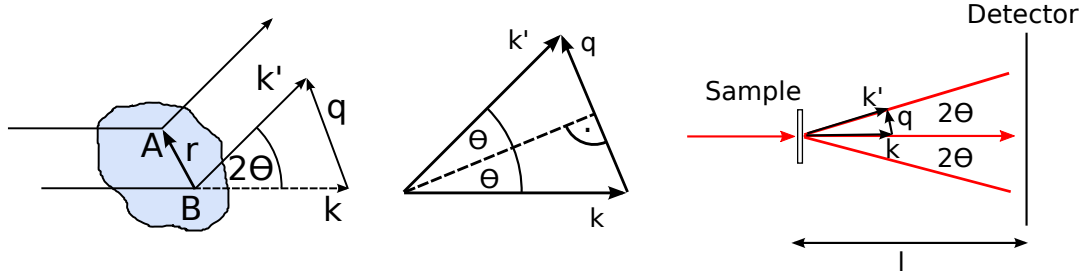


Figure 2.1: Left side: The incident beam with a wave vector k is scattered into the solid angle 2Θ by different volume elements of the sample. The angle 2Θ and the incident wavelength λ are the measurable quantity making it possible to determine the wave vector transfer q (see Eq. 2.1). Middle: The scattering triangle depicts the dependency of wave vector transfer and wave vector on the incident radiation and angle of scattering. Right side: Scattering geometry in a SAS experiment

flux Θ_0 [particles $\text{s}^{-1}\text{cm}^{-2}$] is scattered by the sample into a solid angle Ω .

$$\frac{d\sigma}{d\Omega} = \frac{I_{SC}}{\Theta_0 \Delta\Omega} \quad (2.2)$$

The differential scattering cross section describes what is actually measured in a SAS experiment: the flux of the scattered beam I_{SC} , normalized to the flux of the incident beam Θ_0 and the solid angle Ω covered by the detector, measured as a function of scattering angle. It gives the probability that a photon or neutron is scattered into that solid angle, whereas details of the experiment (flux of incident beam Θ_0 , size of detector Ω) have been normalized away as can be seen by the denominator in Eq. 2.2.

But what is influencing this measured intensity of photons, scattered into a solid angle? We will deal with X-rays first, later addressing neutron scattering. The ability of a particle to scatter is characterized by the scattering length b , having a unit of distance. Every single, free electron has the same ability to scatter, described by the classical electron radius, also called Thomson scattering length, of $b = 2.82 \times 10^{-15}$ m. Scattering length of an atom or compound depends on the number of electrons. The scattering length of a particle can therefore be calculated by multiplication of the Thomson scattering length and the number of electrons in the particle $b_x = b z$. Thus scattering length is proportional to atomic number for X-rays. Materials with higher z show stronger interaction with X-ray radiation, for example higher absorption, and scatter more strongly. For atoms, the ability to scatter X-rays depends on the number of electrons in the atom and is described by the atomic scattering factor f . The atomic scattering factor f is dependent on incident photon energy and angle. In SAXS, dealing with small angles, it is a good approximation that scattering takes place in forward direction, making the angle dependency negligible. The wavelength dependency can be described by Eq. 2.3

$$f = z + f'(E) + i f''(E) \quad (2.3)$$

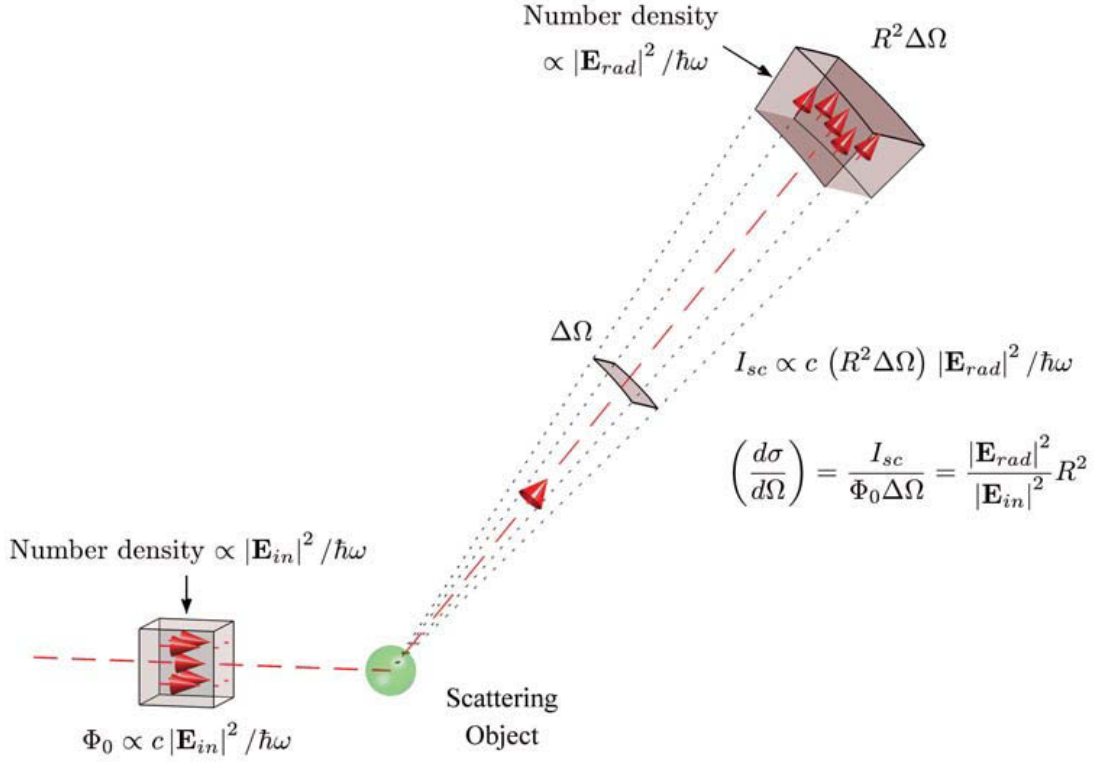


Figure 2.2: Scattering of photons into a solid angle. The incident beam intensity is represented by Φ_0 which is proportional to the absolute square of the incident electric field $|\mathbf{E}_{in}|^2$. Depending on the internal electron structure of the scattering object (green), the incident photons are scattered into a solid angle $\Delta\Omega$. The intensity I_{SC} is the recorded quantity during an X-ray scattering experiment. It can be normalized to experimental parameters like incident beam intensity Φ_0 and solid angle $\Delta\Omega$. Figure taken from J. Als-Nilsen [2].

Here z is the number of electrons of the atom, E is the photon energy and $f'(E)$ and $i f''(E)$ are the dispersion coefficients. The dispersion coefficients are energy dependent. They change distinctly, when an absorption edge is approached and the incident photon has the right quantity of energy to interact with an electronic level in the atom. At adsorption edges $f'(E)$ reaches a minimum. Whereas the imaginary part $i f''(E)$ rises steeply at absorption edges and accounts for absorption effects.

The distribution of electrons within the atom can be assumed to be continuous and can be approximated by the electron density ρ_e . The electrons can be imagined as surrounding the nucleus like a cloud. The quantity we are now interested in is the amount of scattering of all the electrons in an atom. Keeping in mind that the intensity is the absolute square of the scattered amplitude $I_{SC} = |F| \cdot |F^*|$, we can describe the

amplitude of scattering from an atom by

$$f(q) = \int_{\text{atom}} \rho(r) \exp(iqr) dr \quad (2.4)$$

To evaluate the scattering amplitude $F(q)$, the electron density in the atom is weighted by a phase factor and integrated over the whole atom. This equation describes the atomic scattering factor as an integral over all the scattering volume elements of an atom. Equation 2.4 can easily be extended to molecules and particles, as the basic principle of a scattering factor, describing the scattering amplitude of the structure under consideration, remains the same. For molecules the molecular scattering factor F_j^{particle} describes the scattering amplitude of the j -th particle.

$$F(q) = \sum_{r_j}^{\text{particles}} f_j^{\text{particle}} \exp(iqr_j) \quad (2.5)$$

As can be seen in Equation 2.4, the dependency of the scattering amplitude is a Fourier-Transformation of the electronic structure of the sample. This is a key feature of scattering experiments. The mathematical transformation from the so-called real space (electron) structure to a scattering pattern is given by a Fourier-Transformation, linking the sample structure to the reciprocal space (picture space) which is the measured signal after scattering. This becomes even more clear when looking at the inverse Fourier-Transform of Eq. 2.4.

$$\rho(r) = \int_V f(q) \exp(-iqr) dr \quad (2.6)$$

Unfortunately, a direct back transformation to real space is not possible from the measured quantity reciprocal space in SAS. As mentioned earlier, the measured quantity in a scattering experiment is intensity I_{SC} . The phase information of the radiation detected is not included and lost during measurement. As the intensity is a complex function of the amplitude, extraction of both, real and imaginary part, of the single unit of measurement intensity I_{SC} is not possible. Hence, a direct electronic distribution is not obtainable via Eq. 2.6.

To derive information about the internal structure of the sample, the actually measured scattering patterns are fitted by models for the scattering amplitude, i.e. a formula derived for the model of electron density. However, this requires some prior assumptions about the scattering structure to extract information by parameter refinement, because several parameter combinations can achieve satisfying results. Several approaches are possible, some depending on models for the scattering structure, some use direct modeling [157, 199, 207]. Different models have been established[209], like Landau theory [170], asymmetric Lorentz or Teubner-Strey [264], just to name a few. All approaches extract valuable parameters describing the (liquid) structure, when depending on carefully considered sample properties. How liquid structures can be further probed by scattering methods is described in the next section.

The same methods and principles described above also account for neutron scattering. The principle of scattering cross section, leading to a fraction of incident radiation becoming scattered into a solid angle and detected, is the same. Also scattering geometry, as depicted in Fig. 2.2, remains the same. However, special consideration has to be taken on generation, collimation, monochromatization and detection of the neutron radiation. A good introduction into instrumentation can be found in Ref. [57]. Neutrons are uncharged elementary particles, they are scattered by atomic nuclei. The neutron scattering length b is dependent on nuclei properties and varies for different isotopes. For cold and slow neutrons, it is a good approximation that the scattering length is independent of their wavelength. Varying irregularly, the neutron scattering length does not increase with increasing atomic number, as in the case for X-ray. Especially the distinct difference between hydrogen and deuterium enables the use of labeling techniques to achieve good scattering density contrast between structures where X-ray scattering length density contrast is insufficient. Furthermore, composing samples or solvents with diametrically opposed scattering lengths, particles can be made "invisible" in neutron scattering experiments, improving contrast at sites of interest. Particularly for low z -elements, where X-ray scattering contrast is notoriously weak, this is an advantage of neutron scattering. Hence, X-ray and Neutron scattering are complementary techniques due to the similar principle but different centers of scattering.

2.2 Probing Liquid Structure by Scattering Methods

As demonstrated in the previous section 2.1, the measured quantity in scattering experiments is scattered intensity into a solid angle. Here we want to derive how an observed intensity can be used to describe a liquid structure which is characterized by a distribution function.

The scattered intensity I_{SC} was introduced to depend on the atomic scattering factor $f(Q)$. As a liquid is composed of a lot of atoms arranged in a packed manner, this arrangement has to be accounted for. When the system comprises of N identical particles, taking into account the scattering of all the particles leads to Equation 2.7.

$$I_{SC} = N f^2(q) + f^2(q) \sum_n \sum_{m \neq n} \exp(iq(r_n - r_m)) \quad (2.7)$$

$$I_{SC} = N f^2(q) S(q)$$

Here, the first term describes the scattering of the individual particles N and is referred to as the particle form factor $f^2(q)$, whereas the second term describes the inter-particle interactions. The second term can be referred to as the structure factor $S(Q)$ or interference term, taking into account the interference of the radiation scattered by the liquid structure formed by the arrangement of the particles. Hence, the liquid structure factor can be written as:

$$S(q) = 1 + N \sum_k \frac{\sin(q r_k)}{q r_k} \quad (2.8)$$

The distance r_k describes the distances of the k -th particle to the particle at the origin (see Fig. 1.1b). Thus, this equation already includes a description of the interparticle distances, that means the liquid structure, a quantity also described by the radial distribution function $g(r)$. Introducing the radial distribution function $g(r)$ into Eq. 2.8, we derive Eq. 2.9.

$$S(q) = 1 + \frac{N}{V} \int_0^\infty 4\pi r^2 g(r) \frac{\sin(q r)}{q r} dr \quad (2.9)$$

$$S(q) = 1 + n_0 \int_0^\infty 4\pi r^2 g(r) \frac{\sin(q r)}{q r} dr$$

Here it was taken into account that the considered volume element is $4\pi r^2 dr$ and the total volume is V . The number density of particles in the scattering volume is $n_0 = N/V$. The integral denotes that the radial distribution function is a continuous function and replaces the summation. The radial distribution function converges to 1 for large q . In practice, the measured intensity, described by the liquid structure factor $S(q)$ converges to 0. The practically accessible function is the reduced pair distribution function $h(r) = g(r) - 1$.

$$S(q) - 1 = n_0 \int_0^\infty 4\pi r^2 [g(r) - 1] \frac{\sin(q r)}{q r} dr \quad (2.10)$$

Equation 2.10 links the measured intensity signal $S(q)$ with the reduced pair distribution function $h(r)$ which fluctuates around 0. In scattering experiments, the scattered intensity $I_{SC} \propto S(q)$ is linked to the distribution function in real space via a Fourier-transformation. Via a reverse Fourier-transformation analysis, the radial distribution function $g(r)$ is directly accessible by scattering experiments. This is described by Eq. 2.11.

$$g(r) - 1 = \frac{1}{n_0} \int_0^\infty 4\pi r^2 [S(q) - 1] \frac{\sin(qr)}{qr} dq \quad (2.11)$$

In scattering experiments, the liquid structure factor $S(q)$ is quantified by measuring the scattered intensity. From the liquid structure factor $S(q)$ in turn, conclusions can be drawn about the structural arrangement of liquid molecules. Equation 2.11 connects reciprocal space, on the right side, with real space, on the left side. The mathematical operation of Fourier-transformation links information gained in each space.

This demonstrates that scattering experiments are an excellent tool to probe liquid structures. A direct measurement of a statistical quantity, the radial distribution function $g(r)$, immediately describing the structure formed, is accessible. This is appreciated, as liquid structures are especially characterized by their arrangement across larger volumes of molecules. On short distances, a liquid molecule structure can be densely packed, often indicated by a first sharp diffraction peak in scattering patterns (c.f. Fig. 1.1a). What is of special interest is both the short and long range structure within the bulk liquid. Scattering experiments show their advantage in describing both length scales of the liquid structure in a non-invasive manner, having at least molecular resolution. This makes them a valuable tool to research on structures in liquids nearly unmatched by any other technique.

Chapter 3

X-ray Reflectivity

The discussion of this section on X-ray reflectivity (XRR) is based on the detailed introduction into the topic found in the dissertation of M. Mezger [173], P. Reichert [214] and H. Schröder [237], as well as the work by J. Als-Nielsen [2].

3.1 Reflectivity

In the previously introduced scattering experiments the wavevector transfer q has no specific direction and several structure length scales are probed at once. It is possible though to resolve the structure in a specific direction by pointing the wave vector transfer into a discrete angle. When reflecting at an interface, the wave vector transfer stands perpendicular to the interface and the structure perpendicular to the interface is probed (see Fig. 3.1). The interaction of matter with electromagnetic waves is described by the refractive index n .

$$n = 1 - \delta + i \beta \quad (3.1)$$

The real part δ describes the dispersion and the imaginary part β the absorption within the material. Both parts are dependent on the atomic form factor f of the atoms constituting the material and electron density ρ_e in the material:

$$\delta = \frac{\lambda^2}{2\pi} r_e \rho_e \frac{f^1(q)}{z} \approx \frac{\lambda^2}{2\pi} r_e \rho_e \quad (3.2)$$

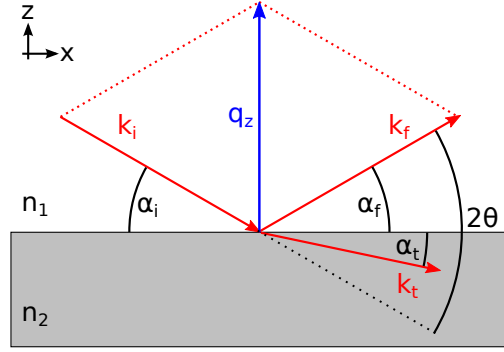
$$\beta = \frac{\lambda^2}{2\pi} r_e \rho_e \frac{f^2(q)}{z} = \frac{\lambda}{4\pi} \mu \quad (3.3)$$

In the optical regime, the refractive index is positive with values of 1.2 to 2.0. When positive, as in the X-ray region, the real part leads to the effect of total external reflection of an impinging electromagnetic wave as the resulting refractive index becomes less than 1. The imaginary part β is related to the absorption coefficient μ . Absorption shows a negative exponential dependency of intensity $I_{ref} = \exp(-\mu l)$ on distance l traveled in the material.

We see that the refractive index is wavelength, that means frequency dependent. As X-ray frequencies are higher than most electronic transition frequencies in atoms, the

3 X-RAY REFLECTIVITY

Figure 3.1: XRR geometry: The incident beam hits an interface at angle α_i . Both incident angle and refracted angle are equal $\alpha_i = \alpha_f$. The two materials have refractive indices n_1 and n_2 , respectively. The incident beam is either totally refracted when $\alpha_i \leq \alpha_c$ or it is refracted and transmitted into the material, as depicted here. The refracted beam in the material is bent towards the interface.



index of refraction decreases to values slightly lower than unity. As the difference to 1 is tiny, the resulting critical angles of total reflection are small. Qualitatively, the transmission of an electromagnetic wave and the resulting angles at an interface are described by Snells law:

$$n_1 \cos(\alpha_i) = n_2 \cos(\alpha_t) \quad (3.4)$$

When considering $n_1 = 1$ to be the refractive index of vacuum and $n_2 < 1$, it is clear that the transmitted beam in the material is bent towards the interface. A keep in mind here is that Snells Law derives from the optical regime, in which, in contrast to most X-ray notations and in contrast to Fig. 3.1, the angles are usually assigned towards the interface normal. Snells law can be expanded to yield the critical angle of total reflection $\alpha_c = \sqrt{2\delta}$. As depicted in Fig. 3.1, the ideal reflecting interface is assumed to be sharp and flat. When applying the boundary condition that the wave refracted at such an interface is continuous, the quantitative distribution of the wave, the reflectivity r and the transmittivity t , are described by the Fresnel equations:

$$r = \frac{k_{i,z} - k_{t,z}}{k_{i,z} + k_{t,z}} \quad (3.5)$$

$$t = \frac{2k_{i,z}}{k_{i,z} + k_{t,z}} \quad (3.6)$$

The reflectivity r and the transmittivity t describe the amplitudes of the reflected electromagnetic waves, not the intensity. The measured quantity in reflectivity experiments however is, just as in scattering, the intensity. For an ideally sharp and flat interface the intensity is hence received by the *Fresnel Reflectivity* R_F .

$$R_F = |r|^2 = \left| \frac{k_{i,z} - k_{t,z}}{k_{i,z} + k_{t,z}} \right|^2 \quad (3.7)$$

$$\approx (4\pi r_e \rho_e)^2 \frac{1}{q^4} \quad \text{for } q \geq 3q_c$$

The *Fresnel Reflectivity* R_F describes the ideal reflectivity at an ideally flat and sharp interface and is the maximum intensity achievable. Reflection is always specular, that

means it is confined to the x-z-plane into which also the primary beam is reflected. As can be deduced from Eq. 3.7, the *Fresnel Reflectivity* R_F is a smoothly but quickly decaying function, as the q^{-4} dependency shows. This is a characteristic behavior of reflectivity experiments. Decay of intensity at higher q , that means at higher angles, is fast. Hence reflectivity measurements often cover several magnitudes of intensity. Especially at higher angles with low signal intensity, this makes measurements sensitive to background scattering. Thorough elimination of background scattering is crucial to achieve good results.

As depicted by Fig. 3.1, the interface so far was assumed to be ideal. This seldom applies, even under laboratory conditions. A real interface is never a discrete step function as it is neither ideally flat nor sharp. Interfacial roughness will influence XRR distinctly. When the Fresnel reflection is the ideally achievable reflection, all surface roughness will diminish intensity from there. Roughness can be described by height fluctuations of the interface and can be correlated or uncorrelated height differences in z-direction.

For uncorrelated roughness an exponential damping factor accounts for intensity decay rooted in the interfacial structure as described by formula 3.8.

$$\frac{I_{SC}}{\Theta_0 \Delta \Omega} = \left(\frac{I_{SC}}{\Theta_0 \Delta \Omega} \right)_{\text{Fresnel}} e^{-q_z^2 \sigma^2} \quad (3.8)$$

Roughness enters the formula as a negative quadratic exponent σ^2 . The parameter σ is the root mean square roughness (rms). When describing the surface roughness by a Gaussian distribution, σ^2 is the roughness parameter, describing the width of the Gaussian error function. It can be shown that for uncorrelated surface roughness, reflected intensity is scattered in specular direction, similar as for a perfectly flat interface.

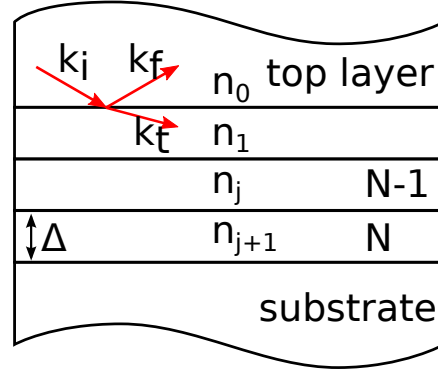
This is different for correlated interfacial structure. A rough interface with correlated structure also results in diffuse scattering, deviating from specular scattering direction. This is accounted for by a diffuse component, as depicted by formula 3.9.

$$\frac{I_{SC}}{\Theta_0 \Delta \Omega} = \left(\frac{I_{SC}}{\Theta_0 \Delta \Omega} \right)_{\text{Fresnel}} e^{-q_z^2 \sigma^2} F_{\text{diffuse}}(q) \quad (3.9)$$

Scattering by correlated roughness surfaces, which are obviously physically far more meaningful than uncorrelated interface structures, decays even stronger in intensity.

This illustrates which huge impact already small deviations from a sharp interface can have. Roughness in the nanometer range severely influences, if not even hampers, reflectivity measurements. Intensity drops fast under the influence of interfacial roughness, obstructing measurements especially at the higher angle regions. This demonstrates that surface preparation is critical for successful XRR measurements. Multiple interfaces, all contributing with their individual, not fully suspendable roughness, aggravate measurements further.

Figure 3.2: Recursive refraction of an incident X-ray beam at a model structure consisting on N slaps. Each slap has a thickness of Δ and a refractive index of n_j . Top layer and substrate are infinite. The intensity reflected from the top layer of such a model structure can be obtained by a recursive solution of the Fresnel formulae at each interface, the Parratt formalism.



3.2 Probing Structures by Reflectivity

So far only refraction at a single interface has been considered. For a single interface the amplitudes for the reflected and transmitted waves are given by the Fresnel formulae given in Eq. 3.5. However, the strong suit of X-ray reflection lies in the elucidation of complex vertical molecular structures. Alteration of electron density due to changes in molecular structure is the source of different local refractive indices, leading to refraction at interfaces detaching them (see Fig. 3.2). A description of this structure can be achieved by a model structure made up of consecutive slaps of different refractive indices n_j with the first and last slap considered to be indefinite. When consisting of multiple slaps N detached by discrete interfaces, refraction/transmission occurs at each consecutive interface. Combining the Fresnel coefficients of the single interfaces under consideration of Snells law at each interface leads to an exact solution for the reflectivity obtained by a complex structure consisting of multiple slaps. The recursive calculation of the reflectivity coefficient r_j at every interface, starting from the bottom layer N up to the top layer $N - (N - 1)$ gives the reflectivity of the whole structure, measured as reflectivity from the top layer, influenced by the interference of the refractions of the structure beneath it. Exact reflectivity results for a multilayered system with ideal interfaces are achieved by this approach which is called recursive Parratt formalism [196]. For each slap a transition coefficient $X_j = r_j/t_j$ and a reflectivity coefficient $r_{j,j+1}$ result as stated in Eq. 3.10 and Eq. 3.11. The reflectivity of the interfering layers is given after N iterations by $R = |X_1|^2 = |R_1|^2$. The Parratt formalism is only valid in the kinematical region, neglecting multiple reflections at one interface. Hence it holds only true far away from the critical angle q_c , in the regime $q \geq 3q_c$.

$$X_j = \varphi_{i,j} \frac{(r_{j,j+1} + X_{j+1} \varphi_{j+1,j})}{(1 + r_{j,j+1} X_{j+1} \varphi_{j+1,j})} \quad (3.10)$$

$$r_{j,j+1} = \frac{(k_{j,z} - k_{j+1,z})}{(k_{j,z} + k_{j+1,z})} \quad (3.11)$$

$$\varphi_{l,m} = \exp(-2i \exp(i\pi(l+m))k_{l,z}z_m) \quad (3.12)$$

The Parratt formalism enables the description of a more complex molecular structure. The reflectivity experimentally measured is the reflected intensity $I_R = |r(q)|^2$, lacking

phase information of the signal. This is obstructing a direct inverse Fourier- Transformation of the signal from reciprocal space to real space. Meaningful information from reflectivity experiments can be gathered by fitting model reflectivity functions, for example derived from the Parratt formalism, to the experimentally obtained data curves. Based on prior information of the sample structure, a model structure is drafted including parameters such as layer material, thickness, refractive index, electron density and more. If more parameters are known beforehand, this adds physical significance to the function as less parameters are volatile. As the shape of the model curve depends on the parameters chosen for the model surface, parameter refinement can lead to an understanding of sample structure properties.

Problems in the optimization process can occur when complex stratified structures with large differences in thickness and electron density have to be considered. Slap thickness can range down to 0.2 \AA to gain required resolution for molecular structures, leading to computationally difficult high numbers of slaps when layers in micro-meter size occur in the structure. This aggravated a quantitative evaluation for the interfacial structure observed in this work. However, qualitative evaluation of the observed reflection signal is still possible.

Chapter 4

Ionic Liquids

The complex liquids used in this work are ionic liquids. Ionic liquids are salts with a melting temperature T_m below 100°C and consist solely of ions [287]. Attractive intermolecular coulombic interactions are reduced by the anions and cations molecular architectures (see chapter 1.1), diminishing crystallization enthalpies [135]. A typical IL is composed of a bulky asymmetric organic cation paired with an inorganic, polyatomic anion which can distribute its negative charge. The chemical structure of each individual ion has a huge influence on physical and chemical properties of the resulting IL. By changing the ion's molecular architecture a wide variety of parameters can be accessed. Also, structure and solvent properties can be tailored by the selection of a specific anion and cation combination [194]. Hence, ILs have a huge chemical design space, leading to the term "designer solvents" [63]. Featuring a wide temperature window in which they are liquid, some ILs exhibit melting temperatures as low as -60°C [287]. Some exhibit a high thermal stability with negligible vapor pressures up to their decomposition temperatures [52]. Decomposition temperatures ranging from 200 to 300°C were reported, depending on the IL [44, 132]. They can also be optimized for a wide electrochemical window and high electrical conductivity [298]. These unique properties make them promising candidates in a variety of applications such as green solvents [223], heterogeneous catalysis [259], and electrochemistry [8].

The easiest approach for a synthesis of standard ionic liquids is a two-step process:

- Formation of desired cation
- Metathesis with a desired anion where necessary

This scheme roots in the chemically easily altered cation structure. Especially for imidazolium based cations chemistry is non-problematic. Cation chemistry results in stable (chemically, thermally, electrochemically), easy to handle, relatively unharmed and cheap ILs, with low melting points. Several imidazolium precursors are commercially available being easily adapted to the required properties. This made imidazolium based ILs the cations of choice for this work. The cations of the ionic liquids used in this work were imidazolium $[C_nC_nim]^+$ based with an alkyl-substitute in position 1 and 3 at the imidazolium ring. The 1 position was substituted by a methyl-group,

4 IONIC LIQUIDS

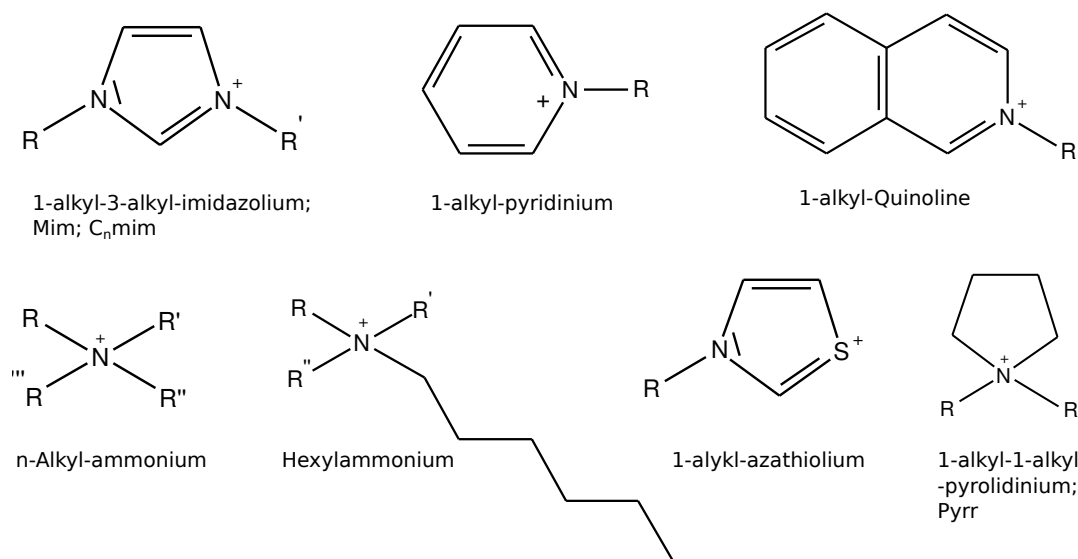


Figure 4.1: Commonly used cations in Ionic Liquids. In this work, imidazolium based cations were used (top left corner). Cations exhibit easy but influential structure adaptation at the positions indicated by R . No chemical formula are given explicitly, as type and length of R have a huge impact on IL properties. Only for imidazolium and pyrrolidinium colloquial abbreviations are stated.

whereas in the 3 position longer alkyl side-chains ($n = 8, 10, 18, 22$) were used. In a *Debus-Radziszewski*-reaction imidazole is achieved by a reaction of glyoxal and formaldehyde in ammonia. For the production of 1-methylimidazole (C_1 im) imidazole is methylated with methanol. This universal precursor is usually commercially available. In a quarterization reaction with for example halogenalkane it can be tailored with a alkyl side-chain of desired length, resulting in a molten salt made of the IL cation and halogen counter ion [308].

A variety of different anions are available (see Fig. 4.2), although IL-anions are chemically less easily accessible. Hence, on a laboratory scale anions are often bought commercially and then introduced in the second step, the metathesis anion exchange reaction. This diminishes the creativity of the experimentalist. The anions of ILs are often perfluorinated to make them chemically more stable. Hydrolysis diminishes IL stability at the anion, when not better protected by perfluorination [64, 280, 292]. Small, simple, often hygroscopic anions like chlorine Cl^- or bromine Br^- can be introduced by the metathesis step. More complex anions like bis(trifluoromethyl-sulfonyl)imide $[NTf_2]^-$ require a multi-step synthesis, often incorporating fluorine chemistry, making it chemically demanding to perform [47, 62]. The anionic structures used in this work were diverse and covered small, hydrophilic anions like chloride Cl^- over medium sized hydrophobic anions like tris(pentafluoro-ethyl)trifluorophosphate $[FAP]^-$ or bis(trifluoromethylsulfonyl)imide $[NTf_2]^-$ to large hydrophobic anions like bis(nonafluorobutylsulfonyl)-imide $[NNf_2]^-$.

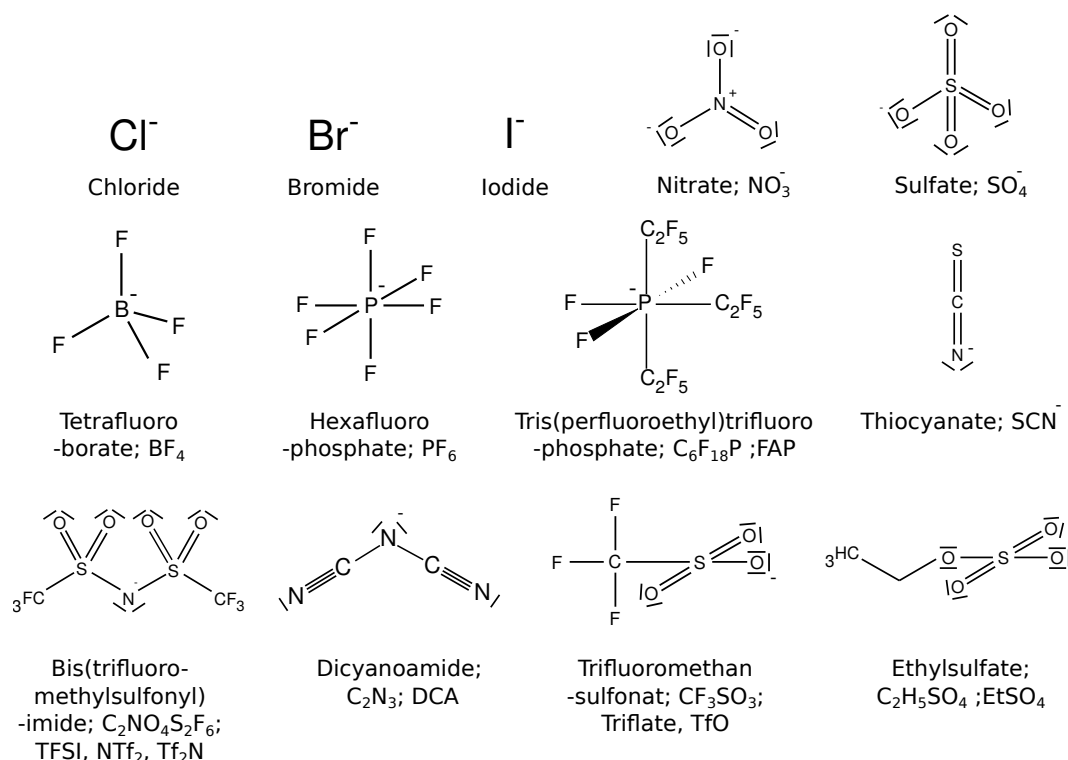


Figure 4.2: Commonly used anions in Ionic Liquids. Ions are labeled by name, molecular formula and abbreviations often found in literature to reference them. Anions used in this work are Cl, FAP, NTf₂ and NNf₂ (not shown).

4.1 Hydrophilicity/Hydrophobicity of Ionic Liquids

Most ILs are more or less hydrophilic, if not even hygroscopic, as can be derived from Tabel 4.1. The chemical structure of the IL molecules directly dictates the solvation behavior [33]. The hydrophilicity of an IL is influenced by both cation and anion structure [287]. However, anion chemical structure has a bigger impact [102].

When looking at the water solubility of the cation, a decreased polarizability decreases water miscibility. Hence, a delocalisation of charge across an aromatic system, as found in for example imidazolium based ILs, is an advantage. Other cations, like ammonium or pyrrolidinium based ILs, have a more localized charge. Furthermore, the cations potential ability to form hydrogen bonds, as well as their side chain length has an important influence. When using 1-methylimidazole (C₁im) substituted with a longer alkyl-side chain in 3-position, no hydrogen bond can be formed, adding to the hydrophobicity of the IL. The substituted alkyl side-chain length additionally enhances water immiscibility. The longer the alkyl side-chain, the more hydrophobic the IL becomes due to the increased apolar part of the molecule [102]. For short side-chain lengths (n=4), ILs and water are fully miscible.

For the anion it holds true that the more organic the anion, the less hydrophilic

it becomes. Halogen anion based ILs are fully water miscible [79]. Whereas tetrachloroaluminates are hydrophilic in a sense that they react with water and decompose [280, 292] when exposed to moisture for a longer time, already Tetrafluoroborat $[\text{BF}_4]^-$ is much more water stable. Very hydrophobic, water stable at higher temperatures and stable in the presence of acids are anions containing fluorinated groups [19]. The fluorination increases hydrophobicity as it distributes the charge across the molecular structure. Most fluorinated anions can not form hydrogen bonds anymore, due to the fluorination. They become non-spherical in shape by the fluorinated groups, hence aggravating the attachment of small molecules such as water [211, 299]. An example for such molecules are trimethanesulfonates (triflate) $[\text{CF}_3\text{SO}_3]^-$ or bis(n-fluoroalkylsulfonyl)imides $[\text{CF}_n\text{SO}_2\text{N}]^-$. In general, polar molecules, especially when they are able to form hydrogen bonds with the ions, are organized around anions [163, 270]. Most small molecules are preferentially located around the anion in a more or less tightly bound manner [181, 235]. In particular, anion properties are crucial for the observed solvation behavior of polar solvents with low molecular weight. The subsequent screening of the anion charge influences the intermolecular interaction, leading to deviations in molecular liquid structure and thus different macroscopic behavior of the liquid.

But do small molecules influence the IL bulk structure? In combination with small molecules, such as water, the IL mesoscopic bulk structure can change distinctly. MD simulations show how the IL mesoscopic structure is influenced even by small amounts of solvents [4, 6, 113, 236]. Smirnova et al. reported that water soluble ILs with long aliphatic chains behave similar to surfactants, where different degrees of mesoscopic segregation or micelle formation are expected when mixed with different amounts of water [251]. For imidazolium-based ILs micelle formation was observed, depending on hydrophilicity of the anion and cation side-chain length ($n=8$) [140]. These systems might form different mesoscopic structures such as micelles or liquid crystalline phases, when mixed with different amounts of water. Hence, this would also apply to the IL used in this work, which has the same side-chain length. When dealing with protic imidazolium-based ILs, a stabilization of structures in connection with water was observed [139]. However, this does not apply in our case, as $[\text{C}_8\text{mim}]^+\text{Cl}^-$ is an aprotic IL. Not all small molecules are taken up similarly. A distinct difference in solution behavior can be observed for polar and apolar molecules [82, 83, 148].

4.2 Ionic Liquid Bulk Structure

The bulk structure of various ILs was extensively studied experimentally by X-ray scattering [23, 29, 42, 65, 66, 120, 174, 175, 176, 185, 227, 229, 233, 243, 271, 272], neutron scattering [42, 65, 87, 89, 271], coherent anti-Stokes Raman scattering [243], and computer simulations [5, 7, 89, 94, 119, 158, 159, 166, 194, 244]. By today, it is believed that ILs, composed of cations with long alkyl chains, exhibit structure on multiple length scales [7, 91, 119]. They originate from correlations of the different molecular

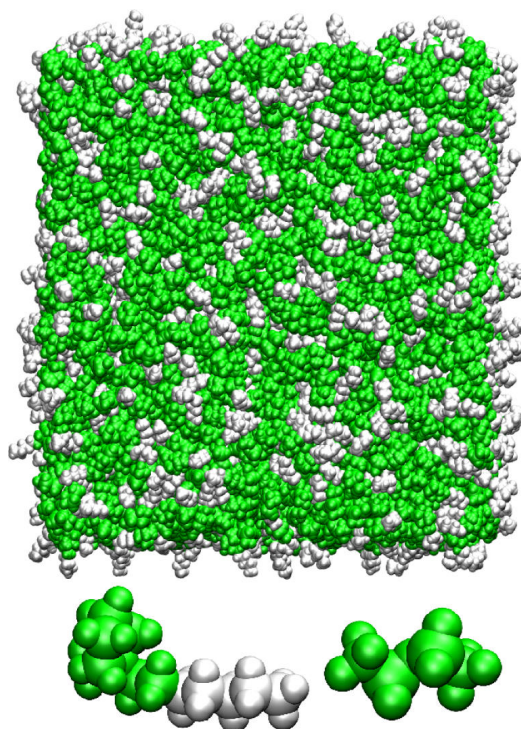
Table 4.1: Water miscibility of ILs. Taken from [19]. Original Table Heading: Water Content at Saturation in Mass%, at 20°C, of the Imidazolium Salts Which Are Liquids or Supercooled Liquids at That Temperature^a

Im ⁺	TfO ⁻	NfO ⁻	Tf ₂ N ⁻	TA ⁻	HB ⁻
3-Me					
1-Me	s		2.5	s	
1-Et	s	s	1.4	s	
1-Bu	s	17.5	1.4	s	s
1- <i>i</i> -Bu			1.5		
1-MeOEt	s		3.0		
1-CF ₃ CH ₂	s		2.5		
3-Et					
1-Et	s		2.0	s	
1-Bu		8.9	1.3	s	
1-Et-2-Me					
3-Me			1.8		
1-Et-5-Me					
3-Me	s		2.2		
3-Et	s		1.7		

^as: water soluble. Determination by Karl-Fisher titration; estimated error: $\pm 7\%$

moieties. Detailed understanding on the local distribution of anions and cations was obtained by comparing information from simulations and scattering techniques using empirical potential structure refinement [87, 233]. One particular feature that draws significant attention, is the appearance of a sharp diffraction peak in the small angle scattering region. For ILs with alkyl chains longer than a butyl group, a so-called pre-peak or first sharp diffraction peak (FSDP) in the total scattering structure function $S(q)$ is observed below 5 nm^{-1} [66, 272]. This momentum transfer corresponds to a real space length scale above 1 nm, indicating intermediate range mesoscopic order. The molecular architectures of these materials show an amphiphilic character. Intuitively, it was suggested that such ILs can form mesoscopic structures by micro-phase separation. Indeed, MD simulations showed that these ILs consist of ionic regions, where the negative and positive charges are located, alongside with non-polar regions composed of the aliphatic moieties [7, 245]. This mesoscopic structure was confirmed by systematic studies using small angle X-ray (SAXS) and neutron scattering (SANS) on a series of $[\text{C}_n\text{C}_1\text{im}]^+$ based ILs with Cl^- , $[\text{BF}_4]^-$, $[\text{PF}_6]^-$, and $[\text{NTf}_2]^-$ anions [23, 65, 66, 87, 227, 228, 229, 271, 272]. This allows correlating the dimensions of the structural inhomogeneities with the cation's alkyl chain length. Analysis of the pre-peak positions q_0 showed that the lengths of the alkyl chains govern the periodicities $2\pi/q_0$ of the underlying structures [87]. Therefore, it was concluded that the pre-peak originates from structural heterogeneities caused by polarity alternations between the polar and

Figure 4.3: Mesoscopic structure in 1-heptyl-1-methyl-pyrrolidinium $[\text{Pyr}_{1,7}]^+$ bis(trifluoromethylsulfonyl) amide $[\text{NTf}_2]^-$ ionic liquid depicted by a snapshot in molecular dynamics simulation. Colors are based on the polarity partitioning of $S(q)$. Bottom: Single ion pair, Left: 1-heptyl-1-methylpyrrolidinium cation, Right: bis(trifluoromethylsulfonyl)amide anion Green: polar, White: apolar. Reprinted (adapted) with permission from H. E. Kashyap et al. [121]. Copyright 2013 American Chemical Society.



apolar moieties [7]. In contrast to the strong effects of the cations, it was postulated that the influence of the anions on the liquid structure is rather weak. For a series of protic ILs Hayes et al. concluded that changing the anions has no significant effects on the structure of the IL [89]. Hettige et al. showed that changes in the peak intensities observed for ILs composed of different anions can be explained by the scattering contrast between polar and apolar moieties rather than changes in the liquid structure [94].

In this work, we systematically studied the temperature dependent liquid structure of a matrix of five ILs with methylimidazolium $[\text{C}_n\text{C}_1\text{im}]^+$, $n = 18, 22$ cations and large tris(pentafluoroethyl)trifluorophosphate $[\text{FAP}]^-$, bis(trifluoromethylsulfonyl)imide $[\text{NTf}_2]^-$, and bis(nonafluorobutylsulfonyl)imide $[\text{NNf}_2]^-$ anions. We present a quantitative analysis of the SAXS and SANS patterns based on a generalized Teubner-Strey model [264]. This analysis technique allows to extract information on the mesoscopic correlation functions $G(r)$ that are beyond the approximated length scales $d_p \sim 2\pi/q_0$ of the liquid structure. This provides information on the interplay between the anions and cations molecular architectures with structural and thermodynamical properties in imidazolium based ILs with long aliphatic side chains (Fig. 6.2 and Tab. 6.1).

Chapter 5

Confined Liquids

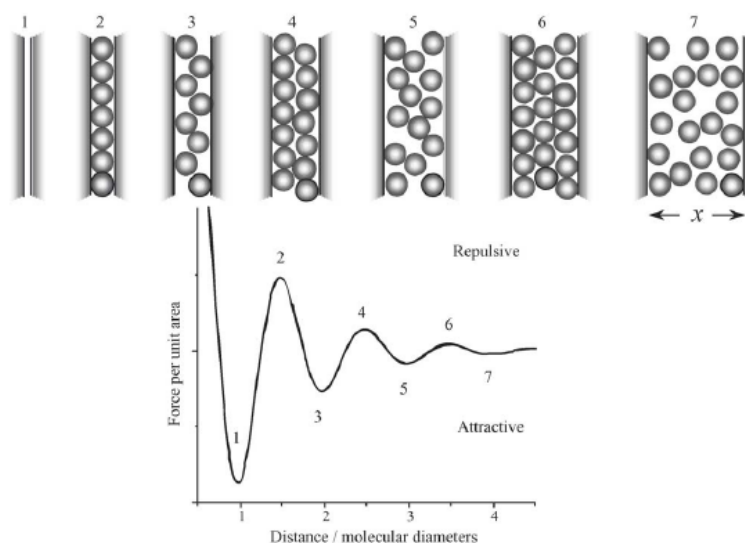
Due to their mobility liquids are frequently found at interfaces or confined between hard walls, for example when entering pores in an electrode-like structure. An interface between the liquid molecules and the solid medium results, with the molecular liquid structure changed from the bulk liquid structure close to the interface. It is well known that the liquid structure at an interface differs from that in bulk [25, 110, 205]. The structure formed often exhibits an oscillatory decaying density profile into the bulk liquid, leading to so called 'solvation layers'. The structure formation is not based on intermolecular forces such as van der Waals or electrostatic forces, but originates in a mere geometric effect introduced by the presence of the interface. Hence, this liquid ordering can also be observed in the absence of attractive surface-liquid interactions [110]. Theoretical descriptions were the first to predict solvation layers as early as the 1970s [1, 141, 254, 277, 278]. Simulation experiments found an oscillatory density profile for spherical molecules confined between two hard walls (see Fig. 5.1). At a solid surface, pronounced layering across several molecular diameters occurs even in simple liquids when solvation forces between particles are significant in comparison to van der Waals forces. The observed 'layering' does not mean particles are immobilized as in a frozen structure. They are just more localized. Despite the more localized structure, particles remain their liquid character and display motion in two dimensions across the surface.

5.1 Molecular Liquids at Interfaces

Indeed, it could be shown experimentally that layering at solid-liquid interfaces occurs. Oscillating density profiles were first observed in simple molecular liquids such as octamethylcyclotetrasiloxane (OMCTS) [99]. Simple molecular liquids, with their isotropic, neutral, large and nearly spherical structure, were easy first benchmark samples. The device making this possible was the newly developed surface force apparatus (SFA) by the group of J. Israelachvili [108] during the late 1970s. SFA continued to shed light on structures at interfaces and remains to be one of the key techniques to measure force oscillations on the nanometer range until today. The solid surface of choice is usually mica in SFA measurements. OMCTS was further investigated [129], but also other

5 CONFINED LIQUIDS

Figure 5.1: Schematic structure of a simple liquid confined between two parallel walls. The order changes drastically, depending on distance, which results in an oscillatory force. Figure reproduced from H. J. Butt et al. [25]



materials were shown to be prone to layering. Christenson observed structures at an interface by SFA in tetrachloromethane, benzene, and 2, 2, 4-trimethylpentane [40]. In tetrachloromethane and benzene structures reached out for about ten periods of molecular diameter, a length scale of about 5 nm. 2, 2, 4-trimethylpentane structure only extends about 2 nm from the interface. A comparison of the layering behavior of these three molecules with cyclohexane, octamethylcyclotetrasiloxane and n-octane showed that the internal rigidity of the molecules is the mayor influence, whereas molecular shape, size, and temperature are of minor influence to the structure. Dynamic characterization of the solvent layers is also possible by SFA. Dynamic SFA measurements of hexadecane and OMCTS were performed by the group of Steve Granick [276]. Both liquids exhibited an oscillatory density profile on mica and also showed an increased viscosity compared to bulk liquid viscosity when sheared in confinement on molecular length scales. This points to a solidification of the ordered structure at the interface for both geometrically spherical and unspherical liquids. The thesis of T. E. Balmer [12] researched on OMCTS in confinement by SFA. Here especially, the influence of relative humidity on OMCTS structure at the mica/liquid interface was elucidated. It was observed that mica adsorbs water and influences the oscillatory structure of OMCTS.

A more complex class of liquids are liquid crystals. Especially biphenyl-based liquid crystals with different side chain lengths have received much attention [184, 230]. Again it was the group of Israelachvili using an SFA to perform static and dynamic measurements on thin films of 4'-n-octyl-4-cyanobiphenyl (8CB) [230]. Layering at a mica surface is accounted for by an improved positional order introduced by confinement. During shear measurements the increased orientational ordering of the 8CB molecules is observed in the structured layers at the interface. This ordering seems to be shear induced, as it vanishes when dynamic oscillations of one of the surfaces stopped. Confining the nematic liquid crystal 4-cyano-4'-hexylbiphenyl (6CB) between mica surfaces, the group of Kurihara could show that the confinement effect can exceed the influence of the electric field orientation of the LC molecules [184].

Other interesting molecular systems are surfactants and the lyotropic systems displayed by them at interfaces. Such systems have been investigated by Parker [195]. Layers of hexadecyltrimethylammonium bromide (CTAB) on solid substrates show swelling when water molecules enter the layer by absorption from humid environment. A similar behavior is displayed by dihexadecyldimethylammonium acetate (DHDA), whereas calcium alkylbenzenesulfonate (CaABS) takes up water at low humidity, leading to swelling, but gets thinner at higher humidity. Zwitterionic phospholipid L- α -dimyristolphosphatidylethanolamine (DMPE) shows no swelling, as the alkyl chains are too close together and interact too strongly, preventing water penetration to the polar head group region. This shows how geometric, orientational and chemical layer properties dictate behavior of structure at the interface. Similar experiments using DHDA were performed by Ninham [197, 198].

Another technique to probe structures at an interface is atomic force measurements (AFM) [25, 68]. When measuring hexadecane on highly oriented pyrolytic graphite (HOPG) with a conducting tip, discrete jumps in tip-substrate conductance can be interpreted as discrete changes in the number of liquid layers [128]. Again, OMCTS, and also mesitylene, on HOPG show layered structures when probed in the magnetic a/c mode of AFM [81]. Probing OMCTS and n-dodecanol by AFM in force modulation mode showed that oscillatory structural forces can also be measured when using one surface with a high curvature, i.e. an AFM-tip with curvatures of $R \approx 14 \text{ nm}$ [193]. The effective viscosity for OMCTS solvation layers at a HPOG surface increases by ≈ 4 orders of magnitude.

Also, X-ray reflection methods are able to demonstrate layered structures at an interface. This method measures the structure at a real single interface, as it does not rely on a second interface as a probe. The group of P. Dutta investigated layered structures of silanes (tetrakis(2-ethylhexoxy)silane (TEHOS), tetrakis(trimethylsiloxy)silane (TTMSS) and octamethylcyclotetrasiloxane (OMCTS)) on a silicon surface [145, 305, 306]. These nearly spherical, non-reactive, insulating, non-polar and non-liquid-crystalline molecules display layering from three to six layers, which corresponds to structure ranges of 3.2 nm up to 6.4 nm. Temperature was shown to have only a small effect on the structure of these liquids [179]. Hexane was also studied by XRR and found to form layers extending up to 4.0 nm into the bulk of the film formed on a smooth silicon surface [50].

All techniques have shown that already simple liquids form layered structures at interfaces. Systems such as ionic liquids, which often have a mesoscopic bulk order, might show much more intriguing effects when perturbed by an interface.

5.2 Ionic Liquids at Interfaces

In Chapter 4 it was shown that ILs can display a rich bulk liquid structure. Whereas the bulk structure is well researched, knowledge on the solid-liquid interface structure is still scarce, although ILs, due to their chemical design space, promise good tuneability of the

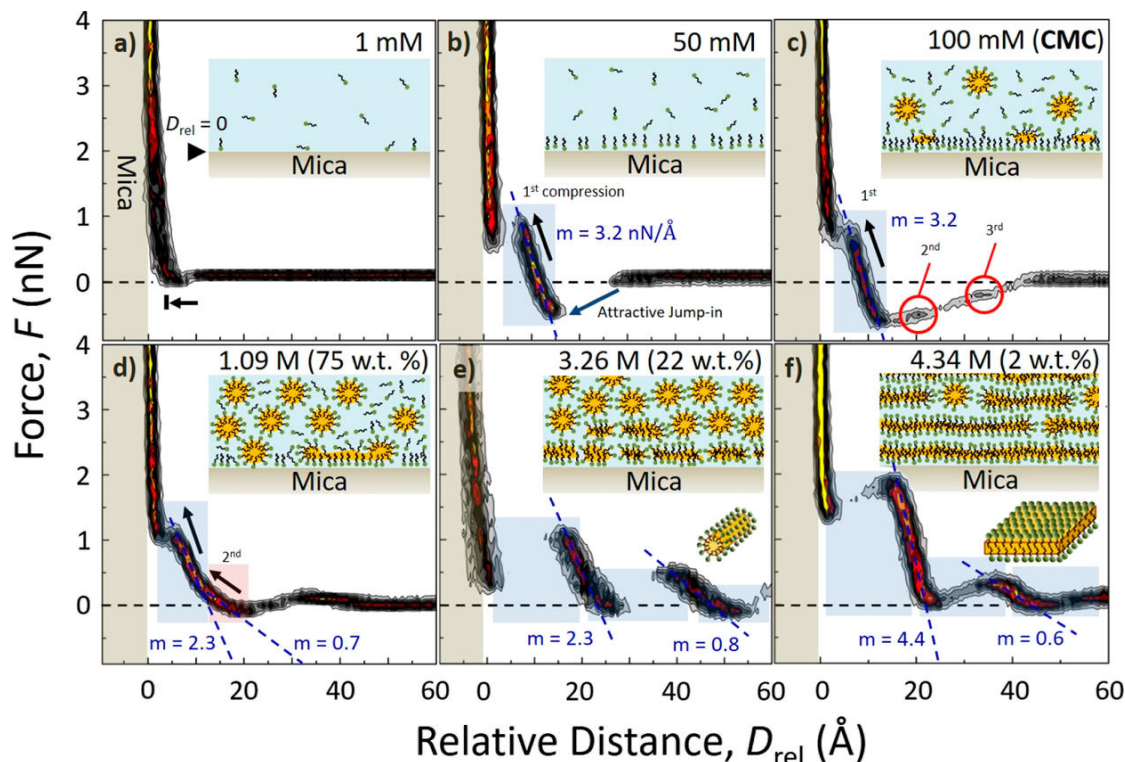


Figure 5.2: 2D-FD AFM measurements of water-concentration dependent interfacial structuring of $[\text{C}_8\text{Mim}][\text{Cl}]/\text{water}$ mixtures on freshly cleaved mica surfaces with schematic structural interpretations as inset. The slopes of compression curve are indicated in blue dash line. Figure and caption reproduced from H.-W. Cheng et al. [38].

interfacial structure. This mesoscopic bulk structure is now influenced by the presence of an interface. The mere presence of an interface would just impose generic geometric effects. A competition between bulk liquid structure and surface effects is observed. The bulk symmetry is broken at solid/liquid interfaces and the IL molecular scale structure is now governed by surface effects such as surface charge or hydrophobicity. However, the intermolecular interactions between the ions, as well as the specific interactions with the solid surface, have to be considered.

When using SFA or AFM to probe the structure, mica surfaces are often the surface of choice due to their inherent atomical roughness. Carrying potassium ions on the surface, the mica interface normally displays positively and negatively charged sites. However, mica becomes negatively charged when the potassium ions leave the surface and dissolves in the liquid, resembling charged metal surfaces.

Just like molecular liquids, ILs show layering at the mica interface (c.f. Fig. 5.2). Measuring by AFM on a mica surface, R. Hayes detected five to six solvation layers in three different aprotic ILs, namely 1-butyl-3-methylimidazolium hexafluorophosphate $[\text{C}_4\text{Mim}]^+ [\text{PF}_6]^-$, 1-ethyl-3-methylimidazolium bis(trifluoromethanesulfonyl)imide $[\text{C}_2\text{Mim}]^+ [\text{TSCFA}]^-$, and 1-butyl-1-methylpyrrolidinium bis(trifluoromethanesulfonyl)-

imide $[\text{C}_4\text{Mpyr}]^+ [\text{TSFA}]^-$ [88]. ILs were tested to be water-free by Karl-Fisher titration before experiments.

Complementary observations were made for the systems 1-butyl-3-methyl imidazolium hexafluorophosphate $[\text{C}_4\text{Mim}]^+ [\text{PF}_6]^-$ and 1-butyl-3-methylimidazolium tetrafluoroborate $[\text{C}_4\text{Mim}]^+ [\text{BF}_4]^-$ [20]. SFA measurements on charge-bearing mica surfaces showed oscillatory force profiles at the interface, extending 5-6 nm from the interface, with force oscillations corresponding to the average diameter of the neutral cation/anion pair. Dynamic measurements showed an increased viscosity of the structure up to 20 nm at the interface when measuring with bare mica surfaces. In contrast to that, mica surfaces coated with methyl-terminated self-assembled monolayers showed no such increased viscosity. Similar experiments of dynamic SFA measurements using a sphere-on-flat geometry, testing ILs under shear conditions, were conducted by Cross and co-workers [70], showing that the oscillatory density structure seems to be independent from confining surface distance.

Angle resolved X-ray photoelectron spectroscopy (ARXPS) showed how the ions of the two imidazolium-based ILs, 1-methyl-3-methylimidazolium bis(trifluoromethylsulfonyl) imide $[\text{C}_1\text{Mim}]^+ [\text{Tf}_2\text{N}]^-$ and 1-butyl-3-methylimidazolium bis(trifluoromethylsulfonyl) imide $[\text{C}_4\text{Mim}]^+ [\text{Tf}_2\text{N}]^-$ are orientated on mica surfaces [48]. On the negatively charged mica surface, the cation is adsorbed first, with the imidazolium ring lying flat on the surface. The cis-oriented anion $[\text{Tf}_2\text{N}]^-$ is located above the cation. The CF_3 groups are pointing away from the surface.

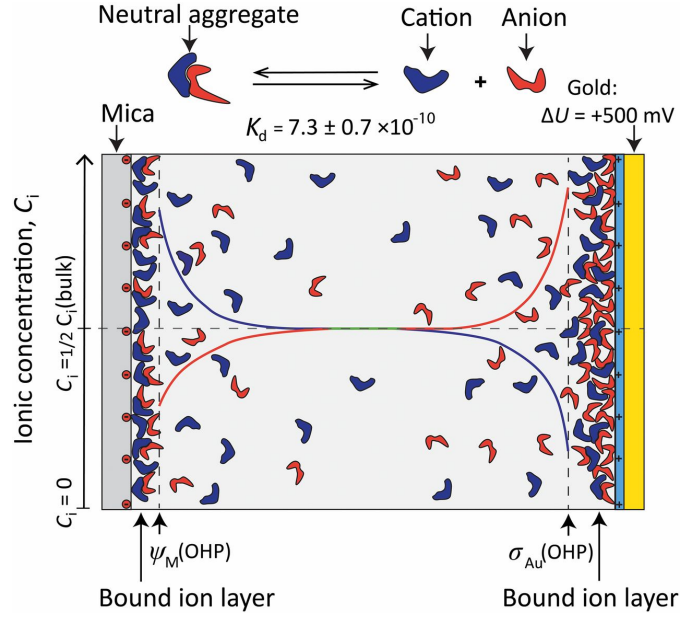
When using mica surfaces, water has been identified as a critical influence by the group of M. Valtiner [36, 37]. Water molecules present in the IL seem to enhance dissolution of surface bound potassium cations [71]. Using AFM and SFA, it could be observed how, due to this increased surface charge, stronger layering effects of the IL result (see Fig. 5.3).

Mica displays the highest charge density of atomically smooth surfaces used. But also other charged surfaces show layered structures of ILs. Silica is, just like mica, a hydrophilic surface, but has a lower charge density. An important difference between mica and silica is that the latter exhibits hydrogen-bonding sites in the form of silanol-groups. Layering of ILs on silica was observed by AFM measurements for the ILs ethylammonium nitrate $[\text{EA}]^+ [\text{NO}_3]^-$, propylammonium nitrate $[\text{PA}]^+ [\text{NO}_3]^-$ and 1-ethyl-3-methylimidazolium acetate $[\text{C}_2\text{mim}]^+ [\text{CH}_3\text{COO}]^-$ [10, 90]. However, the number of observed layers on silica is always less than for mica within one and the same IL.

Sum frequency generation (SFG) spectroscopy executed by the group of Fitchett and Conboy [61, 224] showed that the imidazolium ring is adsorbed first at the silica surface, when imidazolium based ILs are used. The ring is slightly tilted ($16\text{-}32^\circ$), whereas the alkyl chain stands nearly parallel to the interface normal.

The water influence on solvation layers formed in both mica and silica, was demonstrated by Sakai and co-workers [232]. When water is introduced into a hydrophilic IL like 1-butyl-3-methylimidazolium tetrafluoroborate $[\text{C}_4\text{Mim}]^+ [\text{BF}_4]^-$, solvation layers are disrupted and interfacial water adsorbs on silica. No interfacial water adsorption

Figure 5.3: Diagram of the diffuse electric double layers, formed by $[\text{C}_4\text{Mim}]^+ [\text{NTf}_2]^-$ ions for $\Delta U = +500 \text{ mV}$. Analogous electric double layers are formed for all other potentials. The lines overlaying the diagram indicate the relative concentration gradient of dissociated ions: blue represents cations; red, anions; and green, $C_{\text{cation}} = C_{\text{anion}} = 1/2 C_{i,\text{bulk}}$. The bound and diffuse electric double layers are enriched in cations (blue) at the negative mica surface and anions (red) at the positive gold surface. Figure and caption (partially) reproduced from Matthew A. Gebbie et al. [71].



was observed on mica, however. Water introduced into a hydrophobic IL like (1-ethyl-3-methyl-imidazolium bis(trifluoro methylsulfonyl) imide $[\text{C}_2\text{Mim}]^+ [\text{TFSI}]^-$ leads to a formation of interfacial water on both surfaces. This shows how the chemical structure of the IL and the chemical structure of the interface both influence interfacial structure behavior, especially when small polar molecules like water are introduced.

A material also offering atomic smoothness is highly oriented pyrolytic graphite (HOPG), which has seen application in AFM measurements as an electrically conductive substrate [10, 17, 149]. Also on this substrate, layering is observed for the ILs 1-hexyl-3-methylimidazolium tris(pentafluoroethyl) trifluorophosphate $[\text{C}_6\text{Mim}]^+ [\text{FAP}]^-$, 1-ethyl-3-methylimidazolium tris(pentafluoroethyl) trifluorophosphate $[\text{C}_2\text{Mim}]^+ [\text{FAP}]^-$, and 1-ethyl-3-methylimidazolium bis(trifluoromethylsulfonyl) imide $[\text{C}_2\text{Mim}]^+ [\text{TfSA}]^-$. Due to the conductivity of the HOPG, a potential vs. a Pt electrode can be applied, showing that at positive and negative surface potentials layering of the ILs is enhanced. At negative potentials, cations adsorb at the interface, lying flat on the surface due to π - π -stacking of the imidazolium ring and van der Waals attractions between the cation alkyl side-chain and the lattice of the HOPG. Thus, the distance between cation alkyl side-chains is increased, van der Waals interaction between them diminished and by that the cohesion of the ion layer. At positive potentials, anions form the first ion layer. IL layers pack more densely as cations form the second ion layer, orientated parallel and able to get closer to each other.

An inert, hydrophobic surface that can be electrified as well and manufactured to an atomically smooth roughness is gold. It has been especially used as a substrate in AFM and SFA experiments.

How imidazolium-based ILs orientate, depending on the the gold surface charge, was investigated by Y.-X. Zhong and co-workers [311]. Using enhanced force detection AFM measurements, resolution of sub-molecular ordering of the IL 1-octyl-3-methylimidazolium hexafluorophosphate $[\text{C}_8\text{Mim}]^+ [\text{PF}_6]^-$ was possible. At negative gold surface potentials, a consecutive ordering of imidazolium ring, alkyl chain, and then anion, was found. The order is basically reversed for negative potentials: anion, imidazolium ring and then alkyl chain.

Using a polished single crystal gold (100) electrode, AFM measurements in an electrochemical cell could shed light on the layering behavior of ILs at a charged surface [133]. Applying negative surface potentials, up to nine ion double layers were detected in 1-ethyl-3-methyl-imidazolium bis(trifluoro-methylsulfonyl) imide $[\text{C}_2\text{Mim}]^+ [\text{NTf}_2]^-$. Corresponding to that, weakly charged surfaces showed no force profile oscillations.

How the presence of water influences the structure of 1-methyl-3-ethylimidazolium bis(trifluoromethylsulfonyl) imide $[\text{C}_2\text{mim}]^+ [\text{Tf}_2\text{N}]^-$ was researched by Valtiner and co-workers using AFM measurements at an electrified polycrystalline gold surface [37]. The dry and wet IL was considered. Also here, layering and a reverse in the ion layering order for opposite applied potentials is observed. When water is introduced into the IL, significant effects are only found at positive electrochemical potentials of the gold surface. Interactions of water seems to be limited to surface adsorbed ions. No water is found directly at the (hydrophobic, ionophilic) gold surface. The structure at the electrified gold interface seems to be directed by a balance between ions and water, ions and the gold surface and the interactions of gold and water.

Molecular layering on a charged sapphire surface was observed for three different tris(pentafluoroethyl)trifluorophosphate $[\text{FAP}]^-$ -based ILs by M. Mezger [175, 176]. The cations used were 1-butyl-1-methyl pyrrolidinium $[\text{C}_4\text{Mpyr}]^+$, 1-Hexyl-3-methyl imidazolium $[\text{C}_6\text{Mim}]^+$ and tetrabutylammonium $[\text{Tba}]^+$. A gradually decaying structure, attributed to alternating anions and cations, was detected by high-energy XRR measurements for all of them. Structures extended up to 5-6 layers from the interface.

This demonstrates how ILs form pronounced molecular layering on charged surfaces [37, 48, 98, 149, 232, 311]. Via electrostatic interactions, surface charging seems to align cations and anions to form a layered structure in a charge-stacking model. Thus, electrostatically induced stacking is often considered an important driving force for layering in ILs [273], for example for the interpretation of the formation of molecular bilayers in imidazolium based ILs. The IL structure adjacent to an interface depends critically on the charge of the surface. Previously uncharged surfaces can develop a surface charge by ion adsorption. Charge reversal can occur when adsorption of ions leads to overcharging of the original surface charge [208]. Especially in thin films [250] and close to the interface, chemical composition of the ions [266, 267], surface chemistry and the surface charge [206, 215, 274] have a huge influence of the interfacial structure displayed by the IL.

Part III

Bulk Ionic Liquids

Chapter 6

Materials

This chapter is based on the publications "Mesoscopic correlation functions in heterogeneous ionic liquids" [291] by the author and "The Effect of Concentration on the Interfacial and Bulk Structure of Ionic Liquids in Aqueous Solution" [38] to which the author contributed.

6.1 Ionic Liquids for Bulk Structure Analysis

Hydrophilic Ionic Liquids

Two imidazolium-based hydrophilic ILs were investigated for their bulk liquid structure under water influence. They only differ in their alkyl side-chain length. The intrinsic hygroscopy of the ILs originates from the great water affinity of the chloride anion.

The shorter ionic liquid is 1-methyl-3-octyl-imidazolium chloride $[\text{C}_8\text{mim}]^+\text{Cl}^-$ (purity: $\geq 97\%$ HPLC) purchased from Sigma-Aldrich (c.f. Fig. 6.1). Chemical formula: $\text{C}_{12}\text{H}_{23}\text{ClN}_2$, molecular mass $M = 230,78 \text{ g/mol}$, melting point $T_m = 12^\circ\text{C}$, mass density $\rho = 1.01 \text{ g/cm}^3 (20^\circ\text{C})$, CAS-No: 64697-40-1 [35, 247]. $[\text{C}_8\text{mim}]^+\text{Cl}^-$ is liquid at room temperature, however extremely viscous, and completely water miscible. The IL was dried in a vacuum furnace at a pressure $p \approx 10 \text{ mbar}$ and 80°C for 12-14 hours before use. Water uptake occurred from air humidity by exposure to a controlled humidity atmosphere. Karl-Fischer titration was used to measure the water content of the same IL samples. Titration experiments were conducted by the collaboration partner Hsiu-Wei Cheng at the Max-Planck-Institute für Eisenforschung. By the correlation curve obtained it was possible to link water content and humidity exposure time.

The longer IL 1-methyl-3-decyl-imidazolium chloride $[\text{C}_{10}\text{mim}]^+\text{Cl}^-$ was used in X-ray Surface Force Apparatus experiments and characterized regarding the bulk liquid structure prior to confinement experiments using SAXS. The IL was chosen as the longer homologue of $[\text{C}_8\text{mim}]^+\text{Cl}^-$, as a longer real space distance, due to the longer alkyl side-chain, shifts the reciprocal space signal to an easily accessible q -range. The IL was purchased from Sigma-Aldrich (purity: $\geq 96\%$), the impurities are mainly wa-

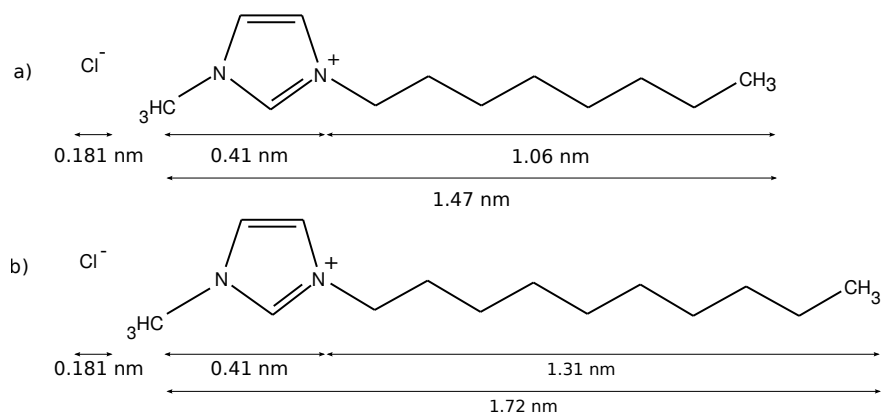


Figure 6.1: Molecular structure of a) 1-methyl-3-octyl-imidazolium chloride $[\text{C}_8\text{mim}]^+\text{Cl}^-$ and b) 1-methyl-3-decyl-imidazolium chloride $[\text{C}_{10}\text{mim}]^+\text{Cl}^-$.

ter. Chemical formula: $\text{C}_{14}\text{H}_{27}\text{ClN}_2$, molecular mass $M = 258,83 \text{ g/mol}$, mass density $\rho = 0.99 \text{ g/cm}^3$ (20°C), CAS-No: 171058-18-7 [34, 246]. The same drying procedure as for the octyl-based IL applied here. Water uptake was achieved by physical mixing with a calculated amount of water. This made water percentage content directly accessible. The IL is a highly viscous liquid at room temperature, mixing with water required good stirring with a spatula to achieve good mixing.

Hydrophobic Ionic Liquids

Hydrophobic ILs in this work are

- 1-methyl-3-octadecylimidazolium tris(pentafluoroethyl)trifluorophosphate $([\text{C}_{18} \text{C}_1 \text{im}]^+ [\text{FAP}]^-)$
- 1-methyl-3-octadecylimidazolium bis(trifluoromethylsulfonyl)imide $([\text{C}_{18} \text{C}_1 \text{im}]^+ [\text{NTf}_2]^-)$
- 1-methyl-3-octadecylimidazolium bis(nonafluorobutylsulfonyl)imide $([\text{C}_{18} \text{C}_1 \text{im}]^+ [\text{NNf}_2]^-)$
- 1-methyl-3-docosylimidazolium bis(trifluoromethylsulfonyl)imide $([\text{C}_{22} \text{C}_1 \text{im}]^+ [\text{NTf}_2]^-)$
- 1-methyl-3-docosylimidazolium bis(nonafluorobutylsulfonyl)imide $([\text{C}_{22} \text{C}_1 \text{im}]^+ [\text{NNf}_2]^-)$

As has been shown in chapter 4.1 the hydrophobicity depends on cation and anion, however anion properties are more influential than cation properties. Small polar molecules, such as water, are preferentially located at the anion when absorbed. In contrast to the hydrophilic ionic liquid $[\text{C}_8\text{mim}]^+\text{Cl}^-$, the hydrophobic ILs display bulky, fluorinated

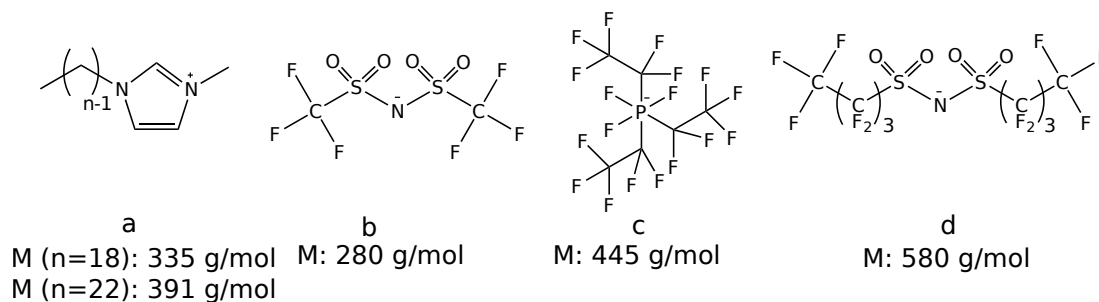


Figure 6.2: Hydrophobic Ionic liquids used in this work. (a) Cation structure featuring alkyl side-chain lengths of n -carbon atoms. (b - d) Anion structure. From left to right, following increasing molecular size: $[\text{NTf}_2]^-$, $[\text{FAP}]^-$, $[\text{NNf}_2]^-$. Hydrophobic ILs were especially used because of their anion geometry (size). Hydrophobicity was an appreciated side effect to avoid moisture influence on structure evaluation. Molecular weights are given below the structures.

anions. The hydrophobic ILs were not used primarily because of their hydrophobicity, but because of this anionic molecular geometry or long cation alkyl side-chains. Hydrophobicity, and along with it chemical and thermal stability, are appreciated side effects, but key properties were molecular geometry of the cation and the anion, i.e. molecular size.

The hydrophobic ILs were acquired as follows: The IL $[\text{C}_{18}\text{C}_1\text{im}]^+ [\text{FAP}]^-$ was purchased from Merck, Darmstadt. All other ILs were synthesized following the route described by Bradley et al. [23]. 1-methyl-3-docosyl-imidazolium bromide ($[\text{C}_{22}\text{C}_1\text{im}]^+ \text{Br}^-$) and 1-methyl-3-octadecyl-imidazolium chloride ($[\text{C}_{18}\text{C}_1\text{im}]^+ \text{Cl}^-$) were synthesized by electrophilic addition from n -methylimidazol with 1-bromodocosane and 1-chloro-octadecane, respectively. The reaction was conducted at 90°C for two days under argon atmosphere. The solid precipitates were washed with ether, dried, and recrystallized from tetrahydrofuran. ILs were formed by metathesis reaction in aqueous solution from the $[\text{C}_n\text{C}_1\text{im}]^+$ halogenides with the $[\text{NTf}_2]^-$ and $[\text{NNf}_2]^-$ lithium salts respectively. The product was recrystallized in a mixture of ethanol/water (75:25). Water-soluble lithium halogenides were washed out with a cold ethanol/water (75:25) mixture. Combined reaction yields were 68.2 % for $[\text{C}_{18}\text{C}_1\text{im}]^+ [\text{NTf}_2]^-$, 90.4 % for $[\text{C}_{22}\text{C}_1\text{im}]^+ [\text{NTf}_2]^-$, 65.9 % for $[\text{C}_{18}\text{C}_1\text{im}]^+ [\text{NNf}_2]^-$ and 89.6 % for $[\text{C}_{22}\text{C}_1\text{im}]^+ [\text{NNf}_2]^-$. Molecular structures are displayed in Fig. 6.2. Their melting points T_m , entropy of fusion ΔS_f , molecular volume V_m and volumetric thermal expansion coefficient α are displayed in table 6.1. Scattering relevant properties such as molecular weight, cation side chain length, mass density, electron density and scattering length density (SLD) for X-ray and Neutron scattering are displayed in Tab. 6.2. Properties for reference compounds are stated as well.

Purification

To remove volatile residues the ILs were dried in a vacuum oven over night. Subsequently, the ILs were purified by zone melting in a glass tube (20 cm length, 5 mm inner diameter, 1.5 mm wall thickness) under vacuum. After at least 15 zoning cycles with a speed of 1 cm/h, the IL from the central part of the tube was used for the experiments.

DSC

Melting points T_m and melting entropies $\Delta S_m = \Delta H_m/T_m$ of the ILs were determined by differential scanning calorimetry (DSC). Measurements on a Mettler Toledo DSC-822 instrument were performed at different scan rates between 1 K/min and 10 K/min (Fig. 6.3a). Extrapolated equilibrium parameters are summarized in Tab. 6.1. All ILs, and in particular $[\text{C}_{18}\text{C}_1\text{im}]^+ [\text{NTf}_2]^-$, can be significantly supercooled [174]. Their stability in the supercooled state allows SAXS measurements of their liquid structure below their melting points.

Molecular Volume

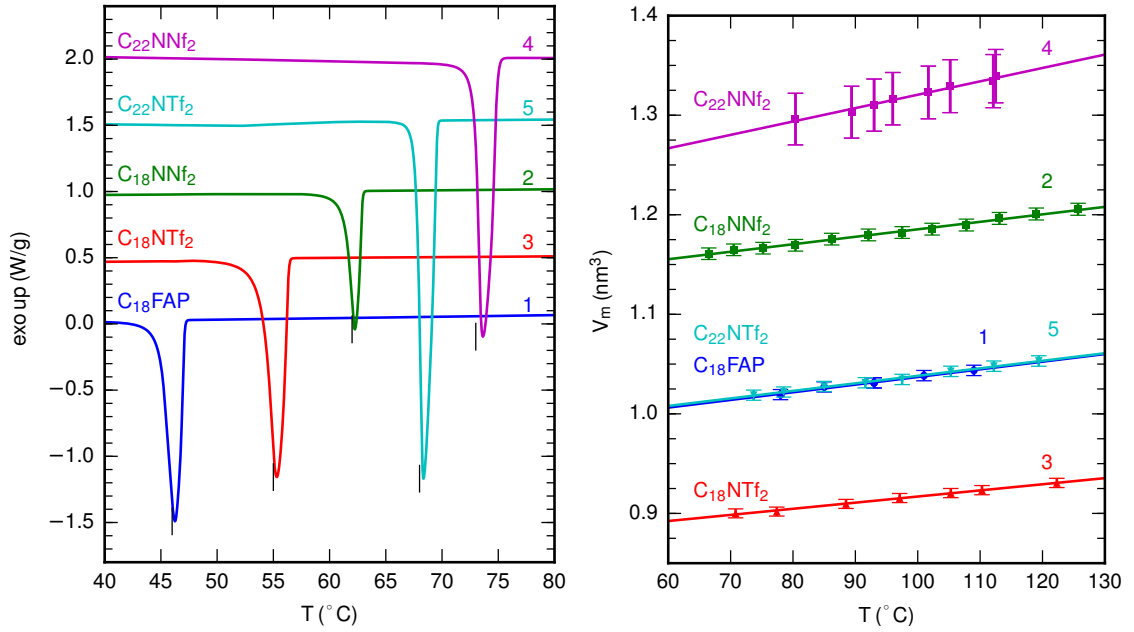
Molecular volumes $V_m(T)$ of ILs were calculated from the mass densities $\rho_m(T)$ of the liquids (Fig. 6.3b). Densities were measured with a glass pycnometer (volume 1 mL for $[\text{NNf}_2]^-$, 5 mL for other ILs) at temperatures T between their melting points and 125° C. The molecular volume at the melting point V_m and the volumetric thermal expansion coefficient α were extracted by linear regression using $V = V_m [1 + \alpha (T - T_m)]$ (lines in Fig. 6.3b and Tab. 6.1).

Scattering Contrast

Table 6.2 summarizes the scattering length densities (SLD) of the studied ILs for X-rays and neutrons. Parameters for compounds similar to the molecular moieties of the anions and cations are provided for comparison. For hard X-rays the SLD is approximately

Table 6.1: Properties of studied ILs: melting point T_m , entropy of fusion ΔS_f , molecular volume at the melting point V_m , and volumetric thermal expansion coefficient α .

IL	T_m °C	ΔS_f J mol ⁻¹ K ⁻¹	V_m nm ³	α 10 ⁻⁴ K ⁻¹
$[\text{C}_{18}\text{C}_1\text{im}]^+ [\text{FAP}]^-$	46	169	0.995	7.7
$[\text{C}_{18}\text{C}_1\text{im}]^+ [\text{NTf}_2]^-$	55	162	0.890	6.9
$[\text{C}_{18}\text{C}_1\text{im}]^+ [\text{NNf}_2]^-$	62	98	1.157	6.5
$[\text{C}_{22}\text{C}_1\text{im}]^+ [\text{NTf}_2]^-$	68	197	1.015	7.4
$[\text{C}_{22}\text{C}_1\text{im}]^+ [\text{NNf}_2]^-$	73	126	1.283	10.4



(a) DSC curves of $[C_{18}C_1im]^+[FAP]^-$ (1, blue), $[C_{18}C_1im]^+[NTf_2]^-$ (3, red), $[C_{18}C_1im]^+[NNf_2]^-$ (2, green), $[C_{22}C_1im]^+[NNf_2]^-$ (4, purple), and $[C_{22}C_1im]^+[NTf_2]^-$ (5, cyan) cooling with a scan rate of 1 K/min. Vertical lines indicate the extrapolated melting points. Curves were vertically shifted by 0.5 W/g for clarity.

(b) Molecular volume V_m vs. temperature T for: $[C_{18}C_1im]^+[FAP]^-$ (1, blue dots), $[C_{18}C_1im]^+[NTf_2]^-$ (3, red triangles up), $[C_{22}C_1im]^+[NTf_2]^-$ (5, cyan triangles down), $[C_{18}C_1im]^+[NNf_2]^-$ (2, green squares), $[C_{22}C_1im]^+[NNf_2]^-$ (4, purple squares).

Figure 6.3: Thermal evaluation of hydrophobic ILs.

given by the electron density ρ_e of the material. Here, the scattering contrast between the hydrocarbon side chains of the cations (c.f. octadecane, docosane) and the ionic parts composed of imidazolium-rings (c.f. 1-Methylimidazol) and the perfluorinated anions (c.f. $HNtf_2$) is similar for all studied ILs. The SLD ratio of the aliphatic moieties with respect to the total IL ranges from 0.65 for $[C_{18}C_1im]^+[FAP]^-$ to 0.72 for $[C_{22}C_1im]^+[NTf_2]^-$. In contrast, for neutrons the variation in SLD contrast for the different ILs is much larger. As shown by the Margulis group [7, 94] this can strongly affect peak intensities of the scattering patterns. Thus, the different peak intensity ratios observed in SAXS and SANS are primarily attributed to the variation in SLD contrast (Fig. 8.2 and Tab. 8.1).

Table 6.2: Molecular mass M of the cations (c) and anions (a) of ILs and reference materials, length of the aliphatic C_n hydrocarbon side chains d_c , mass density ρ_m at the melting point, electron density ρ_e , and scattering length density (SLD) for X-rays (x) at $E = 8.05$ keV and neutrons (n) at $E = 3.27$ meV.

	M_c (g/mol)	M_a (g/mol)	d_c (nm)	ρ_m (g/cm ³)	ρ_e (1/nm ³)	SLD _x (10 ⁻⁶ 1/Å ²)	SLD _n (10 ⁻⁶ 1/Å ²)
[C ₁₈ C ₁ im] ⁺ [FAP] ⁻	335	445	2.32	1.30	404	11.7	1.6
[C ₁₈ C ₁ im] ⁺ [NTf ₂] ⁻	335	280	2.32	1.15	366	10.7	1.0
[C ₁₈ C ₁ im] ⁺ [NNf ₂] ⁻	335	580	2.32	1.31	406	11.5	1.7
[C ₂₂ C ₁ im] ⁺ [NTf ₂] ⁻	391	280	2.82	1.10	352	10.5	0.9
[C ₂₂ C ₁ im] ⁺ [NNf ₂] ⁻	391	580	2.82	1.25	391	11.1	1.5
Octadecane	254		2.36	0.78	268	7.6	-0.4
Docosane	310		2.87	0.78	281	7.6	-0.4
H[NTf ₂]	281		-	1.36	402	11.4	2.4
Perfluorohexane	338		-	1.67	482	13.7	3.5
1-Methylimidazole	82		-	1.04	334	9.1	1.7

Chapter 7

Experimental

7.1 Small Angle Scattering

Small Angle X-ray Scattering

SAXS measurements were done at a self-constructed instrument using a rotating Cu anode X-ray generator (**A**) (Rigaku MicroMax 007; 1.54 Å wavelength) at the Max-Planck-Institute for Polymer Research. The device is schematically depicted in Fig. 7.1. Letters in the text specify parts depicted. The beam was monochromatized and collimated by multilayer optics (**B**) (Osmic Confocal Max-Flux, Cu K_α) and three 4-jaw slit sets (**D**) (500 × 800 μm²) with $l_{coll} = 1500$ mm collimation length. The slits are manufactured by the company JJ X-ray A/S, Denmark and use four independently moving, O-ring sealed, highly polished tungsten carbide blades of 2 mm thickness to define the X-ray beam with micrometer precision. To reduce parasitic scattering, silicon tips were used on the blades in the second, beam defining, slits [151]. An incident X-ray flux of $I = 10^7$ photons/sec at the sample position was measured by an inversion layer silicon photodiode (XUV-100, OSI Optoelectronics) (not shown). Beam intensity generated a current in the range of 2 to 5 Nano-Ampere, which convert to a photon flux of $n = 10^7$ [1/s] = $3.5 \cdot 10^{-9}$ [C/s] · 2.8^{15} [1/C]. The conversion of the current A generated in the photo diode by irradiation with X-ray photons into a photon flux is possible via:

$$\frac{q \text{ [C/s]}}{e} = n \frac{E_{X\text{-ray}} \text{ [eV]}}{3.63 \text{ [V]}} \quad (7.1)$$
$$n \text{ [1/s]} = \frac{q \text{ [C/s]} \cdot 3.63 \text{ [V]}}{e E_{X\text{-ray}} \text{ [eV]}}$$

$$\text{for X-ray using Cu K}_{\alpha} = 8.04 \text{ keV : } n \text{ [1/s]} = q \text{ [C/s]} \cdot 2.8^{15} \text{ [1/C]}$$

Here, e is the elementary charge of an electron ($e = 1.60210^{-19}$ C), $E_{X\text{-ray}}$ is the energy of the incident X-ray radiation used, q is the measured charge generated in the diode in Coulomb $C = A/t$, which is expressed as the measured current in Ampere (C/sec), n is the photon flux.

Samples can be inserted into the device in different holders, depending on their physical state. Liquid samples with low viscosity can be measured using glass capillaries in which they are inserted by a syringe. This system fails for liquids showing higher viscosity as inserting into the very narrow glass capillaries becomes impractical. Here self constructed sample holders holding the viscous IL between two flat windows, sealing them by an O-ring, are used. Window materials can be aluminum foils or single-crystalline diamonds, both having either low absorption or low background scattering, respectively. These holders were applied for the hydrophilic ILs used in this work, as they are highly viscous liquids at room temperature. When mixed with water viscosity even increased as gelation occurred. These samples were either poured into the holder or applied by a spatula. Measurements performed on these samples did not require temperature control and took place at room temperature.

Samples solid at room temperature can be grinded into a fine powder and then be inserted into glass capillaries. This was done here for ILs with melting temperatures above room temperature. The filled, but unsealed glass capillaries are placed into a vacuum oven, in which the sample (here ILs) are molten under vacuum. Venting the oven presses the liquid IL into the glass capillary without trapping air bubbles at the bottom. Capillaries were sealed air-tight afterwards. Hydrophilic ILs used in this work have melting temperatures above room temperature (c.f. Tab. 6.1). Hence, samples were contained in 1 mm glass capillaries made of borosilcate glass by the company Hilgenberg, Germany.

Sample holders were placed in a temperature controlled copper holder (stability better ± 0.05 K) mounted inside the vacuum chamber. The whole beam path, except a 15 cm part of the housing of the Göbel mirror and an ≈ 5 cm path in front of the detector (**K**), is evacuated to minimize air scattering. Vacuum system main housing (**H**) is made of 5 ISO-K 630 flanges installed on a rail system, enabling flexible adjustement of sample-detector distance, making wide angle and small angle scattering experiments possible on the same setup. The slit system is connected by a below tube and can be sealed off by a pneumatic Kapton window (**E**). As a steel tube houses the X-ray beam until shortly in front of the temperature controlled copper holder to suppress background scattering, sealing off the main vacuum part prevents a fast pressure equalization, avoiding high gas velocities around the sample capillary, which would otherwise fracture the capillary. Equalization to normal pressure is done by a by-pass system (**V3**) and flow resistance valve (**G**) and takes ≈ 10 min for the whole system. During evacuation and measurement, when the whole system is at equal pressure, the Kapton window at valve 0 is not in the beam path (valve 0 open). Evacuation of the whole system is achieved by a scroll pump (**F**) (Company: Ilmvac, Germany). To achieve the standard operational vacuum pressure of $p = 10^{-1}$ mbar a time of $t \approx 5$ min is required. This enables measurement of deteriorating samples in a reasonal time span (10-30 min) from sample insertion until detector read out.

2D diffraction patterns were recorded on an online image plate detector (Mar345) (**K**). The primary beam is absorbed by a tungsten beam stop inside the main vacuum chamber minimising air scattering. During exposure to the scattered radiation excited

states are generated in the image plate. A crystalline layer consisting of bariumfluorobromide BaFBr, doped with Europium²⁺, with a thickness of 0.1-0.3 mm is applied on the image plate. When exposed to high energy radiation Europium²⁺ is excited to generate a free electron and become Europium³⁺. The generated electrons are trapped in the conduction band of bromine in the surrounding crystalline structure of the phosphor material, generating a higher energy metastable state. Return of the excited states is achieved by laser light irradiation during which bromine releases an electron into the conduction band. The irradiated laser light is insufficient in energy to create more excited states. Europium³⁺ recombines back with the free electron to Europium²⁺ under release of blue-violet luminescence ($\lambda = 300$ nm). The luminescence is proportional to the amount of excited states which is proportional to the incident radiation. Collected by a photomultiplier tube the luminescence can be digitalized and an electronic image is created. The phosphorous plate can be erased after read-out by irradiation with strong light and then be reused.

Possible errors occur during loss of excited states at higher temperatures of operation, long exposure times or creation of faulty excited states by other sources of high energy radiation. Maximum operational temperature of the MAR345 image plate detector is 24 °C, which was obeyed by an air conditioning to a laboratory temperature of 19 °C. Exposure times during experiment followed manufacturer recommendations and did not exceed 15 minutes during quantitative evaluation of the recorded signals to ensure no excited states are lost. Qualitative signal evaluation would also be possible at longer exposure times when only signal position and not signal shape (breadth of signal) is required. High energy extraterrestrial particles are sources of signal manipulation on a pixel size range and have to be accounted for during signal evaluation.

The sample-detector distance of 2100 mm was calibrated with silver behenate AgBe as reference sample. SAXS data, collected during three independent measurements with 900 s exposure time each, were averaged and corrected by dark images. This was automatized by python-scripts developed in our group in consideration of the huge amount of data created during a measurement run. Artifacts, originating from high energy radiation, were removed by Laplace filtering. 2D datasets were converted to $I(q)$ vs. momentum transfer $q = 4\pi/\lambda \sin(\theta)$ by radial averaging.

Small Angle Neutron Scattering

The specific neutron scattering contrast between the molecular moieties of the IL provides complementary information to the SAXS data (Tab. 6.2). SANS measurements were performed on the KWS-1 beam line operated by Jülich Centre for Neutron Science at the FRM-II reactor, Heinz-Maier-Leibnitz Zentrum (MLZ), Garching, using 5 Å incident neutron wavelength with 10 % energy resolution. The experiments have been carried out at three different sample-detector distances (2 m, 8 m, 20 m) corresponding to momentum transfers of $q = 3.3 \text{ nm}^{-1}$ to 0.31 nm^{-1} , 0.81 nm^{-1} to 0.078 nm^{-1} and 0.327 nm^{-1} to 0.01 nm^{-1} , respectively. ILs were filled in 1 mm thick quartz cells and placed in a temperature controlled sample holder with temperature accuracy below

7 EXPERIMENTAL

± 0.5 K. Scattering patterns were recorded on an Anger type position-sensitive scintillation detector using 20 min, 60 min, and 120 min exposure time respectively [57]. The obtained two-dimensional data were reduced taking into account different detector-matrix corrections, scattering of the quartz cell, instrumental background and thickness and transmission of the samples. The incoherent scattering from the aid of precalibrated plexiglass (acrylic glass) sample has been used as secondary standard. After radial averaging and absolute calibration reduced data were converted to scattering cross-section as function of wave vector q .

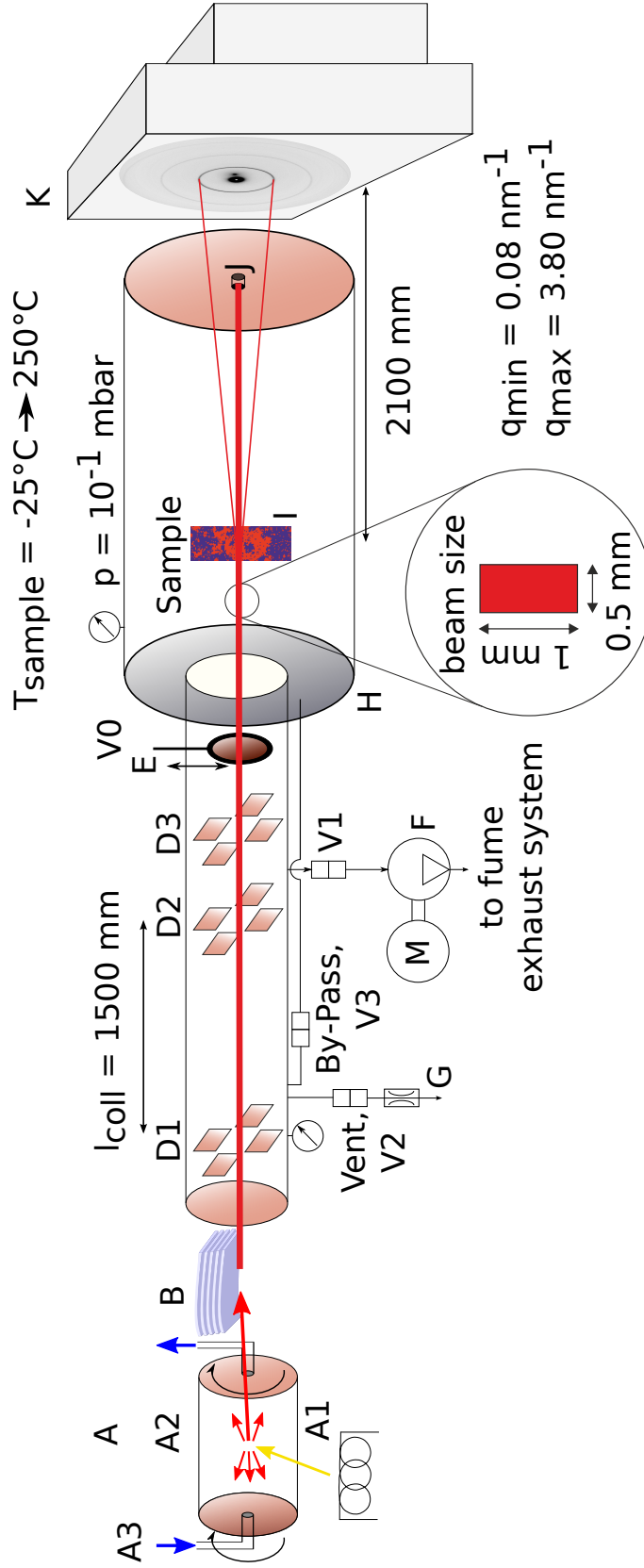


Figure 7.1: Small Angle X-ray Scattering set-up used for this work. **A**: rotating anode (Rigaku MicroMax 007; 1.54 \AA wavelength). **A1**: tungsten filament and Wehnelt cylinder **A2**: copper rotating anode **A3**: cooling water **B**: parallelizing and monochromization by Göbel mirror **C**: Optics vacuum part **D1,D2**: collimation slits of equal size made of tungsten, parallelize the beam. **D3**: Anti-Scatter slits made of silicon, not cutting the beam. **E**: Kapton window seal between optics vacuum chamber and main vacuum chamber **F**: scroll pump **G**: venting valve with flow resistance **H**: Main vacuum chamber including sample holder **I** and tungsten-alloy beamstop **J**. **K**: Online detector (Mar345), sample to detector distance is around 2100 mm during normal SAXS-measurements. Distances and proportions are not to scale. See text for details.

Chapter 8

Data Analysis

8.1 Azimuthal Averaging

Azimuthal averaging is done based on a python script developed in our group¹. Detector read-out generates data files in a pixel file format (.png) featuring 2300×2300 pixel per file, corresponding to each physical pixel on the detector screen (detector diameter $345000 \mu\text{m}$ / $150 \mu\text{m}$ pixel size). Image files are read in using the fabio-package distributed by the ESRF, Grenoble [122, 130]. Using a calibration file generated during Silverbehenic Acid (AgBe) measurements a calibration matrix array of 2300×2300 pixel was generated attributing a specific sample detector distance, and with that a specific wave vector transfer q , to each pixel. Several data pixel files (here three) from independent measurement runs are averaged to one. A dark image is taken and subtracted from sample data to eradicate detector influence. A mask eliminates undesired pixel. The mask pixel array can be modified by indicating specific pixel in the script or manually by adjusting a mask pixel file using a standard pixel file program (f.ex. gimp). Now using this masked data pixel array azimuthal averaging was done summing up the intensities in all pixel featuring a similar q -value (a similar radius from the beam center), resulting in a 1-D array correlating wave vector transfer q and intensity I . This array of q and I values represents 2D-data taken during SAXS measurements and is plotted in f.ex. Fig. 8.2.

8.2 Teubner-Strey Model

A model suited for analysis of scattering data originated by materials displaying mesoscopic structure is the so called Teubner-Strey model [9, 78, 210, 214]. Originally it was invented to phenomenologically describe structures formed in micro-emulsion of water and oil [264]. It proved to be successfully applicable to bi-continuous structures in general, as postulated for ionic liquids. Applying the Teubner-Strey model, quantitative analysis of IL scattering data could be significantly extended. For quantitative

¹Acknowledgment: Julian Mars

analysis, the experimental SAXS and SANS patterns were analyzed by fitting model functions to the pre-peak observed below 3 nm^{-1} . Given an intermolecular potential of finite range, the envelope of an oscillatory total two-point correlation function $G(r)$ in a D -dimensional liquid system asymptotically decays with $r^{(1-D)/2} \exp(-r/\xi)$ as $r \rightarrow \infty$ [84, 168]. Thus, the bulk ($D = 3$) correlation function can be approximated by a damped oscillatory function

$$G(r) \propto \frac{1}{r} \exp\left(-\frac{r}{\xi}\right) \sin\left(\frac{2\pi r}{d} - \varphi\right) =: G_{\text{TS}}(r) \quad (8.1)$$

with periodicity d and correlation length ξ [175]. Here, the correlation length is the exponential decay length of the oscillatory correlation function. The special case of Eqn. (8.1) with $\varphi = 0$ was introduced by Teubner and Strey to describe density fluctuations in microemulsions [264]. Later, it was successfully applied to complex IL/surfactant mixtures [3]. Here, $G_{\text{TS}}(r)$ describes the oscillatory structure comprised of alternating aliphatic and ionic regions including the perfluorinated anions. In X-ray and neutron scattering, these molecular moieties exhibit a significant contrast in the scattering length densities (Tab. 6.2). Therefore, the observed pre-peak in the scattering patterns is assigned to short range order, originating from nano-phase separation between the long alkyl side chains of the cations and the positively and negatively charged moieties [271]. Here, we introduce an additional parameter φ that controls the phase of the oscillations and accounts for the observed asymmetry of the pre-peak. The structure factor $S_{\text{TS}}(q)$ is obtained from the correlation function $G_{\text{TS}}(r)$ via Fourier transformation:

$$S_{\text{TS}}(q) := \frac{4\pi}{q} \int_0^\infty G_{\text{TS}}(r) r \sin(qr) dr \quad (8.2a)$$

$$= 4\pi \frac{\Delta^2 \cos \varphi - (q^2 - q_0^2) \sin \varphi}{\Delta^4 + (q^2 - q_0^2)^2} \quad (8.2b)$$

$$\Delta^2 = \frac{4\pi}{\xi d}, \quad q_0^2 = \left(\frac{2\pi}{d}\right)^2 - \frac{1}{\xi^2} \quad (8.2c)$$

Note that, for $\varphi = 0$ the structure factor $S_{\text{TS}}(q)$ resembles a Lorentz curve in q^2 with a center at q_0^2 and a full width at half maximum of $2\Delta^2$. Accordingly, the oscillation period d and the correlation length ξ can be determined from the peak position q_0^2 and the width Δ^2 by inversion of Eqn. (8.2c).

$$\begin{aligned} d &= \frac{\sqrt{8\pi}}{\beta_+} & \xi &= \frac{\sqrt{2}\beta_+}{\Delta^2} \\ \alpha^2 &= \sqrt{\Delta^4 + q_0^4} & \beta_\pm &= \sqrt{\alpha^2 \pm q_0^2} \end{aligned} \quad (8.3)$$

The integrated area $A = \int_0^\infty S(q) dq$ under the Teubner-Strey peak (Eq. 8.2b) is given by

$$A_{\text{TS}} = \sqrt{2}\pi^2 \frac{\Delta^2 \cos \varphi - \beta_-^2 \sin \varphi}{\alpha^2 \beta_-}. \quad (8.4)$$

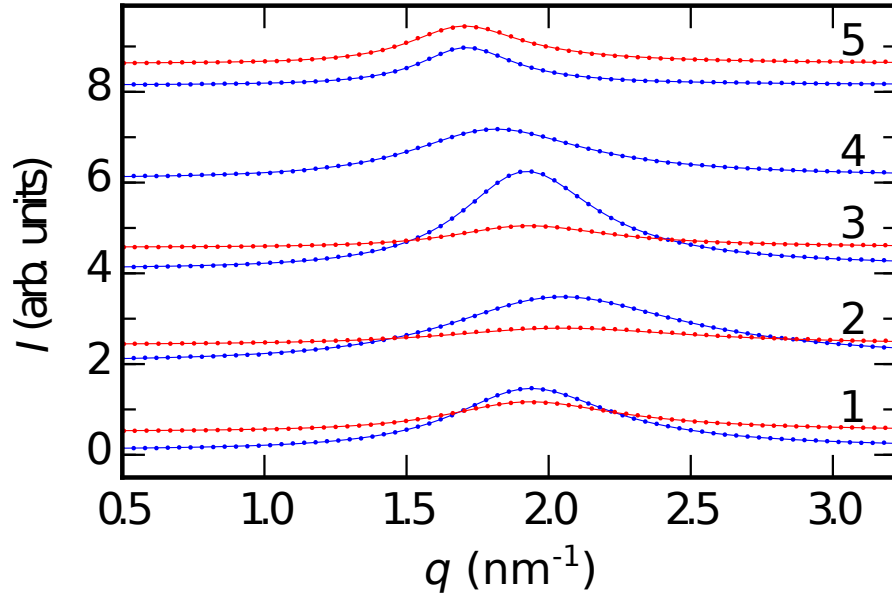


Figure 8.1: Comparison of SAXS (blue) and SANS (red) patterns $I(q)$ of $[\text{C}_{18}\text{C}_1\text{im}]^+ [\text{FAP}]^-$ (1), $[\text{C}_{18}\text{C}_1\text{im}]^+ [\text{NNf}_2]^-$ (2), $[\text{C}_{18}\text{C}_1\text{im}]^+ [\text{NTf}_2]^-$ (3), $[\text{C}_{22}\text{C}_1\text{im}]^+ [\text{NNf}_2]^-$ (4), $[\text{C}_{22}\text{C}_1\text{im}]^+ [\text{NTf}_2]^-$ (5) close to their melting points. Solid lines are fits to the Teubner-Strey model. Curves for different ILs are vertically shifted by 2 units for clarity.

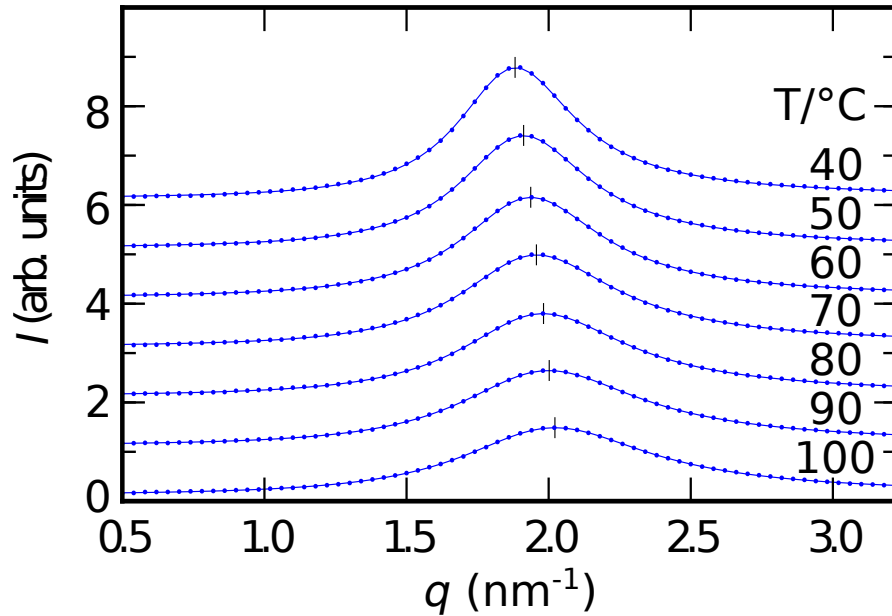


Figure 8.2: Comparison of SAXS signals between 40° C and 100° C for $[\text{C}_{18}\text{C}_1\text{im}]^+ [\text{NTf}_2]^-$. (a) 100° C, (b) 90° C, (c) 80° C, (d) 70° C, (e) 60° C, (d) 50° C, (e) 40° C. Vertical lines indicate the peak maximum q_0 . Solid lines are fits to the Teubner-Strey model. Curves are vertically shifted by 1 unit.

8.3 Asymmetric Lorentz Model

In an alternative approach to the Teubner-Strey model, SAXS and SANS data were analyzed using a generic excess structure factor $S_{\text{AL}}(q)$ based on a asymmetric Lorentzian [174].

$$S_{\text{AL}}(q) := \frac{1}{\pi} \frac{\Delta}{\Delta^2 + (q - q_0)^2} [1 + a(q - q_0)] \quad (8.5)$$

Here, the first term provides a normalized ($A_{\text{AL}} = 1$) Lorentzian line shape with center at $q_0 = 2\pi/d$ and a half width at half maximum of $\Delta = 1/\xi$. The second part with the asymmetry parameter a accounts for the observed asymmetric peak shape (Fig. 8.2).

8.4 Fitting

The structure factor $S_{\text{TS}}(q) \propto I(q) - I_c$ calculated from the asymptotic decay of $G(r)$ is proportional to the scattering intensity $I(q)$ in excess to a smooth background I_c . The constant I_c accounts for incoherent scattering, and other slowly varying contributions in the small angle regime. Therefore, the normalized SAXS and SANS data $I(q)$ were fitted to

$$I(q) = I_0 S_{\text{TS/AL}}(q) + I_c \quad (8.6)$$

where I_0 is the amplitude of the scattering signal $S_{\text{TS/AL}}(q)$. One advantage of the ILs studied in this work is that the scattering peak originating from charge alteration and adjacency appear at much larger q values, e.g. 8 nm^{-1} and 14 nm^{-1} for $[\text{C}_{18}\text{C}_{1}\text{im}]^+ [\text{FAP}]^-$ [174] or 8 nm^{-1} and 13 nm^{-1} for $[\text{C}_{22}\text{C}_{1}\text{im}]^+ [\text{NTf}_2]^-$ (Fig. 9.3). Therefore, the contribution of their peak tails in the analyzed q -range is much smaller than for ILs with shorter alkyl side-chains [7].

For all ILs and all temperatures, the fits using the generalized Teubner-Strey model accurately reproduce the experimental data over the entire measured q -range (Fig. 8.2). Information is gathered by fitting the whole first sharp diffraction peak (FSDP). Peak amplitude I_0 and peak area A can fluctuate due to intensity fluctuations of incoming beam intensity. This effect especially occurs during X-ray experiments where fluctuations of the primary beam of about 20% were observed. Peak position d and width Δ are not affected by fluctuations of peak area A . The two parameters evaluated are robust towards primary beam intensity fluctuations.

Fits using the generic line-shape of an asymmetric Lorentzian yield comparably good agreements with the experimental data of the Teubner-Strey model. The extracted fit parameters using the Teubner-Strey (S_{TS}) and the generic asymmetric Lorentz (S_{AL}) models are summarized in Tab. 8.1. Linear regression was used to determine their temperature dependence Fig.9.1 (solid lines).

For both models similar parameters were obtained for the SAXS and SANS data. This comparison confirms the robustness of the analysis under the different assumptions presumed by the Teubner-Strey and asymmetric Lorentz models. Differences in the SAXS and SANS value d_m for the periodicity at the melting point are below 2%. While

larger differences are observed for the correlation lengths ξ all parameters show the same trends (Fig. 9.1). These differences are attributed to the different scattering length densities of the molecular moieties for X-rays and neutrons (Tab. 6.2). Eqn. 8.1 and Eqn. 8.5 map multiple inter- and intramolecular correlations onto a simplified effective $G(r)$. Therefore, these specific differences are concealed and projected onto the fitting parameters.

Table 8.1: Parameter summary of periodicity d , normalized correlation length ξ/d , and integrated peak intensity $I_0 A$ extracted from the SAXS and SANS data using the Teubner-Strey (TS) and asymmetric Lorentz (AL) models at the melting point T_m and at $90^\circ C$. The length scale $d_p = 2\pi/q_0$ was calculated from the position q_0 of the pre-peak maximum at T_m .

IL	d_p (nm)	d_m (nm)	ξ_m/d_m	$I_0 A_m$ (arb. units)	d_{90} (nm)	ξ_{90}/d_{90}	$I_0 A_{90}$ (arb. units)	$\Delta d/\Delta T$ (10^{-3} nm/K)	$\Delta \xi/\Delta T$ (10^{-2} nm/K)
SAXS									
Teubner-Strey (TS)									
$[C_{18}C_1im]^+[FAP]^-$	3.37	3.38	0.86	15.8	3.19	0.68	13.8	-4.3	-1.6
$[C_{18}C_1im]^+[NTf_2]^-$	3.27	3.32	1.06	21.5	3.20	0.83	20.2	-3.5	-2.5
$[C_{18}C_1im]^+[NNf_2]^-$	3.05	3.12	0.63	25.0	3.03	0.56	25.5	-3.5	-1.1
$[C_{22}C_1im]^+[NTf_2]^-$	3.70	3.74	1.28	5.0	3.67	1.13	4.90	-3.5	-3.0
$[C_{22}C_1im]^+[NNf_2]^-$	3.51	3.56	0.79	11.8	3.49	0.71	11.8	-4.3	-2.2
Asymmetric Lorentz (AL)									
$[C_{18}C_1im]^+[FAP]^-$		3.33	0.87	14.4	3.17	0.69	12.6	-3.4	-1.6
$[C_{18}C_1im]^+[NTf_2]^-$		3.30	1.06	19.5	3.19	0.82	17.8	-3.2	-2.6
$[C_{18}C_1im]^+[NNf_2]^-$		3.13	0.63	21.9	3.05	0.54	21.7	-2.9	-1.1
$[C_{22}C_1im]^+[NTf_2]^-$		3.69	1.31	5.3	3.61	1.16	5.0	-3.7	-2.9
$C_{22}C_1im]^+[NNf_2]^-$		3.54	0.80	12.3	3.47	0.71	12.2	-3.9	-2.2
SANS									
Teubner-Strey (TS)									
$[C_{18}C_1im]^+[FAP]^-$	3.31	3.31	0.82	8.1	3.20	0.66	6.8	-2.5	-1.4
$[C_{18}C_1im]^+[NTf_2]^-$	3.31	3.32	0.90	5.4	3.24	0.76	4.6	-2.4	-1.6
$[C_{18}C_1im]^+[NNf_2]^-$	3.10	3.14	0.59	7.3	3.09	0.54	6.5	-2.0	-0.8
$[C_{22}C_1im]^+[NTf_2]^-$	3.72	3.73	1.11	6.2	3.66	1.00	5.8	-4.1	-2.6
Asymmetric Lorentz (AL)									
$[C_{18}C_1im]^+[FAP]^-$		3.29	0.84	7.4	3.18	0.69	6.1	-2.7	-1.4
$[C_{18}C_1im]^+[NTf_2]^-$		3.29	0.94	4.8	3.21	0.81	4.1	-2.6	-1.6
$[C_{18}C_1im]^+[NNf_2]^-$		3.12	0.62	6.1	3.07	0.57	5.4	-1.9	-0.8
$[C_{22}C_1im]^+[NTf_2]^-$		3.71	1.14	6.2	3.62	1.03	5.5	-4.4	-2.6

Chapter 9

Results and Discussion

9.1 Hydrophobic Ionic Liquid Bulk Structure

Investigation of pure IL bulk structure was achieved by scattering experiments, leading to parameters qualified to give insight into quantitative description of bulk structure length scales. Crucial property to probe bulk liquid structure in scattering experiments is scattering length density, giving rise to the detected scattering pattern (c.f. Chap. 2). As mentioned in Sec. 6.1, scattering length density contrast can effect peak intensities of scattering experiments. Only accounting for intensities, position q_0 and half width at half maximum $\Delta = 1/\xi$ of the pre-peak are affected only slightly (Tab. 8.1). Therefore, the corresponding real space parameters d and ξ appear appropriate to characterize the structure of ILs. As shown in Eqn. 8.1 they also describe the two generic features of an oscillatory correlation function: The periodicity d and the correlation length ξ i.e. the decay length of the oscillatory modulations. Thus those two parameters are used to discuss bulk IL liquid structure in the following quantitative discussion.

9.1.1 Periodicity

The periodicities d , obtained from the quantitative analysis, agree well with the estimated length scales d_p , calculated from the pre-peak position (Fig. 9.1a and Tab. 8.1). Qualitatively, it follows the trends observed previously for other ILs [87, 271]. The longer the C_nH_{2n+1} side chain of the cation, the larger the periodicity d of the correlation function. Their projected chain length $d_c = d_{CC} \sin(\alpha/2) n + d_{CH_3}$ in all trans configuration is calculated from a C-C bond length of $d_{CC} = 0.153$ nm, bond angle $\alpha = 112.9^\circ$, and an extra $d_{CH_3} = 0.03$ nm for the terminal methyl group. This amounts to 2.32 nm for C_{18} and 2.82 nm for C_{22} respectively. Taking into account the size of the bulky anions and the positively charged methylimidazolium ring, this suggests that the observed periodicities d are mainly governed by the cation's side chains. Comparing the values for $[C_{18}C_1im]^+$ and $[C_{22}C_1im]^+$ based ILs with the same anion at their melting points, we consistently find an increase of 0.11 nm per CH_2 group. This value is close to the 0.128 nm expected for one segment of a stretched alkyl chain in all trans

configuration. A significantly larger increase by 0.196 nm per CH_2 group was found by Russina et al. for a series of $[\text{C}_n\text{C}_1\text{im}]^+[\text{NTf}_2]^-$ ILs with $4 \leq n \leq 10$ [229, 272]. Thus, it was suggested that in these ILs the alkyl side-chains are not interdigitated. Hardacre et al. compared the periodicity of a series of $[\text{C}_n\text{C}_1\text{im}]^+$ based ILs with different anions with $n \leq 20$ [23, 87]. They find a phenomenological dependency of $d_n = (0.37506 + 0.26717n - 0.004524n^2)$ nm. For $n = 8$, this equation gives an increase of 0.195 nm per CH_2 group. However, for longer alkyl chains, such as $n = 20$, the extrapolated value of 0.086 nm is much smaller than the 0.11 nm observed in our work. For $[\text{C}_{22}\text{C}_1\text{im}]^+[\text{NTf}_2]^-$, a crystal structure of alternating ionic and aliphatic layers was observed [150]. In the aliphatic layers, tilted alkyl side-chains are interdigitated. The lattice constant along the c-axis of the crystal is 3.17 nm, compared to 3.7 nm in the liquid close to the melting point. This suggests that, unlike for ILs with shorter side-chains, the ILs studied in this work form a structure with interdigitated alkyl chains (Fig. 9.2a). In other ILs, interdigitated side chains were particularly found for systems exhibiting smectic liquid crystalline order [22, 23, 76, 86]. One parameter that determines the tendency for the existence of smectic mesophases is the ratio of the area occupied by the alkyl side chains vs. the area of anions and cation heads in the charged regions. For small anions, interdigitated side chains are therefore often accompanied by the presence of a smectic phase. However, for the large anions studied in this work the ionic moieties take so much space that even for interdigitated chains no stable smectic mesophases are found.

In contrast to this comprehensible effect, induced by the cations side chain lengths, the dependency on the anions seems to be counterintuitive. The molecular mass of the bulky $[\text{NNf}_2]^-$ anion is about twice of its smaller $[\text{NTf}_2]^-$ analog. However, at all temperatures ILs with $[\text{NTf}_2]^-$ anions exhibit a higher periodicity d compared to those comprised of $[\text{NNf}_2]^-$. The contraction within the apolar regions between ILs based on $[\text{NTf}_2]^-$ and $[\text{NNf}_2]^-$ amounts for 10% for $[\text{C}_{18}\text{C}_1\text{im}]^+$ and 7% for $[\text{C}_{22}\text{C}_1\text{im}]^+$. A similar trend can be found in the data summarized by Russina, while no explanation for this effect was provided [229]. Apparently, ILs containing larger anions exhibit a shorter periodicity. We explain this paradox by the tilt and conformation of the alkyl side chains (yellow cylinders, Fig. 9.2c), acting as spacers between the charged layers containing the anions (blue spheres) and the positively charged imidazolium rings (red spheres). The larger the anions, the larger is the projected area $\sigma = V/d$ per alkyl chain. From the molecular volume V_m (Tab. 6.1) we obtain an area between 0.27 nm² for $[\text{C}_{18}\text{C}_1\text{im}]^+[\text{NTf}_2]^-$ and 0.37 nm² for $[\text{C}_{18}\text{C}_1\text{im}]^+[\text{NNf}_2]^-$ at their melting points. This area is much larger than $\sigma_0 = 0.20$ nm² in octadecane crystals [46]. In ILs, the excess area provided by larger anions lead to a lower Van-der-Waals interaction between the chains. To maintain the preferred distance between neighboring CH_2 groups, the chains tend to collapse with increasing σ . Therefore, the periodicity d is decreasing.

With increasing temperature, the peaks shift to higher q values (Fig. 8.2). This is reflected by the negative thermal expansion dd/dT of the long axis of the IL-molecule observed for all ILs in this study (Fig. 9.1a) and agrees with our earlier findings on $[\text{C}_{18}\text{C}_1\text{im}]^+[\text{FAP}]^-$ [174]. Similar effects were observed in a liquid crystalline ILs [42]

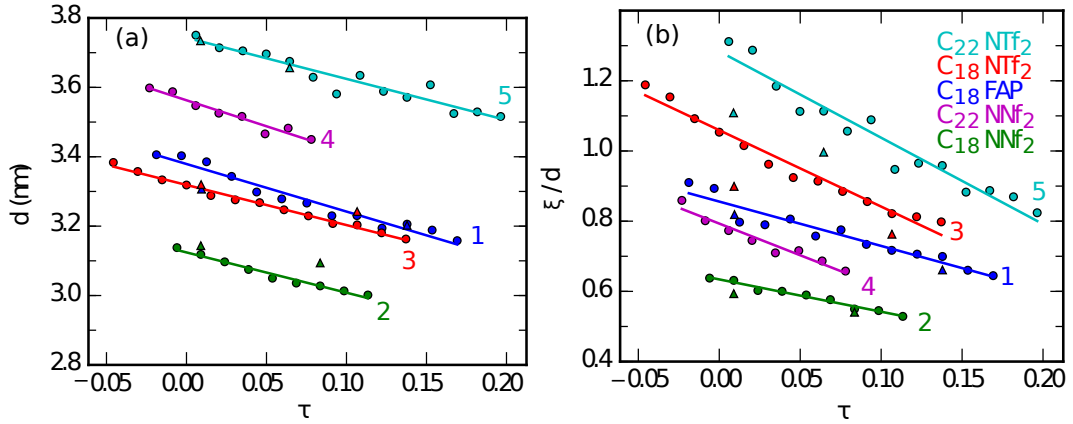


Figure 9.1: (a) Periodicity d and (b) normalized correlation length ξ/d vs. reduced temperature $\tau = \frac{T-T_m}{T_m}$ extracted from the results of fitting Eqn. (8.2) to the SAXS (dots) and SANS (triangle) data and from the peak position by $d_p = 2\pi/q_0$. $[\text{C}_{18}\text{C}_1\text{im}]^+ [\text{FAP}]^-$ (1, blue), $[\text{C}_{18}\text{C}_1\text{im}]^+ [\text{NNf}_2]^-$ (2, green), $[\text{C}_{18}\text{C}_1\text{im}]^+ [\text{NTf}_2]^-$ (3, red), $[\text{C}_{22}\text{C}_1\text{im}]^+ [\text{NNf}_2]^-$ (4, purple), $[\text{C}_{22}\text{C}_1\text{im}]^+ [\text{NTf}_2]^-$ (5, cyan). Solid lines are linear regressions to the Teubner-Strey parameters extracted from the SAXS data.

and surfactants [93]. In these systems, alkyl chains act as spacers in mesoscopic lamellar structures [93]. The observed thermal compression is assigned to an increase in accessible conformations of the alkyl chains (Fig. 9.2b). In alkyl-imidazolium based ILs the ration between trans and gauche conformations varies [249]. The larger the concentration of gauche conformations in the side chain, the larger the blue shift of the symmetric and asymmetric methylene CH stretching modes in the IR spectra. For $[\text{C}_{18}\text{C}_1\text{im}]^+ [\text{FAP}]^-$, with increasing temperature a continuous shift towards higher wavenumbers was observed [174]. This indicates an increase in gauche conformations leading to a decreasing distance between the ionic and aliphatic regions. For cations with shorter alkyl side-chains this temperature induced contraction is expected to be smaller. Temperature dependent measurements by Fujii et al. give a contraction of approx. $-2 \cdot 10^{-3} \text{ nm/K}$ for $[\text{C}_{12}\text{C}_1\text{im}]^+ [\text{NTf}_2]^-$ while no pronounced trend is observed for the peak position in $[\text{C}_8\text{C}_1\text{im}]^+ [\text{NTf}_2]^-$ [66].

9.1.2 Correlation Length

This interpretation of the periodicities d is confirmed by the analysis of the correlation lengths ξ . The larger the widths of the pre-peaks shown in Fig. 8.1 and Fig. 8.2, the smaller is the correlation length ξ of the underlying oscillatory $G(r)$. Pronounced changes in the peak widths can be observed at different temperatures [272] and cation side-chain lengths [65, 87, 229] in the datasets presented in literature. However, this parameter has been largely overlooked and so far only few authors noted that the pre-peaks get sharper for cations with longer alkyl side-chains [87, 89]. From our quantitative analysis, three trends are observed for the normalized correlation lengths ξ/d extracted

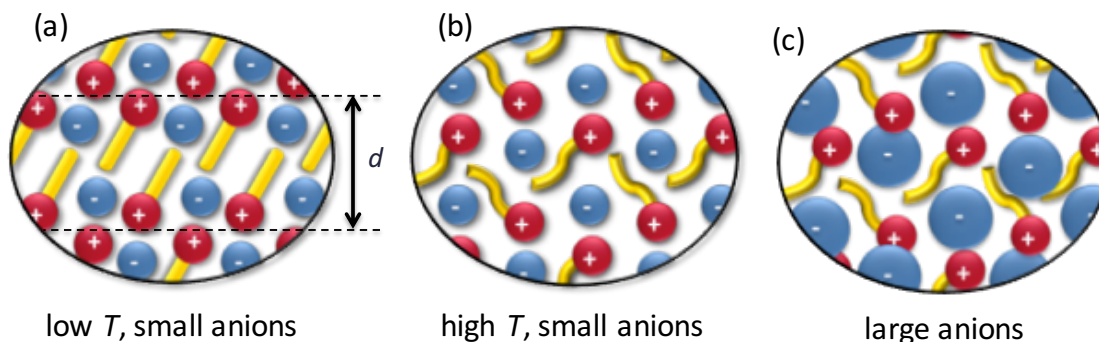


Figure 9.2: (Color) Sketch of the proposed decrease of local alkyl chain ordering (yellow) with (b) increasing temperature and (c) increasing anion size. The increasing number of gauche defects in the alkyl chains lead to a contraction of the periodicity d . Figure reproduced from H. Weiss et al. [291].

by fitting the SAXS and SANS data (Fig. 9.1b): First, homologues with longer alkyl side-chains show larger correlation lengths, even when normalized by their larger periodicity d . Note that the lengths of the C_{18} and C_{22} side chains are only between three and four times the polyethylene persistence length of about 0.7 nm [226]. In $[C_{22}C_1im]^+$ based ILs, adjacent alkyl chains have stronger Van-der-Waals interactions. Therefore, the concentration of gauche conformations is reduced. Thus, local fluctuations of the separation distance between the ionic regions are smaller. This results in a larger normalized correlation length ξ/d .

Second, ILs composed of $[FAP]^-$ and $[NTf_2]^-$ anions show larger correlation lengths compared to the more bulky $[NNf_2]^-$. This observation is evoked by the same effects as discussed for the periodicity. The increased area per alkyl chain diminishes the Van-der-Waals interactions in the apolar regions. This causes a less coherent structure with reduced correlation lengths (Fig. 9.4). As an extreme case, for ILs with long side chains and very small anions such as $[C_{16}C_1im]^+[PF_6]^-$ or $[C_{18}C_1im]^+ Cl^-$, $[BF_4]^-$, and $[PF_6]^-$ liquid crystalline smectic-A phases with long range translational order have been observed [22, 23, 42, 76, 86, 96, 150, 185]. Likewise, for $[C_{12}C_1im]^+ [NTf_2]^-$, i.e. the IL with the largest normalized correlations length studied in this work, a metastable liquid crystalline smectic-A phase is observed upon supercooling below its melting point [150]. Third, on temperature increase structures of higher entropy with reduced short range order are favored. This is consistent with the decreasing normalized correlation length observed in Fig. 9.1b.

9.1.3 Temperature Effects

To understand the above described overall trends, we compare the derivatives dl/dT and $d\xi/dT$. The larger the anions, and the shorter the side chains, the higher the concentration of gauche conformations upon melting. Therefore, a further increase in tempera-

ture tends to affect the periodicities d and the normalized correlation lengths ξ/d less (Tab. 8.1). While this simplified rule is not strictly valid for all anion/cation combinations studied in this work, it clearly reproduces the dominating trends. Recently, Fujii et al. used an analysis technique based on truncated mutual Fourier transformations to study the temperature dependence of the pre-peak in $[\text{C}_{12}\text{C}_{1}\text{im}]^+ [\text{NTf}_2]^-$ [66].

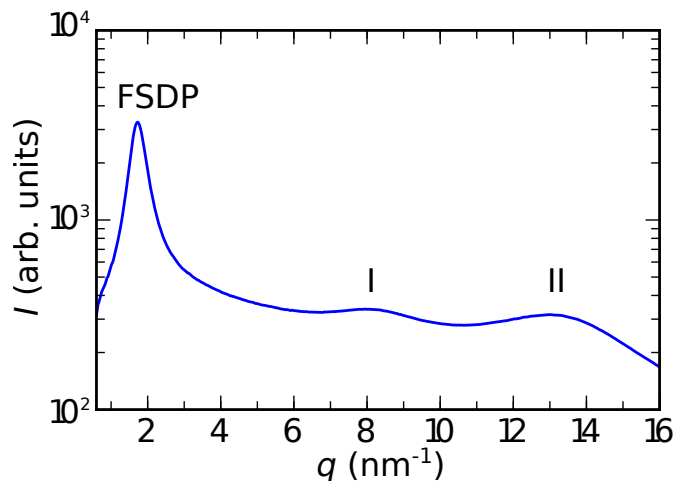
9.1.4 Anions and Cations

As long as only the periodicity d is considered, the structure of the ILs seems to be dominated by the cations. The increase in periodicity for larger anions observed in this work is only a second order effect that arises from an increasing number of gauche conformations in the cations alkyl side-chains. For shorter alkyl chain lengths, this anion effect is expected to be less pronounced. Furthermore, for cations with side-chains shorter than octyl, the polarity i.e. the pre-peaks and the charge alternation peaks start to interfere [66, 229]. In general, this makes the observation of small anion effects from shifts in the peak position unfeasible. Therefore, it has been proposed that anions have comparably little effect on the liquid structure, but mainly influence the SAXS and SANS patterns by providing the scattering contrast between the ionic and aliphatic regions [94].

In contrast to the periodicity d , Fig. 9.1b shows that anions have a remarkably strong influence on the correlation length ξ . However, to our knowledge this important structural parameter has never been quantitatively analyzed and discussed for ILs. The normalized correlation length ξ/d decreases by a factor of approx. 3/2 if the $[\text{NTf}_2]^-$ anion is exchanged by its larger $[\text{NNf}_2]^-$ analogue with about twice the molar mass. This strong effect can be directly observed in the SAXS peak broadening, even without fitting of a specific model (Fig. 8.1a).

The ILs investigated in this work differ in two respects from those commonly used in many other studies. Their cations C_{18} and C_{22} alkyl chains are longer than most frequently studied chains that are typically shorter than dodecyl. The molecular mass of $[\text{NNf}_2]^-$ and $[\text{FAP}]^-$ is larger and their structure more complex compared to the more often used Cl^- , $[\text{BF}_4]^-$, or $[\text{PF}_6]^-$ anions [91]. Therefore, a vast generalization of our finding, i.e. that for all ILs the normalized correlation length is strongly depending on the size of the anion, might be misguided. However, the results evidently question the statement that anions have no significant effect on the liquid structure. Another interesting question concerns possible relations between the correlations within the charged domains and the correlation length ξ of the polarity alternations. Therefore, it might also be interesting to investigate possible dependencies between the decay lengths extracted from the FSDP and the structural information encoded in the wide angle scattering patterns containing the charge alternation and adjacency correlations (Fig. 9.3). However, in contrast to the FSDP, the second and third scattering peaks are affected by multiple correlations and anti-correlations [7, 94]. This precludes a direct interpretation and comparison of their peak shapes and intensities.

Figure 9.3: Wide angle X-ray scattering pattern of liquid $[\text{C}_{22}\text{C}_1\text{im}]^+ [\text{NTf}_2]^-$ at 96°C . The first sharp diffraction peak (FSDP) originates from polarity alternations caused by microphase separation between ionic and aliphatic moieties [5, 7, 94, 272]. Peak II at 8 nm^{-1} and peak III at 13 nm^{-1} are attributed to charge alternations and adjacency correlations between neighboring atoms respectively [7, 120]. Figure reproduced from H. Weiss et al. [291].



9.1.5 Entropy of Fusion

Comparing the entropy of fusion ΔS_f between the $[\text{C}_{18}\text{C}_1\text{im}]^+$ and $[\text{C}_{22}\text{C}_1\text{im}]^+$ based ILs shows that ΔS_f increases by $7.25\text{ J}/(\text{mol K})$ and $8.75\text{ J}/(\text{mol K})$ per CH_2 group for $[\text{NTf}_2]^-$ and $[\text{NNf}_2]^-$ respectively (Tab. 6.1). These values agree with the calculated conformational entropy difference per C-C bond between an all trans chain and all possible conformations without steric hinderance $\Delta S_{\text{CC}} = N_A k_B = 9.13\text{ J}/(\text{mol K})$ [190]. The interpolated experimental value for alkanes is about $8.16\text{ J}/(\text{mol K})$ per CH_2 group [39]. For the ILs studied in this work a linear dependency between the normalized correlation length ξ/d at their respective melting point vs. the normalized entropy of fusion $\Delta S_m/\Delta S_{\text{CC}}$ (Fig. 9.4) is observed. This interesting relation connects structural parameters on the molecular length scale with a thermodynamic bulk quantity. The ILs behave differently than long chain alcohols (red circles) [269], where similar mesoscopic heterogeneities were observed [18]. Apparently, more experimental data and theoretical calculations are required to study this fundamental relation.

9.1.6 Conclusions

From the systematic comparison of the correlation functions of five different anion/cation combinations we deduce a model that describes the short range correlations in ILs with long aliphatic chains. The pre-peaks observed in the SAXS and SANS patterns originating from mesoscopic polarity alternation are quantitatively reproduced by a generalized Teubner-Strey model. In addition to the periodicity d , commonly obtained from the peak position using Bragg's law, this analysis technique also yields the correlation length ξ , i.e. the exponential decay length of the asymptotic oscillatory correlation function. Comparison between different ILs shows a pronounced anion dependence of the corre-

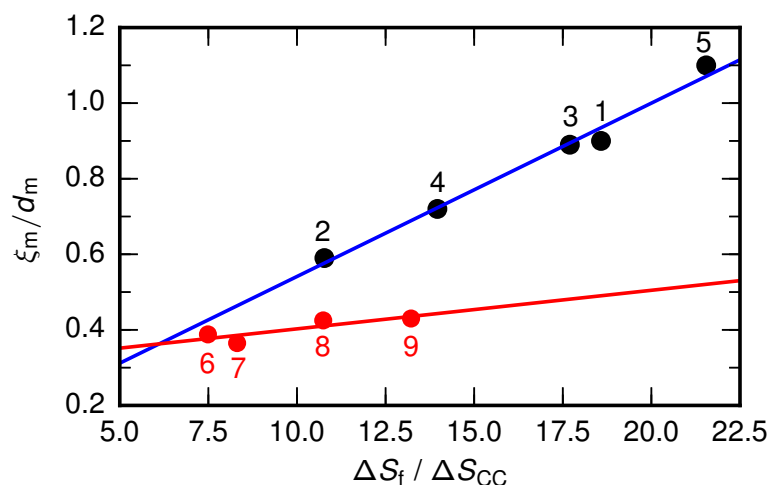


Figure 9.4: Normalized correlation length ξ_m/d_m at the melting point vs. entropy of fusion $\Delta S_f/\Delta S_{CC}$ for the ILs (black circles) $[C_{18}C_1im]^+ [FAP]^-$ (1), $[C_{18}C_1im]^+ [NNf_2]^-$ (2), $[C_{18}C_1im]^+ [NTf_2]^-$ (3), $[C_{22}C_1im]^+ [NNf_2]^-$ (4), $[C_{22}C_1im]^+ [NTf_2]^-$ (5). Lines are linear regressions to the datapoints. Values for linear alcohols $C_6H_{13}OH$ (6), $C_7H_{15}OH$ (7), $C_8H_{17}OH$ (8), $C_{10}H_{21}OH$ (9), were extracted from Ref. [269] (red circles). Figure reproduced from H. Weiss et al. [291].

lation length. Therefore, it is concluded that for the studied ILs not only the cations but also the anions have a strong influence on the liquid structure. In summary: the envelop of the oscillatory correlation function $G(r)$ for ILs comprised of larger anions, shorter alkyl side chains, at higher temperatures decays faster. Comparison of the normalized correlation lengths ξ/d of the studied ILs with thermodynamic quantities shows an intriguing relation. A linear dependency of ξ/d at the melting points with their entropies of fusion was found.

The bulk correlations $G(r)$ drive an oscillatory interfacial structure on the nanometer length scale [174]. These structures can affect the mobility and segregation of guest molecules at IL surfaces. Therefore, the observed dependencies have important implications for technologically highly relevant processes occurring adjacent to IL interfaces. Thus, to understand and improve electrochemical processes [8] and SILP catalysis [160, 221, 259] a detailed knowledge on the mechanisms affecting the bulk correlations in ILs are highly desirable.

9.2 Hydrophilic Ionic Liquid Water Mixtures

The elucidation of $[\text{C}_8\text{mim}]^+ [\text{Cl}]^-$ under water influence was a contribution by the author to a collaboration with the Max-Planck-Institute für Eisenforschung, Düsseldorf [38]. Chap. 4.1 introduced how water can distinctly alter the IL bulk structure. Here, water uptake takes place during exposure of the IL to an environment of controlled humidity for a specific time. This enables tracking of the IL bulk structure evolution. A similar humidity set-up is used as described in Chap. 11.6. Humidity was measured by a hygrometer and adjusted to 35-40% RH, exposure times varied from 0 to 120 min. Karl-Fischer titration, performed in Düsseldorf, achieved a calibration curve for this IL, correlating exposure time at the adjusted humidity to water uptake in weight percent [38]. Before water exposure, the IL was dried for 24 h under high vacuum (10-5 mbar).

9.2.1 1-methyl-3-octyl-imidazolium chloride

Fig. 9.5 and Fig. 9.6 show that three distinct liquid macroscopic structures were found for different water concentrations. A mesoscopic domain structure under dry conditions ($t = 0$ min; w.t. % = 0), a water swollen mesoscopic domain structure between $t = 30$ min; w.t.% $0 < 15$ and a hexagonal columnar structure beyond $t = 60$ min; w.t.% > 15 .

When the IL is dry, the azimuthally integrated scattering pattern exhibits a so-called first sharp diffraction peak (FSDP). This is indicated by the red curve in Fig. 9.5. FSDP position around $q_{\text{max}} = 2.78 \text{ nm}^{-1}$ corresponds to a real space distance $d = 2\pi/q_{\text{max}} = 2.26 \text{ nm}$. Indicating liquid-like intermediate range correlations [291], the FSDP accounts for microphase separation between aliphatic and ionic domains [94]. Different ILs with long aliphatic side chains lead to similar scattering patterns [21, 58, 59, 87, 228, 291]. The distance between aliphatic and ionic domains is an intricate interplay between alkyl side-chain length, increasing van der Waals interactions between alkyl chains, and ionic domain molecular size. In Sec. 9.1 it has been shown, how anion molecular size increases alkyl side-chain distance, diminishing van der Waals interactions, leading to a shift in FSDP position. The measured FSDP real space distance of 2.26 nm corresponds well to the calculated distance of the C_8 alkyl side chain length of 1.06 nm [21]. Peak width is broad in comparison to the other signals. This indicates a fast decay of correlation length of the structure. In total, the dry signal of $[\text{C}_8\text{mim}]^+ [\text{Cl}]^-$ is a typical signal of a mesoscopically structured ionic liquid. Without water influence the expected polar and apolar domain structure has developed.

The green curve is recorded after an exposure time of 30 min. Firstly, a peak shift to smaller q values is observed. The shift to a lower momentum transfer of $q_{\text{max}} = 2.69 \text{ nm}^{-1}$ can be explained by an increase of the structural dimension to 2.34 nm, i.e. swelling by 3.5%. Structure periodicity d has increased, assumingly by water absorption around the anion. Furthermore, it can be seen that FSDP width has decreased. This indicates an increased correlation length ξ [291]. Water, absorbed by the already in a dry state mesoscopically ordered structure, has increased ordering in the bulk of $[\text{C}_8\text{mim}]^+$

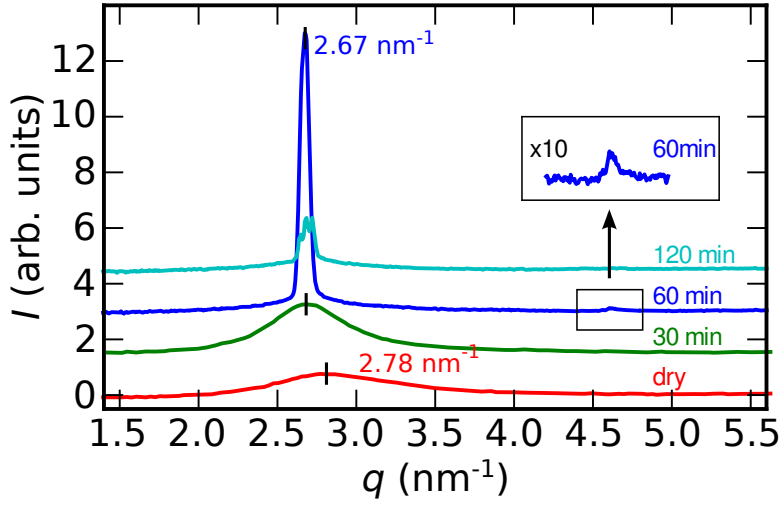


Figure 9.5: Azimuthal integrated pattern of structure evolution as a function of exposure time of $[\text{C}_8\text{mim}]^+ \text{Cl}^-$ are measured by small angle X-ray Scattering (SAXS). Inset: Detailed display of higher order signal at $\sqrt{3} q_{\text{max}01}$ indicating hexagonal structure. Figure reproduced from H.-W. Cheng et al. [38].

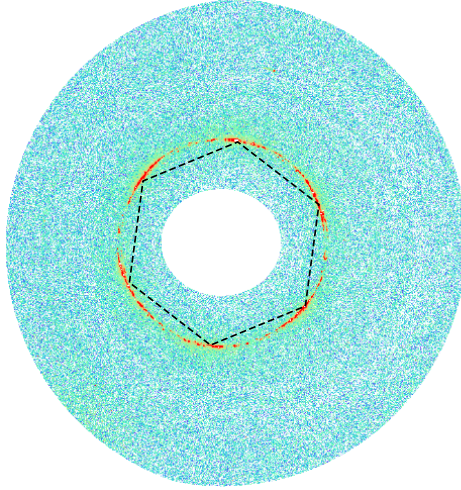


Figure 9.6: 2D-scattering pattern of $[\text{C}_8\text{mim}]^+ \text{Cl}^-$ at $q = 2.67 \text{ nm}^{-1}$ at 60 min of exposure under controlled humidity of 35-40% RH. Clearly the orientation of the FSDP signal at $q_{\text{max}01} = 2.67 \text{ nm}^{-1}$ into a six-fold structure is visible. The hexagon shall guide the eye. Figure reproduced from H.-W. Cheng et al. [38].

$[\text{Cl}]^-$ in comparison to the dry IL. This might be attributed to solvophobic effects of the present water. Water presence itself leads to an increased exclusion effect of hydrophobic domains, i.e. the aggregation of alkyl side-chains. Also, screening of the anion charge by the formation of an hydration shell, increases polarity effects within the polar domains. All this contributes to a further increase of exclusion effects between apolar domains and domains with increased polarity. Hence, water has a structure inducing effect when absorbed in $[\text{C}_8\text{mim}]^+ [\text{Cl}]^-$.

Longer exposure to moisture leads to a more distinct change in mesoscopic structure. This is indicated by the now very sharp blue and cyan curves in Fig. 9.5 after exposure time of 60 min and 120 min, respectively. The Bragg peak at $q_{\text{max}} = 2.67 \text{ nm}^{-1}$ (blue curve) sharpens distinctly after an exposure time of 60 min. A weak higher order reflection can be observed at $q_{\text{max}} = 4.7 \text{ nm}^{-1} = \sqrt{3} q_{\text{max}}$. An inset with a tenfold magnification demonstrates, that this signal indeed is distinct from the background signal. In general, more focused scattering of a structure indicates higher ordering. Thus, the ob-

served signal structure of sharp scattering points to a liquid crystalline structure within the IL. Signal structure of $q_{\max} : \sqrt{3} q_{\max}$ indicates hexagonal nearest neighbor distance, similar to observations for other ILs under water influence [58]. Higher signal orientation can also be seen in the 2D-scattering pattern shown in Fig. 9.6. A sharp scattering ring with a sixfold orientation is visible, pointing to a hexagonal liquid crystalline structure as well. These two indicators of a hexagonal packed structure correspond to the pronounced texture with six-fold symmetry comprised of hexagonal packed columns for the bulk liquid found in other ILs under water influence [59]. Longer exposure to moist air is depicted by the cyan curve. It is at the same q position as the blue curve, but signal height is corrupted. Width of the signal peak is comparable. Due to the liquid crystalline signal formed (c.f. Fig. 9.6), intensity focuses on a narrow ring on the detector. Resolution is aggravated by this, explaining the corrupted signal. Fine resolution of peak maximum is not possible anymore. However, a distinct change with longer exposure time can be excluded. A prolonged exposure time to a humidity of 35-40% RH, beyond 60 min, seems to have no influence on IL bulk structure.

The highly orientated structure influences macroscopic behavior of the IL. In the regime of water uptake used here, gelation is observed with increasing water uptake. While the dry IL is highly viscous, increasing water uptake solidifies the IL to a gel. Even higher water uptake than achieved in this set of measurements, beyond 50 w.t.% and more, would lead to a turn-around of phase behavior [21, 281]. As focus was laid on smaller amounts of water absorbed by ILs, these phases are not dealt with here.

Signal evolution of $[\text{C}_8\text{mim}]^+ [\text{Cl}]^-$ under water influence shows the distinct phase change from mesoscopically ordered decaying phase, to highly orientated long range ordered liquid crystalline phase. The threshold of phase change can be identified to be in the range of an exposure time of 30-60 min, which corresponds to a water uptake between 10-15 w.t.%. Segregation is driven by the presence of water. Water absorption to polar domains increases the contrast between polar and apolar parts already present in the IL. Orientation in the IL is increased by solvophobic effects. Polar domains are ordered by increased polarity, while apolar domains are excluded due to presence of water. Water is primarily absorbed to the polar domains, hence packing apolar domains closer together, increasing van der Waals interactions between them. Stronger interactions within the domains favors the evolution of long range structures. The structure identified corresponds to a densely packed structure of micelles of sixfold symmetry. The percolating network, first only swollen by water absorption, switches to discrete micelle pillars of apolar domains, excluding water-rich polar domains. Water absorption drives IL molecular structure and viscosity, making it possible to adjust bulk IL molecular structure by operating at a controlled water percentage within the IL. How the presence of interfaces influences the IL structure under water influence will be investigated in the upcoming chapters.

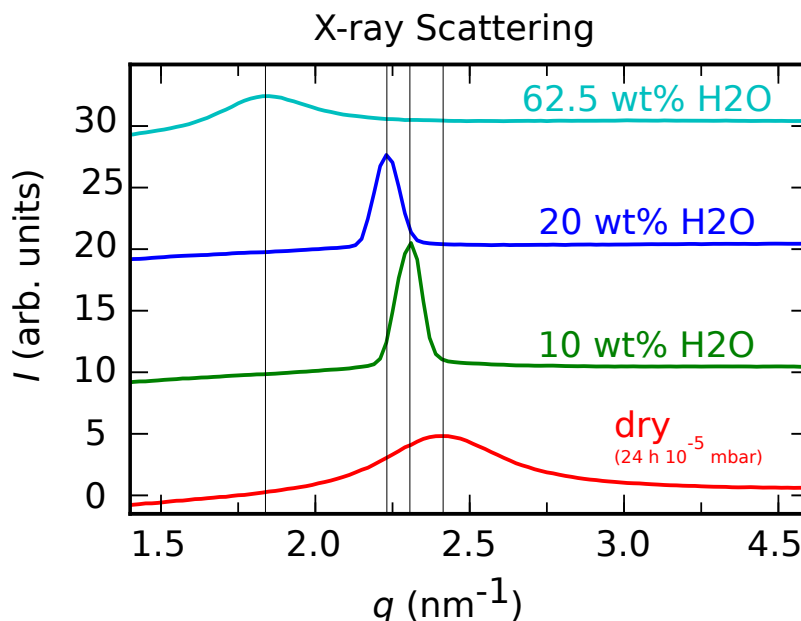
9.2.2 1-decyl-3-methyl-imidazolium chloride

The previous chapter showed which intriguing structural behavior is displayed by $[\text{C}_8\text{mim}]^+ [\text{Cl}]^-$ under water influence. However, for dynamic measurements in a slit-pore confinement, the system featuring the longer homologue 1-decyl-3-methyl-imidazolium Chloride $[\text{C}_{10}\text{mim}]^+ \text{Cl}^-$ was chosen to be elucidated by XSFA measurements. Prior to be used as a sample in confinement experiments, the bulk liquid structural behavior under water influence of 1-decyl-3-methyl-imidazolium Chloride $[\text{C}_{10}\text{mim}]^+ \text{Cl}^-$ was characterized during in-house SAXS experiments. In contrast to $[\text{C}_8\text{mim}]^+ [\text{Cl}]^-$, which was moisturized by exposure to a controlled humid atmosphere, $[\text{C}_{10}\text{mim}]^+ \text{Cl}^-$ was physically mixed with water. The real water content can be indicated. For details on sample preparation see Sec. 6.1. Figure 9.7 shows the acquired SAXS-pattern.

During dry conditions the expected mesoscopic structure signal, indicated by an FSDP at 2.41 nm^{-1} , can be observed (red curve Fig. 9.7). This corresponds to the segregated domain structure, into which polar and apolar parts migrate. A real space distance of $d = 2\pi/q = 2.61 \text{ nm}$ results. Comparing with the real space length scale of $[\text{C}_8\text{mim}]^+ \text{Cl}^-$ having $d = 2.26 \text{ nm}$, the difference between $[\text{C}_{10}\text{mim}]^+$ and $[\text{C}_8\text{mim}]^+$ is not equal to the length of 2 CH_2 -groups ($2 \text{ CH}_2 = 2 \times 0.128 \text{ nm} = 0.256 \text{ nm}$). The length of the $[\text{C}_8\text{mim}]^+$ cation is shorter than the 2.354 nm resulting when subtracting the 2 CH_2 group distance from the $[\text{C}_{10}\text{mim}]^+$ real space distance length. This can be explained by the stronger van der Waals interactions between the C_{10} -chains, leading to more anti-conformations and by this a longer alkyl side-chain length. In contrast to that, apolar domains of $[\text{C}_8\text{mim}]^+ \text{Cl}^-$ exhibit less van der Waals interactions. Hence, the alkyl side-chains take up more gauche conformations, leading to a diminished observed real space distance between domains. This observation corresponds well to the results observed in Chap. 9.1 for the hydrophobic ionic liquid bulk structure. There also, increased van der Waals interactions between longer alkyl side-chains were observed.

Upon a water addition of 5-60 w.t.% H_2O to the IL, a liquid crystalline gel results (green and blue curve Fig. 9.7) [59]. Signal position shifts to lower q , indicating an increased real space distance. Signal sharpness increases drastically, indicating increased correlation length. Peak width is now in the order of the device resolution. No further information can be extracted about peak width evolution. The green curve corresponds to a water content of 10 w.t.%. When comparing signal position at $q_{\text{max}} = 2.31 \text{ nm}^{-1} = 2\pi/q = 2.72 \text{ nm}$ with the real space distance at dry conditions, a swelling of 4.2 % is observed. This is in the same range as the 3.5 % of swelling observed for $[\text{C}_8\text{mim}]^+ \text{Cl}^-$. It is likely that the water enters the polar domains, forming a hydration layer around ions, having two effects. Firstly, ions within the polar domains will be further separated from each other. Secondly, ionic charge is shielded. When one ionic species is preferentially hydrated this increases polarity in the bulk liquid as only the charge of this specific ion is shielded, whereas the other ion is partially lacking its counterpart. This might explain the increased orientation observed in the IL. The increased signal sharpness points to an increased correlations length. The bulk liquid

Figure 9.7: Bulk liquid structure evolution of 1-decyl-3-methyl-imidazolium Chloride $[\text{C}_{10}\text{mim}]^+\text{Cl}^-$ as a function of water content measured by Small Angle X-ray Scattering (SAXS). See text for details.



structure under water influence is much more ordered than the dry IL. An explanation might be the increased polarity keeping polar domains apart. The emerging longer ranged forces would increase the order.

When adding 20 w.t.% of water, the signal still indicates liquid crystalline structure, having a very sharp signal. Signal position shifted to $q = 2.23 \text{ nm}^{-1}$ which corresponds to $d = 2.81 \text{ nm}$. This indicates a further swelling by 3.7% of the structure when comparing to 10 w.t.% water content. The second swelling is a little bit less than upon the first addition of 10 w.t.%. Upon first water addition, water molecules form a hydration layer around ions, increasing polarity. A further addition of water still leads to swelling, ergo a larger distance between ions in the polar domains, but not to further shielding of the ions. This points to the idea, that not the distance increase upon formation of a hydration layer around an ion, leads to polarity increase. It is the shielding of one preferred ion that increases polarity due to the lack of shielding of the counter-ion. Coulombic interactions between ion pairs are diminished, leaving one ion less shielded. Polarity on polar domains increases, hence long range forces increase, having an ordering effect on the mesoscopic structure due to the repulsive interactions.

Exceeding a water content of 62.5 w.t.% in the mixture, signal structure changes distinctly. The signal becomes much broader and shifts to low q , the structure is not liquid crystalline anymore. Peak positions at $q_{\text{max}} = 1.85 \text{ nm}^{-1}$ corresponds to a much larger real space length scale of $d = 3.40 \text{ nm}$. This signal can be explained by assuming a micellar structure of IL cations in water, with the chloride anions hydrated and dissolved. A phase reversal from a continuous IL phase to a now continuous water phase occurred. When taking into account the length of two cations (c.f. Fig. 6.1), one readily arrives at a length scale of $d = 3.44 \text{ nm}$ which corresponds well with the observed length scale. It seems reasonable to assume micelles made up of IL cations, with the hydrophobic tail

orientated inwards. The chloride anion is fully hydrophobized and is dissolved in the continuous water phase. In this regime, ILs form similar structures to tensides. Peak width is broad, reflecting the heterogeneous size distribution of the micelles. All in all the signal structure at 62.5 w.t.% water content points into the direction of an IL in water structure, in which water forms the continuous phase.

Macroscopic observations correspond to that. Upon water absorption, for the liquid crystalline phase, gelation was observed. But crossing the tipping point of phase change by adding more water than 60 w.t.%, the mixture became liquid again. Viscosity decreased immensely compared to the previously observed gel phases. This backs up the interpretation of the formation of an IL in water phase.

This preliminary characterization showed that a liquid crystalline structure induced by water absorption occurs in $[\text{C}_{10}\text{mim}]^+\text{Cl}^-$. If a similar structure forms under water influence in molecular confinement and how the structure behaves under shear stress, was researched on by XSFA experiments. Results are presented in Chap. 13.2.

Part IV

X-ray Surface Force Apparatus

Chapter 10

Materials

The construction of the X-ray Surface Force Apparatus was the main project of this thesis. During the thesis two experiments were performed. Planing, calculation and coordination of these joint experiments was done by the author. The device is designed to perform experiments at a synchrotron beamline. Assembly of the device takes place prior to the synchrotron experiment on site. Successful performance of experiment requires close collaboration of both Surface Force Apparatus controller and X-ray operator. SFA control was done by the collaboration partner, the group of Markus Valtiner, during each experiment¹. The device is based on the design principle drafted by the collaboration of Prof. Dr. Markus Valtiner, Prof. Dr. Frank Uwe Renner and Jun.-Prof. Dr. Markus Mezger.

10.1 Liquid Crystal 4'-octyl-4-cyano-biphenyl (8CB)

During the first synchrotron beamtime experiment of the newly constructed XSFA in February 2016, characterization of the device using a benchmark system was neces-

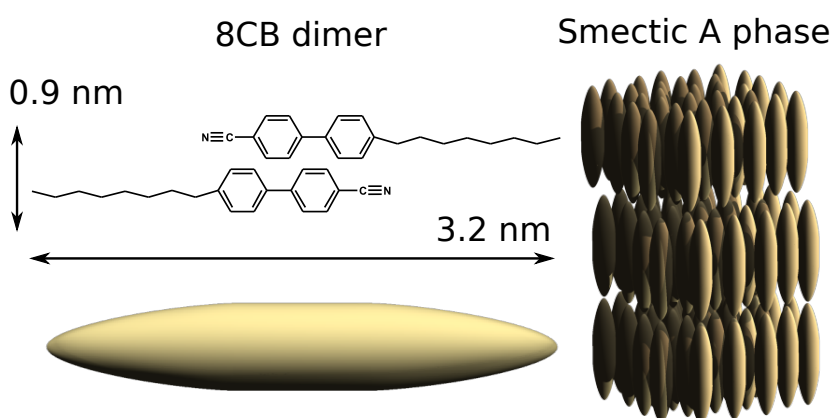


Figure 10.1: Rod like structure of 4'-octyl-4-cyano-biphenyl (8CB) dimers (left) and molecular alignment of mesogens in the liquid crystalline smectic A phase (right).

¹Acknowledgment: Prof. Dr. Markus Valtiner, Dr. Hsiu-Wei Cheng, Claudia Merola, Sadhanaa Buvaneshwaran, Dr. Christian Weber, Kai Schwenzfeier

sary. As a model system, which has also been well characterized by other groups, we choose the liquid crystal 4'-octyl-4-cyano-biphenyl (8CB) (Sigma-Aldrich, purity: 98 %, CAS: 52709-84-9). Being a liquid crystal 8CB displays several phases, the order of phase transitions and their respective melting points are: Crystalline / Smectic A (21.5°C); Smectic A / Nematic (33.7°C) ; Nematic / Isotropic (40.6°C). We see that at 22°C, 8CB exhibits a smectic A phase (Fig. 10.1). 8CB is known to form dimers by π - π -stacking effects of the adjacent rings, hence leading to dimer-molecule dimensions larger than the single monomer (Fig 10.1) [230]. Other groups already researched on the structure of 8CB in SmA phase in confinement under static [184] and dynamic [260] stress conditions. Complementary to that, we study the influence of compression/decompression forces on the structure of 8CB under confinement. Due to interactions of the unsaturated ring system with a polar surface, 8CB dimers lie down flat [230] on polar surfaces. To induce a perpendicular orientation of the 8CB molecules at a surface, hydrophobization, i.e. functionalization with a Self-Assembled Monolayer (SAM), is necessary. Different surfaces (mica, silica, gold, HOPG, sapphire, etc.; c.f. Chapter 5) require different SAM-functionalization treatment. As we will see in the following chapters, the XSFA confining surfaces are made of two different materials. Thus, upper and lower confining surface of the XSFA were hydrophobized by a self-assembled monolayer of hexadecane-thiol and octadecyl-trichlorosilane, respectively. During the XRR and in-plane scattering experiments, the liquid crystal was confined to two gap widths of 120 nm as well as 1700 nm, in order to study the dynamic response during increasing confinement over one order of magnitude. The gap widths correspond to about 38 and 532 layers of 8CB dimers, respectively, when the dimers are stacked in a SmA phase with their long axis parallel to the surface normal. The arrangement of the rod-like molecules in smectic layers gives rise to a pronounced scattering peak in the small angle scattering (SAXS) regime (Fig. 11.1b). Very small amounts of sample are needed using the XSFA, usually about a droplet (≈ 0.1 mL) is sufficient to perform a set of measurements. The sample is placed onto the confining surfaces using a spatula or syringe.

10.2 Hydrophilic Ionic Liquid 1-decyl-3-methyl-imidazolium chloride

The second beamtime performed using the XSFA researched on structure evolution in a molecularly confined hydrophilic IL under moisture influence. The sample system chosen was 1-decyl-3-methyl-imidazolium chloride $[\text{C}_{10}\text{mim}]^+[\text{Cl}]^-$ (Sigma-Aldrich, purity: 98 %, CAS: 171058-18-7, $M = 258, 83$ g/mol, $T_c = -2.1^\circ\text{C}$ [185]). The IL is a viscous liquid at room temperature featuring a small, hydrophilic anion. Due to the rather long alkyl side-chain, the molecular geometry anticipates a periodicity in a range of reciprocal space well visible in X-ray experiments, when forming an ordered molecular orientation. IIs featuring longer alkyl side-chains have higher melting points, prohibiting a use in the liquid state at a temperature of 22°C. Shorter cation

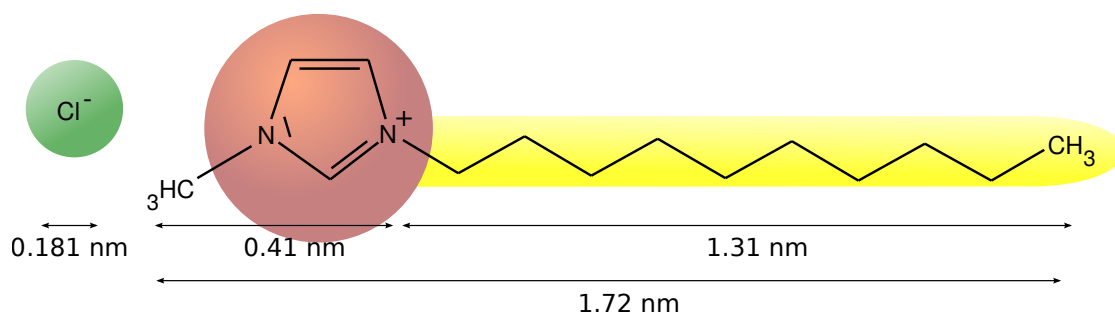


Figure 10.2: Molecular structure of 1-decyl-3-methyl-imidazolium chloride $[\text{C}_{10}\text{mim}]^+[\text{Cl}]^-$. This IL was used as sample system in the second XSFA beam-time.

side-chains lead to shorter real space distances which are not well visible in the accessible q -range of the XSFA, making an imidazolium based IL featuring a decyl-side-chain and a hygroscopic anion the system of choice. In preliminary wide-angle X-ray scattering experiments the phase behavior of the IL under water influence was elucidated (see Sec. 9.2.2). In a dry state, a mesoscopically ordered structure was observed, indicated by the the previously also in $[\text{C}_8\text{mim}]^+[\text{Cl}]^-$ observed FSDP. A liquid crystalline phase with high order was detected in a range between 10-60 w.t. %. Until about 60 w.t. % water is absorbed in the ionic liquid, beyond that a phase switch takes place and the IL is dissolved in a continuous water phase. The IL was dried before use for 24 h under high vacuum $p = 10^{-5}$ mbar. $[\text{C}_{10}\text{mim}]^+[\text{Cl}]^-$ is significantly hygroscopic on a time scale of minutes (5-10 min). Hence, handling and application once removed from vacuum were performed stringent. Within the XSFA chamber the sample liquid is surrounded by dry helium gas under constant flow, excluding and resorbing possible traces of absorbed water within the IL during handling and insertion. During the experiment, when confined between the two surfaces, moisture is taken up by the IL from the surrounding controlled humidity in the helium purging gas. Again, only very low quantities of sample were needed to perform measurements. Application onto the confining surfaces can again be done by a spatula.

Chapter 11

Experimental Technique

11.1 Compendium on X-ray Surface Force Apparatus Concept

By today, most structural information of confined fluids is obtained by computer simulations [77, 234] or indirectly deduced from force-distance curves measured using a Surface Force Apparatus (SFA, Fig. 11.1d), Colloidal Probe (Fig. 11.1e), or Atomic Force Microscopy (AFM). In particular, the Surface Force Apparatus (SFA) is an established experimental setup to simultaneously measure forces and distances across two surfaces approaching each other on a range from micrometers down to nanometers with Ångstrom precision.

This instrument can hence be used to create a controlled slit-pore confinement with dimensions on the molecular length scale [109]. Also, an SFA can very precisely apply stress on the confined material and measure its viscoelastic response. However, the force measurements in an SFA, colloidal probe, or AFM, actually do not probe the spatial arrangement of the molecules [126, 138]. Structural information are always extracted from force measurements using "reasonable" assumptions aiming to explain the measured data [169, 257]. On the other hand, X-ray scattering and reflectivity (XRR) are powerful techniques to directly probe structures on molecular length scales in bulk and at interfaces [55, 242, 294]. Today, high-brilliant synchrotron sources even allow in-situ studying of the structural dynamics on sub-microsecond time scales [212, 307].

For instance, extensive work has been conducted on the molecular scale structure of soft matter confinement in porous bulk-like materials using X-ray and neutron scattering techniques [27, 28, 127, 261, 262, 301]. Today, nearly mono-disperse cylinders in silica or aluminum oxide with diameters ranging from 5 nm to 1000 nm are available [101, 146, 155, 239, 310]. A good review on the behavior of ILs confined into pores is given by Shiguo Zhang et coworkers [309]. The work of M.N. Garaga et al. showed how the bulk liquid structure dynamics of an imidazolium-based long alkyl side-chain IL is influenced by nanopore confinement [69]. The observed faster molecular dynamics in

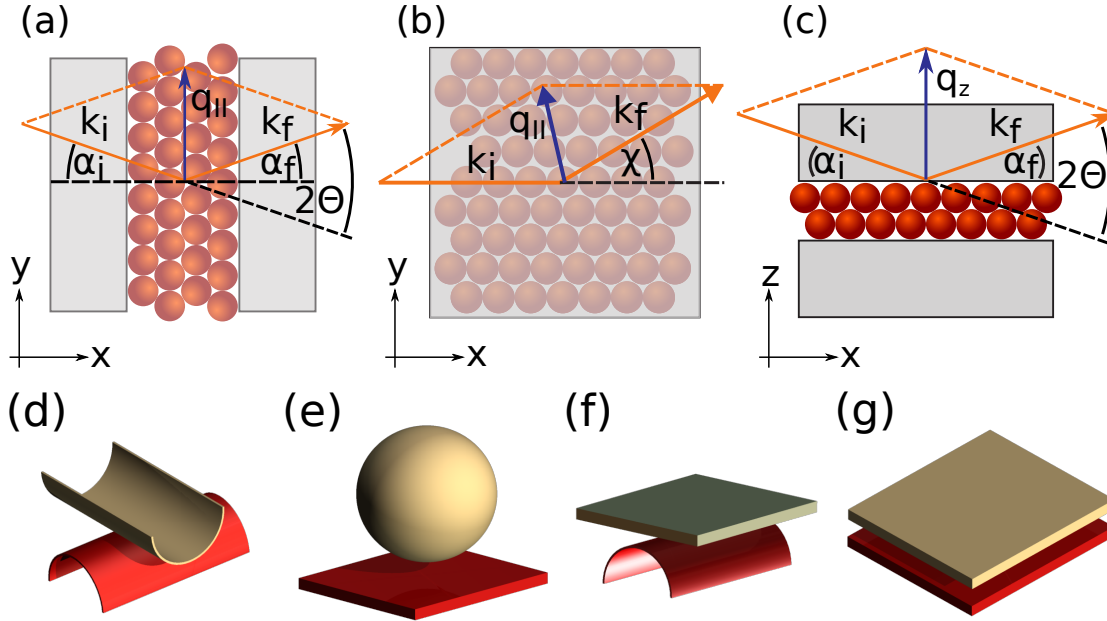


Figure 11.1: Overview of various experimental geometries to study confined liquids by X-ray scattering. The surface normal of the slit pore walls (grey) can be aligned perpendicular to the momentum transfer of the scattering vector $q = k_f - k_i$ in transmission (a) or in-plane scattering geometry (b). Specular reflectivity with q parallel to the surface normal of the slit pore walls probes the interfacial profile along the z -direction, i.e. across the slit pore (c). Confinement can be created in the standard SFA crossed cylinders geometry (d), the colloidal probe plane-sphere geometry (e), the plane-cylinder geometry (f), or the plane-plane geometry (g).

confinement were attributed to the weak surface interactions. The walls of the nanotubes were hydrophobized.

However, when dealing with materials confined to a porous structure the pore geometry has an influence. Due to the Gibbs-Thomson effect [171, 219, 265], the large curvature in nano-sized porous materials strongly affects the phase behavior of confined fluids [85]. Another problem in data analysis of scattering experiments of confined liquids in the porous material arises from the averaging of different directions. Moreover, dynamic studies during shear, compression, and decompression are intrinsically difficult to realize experimentally in a porous system. Therefore, to probe the intrinsic structure and dynamics of liquids confined between two parallel walls, other geometries have to be employed.

An X-ray Surface-Force-Apparatus (XSFA) simultaneously combines the two complementary experimental techniques of force-distance measurements and X-ray scattering [109]. This unique combination promises results not accessible by any other experimental method. Therefore, the development of an XSFA, that allows to drive the structure of the confined liquid out of equilibrium and record its relaxation by scatter-

ing techniques, will open up new ways to study the structural relaxation dynamics of confined liquids.

The first X-SFA for transmission experiments (Fig. 11.1a) in crossed cylinder geometry (Fig. 11.1d) was introduced in 1993 by the groups of J. Israelachvili and C. Safinya [73, 74, 104, 105, 106, 131, 152]. Experiments on the liquid crystal 4'-octyl-4-cyanobiphenyl (8CB) demonstrated, that a 10 nm thick 8CB film provides sufficient scattered intensity to extract static information on the molecular orientation induced by the confinement between the two mica cylinders.

Later, two different teams, lead by H. Reichert and F. Mugele at ID10C [13], ESRF and J.F. van der Veen and M. Heuberger at the Swiss Light Source [188], used a similar geometry. The latter team also explored the potential of an X-SFA in reflectivity (Fig. 11.1c) using the crossed cylinder geometry (Fig. 11.1d) [201, 202, 203, 204]. However, due to the large curvature of the cylinders, data can only be taken at large $q_z > 4.0 \text{ nm}^{-1}$. This precludes conventional XRR measurements. Therefore, the structure of the confined liquid can only be deduced from the crystal truncation rods (CTR) using a rather complex data analysis [204]. No structural in-plane information (Fig. 11.1 b) is accessible in this geometry, since a defined confinement is only established at the very center of the crossed cylinders.

More recently, the group of O. Seeck and M. Lippmann at PETRAIII designed an X-SFA in plane-plane geometry (Fig. 11.1g) [156]. The confining walls were made of two diamond culets (200 μm diameter), normally used in Diamond Anvil Cells, cut in crystallographic (100) direction. To achieve molecular scale confinement, the force of several tens of Newton is applied to the diamonds. With a maximum possible pressure of 100 N onto the 200 μm diameter culets, a pressure of about 3 GPa can be achieved. However, normal operation mode is around several hundreds of MPa to avoid sample changes and artifacts by the high pressure. This device was used in X-ray scattering and specular reflectivity experiments of the confined liquid benzene of thicknesses down to 5 nm. However, parallel alignment of the apposing macroscopic planar interfaces can be challenging and the roughness of $\text{RMS} \approx 1 \text{ nm}$ with peak-to-valley roughness of up to 1.4 nm of the diamond surfaces sets a limit to the information extracted from the scattering patterns.

Application of dynamic conditions was also performed in the crossed cylinder geometry [268]. The group of Kazue Kurihara demonstrated synchrotron measurements on confined ($[\text{C}_4\text{mim}][\text{BF}_4]$) between silica surfaces. Surface separation was in a range of 2 to 500 nm.

A different approach is to design cells and surfaces for Neutron experiments. These devices usually feature large confinement areas up to square centimeters to accommodate the large footprint. This aggravates a reproducible, exact confinement over the whole area. The group of T. Kuhl succeeded in creating a confinement of around 100 nm with a gap divergence of 35 nm [136, 137]. In this cell shear experiments are possible in the range of 0.001 to 20 Hz and it was especially used to investigate polymer films [80]. In a device by the group of S.W.Prescott a flexible membrane was used to create a confinement across the large area required [43, 288]. Only stress vertically to the con-

fining surfaces can be created by applying a different amount of gas pressure onto the membrane. Also in this device it proved crucial to keep the large confinement area free of contaminating particles, which are prone to corrupt measurements when trapped in confinement. A task becoming more challenging when dealing with larger confinement areas.

Neutron reflectivity was also employed to probe changes on the interfacial profiles of hexadecane under shear rates up to $\dot{\gamma} = 1000 \text{ s}^{-1}$ in a cone-plate rheometer [295, 296, 297]. A setup using a modified plate-plate rheometer was employed to study the influence of shear forces on the structure of bulk liquids by X-ray scattering techniques [240, 260]. However, most experimental designs based on conventional rheometers are not able to reach high enough shear rates to detect fast interfacial relaxation processes on the molecular length scale such as adsorption and desorption [177, 182].

How the device constructed during this work contributes to the work done on X-ray surface force apparatus research so far and how it avoids and ameliorates flaws and drawbacks of the devices presented is dealt with in chap. 11.2.

11.2 X-ray Surface Force Apparatus

We present a novel design of an X-SFA in planar-cylinder geometry (Fig. 11.1f) for in-plane scattering (Fig. 11.1b) and specular XRR (Fig. 11.1c). Using white light interferometry, this device can realize a controlled confinement in a slit pore geometry with gap thicknesses D ranging from several $10 \mu\text{m}$ down to molecular length scales. With this set-up, we can precisely control the thickness of the confined liquid, probed by the X-ray beam, over a lateral area up to $l = 4\text{--}5 \text{ mm}$ along the cylinder apex and a width of $w \approx 80 \mu\text{m}$. The instrument is capable to apply and monitor effects during dynamic changes through lateral (shear stress) and vertical (compression/decompression) motion of the lower one of the confining interfaces. Simultaneously, normal and frictional forces can be measured by strain gauges. Thus, XSFA experiments can provide complementary information to force distance measurements and conventional X-ray and neutron scattering studies in nano-porous materials.

In the present X-SFA setup (Fig. 11.2), confinement is realized between a stationary upper planar surface and a cylindrically curved lower surface in a flat-on-cylinder geometry (Fig. 11.1f). For dynamic studies, the lower surface can be moved vertically and horizontally with nanometer precision, while the upper planar surface remains static.

The upper surface is provided by a template stripped atomically smooth gold layer on an Al_2O_3 single crystal (Fig. 11.4) [154, 256, 258, 283]. A mica sheet, back coated with a semitransparent silver mirror serves as lower surface. For mechanical support, the thin mica is glued on a glass cylinder using UV hardened epoxy resin. Due to the compressibility of the glue, the mica sheet can comply with the planar upper surface when pressed against each other. This generates a slit-pore with a length l that is similar to the width of the crystal used, as well as a width w that depends on the applied pressure.

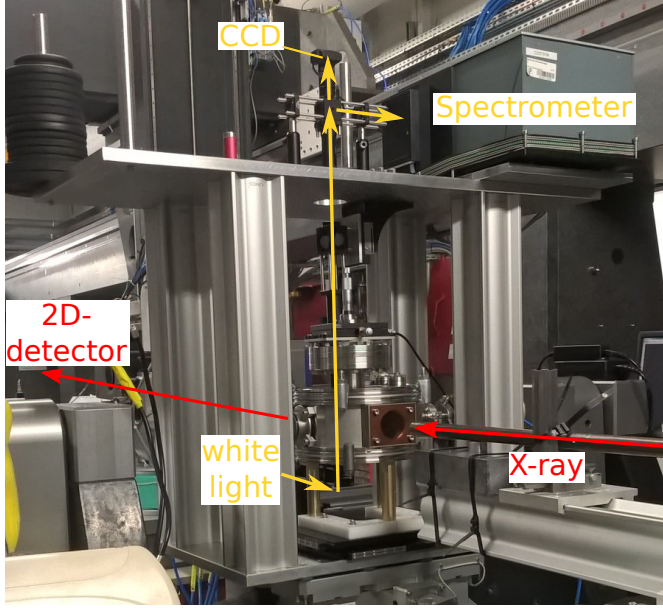
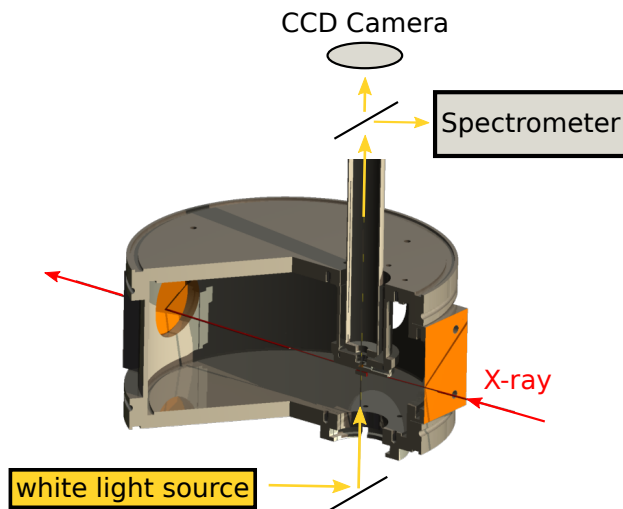


Figure 11.2: Photography of the X-SFA setup mounted on the HEMD diffractometer at ID31 ESRF. Arrows indicate white light (yellow) and X-ray (red) beam paths. The sample is located at the diffractometers rotation center inside a helium-filled stainless steel chamber. X-rays enter and leave the chamber horizontally through $80\text{ }\mu\text{m}$ Kapton windows. White light from a fiber light source is fed in via a mirror from below. Microscope objective, beam splitter, alignment camera, and spectrometer are mounted on the upper instrument level.

As a result, in this geometry, the confined area is much larger than for the conventional crossed cylinder setup (Fig. 11.1d). Typically, the plane-cylinder configuration provides a large scale confinement over an area A of $80\text{ }\mu\text{m} \times 4\text{--}5\text{ mm}$. For a $D = 2\text{ }\mu\text{m}$ slit-pore gap width, a total volume V up to $3 \times 10^{-3}\text{ mm}^3$ is probed by the X-ray beam. This is about 10-50 times the scattering volume probed by other XSFA setups in reflection geometry, depending on the applied pressure and hence contact area [156, 201]. When confining to a smaller gap thickness D the scattering volume decreases, but, as we show in Sec. 13, due to the long confinement length l still enough signal is generated by the material in the gap.

Both surfaces in direct contact with the liquid are atomically smooth with $RMS < 0.5\text{ nm}$ roughnesses. Surface properties can be tuned from hydrophobic to hydrophilic by functionalization with self assembled monolayers. Alignment of the nanometer confinement is actively measured and controlled using an interference microscope based on multiple beam white light interferometry. The incident X-ray beam enters through the side of the upper substrate in direction of the cylinder apex [103]. This avoids scattering artifacts from the mica edges. The Al_2O_3 single crystal reduces background scattering from the substrate. As the beam has to penetrate through several millimeters of Al_2O_3 , high energy X-rays are essential. The SFA is mounted inside of a gas tight stainless steel chamber (Fig. 11.3). A helium atmosphere improves the thermal stability of the setup and reduces background scattering. In addition, a humidity sensor and a humidifier allow online control of the relative humidity from $0 - 90 \pm 3\%$ relative humidity (r.h.) by moisturizing the helium flow constantly purging the cell.

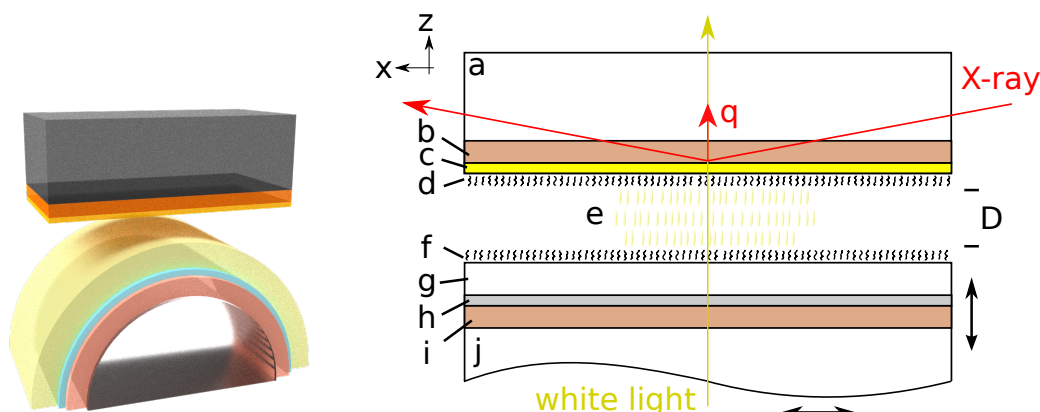
Figure 11.3: Sketch of the sample cell. The sample-cell accommodates the SFA moving parts while surrounding the confining surfaces with a Helium atmosphere to reduce background signal. White light (yellow) enters the cell from below, impinges the confining surfaces and is tracked by white light optics brought close to the confining surfaces from the top. The X-ray beam enters horizontally. Two Kapton windows (orange) enable background reduced X-ray beam (red) entrance.



11.3 Confining Surface Fabrication

To produce flat, atomically smooth, and reflecting surfaces, gold layers were template stripped from silicon wafers onto single crystalline corundum (Al_2O_3) cuboids. Corundum blocks ($10 \text{ mm} \times 4.8 \text{ mm}$, thickness 3 mm) were cut from flat optical grade polished discs (CrysTec, Berlin). To avoid parasitic scattering from the edges in grazing incidence measurements, the side facets and edges were polished. Hydrophilic corundum blocks and silicon wafers (approx. $20 \text{ mm} \times 10 \text{ mm}$) were prepared by immersion in freshly prepared Piranha solution (1 part H_2O_2 , 35%; 3 parts H_2SO_4 , 98%) for 20 minutes. Subsequently, substrates were rinsed with ultrapure water and blown dry with nitrogen. A $40 \pm 1 \text{ nm}$ thick gold (purity 99.9999 %) layer was evaporated at $2 \times 10^{-5} \text{ mbar}$ (BAL-TEC, MED 020) onto the silicon wafers with angstrom roughness. Epoxy resin (Epo-Tek 377) was spread on the corundum cuboids and degassed for 30 min at 10^{-1} mbar . Subsequently, the gold coated silicon wafers were glued on the cuboids and cured for 2 h at 150° . An epoxy mass density of $\rho_m = 1.272 \pm 0.009 \text{ g/cm}^3$ after curing and an epoxy layer thickness of $t_{\text{epoxy}} = 10 \pm 1 \mu\text{m}$ was determined by gas pycnometry (Quantachrome Pentapyc 5200e) and AFM (JPK NanoWizard 3). After immersion in ethanol (97%, Carl Roth) for approx. 1 h, silicon wafers were stripped from the corundum cuboids. To prepare hydrophobic gold surfaces of low roughness 1 mM hexadecane-thiol (97%, Alfa Aesar) can be added to the ethanol solution [72, 92]. After SAM assembly for 8 h the blocks were rinsed with ethanol and dried in a stream of nitrogen.

To produce atomically smooth mica surfaces, mica sheets with a thickness ranging from $t_{\text{mica}} = 4 - 8 \mu\text{m}$ were hand cleaved from Grade V1 mica sheets (refractive index $n = 1.56$). A $40 \pm 1 \text{ nm}$ silver film was evaporated onto the mica sheets. Mica sheets were then glued onto glass cylinders (refractive index $n = 1.46$) silver side down by



- (a) Cylinder-on-flat geometry. Layers are explained in 11.4b. Layer size not to scale.
- (b) X-SFA in plane-cylinder geometry; white light (yellow) and X-ray beam path (red), Al_2O_3 single crystal (a), epoxy resin Epo-Tek 377 (b), gold mirror (c), optional gold surface functionalization (e.g. alkanethiol) (d), confined liquid (e), optional mica surface functionalization (e.g. alkanesilane) (f), mica (g), silver mirror (h), UV hardening epoxy resin NOA-81 (i), supporting glass cylinder (j). For details see text or Tab. 11.1.

Figure 11.4: Detailed view of confining surfaces

using optical index matched glue NOA-81 ($n = 1.56$) which was cured by UV-light for minimum 4 h. The mica covered glass cylinders were mounted onto the sample holder. The mica surface can be functionalized, i.e. hydrophobized by deposition of self assembled monolayers (SAMs) of octadecyl-trichlorosilane (OTS, Aldrich; 90%). For silane based SAMs we use a vapor phase deposition in order to avoid multilayer formation. For this, a vial with pure OTS was placed into a dedicated desiccator together with the samples. The clean mica substrates, that were already glued onto the glass cylinders, were kept in the deposition atmosphere at room temperature for more than 8 hours, and were rinsed twice in fresh n-hexane and ethanol after removal.

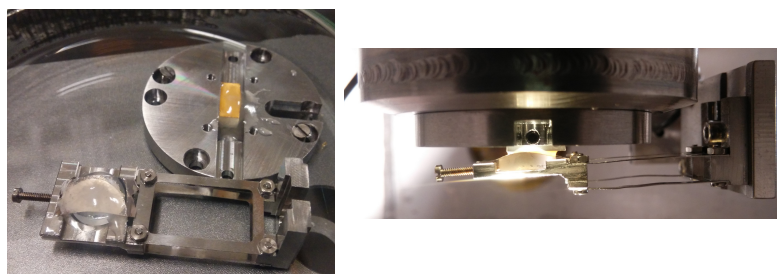


Figure 11.5: XSFA surfaces. (Left) Surfaces in their specific sample holders. Both substrates are transparent to white light. The flat surface already carries 8CB on it. (Right) The two mounted surfaces seen in the direction of the X-ray beam.

Table 11.1: Physical properties of materials: mass density ρ_m , optical refractive index n_{opt} , real part of refractive index δ and imaginary part of refractive index β in the hard X-ray regime at 70 keV. Wave lengths used for optical refractive index: * (632 nm) , ** (589 nm). Material order follows structure in Fig. 11.4.

material		ρ_m [$\frac{\text{g}}{\text{cm}^3}$]	n_{opt}	δ [10^{-7}]	β [10^{-10}]	thickness t [μm]
corundum	Al_2O_3	3.994	1.768	1.53	0.17	3
Epo-tek 377	$\text{C}_{27}\text{H}_{42}\text{N}_4$	1.272	1.5295**	0.554	0.01	10 ± 0.1
gold	Au	19.32	0.23** [115, 238]	6.322	69.05	0.040 ± 0.0005
8CB	$\text{C}_{21}\text{H}_{25}\text{N}$	1.027	1.52*	0.4714	0	—
mica	$\text{KMg}_3(\text{AlSi}_3\text{O}_{10})(\text{F,OH})_2$	2.82	1.6138	1.202	0.16	10
silver	Ag	10.49	0.060** [115, 238]	—	—	0.040
NOA-81	$\text{C}_{15}\text{H}_{21}\text{N}_3\text{O}_5\text{S}$	1.347	1.56	—	—	10000
glass	SiO_2	2.203	1.4585**	—	—	—

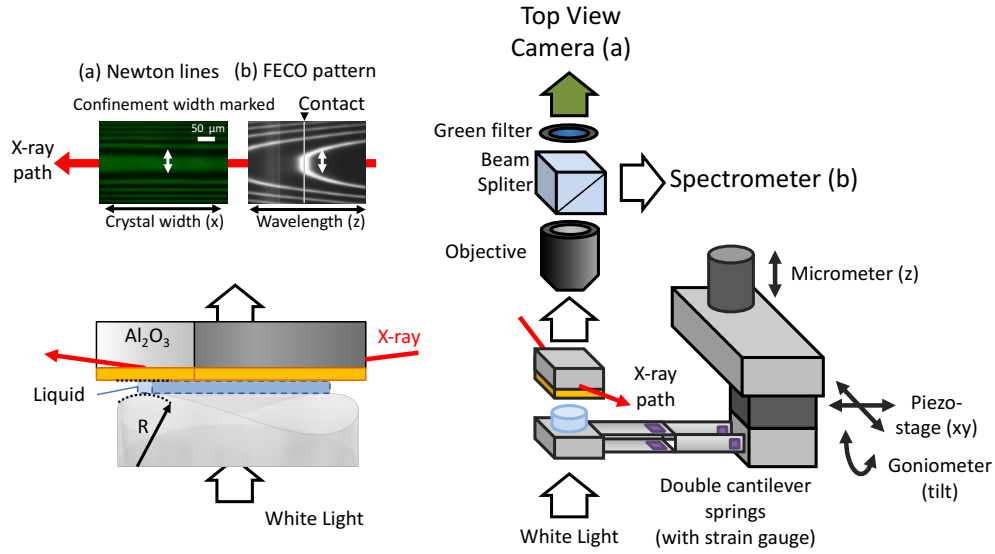


Figure 11.6: (right) Schematic of the SFA controls, strain gauge springs and optical setup for recording Newton's interference and fringes of equal chromatic order (FECO). (a) Top-view of the confined 8CB by video microscopy indicating perfect parallel alignment of the apposing surfaces. (b) FECOs are used to determine the gap width. Figure reproduced from [290].

11.4 Surface Positioning and Force Measurements

Chapters 11.4 and 11.5 were not written by the author and are citations from ref. [290]. They are contributions by the group of M. Valtiner, designing the SFA part of the XSFA device.

The X-SFA setup displayed in Fig. 11.6 includes two linear piezo-stages (Physical Instruments, Karlsruhe, Germany) with $100\ \mu\text{m}$ travel range that are mounted perpendicular to each other for simultaneously applying both, shear stress and compressive stress by lateral and vertical motion of the lower surface (mica), respectively. In a shear experiment, the mica cylinder is aligned in such a way, that the surface slides along the apex direction. This ensures that the confined region remains at the same location of the single crystal mounted on the upper surface, exactly where the X-ray probe is aligned during experiment.

The deflection of two perpendicular mounted double cantilever springs on the lower sample mount can be recorded with strain gauges (ME-Messsysteme, Henningsdorf, Germany) with an experimentally verified detection limit of $F/R > 0.1\text{mN/m}$ for a contact of two crossed cylinders. Hence, for the flat-on-cylinder geometry, which features generally larger and longer ranged forces, the sensitivity is sufficient for characterizing and controlling both lateral and vertical forces with an absolute accuracy of $1\ \mu\text{N}$.

Oscillatory stress in vertical or lateral directions can be applied to the sample by a home-build piezo controller that is based on OEM parts from Physical Instruments.

A home build LabView software controls the piezo and reads out the amplified strain gauge voltages.

In this setup, the hydrophobized corundum block (Al_2O_3) and the cylindrical hydrophobized mica sheet can be aligned perfectly parallel to each other using a manual 1D goniometer stage (Thorlabs, Newton, NJ, USA) to rotate the cylinder with respect to the corundum block. In a future version, the manual goniometer will be exchanged for a piezo-driven rotation, in order to make this critical alignment computer controlled and more efficient.

Fringes of Equal Chromatic Order (FECO) as well as Newton lines recorded with the top view camera are used to guide the alignment procedure. After successful alignment of the apposing surfaces the Newton lines are perfectly parallel over the entire contact area as shown in Fig. 11.6. The parallel Newton lines indicate a perfect alignment, while the FECO of the contact indicate a flat contact region at the apex (cf. figure caption for details). FECO are recorded with the spectrometer slit aligned perpendicular to the long-axis of the confinement, allowing the measurement of the radius of curvature. This 2D contact profile can be scanned along the entire apex by moving the entire setup with a lateral x/y translation stage.

11.5 Light Microscopy and FECO

The XSFA uses white light interference between two semipermeable mirrors to measure the distance between two atomically flat surfaces. For optical interference measurements, the lower and upper surfaces were coated with semi-transparent mirrors as described above. Collimated white light from a tungsten filament is guided through the contact of the apposing surfaces. Constructive and destructive interference leads to standing waves at distances, that are roughly even and odd multiples of the standing waves wavelengths. Shifts of these wavelengths indicate an absolute shift of the distance across the two mirrors.

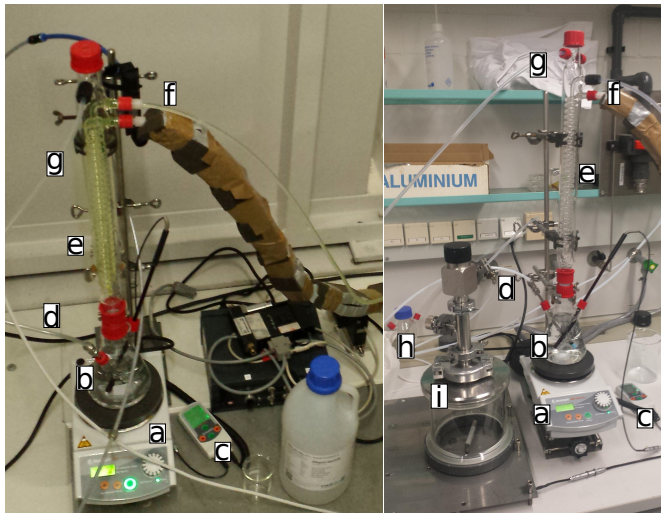
First, as shown in Fig. 11.6a, the interference pattern can be visualized using a video camera after passing through a band-pass filter (here green, from Thorlabs). This results in so-called Newton's interference pattern. In a crossed cylinder geometry, this results in well known Newton rings that also occur at the contact of two glass plates. Here, the geometry results in the appearance of Newton lines if the cylinder is aligned perfectly parallel to the flat gold surface. In particular, a bright line as shown in the figure, corresponds to one standing green wave, and the parallel alignment of the lines indicates that the surfaces have a uniform surface separation along this line. The Newton lines are used to align the surfaces parallel to each other before an X-ray experiment is started. The most critical alignment step is the rotation of the cylinder. Only if the cylinder is rotated into parallel alignment, Newton lines do appear, serving as an alignment feedback control and indicator. Using a 20/80 beam splitter (Fig. 11.6 right), 80% of the interfering white light can be simultaneously guided into an imaging spectrometer, to split it up into the individual standing wavelengths. This results in the detection of so

called Fringes of Equal Chromatic order (FECO) shown in Fig. 11.6b. Using an analysis of the interference pattern based on the multiple matrix methods (using our software code SFA-Explorer [118]) allows determination of the mica thickness in dry contact. This reference measurement defines the "zero" distance, where the surfaces are in close so-called "hard" contact. The reflecting metal surfaces cannot approach to any closer distance, defined by the mica thickness t_{mica} . After wetting the contact with a fluid the thickness of the fluid, that ingresses into the contact area, can hence be directly calculated based on the resulting wavelength shifts. For details of FECO analysis in an SFA experiment the reader is referred to previous work [37, 109, 111, 275]. As such, using both Newton lines and FECO pattern, the surfaces can be aligned with respect to each other and the confined area and the fluid gap height can be monitored and controlled with respect to the X-ray beam.

11.6 Sample Atmosphere Control

During measurements the sample was kept under a controlled atmosphere. The XSFA sample cell is designed to withstand vacuum and can be sealed air tight. Under standard operation the cell is flushed by a slow but steady stream of Helium (technical grade Helium (N4.6), purity = 99.996 %). The inert helium atmosphere reduces scattering and avoids side reactions of the sample during longer measurement runs, hence also reducing beam induced damage. A diffusor on the gas inlet finely dispenses the inserted gas flow, avoiding liquid sample perturbation by the gas stream. On the outlet a gas washing bottle was used to supervise the gas stream as well as avoiding inward diffusion into the sample cell. A humidity sensor HTM2500LF by the company *Measurement Specialty* is accommodated inside the cell. Sensor signal was incorporated into the online control software, enabling simultaneous recording of humidity signal. Sensor sensitivity ranges from 10 to 95 % relative humidity (r.h.), featuring an error of 5 % from 10 to 35 % r.h., an error of 3 % between 35 and 78 % r.h. and again 5 % beyond 78 % r.h. A self constructed humidity set-up enables humidity adjustment of the inflowing helium gas stream (see Fig. 11.6). Helium gas seeps through a bath of deionized water. Water bath temperature and a downstream Liebig cooler can be used to adjust Helium flow humidity. The downstream arrangement of the Liebig cooler, set to a temperature colder than sample cell temperature, avoids condensation of water anywhere past this cold sink. This guaranteed that no water condensated anywhere in the tubing or sample cell. Measured humidity inside the sample cell is hence accurate and reliable. Gas flow was high compared to sample volume inside the cell. A local fluctuation due to water uptake by the very little amount of sample can be neglected. The sample is always surrounded by a sufficient amount of fresh atmosphere.

Figure 11.7: Humidity set-up used to adjust the humidity of the sample environment. Left: Set-up as used during the second experiments performed at ID-31, ESRF-The European Synchrotron. Right: Set-up as used for bulk liquid measurements in-house. a: Heating plate and magnetic stirrer for water bath; b: water bath; c: Temperature control of water bath; d: Helium supply pipe; e: Liebig cooler; f: Cooling water supply; g: moist Helium to sample cell; h: back-pressure reservoir, condensation check; i: sample cell, inside visible: humidity sensor



11.7 In-Situ X-Ray Scattering and Reflectivity

X-ray scattering experiments have been performed at the high energy beamline ID31 at ESRF-The European Synchrotron, Grenoble, France. Figure 11.9 shows a sketch of the beamline layout and X-ray optics. The X-ray beam from a cpmU22 undulator is parallelized by the first CRL transfocator (TF1) [252, 253] and monochromized by a multilayer mirror (MLM, energy 70.0 keV). A second CRL transfocator (TF2) focus the beam onto the sample position with a $5 \times 20 \mu\text{m}^2$ spot size normal and parallel to the slit pore, respectively. To minimize the radiation dose on the sample, a 7 stage absorber (PA) and fast shutter (FS) are used. For sample positioning and orientation, the XSFA was mounted onto the High Energy Micro Diffractometer (HEMD) setup for surface and interface studies [97, 213]. Scattered intensities are alternatively detected by two 2D hybride pixel detectors. High resolution and low background signal is achieved by the CdTe MAXIPIX system (1478×1679 pixels, $55 \mu\text{m}$ pixel size) mounted behind a collimation system (CS, DS). The Dectris PILATUS3 X CdTe 2M detector (1478×1679 pixels, $172 \mu\text{m}$ pixel size), behind a beam stop (not shown) to absorb the primary and specular reflected beam, is mounted on a dolmen like granite construction [100].

To probe buried interfaces the high energy X-ray beam impinges the slit pore through the side of the corundum (Al_2O_3) single crystal (Fig. 11.4, length 4.8 mm, X-ray transmission 67.5%). Background scattering from the single crystalline substrates is primarily caused by Compton and thermal diffuse scattering and significantly reduced compared to amorphous materials. At the critical angle $q_c = 0.768 \text{ nm}^{-1}$ of gold the footprint on the substrate is 0.477 mm.

Density profiles perpendicular to the confining interfaces were investigated by X-ray

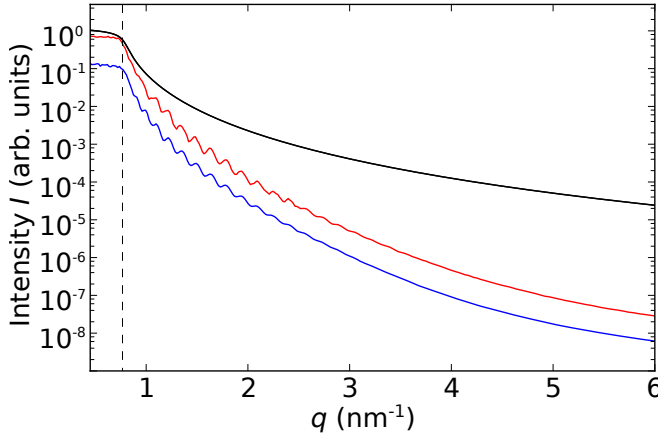


Figure 11.8: XRR curve of the upper template stripped gold substrate recorded at 70 keV. Specular signals were recorded in conventional XRR geometry (blue) and the incident and reflected beam penetrating through the bulk Al_2O_3 single crystal (red, Fig. 11.4). Black curve is the calculated Fresnel reflectivity of gold. Vertical lines indicate the critical angles of total reflection α_c . Curves are vertically shifted by one order of magnitude.

reflectivity (XRR) (Fig. 11.1c). Scattering experiments with the momentum transfer q parallel to the slit pore probe the in-plane structure of the confined liquid (Fig. 11.1b). Scattering angles were converted to momentum transfer using $q = 4\pi/\lambda \sin(\theta)$.

11.8 Instrument Characterization

To characterize the instruments performance, prior to sample measurements, the free gold surface was measured in XRR geometry. Figure 11.8 shows two curves recorded during XRR runs at a free gold surface and the corresponding calculated Fresnel-decay of intensity in this angular regime. Both measured graphs show the expected plateau for total reflection before the drop at the critical angle. A sharp drop at the calculated critical angle of $q_c = 0.768 \text{ nm}^{-1}$ (dashed vertical line) corresponding to an interface between Al_2O_3 and gold is observed. The electron density of Al_2O_3 ($\rho_e = 3.94 \times 10^{29} \text{ 1/m}^3$) and the epoxy-glue layer $\rho_e = 4.36 \times 10^{29} \text{ 1/m}^3$ are similar, but small in comparison to gold ($\rho_e = 4.58 \times 10^{30} \text{ 1/m}^3$). The electron density contrast of the interface Al_2O_3 -glue has only a weak influence on the beam and is negligible. This supports the idea that reflectivity is measured at the gold-sample interface, not at the Al_2O_3 -glue or glue-gold interface. For small angles the measured intensity behavior follows a Fresnel-decay for an ideally flat gold surface (black curve), for higher angles the reflectivity decays faster for the blue and red curve. Kiessig-Fringes of the gold layer can be recognized for both curves. Calculation of the gold-layer thickness from the experimentally observed Kiessig-Fringes gives $40 \pm 1 \text{ nm}$, which corresponds well with the targeted $t_{\text{Au}} = 40 \text{ nm}$. The intensity behavior over the whole angular regime is sufficient for XRR measurements. This shows that reflectivity measurements probing the structure perpendicular to the reflecting surface are possible in the XSFA.

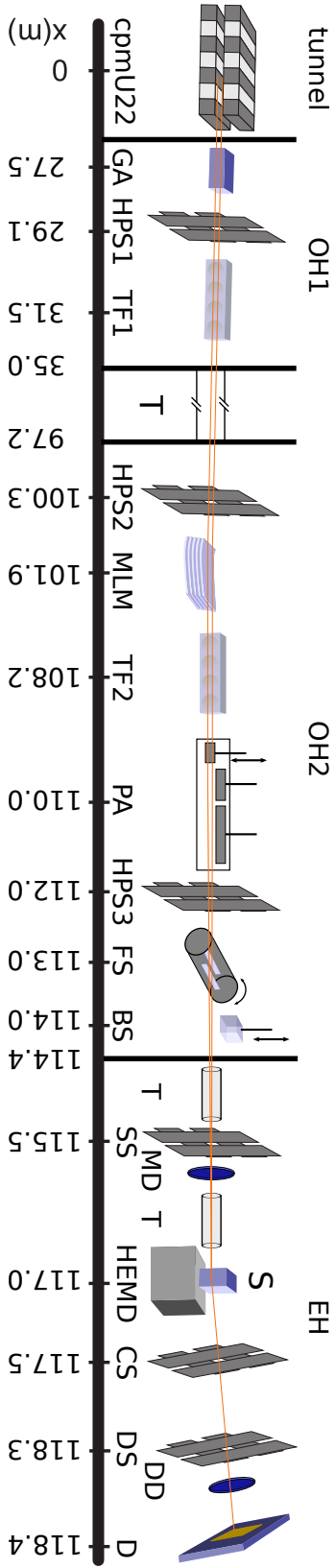


Figure 11.9: Beamline setup for high energy scattering experiments at ID31, ESRF (Feb. 2016): (OH1/2) optics hutches; (EH) experimental hutche; (cpmU22) 22 mm periode permanent magnet cryo-cooled in-vacuum undulator; (GA) gas absorber (1 m Ar-gon 300 mbar); (HPS1/2/3) high power slits; (TF1/2) compound refractive lens (CRL) transfocators; (MLM) multilayer mirror monochromator; (PA) PEEK (polyether ether ketone) absorber set; (FS) rotary fast shutter; (BS) beam safety shutter; (T) flight tube; (SS) secondary slits; (MD) silicon PIN monitor diode; (HEMD) high-energy microdiffraction setup; (S) sample position; (CS) collimator slits; (DS) detector slits; (DD) silicon PIN detector diode; (D) 2D detector (CdTe MAXIPIX); Distances are not to scale.

Chapter 12

Analysis

Analysis of XSFA data takes place in a combined approach. Data recorded by both methods involved, the Surfaces Force Apparatus and the X-ray methods, are analyzed complementary to each other. X-ray techniques and surface distance measurements supply supplemental information.

12.1 Mechanical Analysis

The SFA supplies three types of experimental data (see Chap. 11.4 and Fig. 11.6): The whole length of the confinement apex is observed by video microscopy. The acting relative forces onto the movable cylinder surface are recorded by strain gauges. The confinement gap distance is tracked by FECO.

Macroscopic observation by video microscopy supplies information about sample behavior under confinement. The focus visualizes large parts of the confinement apex and adjacent sample. Crystallization processes, beam damage or contaminations are traceable by this tool.

Tracked by strain gauges the forces exerted onto the sample can be interpreted against the sample structure probed by X-ray. Changes in sample structure can be related to changes in force measurements and vice versa. Temporal resolution of the signal evolution of both signals, deflection/force and X-rays signal, can be used to gain insight into the rheological behavior of the sample. Sample structure evolution can be compared to onset of perturbation by force application.

Ångström resolution of the gap distance is achieved by FECO recording. A static confinement situation can be created. Measurement of normal forces during confinement gives insight into mechanical properties of the sample. Evolution of sample structure, traced by X-ray methods, can be interpreted against the background of normal force evolution. This enables research on structures in a static pore geometry.

Dynamic measurements of the confined sample are possible by deflection of the cylinder surface. Shear and normal forces can be applied by Piezo stages, stressing sample structure while tracking structure evolution by X-ray methods. During compression/decompression cycles of normal force oscillation, the actual gap distance is

resolved by the FECO measurements, providing the gap distance is small enough for the gap to be transparent. Recording deflection while applying stress gives insight into mechanical properties of the sample structure. Linking information about the chemical sample structure and sample rheology is possible this way. For viscous samples deflection of the compressing surface is often observed to require a larger force, diminishing the resulting deflection. Shear force is applied by deflecting the cylinder surface horizontally, along the confinement apex. Two different mode of operation are possible: A step-wise application of shear stress consecutively deflects the cylinder surface in discrete steps. No shear rate results as the cylinder surface remains static after the deflection step. Viscoelastic sample properties can be probe by this mode, detecting if structural sample effects occur by recording X-ray and strain gauge signal during the static application of shear strain σ . Dynamic shear oscillations can be applied using different oscillation profiles via a wave generator. Shapes like sine-wave or triangular wave profiles for shear force oscillation is possible. In this mode, a discrete shear rate $\dot{\gamma}$ and viscosity of the material is yielded.

12.2 Analysis by X-ray Methods

Sample structure is elucidated by two different X-ray techniques: X-ray Reflectivity (XRR) and X-ray Diffraction (XRD). Complementary to that, two different detectors are available. A high spatial resolution detector for reflectivity experiments (CdTe MAXIPIX system) and a large area detector for scattering experiments (PILATUS3 X CdTe 2M system) (see Chap. 11.7). Using the MAXIPIX system specular intensities were extracted from the 2D patterns by integration over an designated region of interest (ROI). The ROI was of a line shape having 8×1 detector pixels to achieve good angular resolution. The MPX detector is especially suited for visualization of the specular signal during XRR, but less suitable for XRD, as the detector area is small and usually can not record the whole scattering pattern. The large area detector PILATUS P3 can be used for both, extraction of specular intensities (XRR) as well as recording the whole 2D scattering patterns (XRD). Specular ROI was set to 40×20 pixel. In-plane intensities were integrated over 10×30 pixel. An example of ROI to signal size ratio and ROI positioning is shown in Fig.12.1.

As introduced in Chap. 3, XRR especially probes the structure perpendicular to an interface (see Fig. 11.4). By pointing the wave vector transfer q into a discrete solid angle, structure information can be gathered in this specific direction. Momentum transfer q_z is perpendicular to the sample surface. During XRR measurements only the specular beam is recorded. The primary beam is masked by appropriate slit settings. Resolution across molecular length scales is reached by scanning up to sufficiently high angles. The specular reflected X-ray beam was recorded up to incident angles $\alpha_{max} \leq 0.75^\circ$. This converts to a maximum momentum transfer of $q_z = 4\pi/\lambda \sin(\alpha_{max}) \leq 9.3 \text{ nm}^{-1}$. Intensity adjustment to detector sensitivity is achieved by measuring at different absorber settings. Up to six different absorbers were used during one scan. Absorber intervals

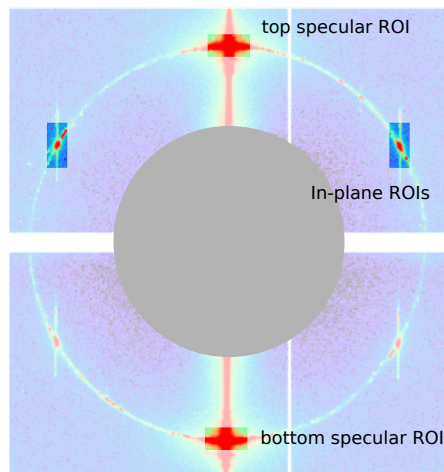


Figure 12.1: Example of ROI positioning and size on the P3 detector area. Figure does not show full detector area. Positioning of ROIs was adjusted to measurement. Highlighted areas are used to yield integrated intensity values shown in this work. Depending on geometry, only selected ROIs are plotted.

were merged and interpolated to an equidistant q_z -grid. Background signal is low due to the single crystalline substrate used. The background signal mainly originates from the diffuse scattering contributions of the Kapton windows and the amorphous glue layer. At higher angles, strong reflexes, generated by the mica sheets on the lower confining surface, have to be masked by appropriate absorber settings.

Gathered signal can be analyzed according to confinement situation. During static confinement, real space sample structure d is accessible by reciprocal signal position $d = 2\pi/q$. Reasonable assumptions on molecular orientation in the confinement gap can be achieved from comparing molecular dimensions to measured signal position. Sample amount and sample orientation contribute to signal intensity. Under static confinement sample structure is unperturbed and signal intensity remains static as well. A highly orientated sample leads to a strong signal intensity scattered into a narrow solid angle. During dynamic confinement signal intensity changes according to sample structure. To extract information about sample structure, XRR intensity signal evolution under dynamic stress is related with gap width measurements. Gathering intensity at an angular position corresponding to sample signal position accesses sample structure evolution. Following the perturbation, signal intensity changes when molecular structure is driven out of equilibrium. A less orientated structure exhibits less focused scattering, resulting in a diminished intensity scattered into the solid angle probed. Recording the signal intensity during dynamic measurements gives insight into sample structure. Only qualitative analysis of the XRR signal was possible due to the intricate stratified inter-facial structure. Fitting a model interface structure to the XRR signal obtained was unsuccessful. Multiple interfaces and interfacial roughness contribute to the signal decay. Kiessig fringes, originating from the gold layer, overlap the sample signal.

In Small-Angle X-ray Scattering geometry, the material along the whole confinement apex is probed. The whole angular range is recorded in the 2D pattern acquired. Measurements at different angular positions (different ROIs on detector) of the scattering pattern resolves sample structure orientation. Confinement dynamics will change orientation and by this scattering angle.

Chapter 13

Results and Discussion

13.1 Benchmark System 4'-octyl-4-cyano-biphenyl

In this chapter, first proof of principle experiments on the smectic liquid crystalline benchmark system 4'-octyl-4-cyano-biphenyl (8CB) in confinement demonstrate the capability of the newly constructed device. Previously, this system was extensively studied using crossed cylinder XSFA's in transmission geometry [104, 105, 106, 184, 231], making it an ideal benchmark system. Time resolved experiments on confined 8CB were carried out during active compression and decompression cycles. The recorded X-ray scattering and reflectivity data was complemented by simultaneous interferometry based thickness measurements. The results demonstrate the feasibility of the cylinder-on-flat geometry and the increased sensitivity and capability of the new instrument.

13.1.1 Static Structure of 8CB in Confinement

During the XRR and in-plane scattering experiments, the liquid crystal was confined to two gap widths of 120 nm as well as 1700 nm, in order to study the dynamic response during increasing confinement over one order of magnitude. The in-plane scattering geometry probes the structure in the x-y-plane, parallel to the solid/liquid interface (Fig. 11.1b). This yields $I(q_{||})$ with $q_{||} = \sqrt{q_x^2 + q_y^2}$. In-plane scattering experimental data of 8CB confined to $D = 1700$ nm are summarized in Figure 13.1. The associated scattering pattern in Fig. 13.1a exhibits a sharp peak (I) at $q_I = 2.0 \text{ nm}^{-1}$ corresponding to $2\pi/q_I = 3.14 \text{ nm}$ real space distance. This value is in good agreement with the dimensions of the long axis of 8CB dimers (Fig. 10.1) and also compares well to the periodicity of 3.2 nm for the smectic mesophase of 8CB confined in between two hydrophobized surfaces as observed in SFA experiments [230]. The observed peak shape is consistent with quasi long range liquid crystalline smectic order. A second, broad peak (II) appears around $q_{II} = 14 \text{ nm}^{-1}$. This 0.45 nm periodicity corresponds to the short distance between the rod-like 8CB molecules within the smectic layers. The large FWHM of 4 nm^{-1} originates from the short range order perpendicular to the long axis of the molecules. This signal structure is typical for liquid crystals in the smectic A phase

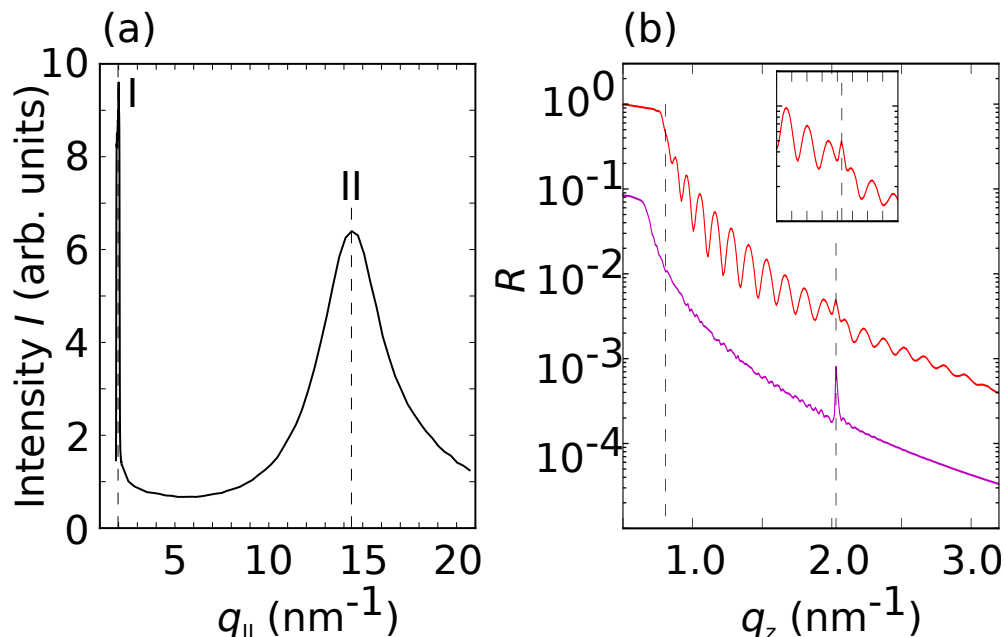


Figure 13.1: Scattering signal from confined 8CB. (a) In-plane pattern recorded in the scattering geometry depicted in Fig. 11.1 b. (b) Measured (red) specular X-ray reflectivity R . Model calculated reflectivity curve (purple) from a periodic arrangement of 560 smectic 8CB layers arranged with their long axis perpendicular to the solid/liquid interface. For clarity, curves are shifted vertically by one order of magnitude.

[41]. In the smectic A phase the molecules are arranged in layers with the molecule director all pointing in one direction (Fig. 10.1), displaying high order in the long-axis orientation, however low order perpendicular to this direction.

Specular reflectivity $I(q_z)$ probes the density profile perpendicular to the solid/liquid interface (Fig. 11.1c, red curve in Fig. 13.1b). The critical angle of total reflection at 0.768 nm^{-1} is given by the large scattering contrast between the gold mirror and the Al_2O_3 block. At higher q_z , the X-ray beam is transmitted into the gold layer and the slit-pore filled with 8CB. Kiessig fringes of periodicity $\Delta q = 0.15 \text{ nm}^{-1}$ originate from interference at the 40 nm thick gold layer. At approximately 2 nm^{-1} a sharp Bragg-like peak is observed. Like peak I observed in the in-plane scattering geometry (Fig. 13.1a), this reflection is attributed to the smectic order, i.e. the long-axis, of 8CB.

The purple curve in Fig. 13.1b shows a calculated XRR curve based on a simplified model consisting of 560 smectic 8CB layers with 3.2 nm periodicity on top of a semi infinite gold substrate.

The scattered intensity found in specular condition, i.e. with the momentum transfer perpendicular to the solid/liquid interface (z -direction), is orders of magnitudes stronger than the intensities found for other directions (Fig. 13.2a). The angular intensity distribution over the scattering rings of constant total momentum transfer originates from the anisotropic structure caused by the confinement. The observed scattering patterns

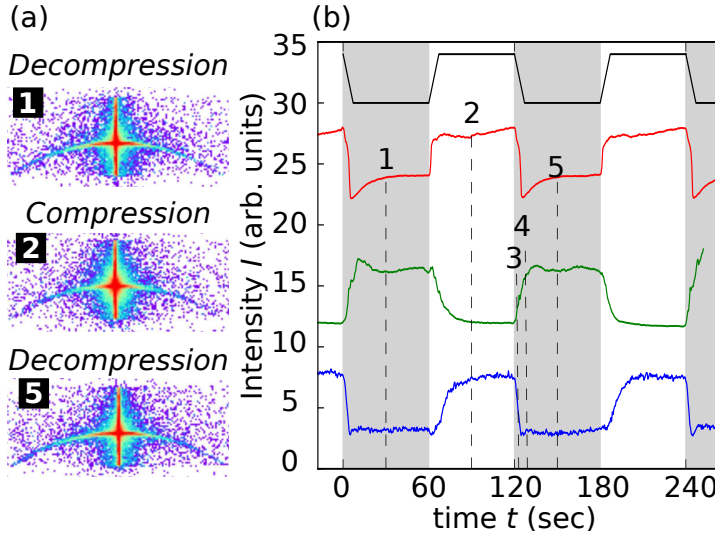


Figure 13.2: Time resolved X-ray scattering experiments. Numbers compare to point of measurements depicted in (b);

(a) Specular signal evolution under stress;

(b) Signal evolution under stress for different signals; Black: Oscillatory stress signal (60 s holding time; 8 s ramp); Red: Specular first order signal; Green: In-plane first order signal (90° tilted towards Red); Blue: Specular second order signal;

indicate that the smectic layers of the confined 8CB are preferably arranged with their long axis perpendicular to the solid/liquid interfaces. This layered structure can now be stressed by the compression oscillation exerted on the liquid structure in the confinement gap, by applying vertical motion of the lower mica cylinder (Fig. 11.6).

13.1.2 Relaxation Dynamics

After having elucidated the 8CB structure in confinement, it is demonstrated how the liquid crystalline structure in the slit-pore confinement is brought out of equilibrium by periodic compression and decompression cycles. Changes in the gap width $D(t)$ are continuously monitored by the FECO interference pattern. Simultaneously, the structured arrangement of the 8CB molecules is probed in real-time using specular XRR and X-ray scattering. The confining surface distance is still $D = 1700$ nm, corresponding to about 560 layers of 8CB molecules (Fig. 10.1).

Figure 13.2b shows the time evolution over two compression/decompression cycles. Grey shaded areas indicate decompression, white areas compression force application. The top most black curve depicts the compression/decompression voltage signal. A step signal was applied featuring 8 sec ramp and 60 sec holding time. Recorded X-ray signals are shown in red, green and blue. The red curve shows the first order signal evolution (see Fig. 13.1, peak I) for momentum transfer pointing in z at $q_I = 2.0 \text{ nm}^{-1}$ (specular XRR). The green curve describes signal behavior in x - y direction (in-plane XRD) at $q_I = 2.0 \text{ nm}^{-1}$, respectively. The blue curve describes intensity scattered into in-plane direction at a wavevector transfer of $q_{II} = 14 \text{ nm}^{-1}$ (peak II).

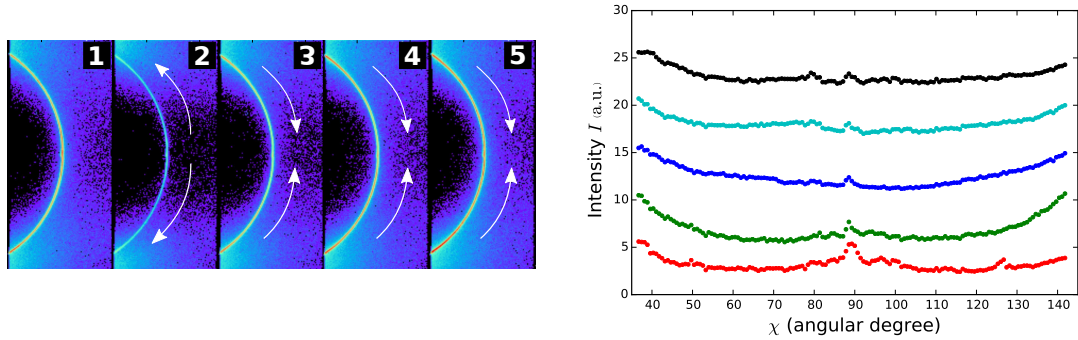
At $t = 0$ the confinement gap is decompressed. The intensity scattered into specular direction (red) drops rapidly. Order within the liquid crystal has decreased. The less

ordered molecular structure now does not scatter intensely in specular direction anymore. Redistribution of scattered intensity from the specular direction to a ring of equal wave vector transfer in reciprocal space occurs. This leads to an increase of in-plane scattering, marked by a rise in intensity observed in the green curve. The increase is prompt after decompression at $t = 0$. Also molecular order within the smectic layers seems to decrease with less compressive stress. The blue curve drops as well at $t = 0$. Less intensity is scattered into in-plane direction at a wavevector transfer of peak II.

Viscoelastic behavior of the LC structure is indicated by the signal evolution after decompression. While intensity scattered in specular direction dropped at first, it recovers during the subsequent 60 sec holding time. The red curve converges towards a plateau. An increase of molecular order within the gap would justify such a behavior. The 8CB molecules reorientated their long axis perpendicular to the confining surfaces. Orientational order to a degree comparable to the state observed under compression stress is not regained, though. Signal intensity does not reach prior values. The reorientational process occurs on a time scale of around 20 seconds. Viscous behavior of the 8CB molecules within their smectic layers can explain such signal behavior. Deflected from an orientation parallel to the surface normal due to the decompression, the molecules tilt back to this parallel position.

Upon compression ($t = 60$ s), intensity is not preferably scattered along the ring of equal wavevector transfer anymore, but more into specular direction again. The red curve rises instantaneously. This indicates that compressive stress is increasing the alignment of the liquid crystalline smectic layers relative to the confining surfaces. Anisotropy in the angular intensity distribution, that means, the order within the liquid, increased. Backing up this idea, the intensity of the second broad scattering peak at $q_{xy} = 14 \text{ nm}^{-1}$ (in-plane, blue curve), shows complementary signal modulation. The blue curve rises upon application of compressive stress. Also the distance distribution within the smectic layers became more uniformly. In contrast to that, intensity in the green curve drops upon compression application. Scattering in the in-plane direction has decreased because the source of scattering, the molecules, are well ordered now and scatter more uniformly into a discrete solid angle. Adoption of well ordered orientation takes place viscoelastically again. In the same manner as observed after structural perturbation due to decompression, also the adoption of the equilibrium position under compression takes around 20 seconds. This is indicated by the relaxation of signal in the green curve. Intensity scattered into in-plane direction decreases after compression stress application and converges towards a plateau after around 30 seconds.

The structural relaxation upon compression and decompression is visible in the according 2D scattering patterns. Figure 13.2a shows a selection of 2D data recorded at specular condition. Numbers compare to point of measurement in Fig. 13.2b. As can be seen, upon decompression (1 and 5), scattering stretches out over the diffraction ring. Intensity is not focused into specular direction anymore, but is tilted slightly away from it. Accordingly, we observe an increase in the in-plane direction. Upon compression (time point 2), the molecular structure scatters more uniformly into specular direction again. Intensity on the ring decreases.



(a) XRD signal evolution of confined 8CB under stress. Numbers compare to time of measurement, see Fig. 13.2 b. 2D-images in in-plane direction depicting signal intensity evolution under stress. Black: low intensity, Red: high intensity. Arrows should guide the eye.

(b) Angular intensity distribution of 1 (red) to 5 (black). Curves are vertically shifted by 5 for clarity.

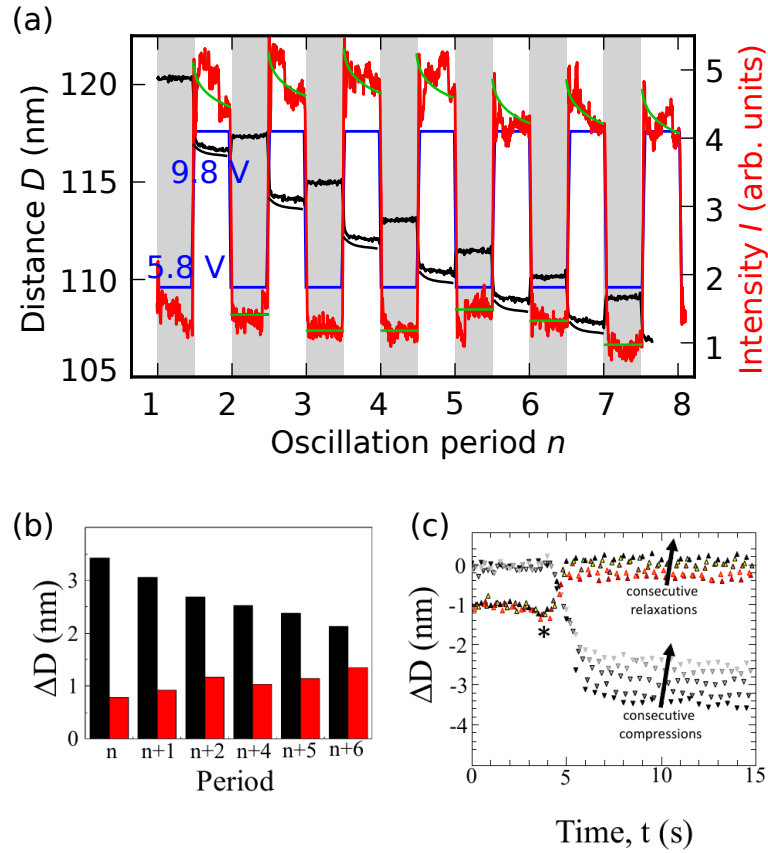
Figure 13.3: Decompression (1): Intensity across the ring is high; Compression (2): specular intensity increases, low intensity in in-plane direction; Decompression (3-5): in-plane intensity increases.

Complementary behavior is observed in the 2D-images showing in-plane direction intensity in Fig. 13.3a. Again, numbers compare to time of measurement in Fig. 13.2b. The angular distribution of intensity is shown in Fig. 13.3b. Angular range is 0° (bottom) to 180° (top). Areas of high intensity at 180° and 0° are masked to protect the detector. Thus, intensity data ranges from 18° to 162° in Fig. 13.3b.

Upon decompression (point 1, red data points), overall intensity across the ring is high. Maxima are observed at 0° , 90° and 180° direction. Compared to the intensity scattered into 45° or 135° , intensity at in-plane condition (90°) is high. This indicates structural orientation in in-plane direction. The ratio in-plane/off-plane does not reach such a high value again for consecutive decompression cycles. Compressing the LC structure leads to orientation of the structure, indicated by focused scattering into discrete solid angles. Intensity vanishes from the recorded in-plane detector area and is focused to 0° and 180° . As can be seen in point 2, a ring is still visible, however intensity is low. The green curve shows that overall intensity in in-plane direction under compression stress is low and intensity is evenly distributed. Tracking the decompression in point 3 to 5 shows how the liquid crystal orientation decreases. Intensity is scattered across the ring again, being deflected from top and bottom orientation. Intensity over the ring is as high again as during the first compression cycle as can be seen in Fig. 13.3b when looking at curves 3 to 5. Also, signal orientation into 90° degree direction increases over the course of curve 3 to 5.

The data for dynamic decompression/compression cycles on the liquid crystal 8CB in smectic orientation, confined to a slit-pore of 1700 nm, demonstrate the viscoelastic

Figure 13.4: Time resolved X-ray scattering experiments. (a) Evolution of surface distance and specular signal during compression cycles; Blue: Oscillatory stress (30 s holding time, 2 s ramp); Black: Distance of confining surfaces. Start: 120.3 nm, End: 107.0 nm, see text for details; Red: Specular first order signal evolution; Green lines should guide the eye.



behavior of the LC structure. Compression stress enhances orientation within the smectic layers. Reorientation after structural perturbation, might it origin in application of compression or decompression stress, occurs viscoelastic on a timescale of around 20 seconds.

After presenting a bulk like confinement gap of 1700 nm, results obtained using a smaller confinement of 120 nm are presented subsequently. A confinement of 120 nm compares to 38 layers of 8CB dimers. The confining surface distance can be precisely measured by FECO, as the material in the gap is not absorbing the white light anymore.

Fig. 13.4a combines gap distance and XRR signal intensity evolution. The applied voltage signal profile is shown in blue, ranging from 5.8 to 9.8 V. Gap distance is shown in black, decreasing from 120 nm to 107 nm over the course of 7 compression oscillations. The corresponding XRR signal is plotted in red.

Without sample contact, this voltage range of 4 V would correspond to a cylinder surface deflection of $40 \mu\text{m}$. However, due to the discrete measurement of surface distance, it is visible that the surfaces do not move by more than a few nanometers, indicating that we are only modulating the applied pressure. With a displacement of 3.4 nm and a spring constant of 54 N m^{-1} a force oscillation of $0.1836 \mu\text{N}$ results. In a confinement apex of area $A = 5 \text{ mm} \times 100 \mu\text{m} = 0.5 \text{ mm}^2$, this converts to a pressure of $p = 0.1836 \mu\text{N} / 0.5 \text{ mm}^2 = 0.3672 \cdot 10^{-6} \text{ N/mm}^2$.

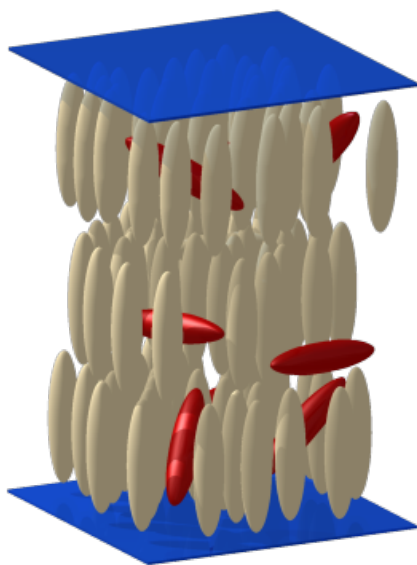


Figure 13.5: Possible molecular structure in 8CB after compression cycles. The smectic A structure is broken up by molecules laying flat between smectic layers due to mechanic stress during compression.

The periodic application of pressure influences the sample structure. Indicated by the red curve, gap width D drops upon compression from 120.4 nm to 117.0 nm. A decrease by 3.4 nm, a length scale comparable to the molecular long axis dimension. Consecutive decompression however does not induce a strong rise in gap width. Merely a gap width recovery of 0.8 nm is observed. Hence, a continuous overall decrease of gap width from 120 nm to 107 nm is detected. Fig. 13.4b summarizes gap width change upon compression (black) and decompression (red). It can be observed that gap distance change during compression continuously decreases from 3.4 nm to 2 nm, while the distance change during decompression remains rather constant around 1 nm. Fig. 13.4c depicts gap distance evolution during holding times.

The specular signal shown in Fig. 13.4a (red) indicates a signal increase upon compression, and hence a more ordered structure of the liquid molecules. Decompression leads to an instantaneous drop. Modulation of intensity does not change significantly overall, although a smaller increase for the last three oscillation periods is observed. Whereas on compression a signal relaxation is observed during the 30 sec holding time (curved green lines), no such effect is observed upon decompression in the XRR signal (flat green lines). XRR signal intensity also returns to a nearly constant value during consecutive decompression. Significant material loss due to push out of larger amounts of material would lead to an overall intensity decrease.

The decrease in gap width, compared to the rather constant XRR intensity points to an ordering effect instead of a push-out effect. No significant amount of material is squeezed out of the gap. Only during the first compression the decrease of gap distance corresponds exactly to the molecular layer dimension. Consecutive cycles do not show this constant value of 3.4 nm again, gap distance change ΔD decreases. It seems that no material is lost, but that gap distance decrease is achieved by compacting and pertur-

bating the LC structure. This points towards an effect depicted in Fig. 13.5. So called parking-lot-states are induced by the compression stress cycles. LC molecules are lying in their smectic layers in a disordered way. This reorientation is already postulated during normal diffusion behavior of rod-like LC molecules from simulation experiments [183]. Time scales are much faster there, but this shows that smectic LC molecules can display this structural behavior. Mesogenes are not lying in between layers as this would increase repetition unit distance, which was not observed in XRR measurements. This disordered structure does not scatter uniformly into specular condition anymore and XRR intensity decreases. Compression leads to ordering of the structure. After compression, molecular orientation relaxes and loses alignment during the holding time. An effect not observed under decompression.

13.2 Ionic Liquid Crystal System 1-decyl-3-methyl-imidazolium chloride

During the second beamtime performed using the XSFA in February 2017, focus was laid on the ionic liquid crystal system 1-decyl-3-methyl-imidazolium chloride $[\text{C}_{10}\text{mim}]^+\text{Cl}^-$.

Measurement of structures formed in ionic liquids by combined force measurements and X-ray techniques have not been performed to the best of our knowledge. ILs have been probed by single techniques extensively, but not by complementary force and radiation probe measurements. Especially behavior under dynamic force conditions are interesting, but have only been probed without direct elucidation of molecular structure. Ionic liquids have been researched on by SFA-techniques on different surfaces [200]. From experiments [20] and simulation [31] of confinement between two surfaces in an SFA it can be shown that ILs display an oscillatory interaction force. This is interpreted as molecular layering by the surface force community. The same accounts for AFM measurements, which point to layering of IL molecules between confining interfaces but lack direct molecular probing. Hence by the following results presented, we expect to be the first to shed light on IL structural behavior under static as well as dynamic conditions under molecular confinement.

In Chap. 9.2.2 it has been shown in SAXS bulk measurements, that $[\text{C}_{10}\text{mim}]^+\text{Cl}^-$ forms well ordered structures under water influence. The IL forms liquid crystalline phases when containing 10-60w.t.% water. A static confinement situation is evaluated first. Here, IL structure evolution in confinement under water influence is observed. Consecutively, dynamic force measurements were applied onto the IL structure formed.

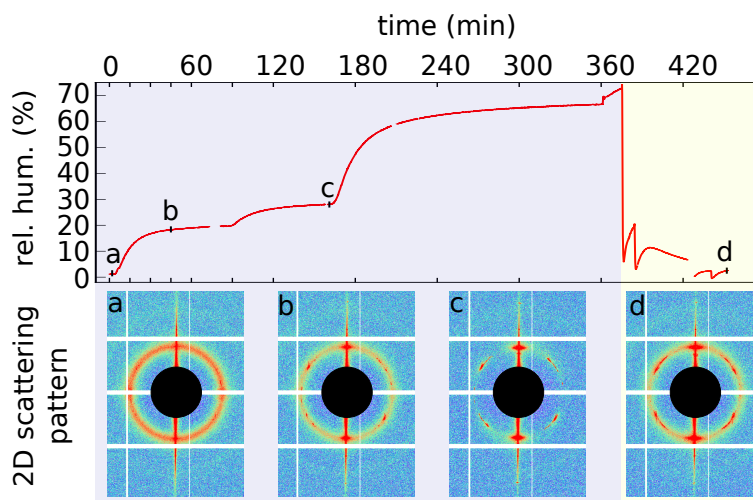
13.2.1 Water induced IL structure under static confinement

Figure 13.6 displays the measured humidity in the cell over time. The recorded scattering patterns demonstrate the structural evolution of the IL over exposure time to the controlled atmosphere. The dried sample is inserted swiftly to avoid long exposure to surrounding air. Afterwards the sample is dried by purging the cell with dry Helium for one hour. The XSFA surfaces are confining the sample down to 800 nm gap size. Further confinement can not be achieved as the sample is very viscous and resists further confinement. Normal forces onto the confining surfaces are too high. The XRD geometry probes the whole volume in the confinement gap.

When the IL is dry, a homogeneously distributed scattering ring is observed (see point a). The signal is completely unorientated, pointing to an unorientated sample structure, accounting for mesoscopic liquid structure. An influence of the confinement is not evident.

Water is introduced into the cell via the helium stream. Relative humidity is adjusted to $20 \pm 3\%$ and reaches the desired value after about 30 min. Already after an exposure time of 45 min to humid Helium, a strong orientation of the ring can be observed (see point b). Signal structure is now liquid crystalline like, with the scattering ring be-

Figure 13.6: H_2O absorption kinetics of 1-decyl-3-methylimidazolium chloride and subsequent oriented structure evolution in 800 nm confinement. Top: Relative humidity measured in the sample cell over time. Bottom: X-ray scattering signal evolution. Characters indicate time of picture taken corresponding to upper graph.



coming narrow and scattering intensity being concentrated to spots of high intensity. A sixfold signal orientation is emerging, pointing to a sixfold structure in the liquid. This demonstrates that already an exposure time of 30 minutes to low humidity has a distinct effect onto IL structure. $[\text{C}_{10}\text{mim}]^+\text{Cl}^-$ takes up water, with a resulting structure change, on a timescale of 20 to 30 minutes. A sixfold structure emerges in confinement.

Increasing humidity in the cell to $28 \pm 3\%$ fully orientates the IL structure (see point c). After an exposure time of 155 min, a clear sixfold orientation of the signal developed. Intensity along the ring is nearly fully scattered into distinct reflexes. Afterwards, humidity was increased further to the highest saturation achievable. However, no further signal orientation is observed thereafter.

After no further structure change was observed on increase of humidity after point c, the sample cell was purged with dry helium. The detected signal changes back to a more unoriented liquid crystalline signal again. Dry Helium resorbs the water from the sample again and the sample structure dries out. Structure within the IL vanishes after an exposure time of 80 min to a dry atmosphere. This corresponds to the time scale of structure change due to water uptake, being in the 20 to 30 min range.

The sixfold signal structure originates from domains of hexagonally packed columns of IL molecules (see Fig. 13.7 and Fig. 13.8a). Within the domains the columns display a high relative orientation. Domains not oriented along confinement are not visible by the X-ray signal, as their high real space length and high polydispersity lead to a broad scattering signal around the beam stop (see Fig. 13.8a). It is assumed that a continuous phase embeds the columnar structure, made of a polar network, excluding the apolar domains into columnar centers. This interpretation is based on the idea that the observed water absorption is favored by a high mobility of the water molecules. Water absorption will take place preferentially in the polar domains. Diffusion of water between hydration layers within the polar network favors the proximity of ions. A continuous phase of

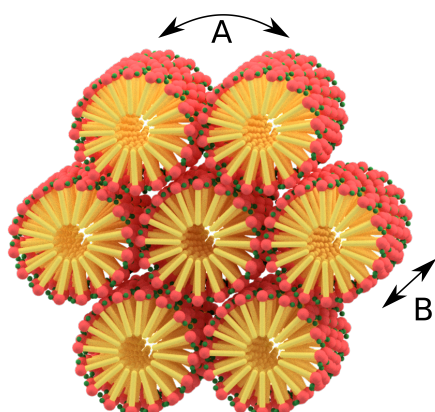
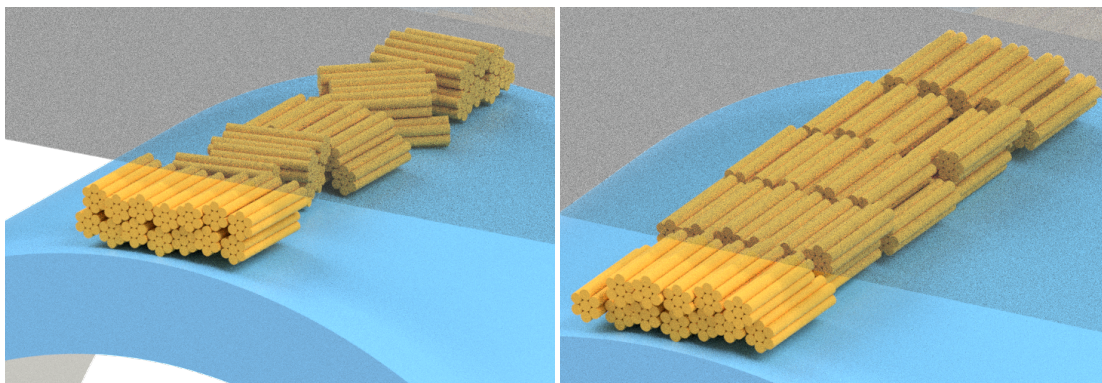


Figure 13.7: Sketch of the assumed hexagonal phase in $[\text{C}_{10}\text{mim}]^+\text{Cl}^-$ at a water content between 10-60 w.t.%. Cationic imidazolium head groups are shown in red, alkyl chains in yellow, chloride in green. The cation ratio of head/tail cross section favors micelle formation. Arrow A indicates cation diffusion between pillars, which is a slow process. Arrow B indicates the much easier diffusion process of the cation along pillar long axis.

polar domains enables good intermolecular diffusion of water molecules. A preferential hydration of one of the ions is assumed to lead to an increased polarity in the structure, driving structure formation. Less shielding of the cation charge, due to preferred hydration of the counter-ion chloride, would lead to a repulsion of the imidazolium-rings. This favors a columnar structure, in which imidazolium-rings have a discrete distance from another, while remaining in proximity of the chloride anions.

Intricate molecular dynamics are observed in the water induced hexagonal liquid crystalline structure. Considering the dynamics in a water free structure gives insight into unperturbed IL dynamics. As observed by the group of G. Voth in simulation experiments, the alkyl-imidazolium side chains aggregate in domains, which are very stable [285]. Although the system is in a liquid state, domain position is rather fixed. Tail groups can diffuse, moving within the domain. This structure supports the idea of a domain structure, that can follow dynamic stress in a liquid like manner. Q. Berrod et al. probed diffusion behavior in the mesoscopically ordered ionic liquid $[\text{C}_4\text{mim}]^+ [\text{TFSI}]^-$ on different length scales [14]. On the nanometer/nanosecond-scale, a cation is observed to diffuse within domains of a size of $11.4 \pm 1.2 \text{ \AA}$. When leaving this nano-domain, diffusion is observed on length scales of micrometer. This shows different molecular dynamics for the nano-segregated structure, as diffusion inside of the nano-domains happens differently than outside.

When water is introduced into the structure, molecular dynamics change. Theoretical considerations of the interactions of IL and water were first to perceive an interaction between small anions with a high surface charge and polar solutes like water [82]. Studying the structure of 1-decyl-3-methyl-imidazolium bromide aqueous solution by MD simulation gave further insight into water influence [15]. Self-assembly of cations into micellar aggregates occurs. The decyl side-chains form the inside part of the micelles avoiding water contact, the polar head groups face towards the water. Dynamics of heavy water in 1-butyl-3-methylimidazolium chloride was elucidated by Yasaka et al. using NMR-techniques [303, 304]. The exchange rate of H/D between heavy water and the hydrogen bound at the second position of the imidazolium ring gave an insight into



- (a) Possible domain like structure formed by the hexagonal structure in the confinement gap. Domains of hexagonally densely packed pillars are packed into domains with different orientations. The orientation within a domain is uniform but contains defects.
- (b) Possible domain structure after shearing. As cylinders in a non-parallel angle can not follow shearing motion without moving, an orientation with the long axis parallel to the shearing direction is energetically favorable.

Figure 13.8: Domain orientation in equilibrium (13.8a) and after shear force application (13.8b).

water position. During low water content the H/D exchange rate is low as all the water is located close to the chloride anion, bound by hydrogen bonds. Excess water diffuses throughout the structure as it is not part of the hydration layer around the chloride anion and contributes to the H/D exchange rate.

Whereas the dynamics of anion and cation diffusion in neat ILs, as well as the dynamics of water in a mesoscopic IL structure, are well researched, this does not account so for the molecular dynamics in a water induced liquid crystalline structure. Most work in this field was done on lyotropic hexagonal liquid crystalline structures formed by tensides. Water dynamics confined in a hexagonal lyotropic crystal phase was theoretically elucidated by Mantha and Yethiraj [165]. Simulated QENS curves gave insight into diffusion dynamics of water, showing a decrease of water dynamics when confinement increases. Willis and coworkers probed the diffusion dynamics of water in a hexagonal tenside phase [293]. Probing by NMR and simulation methods, focus was laid on the diffusion of molecules/ions around the cylinders. Water is diffusing faster throughout the structure than ions do, although ions used in this study differ quite much from ionic liquids. Observing the diffusion dynamics of tracer particles as a probe in a hexagonal columnar liquid crystal, Gambin and Coworkers saw a difference in diffusion [67]. Diffusion direction along the pillars is orders of magnitudes faster than perpendicular to the pillars. Pace of diffusion perpendicular to the pillars is controlled not by distance travelled, but by pillars overcome.

These literature results show that the hexagonal structure influences diffusion dynamics of ions and water differently. Different diffusion behavior is also observed within the different domains (apolar/polar). Mostly, water dynamics were observed

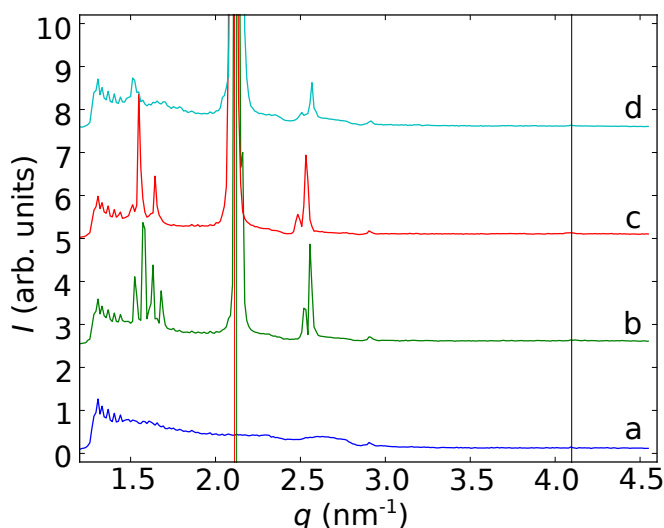
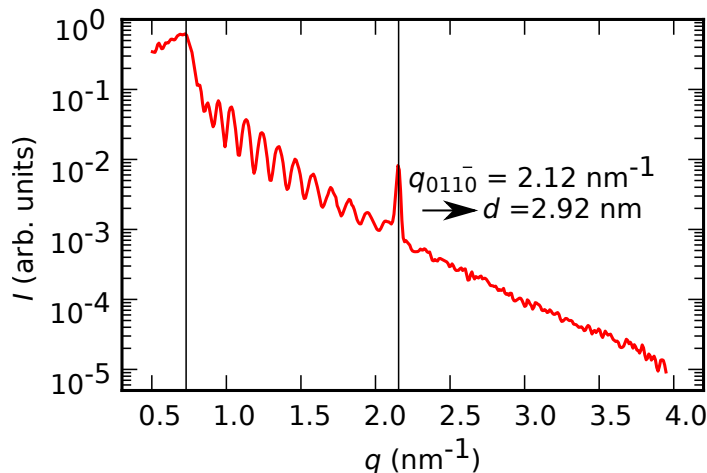


Figure 13.9: Azimuthal average of 2D-pictures depicted in Fig. 13.6 bottom, characters compare to figure. Colored vertical lines indicate maximum of intensity of corresponding graph. Black vertical line indicates position of higher order signal of maximum. Graphs were shifted vertically by 2.5 for clarity.

to be faster when unconfined and were also faster than ion dynamics in general. This backs up the idea of a continuous polar phase as this enables good water diffusion. Also the idea of ion diffusion mainly taking place along a columnar domain is supported by the observations of slowed ion dynamics.

The 2D-SAXS-patterns depicted in Fig. 13.6 were azimuthally averaged. Figure 13.9 compares the four patterns. Small oscillations at the beginning of all curves are an artifact of low pixel statistics during azimuthal averaging at low q . The blue curve (a) (dry IL), has a signal intensity orders of magnitude lower compared to the liquid crystalline signals. No discrete signal can be recognized, as intensity is scattered across a broad ring. The green curve (b) shows strong and sharp liquid crystalline peaks when water is introduced, three major signals can be recognized. The first signal occurs at around $q = 1.65 \text{ nm}^{-1}$, splitting up into different maxima. The strongest and sharpest signal at this position occurs in the red curve. The main signal, which remains the strongest during all exposure times, occurs at $q_{\text{max}} = 2.12 \text{ nm}^{-1}$. It is indicated by vertical lines and converts to a real space length of $d = 2.96 \text{ nm}$. This signal corresponds to scattering in specular direction (see Fig. 13.10). A third signal at $q = 2.65 \text{ nm}^{-1}$ is also visible. For the red and cyan curve a weak higher order signal is observed at $2 \times q_{\text{max}} = 2.12 \approx 4.15 \text{ nm}^{-1}$. This demonstrates the increase of long range order, induced by longer exposure to the humid atmosphere. All signals become sharper from (b) to (c), indicating increased orientation of sample structure under longer exposure time. Upon water content decrease, in the cyan curve (d), overall signal intensity has decreased, indicating that structure is vanishing. The liquid crystalline peak at $q_{\text{max}} = 2.12 \text{ nm}^{-1}$ has broadened slightly, indicating a decrease of long range structure. All in all the influence of water absorption induces a hexagonally ordered structure in 1-decyl-3-methyl-imidazolium chloride. In the presence of water, order within the liquid drastically increases. Strong and sharp signals with a hexagonal order evolve. A mesoscopically ordered dry structure converts to a highly ordered liquid crystalline structure.

Figure 13.10: X-ray reflectivity of 1-decyl-3-methyl-imidazolium chloride $[\text{C}_{10}\text{mim}]^+\text{Cl}^-$. The IL is confined to an 800 nm slit pore and was exposed to a controlled atmosphere of humidity of 65% until equilibrium was reached and no more signal change occurred.



Elucidation of sample structure perpendicular to the confining surfaces was also done in X-ray reflectivity geometry. Figure 13.10 shows XRR measurements of the IL sixfold structure. After the critical angle of $q_c = 0.73 \text{ nm}^{-1}$ the signal decays showing Kiessig-fringes induced by the 40 nm gold layer on top of the single crystalline substrate (see Fig. 11.4). Sample signal is visible in a strong reflection at $q_{011\bar{0}} = 2.12 \text{ nm}^{-1}$. Signal q -position is the same reflex as the strong signal visible in Fig. 13.9. This points to structure with a layered texture in q_z , which is parallel to the confining surfaces, with a periodicity of $d = 2.92 \text{ nm}^{-1}$. This observed length scale can be explained by the micellar arrangement of the pillars. A structure consisting of micelles made of $[\text{C}_{10}\text{mim}]^+\text{Cl}^-$ would have a repetition of polar domains and apolar domains. The polar domain size is only limited by the large imidazolium ring, whereas the smaller chloride anion is not limiting polar domain size being located above the imidazolium ring. The length of two times the C_{10} alkyl side-chain plus the imidazolium ring gives a length of about 3 nm which corresponds well with the observed periodicity of $d = 2.92 \text{ nm}^{-1}$. Hence, the strong XRR signal backs up the idea of a sample structure made up of domains of hcp layered pillars.

13.2.2 Dynamic stress of water induced IL structure under confinement

A SAXS pattern recorded in 400 nm confinement at XRD geometry is presented in Fig. 13.11. The figure compares well to Fig. 13.6c and shows further increase of signal orientation. Assuming a molecular length scale of 1.9 nm for $[\text{C}_{10}\text{mim}]^+\text{Cl}^-$ (see Fig. 10.2), the confinement gap of $D = 400 \text{ nm}$ corresponds to about 210 atomic layers. The sixfold signal orientation became more sharp and focused. Discrete assignment of the reflexes to the lattice planes of the hexagonal structure is done here. Character l indicates direction parallel to the long axis of the columnar structure. Especially intense are the specular first order signals $(01\bar{1}l)$ and $(0\bar{1}1l)$. Higher order reflexes are

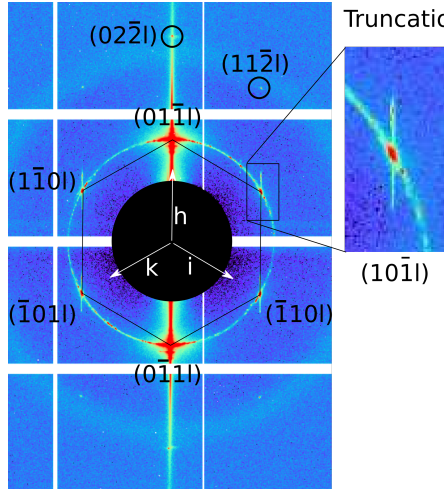


Figure 13.11: Scattering pattern of 1-decyl-3-methyl-imidazolium chloride $[\text{C}_{10}\text{mim}]^+\text{Cl}^-$ in equilibrium with 65.2% r.h., confinement gap $D = 400$ nm. Plane directions are indicated by hki . The plane parallel to the beam direction is unresolved and indicated by l . Numbers indicate Miller indices of associated hexagonal lattice planes. Inset shows details of liquid crystalline truncation rod signal. The hexagon guides the eye.

clearly visible now in both specular directions. The broad diffraction ring in the pattern, which appears slightly below the second order reflex $(02\bar{2}l)$, originates from the Kapton windows.

First order signals on the ring indicate a truncation rod structure [56, 117, 222, 263]. The name Crystal Truncation Rod (CTR) refers to the signal shape, scattering in a rod like structure. This signal structure occurs, when a highly ordered phase is truncated by a surface. The surface of the semi-infinite highly ordered structure creates a diffraction pattern. CTRs are a surface effect. An infinite highly ordered structure would lead to Bragg diffraction spots only, scattering in a Dirac delta distribution. However, the bulk diffraction spots are extended here. Extension of the scattering pattern takes place normal to the surface of the structure. Hence, CTR orientation indicates confinement direction. The confining surfaces are orientated perpendicular to the CTR signals in Fig. 13.11. This backs up the picture of micelles order in a layered manner. All in all, this signal structure is a strong indicator of a highly ordered sample structure in the confinement. Considering that the sample is still in a liquid crystalline phase, the order inducing confinement effect on a liquid molecular structure is illustrated.

Reflexes at $q = \sqrt{3} \times (01\bar{1}l) = 3.64 \text{ nm}^{-1}$ indicate the hexagonal close packed structure of the pillar arrangement. This reflex corresponds to the $(11\bar{2}l)$ -plane. All four of the corresponding reflexes of this type of planes are visible in the 2D-pattern. Figure 13.12 illustrates the layer distances and orientation in the structure. The long axis aligned along the confinement apex can not be resolved in this geometry. The faces of the micellar columns are assumed to be orientated perpendicular to the X-ray beam.

Taking the azimuthal average of Fig. 13.11 corroborates the liquid crystalline structure of the sample. Reflexes of first order along the ring are the strongest. The reflex is sharp and focused, pointing to a high order along the y - z -plane of confinement. Signal maximum of $q_{\text{max}} = 2.10 \text{ nm}^{-1}$ is the same as during measurement in 800 nm confinement. Structure itself did not change, just long range orientation increased. The second order signal at $q = 2 \times q_{\text{max}} \text{ nm}^{-1}$ is already orders of magnitude weaker. Being too weak the signal at $q = \sqrt{3} \times (01\bar{1}l) = 3.64 \text{ nm}^{-1}$ is not visible in the azimuthal average.

Figure 13.12: Orientation of the hexagonal structure in confinement towards the confining surfaces. Layer distance $d = 2.92$ nm is perpendicular to the confining surfaces and reflects into specular direction. Due to the destructive interference at distance d only the short distance $d/2$ yields visible reflects. The layers corresponding to a distance of $d = 1/2 \cdot \sqrt{3} \cdot d$ are tilted by 30° and for example yield reflex $\bar{1}10l$ in Fig. 13.11.

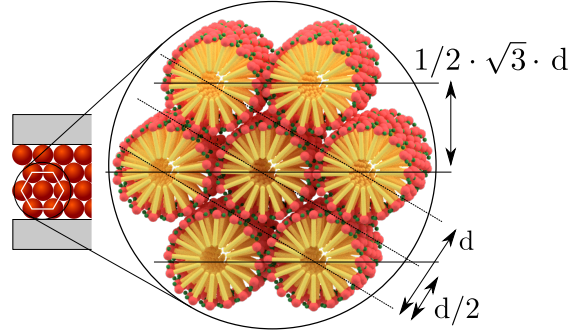
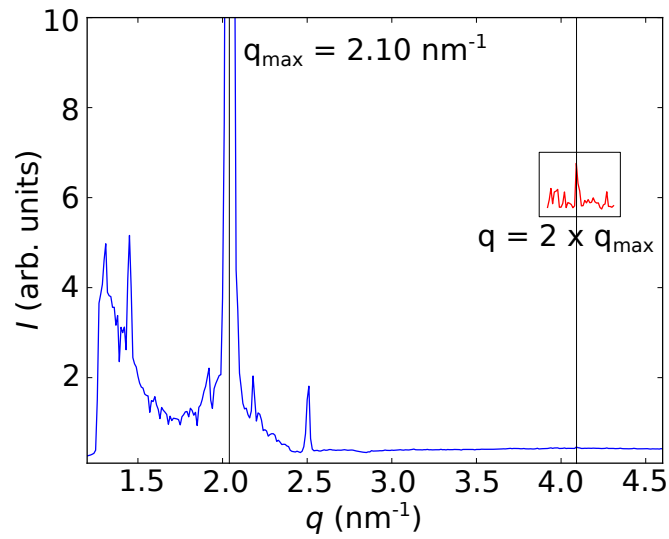


Figure 13.13: Azimuthal average of Fig. 13.11. The liquid crystalline signal is orders of magnitudes stronger than the other signals. Inset shows the higher order signal. Due to weak intensity the reflex pointing to hexagonal structure at $q = \sqrt{3} \times (01\bar{1}l) = 3.64 \text{ nm}^{-1}$ is not visible in the 1D spectrum.



Dynamic stress in 180 nm confinement

This structure is now stressed by deflection of the curved surface parallel to the X-ray beam. Being in XRR geometry the angle is adjusted to track first order signal evolution at $q = 2.1 \text{ nm}^{-1}$. Normal force (relative force) was adjusted to 0 mN.

Application of step-wise shear

At first, shear force is applied in steps of 0.5 V piezo voltage, resulting in a step-wise stress increase. Figure 13.14 shows three different signals: Gap width (black) in a range from 177 nm up to 184 nm, Forces (cyan) in milli-Newton from 0 to 35, X-ray intensity (red) is set to 100% for the highest intensity in this scan.

Gap width is constantly increasing over the course of measurement and shows no sign of influence by the shear steps applied. Over the course of 40 min a nearly linear increase of the gap size from 177 nm to about 184 nm is observed. Gap size corresponds to about $177 \text{ nm} / 2.53 \text{ nm} = 70$ layers. The increase of 7 nm converts to 3.8% expansion of the gap width. Being a small but steady overall increase, this which might be interpreted as sample swelling due to continuous water uptake, as the sample has not

reached equilibrium yet.

Reaction of strain gauges to applied stimulus was prompt throughout the whole measurement. This means that the cylinder was not deflected at all but shear force application was absorbed by the springs holding the lower cylinder. Increasing above a shear stress of 15 mN, force relaxation is observed. This indicates a motion of the cylinder over timescales of 4-5 minutes. Force never relaxes below 20 mN. Later deflection step above 25 mN are fully relaxed.

XRR intensity (red curve) shows distinct drops which occur at the same time as shear step deflection onset. Reaction is prompt and constant over time in the beginning. Over the course of the scan intensity decreases by about 28% due to deflection. Specular signal position did not change upon force application, therefore a misalignment of the device can be ruled out to be responsible for X-ray intensity change.

The first application of shear is not accompanied by a decrease in XRR intensity. Only the application of a shear stress of 7.5 mN (Piezo 1 V, second step) has an impact on XRR intensity. XRR intensity drops by 5%. Similar behavior is observed for the second and third shear step (1.5 V and 2 V, respectively).

From about the fourth step ($F = 17.5 \pm 1$ mN) onwards, shear force relaxation during holding time is observed. The material starts to behave viscoelastic. Shear strain σ is calculated from the applied force F over the area of stress application $A = 5 \text{ mm} \cdot 0.1 \text{ mm} = 0.5 \text{ mm}^2 (= 5 \cdot 10^{-7} \text{ m}^2)$, using a confinement apex width of $100 \mu\text{m}$. For the fourth step, this yields a shear strain of $\sigma = 0.035 \text{ N/mm}^2$. This seems to be the threshold for creep in the LC structure [184, 260]. The effect of stress relaxation increases with increasing deflection of the surface. Later shear applications are nearly fully relaxed when shear force is in a range of about 25 ± 1 mN. From the point on when creep is observed no drastic changes in XRR intensity are recorded anymore. The application of shear force is not followed by structural change in the sample anymore.

This signal behavior can be interpreted by assumption of an LC sample structure in the confinement gap featuring different LC domains. Being in a preferred order in the beginning, the structure of IL domains is misaligned by shear stress. The structure within the single domain, which can be imagined to be composed of a pillar structure, remains the same. Reaching a level of shear strain of $\sigma = 0.035 \text{ N/mm}^2$ the structure starts slipping, leading to the decrease of shear tension, while XRR signal remains unchanged because the LC structure is not deflected anymore.

Application of oscillatory shear

The step-wise shear measurements were continued with dynamic oscillatory shear measurements. A triangular excitation wave of deflection motion is applied to the surface. Combined results of X-ray and SFA are shown in Fig. 13.15. No FECO were recorded here, so no gap width can be shown. However, no distinct changes were detected in force or X-ray recording, so the assumption of the previous gap distance of 180 nm is reasonable.

Figure 13.14: Evolution of XRR first order signal under stepwise shear from 0 V to 5.5 V in steps of 0.5 V. Relative humidity: 55-53%, Gap width (black), Forces (cyan) and X-ray intensity (red). X-ray intensity is set to 100% for the maximum during this scan. Black lines should guide the eye.

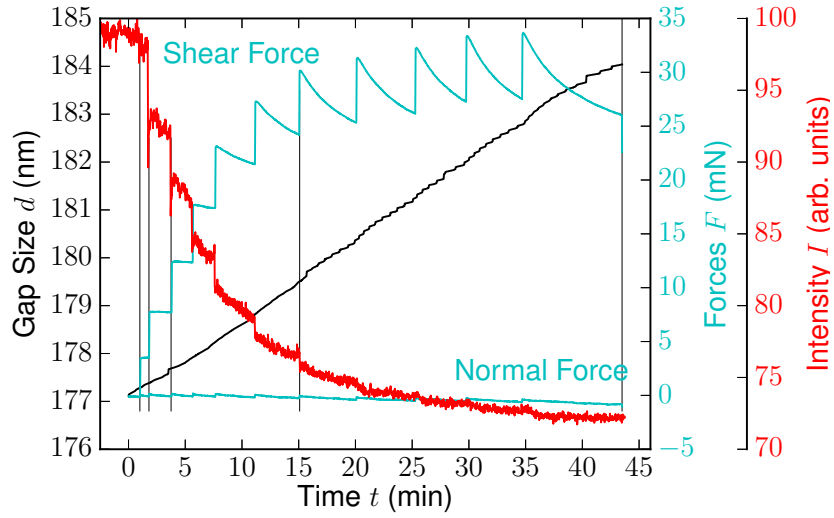


Table 13.1: SFA Parameters applied in Fig. 13.15.

Ampl. U	Frequ. f	Force F
[V]	[mHz]	[mN]
0.1	30	1
1	30	25
2	30	50
2	15	50
3	15	100
4	15	130
5	15	160

The mesoscopic structure of hexagonally packed pillars of $[\text{C}_{10}\text{mim}]^+\text{Cl}^-$ is now stressed at different shear forces. As can be observed in Fig. 13.15, especially the amplitude of shear has an impact. During the first part, applying 1 mN, no significant change in XRR intensity is observed. The sample structure is uninfluenced by such mechanical stress. A tiny intensity increase is observed in the second part, applying 25 mN, but still no significant sample restructuring due to mechanical stress occurs.

Applying an amplitude of 2 V at the same frequency however, an increase of 15% in XRR intensity over 23 min results. Increase of XRR intensity converges towards a plateau of finite intensity. Reflected intensity rises, the sample scatters more uniformly. This points to an increase of order within the sample for shear forces $F > 50$ mN.

In the subsequent step, shear frequency was lowered to 15 mHz and and amplitude of 2 V. Again, at this shear force no change in XRR signal intensity results. Sample

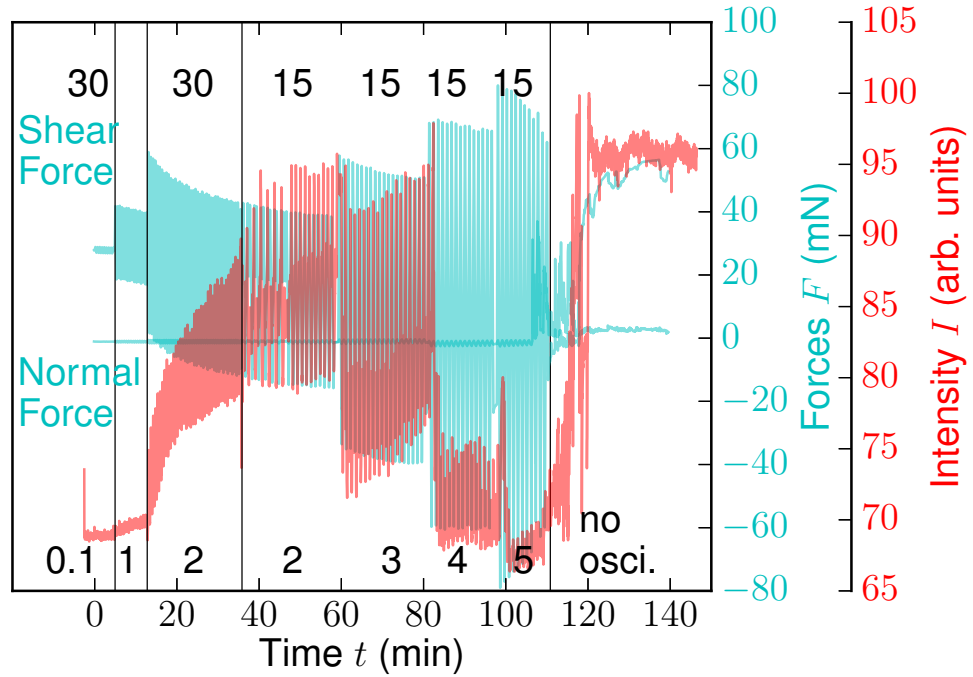


Figure 13.15: Dynamic shear force measurements and corresponding XRR first order signal evolution. Forces in cyan, XRR intensity in red. Top numbers: shear frequency (mHz), bottom numbers: amplitude (Volt). Maximum intensity of XRR signal during the scan was set to 100%. Humidity: 53.0 to 50.5%r.h.

structure seems to be uninfluenced by shear forces $F \leq 50$ mN.

Upon the application of $F = 100$ mN (3 V; 15 mHz), XRR intensity drops by about 9%. During the course of shearing though, a slight increase of signal intensity is visible again. Structure seems to recover from the initial disturbance by a higher shear stress, but it does not reach prior intensity levels again.

Switching to an even higher shear force $F = 130$ mN, a drop of XRR intensity of 15% is observed upon shear application. The orientation in the LC-structure has decreased. Shear seems to not only induce structure orientation, but also to misalign the structure when applying shear forces higher than $F = 100$ mN. Backing up the idea of an LC domain structure being deflected by shear force application, is the observation of stable XRR intensity during shear. Disturbance of structure occurs instantly upon force application.

The same behavior is observed at the highest shear force $F = 160$ mN applied. XRR intensity drops to the lowest value of 67% and remains at this value during shear application.

When shearing is stopped, XRR intensity rises reaching even higher levels than before. Intensity plateaus after about $t = 11$ min. This observation coincides with a rise in normal force. Whereas shear force stays around zero, normal force rises from

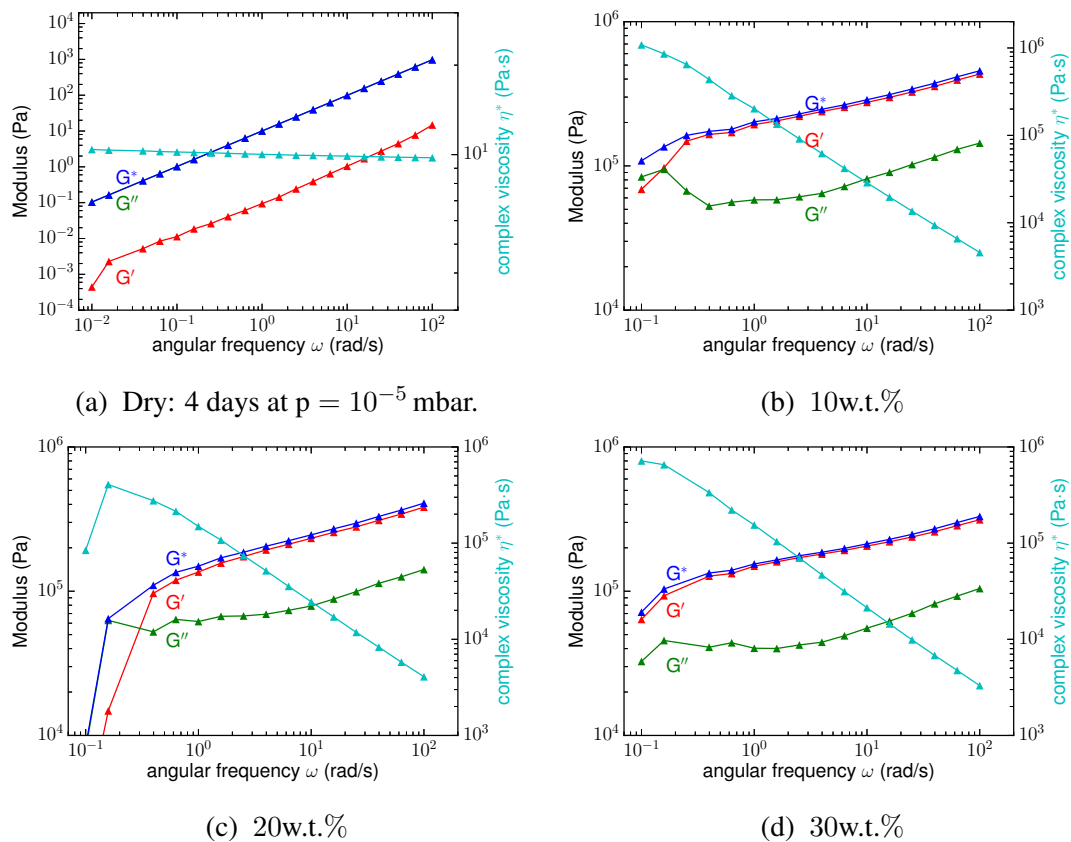


Figure 13.16: Rheology: Frequency sweep measurement of $[\text{C}_{10}\text{mim}]^+\text{Cl}^-$ at different water contents; $T = 23^\circ\text{C}$ at all measurements. Storage modulus G' , loss modulus G'' and complex shear modulus G^* are plotted in Pa on the left y-axis. Complex viscosity $\eta^* = G^*/\omega$ is plotted in $\text{Pa} \cdot \text{s}$ on the right y-axis.

0 to about 60 mN. This points to a structural reformation after the structure has been strongly disturbed by shear force application. Seeding within the gap, the newly formed structure is not slowly formed under equilibrium conditions as before. This leads to a confinement effect, in that the structure “sees” the confining surface as obstacles while restructuring.

Comparison of bulk and confinement viscosity

For comparison between bulk and confinement viscosity behavior, frequency sweep measurements were conducted on dry and wet bulk $[\text{C}_{10}\text{mim}]^+\text{Cl}^-$. Results are presented in Fig. 13.16. Three different water contents (10w.t.%, 20w.t.%, 30w.t.%) were measured in a frequency range from 0.1-100 rad/s.

Dry $[\text{C}_{10}\text{mim}]^+\text{Cl}^-$ displays liquid like features (Fig. 13.16a). Loss modulus G'' is much higher than storage modulus G' indicating low elastic properties but high viscous properties of the IL structure. Accordingly, storage and loss modulus ratio has high

values of $\tan(\delta) = 9 - 29$. No structural order is present to store energy elastically, shear energy is fully dissipated. Complex modulus G^* is fully determined by G'' and both curves overlap. Complex viscosity is low at $|\eta^*| = 10 \pm 1 \text{ Pa} \cdot \text{s}$. These viscosity values are in a similar range to other dry ILs having mesoscopic structure. For $[\text{C}_8\text{mim}]^+\text{Cl}^-$ in a dry state ($\text{H}_2\text{O} = 0.1 \text{ w.t.}\%$), a viscosity of $\eta = 33.07 \text{ Pa} \cdot \text{s}$ was measured [241].

The liquid-like behavior only applies for neat ILs in a non-liquid crystalline state. When being in a LC state, the internal structure has a distinct influence on mechanical properties. The viscosity of imidazolium based ILs is known to vary distinctly with trace amounts of chloride and water [217, 241, 287]. Already amounts of 2 w.t.% (20 mol%) can lead to a reduction of 50% of the viscosity. However, most work observes a reduction of viscosity, not an increase, upon water absorption. Most of these ionic liquids do not form liquid crystalline phases, though. For $[\text{C}_{10}\text{mim}]^+\text{Cl}^-$, macroscopic gelation is observed when a liquid crystalline phase is induced by water. This is shown in the bulk measurements at higher water content in Fig. 13.16b to d. Here G' is higher than G'' and dictates complex modulus G^* behavior. The material has a stronger elastic component now and behaves like a viscoelastic material. The hexagonal structure is able to store stress elastically. This also compares to the range of $\tan(\delta) = 0.3 - 0.5$, which is in the range of a viscoelastic gel or solid. Complex viscosity $|\eta^*|$ is much higher than during dry conditions at a range of 10^6 to $10^4 \text{ Pa} \cdot \text{s}$. The constant decrease with increasing shear rate is a typical behavior of a material with a strong elastic component. Energy is stored elastically in the structure and the sample behaves like a viscoelastic body. Whereas the neat IL can often be described as a Newtonian-Liquid, the liquid-crystalline phase shows typical behavior of a hexagonal lyotropic phase, as usually found in surfactant solution systems [218].

Dynamic stress in confinement less than 100 nm

Using the Pilatus Dectris detector system, the dynamic measurements were continued in XRR geometry. Results are shown in Fig. 13.17. To reach a lower confinement gap, a normal force of 190 mN was applied during this experiment, yielding a pressure of 0.38 mbar in the gap ($p = F/A = 190 \text{ mN}/5 \text{ mm} \cdot 0.1 \text{ mm}$). This pressure is orders of magnitudes lower than the compressibility of liquids, thus the structure within the liquid can be assumed to remain unchanged. Shear stress application splits in step-wise shear force application and dynamic oscillation. Step-wise shear was performed first (Fig. 13.17a), followed by three dynamic measurements (15 mHz, 5 V; 15 mHz, 5 V; 1 Hz; 5 V). During step-wise shear stress application, firstly the surface was deflected in steps of $U = 0.5 \text{ V}$, yielding strain gauge forces of 3.6 to 5.9 mN. Gap distance decreases from 100.9 nm to 96.9 nm. The first two steps of deflection are not influencing the gap distance. Only after the third step, at a force of $F = 22.4 \text{ mN}$ (shear strain $\sigma = 44.8 \text{ mN}/\text{mm}^2$), a decrease in gap distance follows. Later force application is not directly followed by a decrease in gap distance, but gap distance changes occur randomly. This points to a restructuring of the LC domain structure. Following the decrease in gap distance, XRR intensity decreases by 28.0% during the application

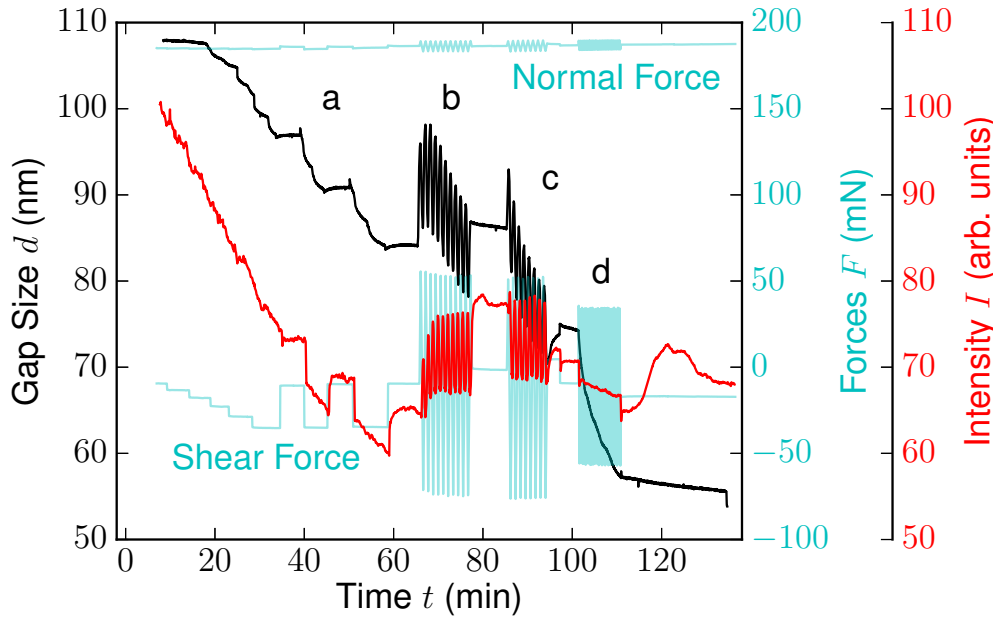


Figure 13.17: Step-wise and oscillatory shear force measurements and corresponding XRR first order signal evolution performed in a confinement regime of 110 nm to 55 nm. Gap size (black); Normal Force and Shear Force (cyan); XRR intensity (red). Normal Force set to $F = 195$ mN, Shear Force: $F = 0$ mN, XRR intensity was to to 100% for the highest value of the scan. Relative humidity 60-62% r.h.

of the $U = 0.5$ V deflection steps. This indicates a perturbation or deflection of the LC structure.

Application of step-wise shear

Detailed view of the 2.5 V shear steps is shown in Fig. 13.18. Confinement is now at $D = 99$ nm ≈ 37 micelle layers. A shear force step of 2.5 V at 35 min is promptly followed by a force increase of $F = +25$ mN (shear strain $\sigma = 50$ mN/mm²). Again, the cylinder surfaces was not deflected, but remained stationary. The applied deflection force is absorbed by the sample liquid. Force application is followed by only a small response in gap distance of less than +0.5 nm and by an XRR signal oscillation of less than 1%.

During the subsequent holding time, gap distance, as well as XRR intensity, is not decreasing but remains constant. Considering that the surface is in equilibrium position, it can be assumed that no shear force is acting upon the structure anymore. As all signals remain constant, structural changes only occur, when the structure is stressed. However, also no structural recovery is observed.

At 40 min a deflection in the opposite direction (5 V to 2.5 V) is applied. This is answered by an immediate decrease of XRR intensity of about 5%, but no instant change of

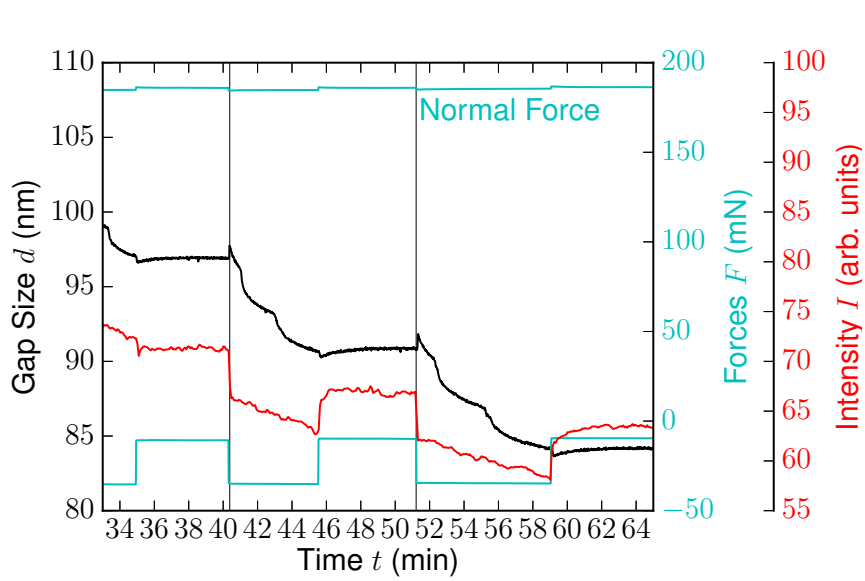


Figure 13.18:
Step-wise shear
force applica-
tion of ± 2.5 V
(Fig. 13.17a).
Response in
force (cyan),
gap distance
(black) and XRR
intensity (red).

gap distance. Sample structure seems to be driven out of equilibrium without a gap distance change. During the subsequent holding time the gap distance decreases viscoelastically in two distinct steps of 3 nm from 97 nm to 90 nm, a length scale corresponding to the micellar dimension. Material seems to be squeezed out of the gap. Meanwhile XRR intensity shows a slow but linear decrease of 4%, which is in the range of assumed loss of material in the gap (i.e. two micelle layers out of $37 \approx 5\%$).

For the next deflection period the same behavior is observed. When shear force switches back to 5 V at around 45.5 min, no gap distance change is observed, however again an increase of XRR signal intensity of 5%. The structural changes happening instantly upon deflection seem to be reversible in deformation. At 51 min the relaxation process is observed again. During a holding time of 8 min the relaxation of two times the micelle dimension is visible accompanied by an XRR intensity decrease of 3 to 4%.

Two effects are reasoned from this observation. The LC domain structure is reversibly deflected when stressed (instant XRR intensity drop), but also releases stress by a squeeze out of layers. When the deflected surface is in equilibrium position, neither a gap distance change, nor a change in XRR intensity is observed. The LC structure does not change further, but the structural perturbation induced by shearing is also not recovered, as XRR intensity does not increase again.

When comparing step-wise shear force application in 180 nm (Fig. 13.14) and in 90 nm (Fig. 13.18), signal behavior points to a structure consisting of deflected hexagonally layered LC IL-domains. When the sample is stressed by 2.5 V in Fig. 13.14, a relaxation of force by about 8% from 24 mN to 22 mN is observed over the course of 5 minutes. In later force applications of 2.5 V on the same sample (Fig. 13.18), non such force relaxation occurs. Sample structure seems to have increased in rigidity when being in equilibrium now (fully saturated with water). This corresponds to the gap distance increase in Fig. 13.14, which can be explained by swelling of the structure, as equilibrium water saturation was not reached yet. The increase over time observed there is small

with 7 nm over the course of 44 min. When material is squeezed out of the gap, gap distance change is much faster, in Fig. 13.18 gap distance change of 7 nm happens in 5 min. This observation backs up the idea of a slow swelling of the LC structure, which is still absorbing water in Fig. 13.14, as the first measurement was performed one hour after water introduction, the second measurement several hours after water introduction. In the later experiment (Fig. 13.14) water saturation was reached and gap distance only changed upon structural perturbation following shear force application. The majority of the structure however is already in the hexagonally layered LC structure after about one hour. This is indicated by the constant XRR intensity in the measurement at 180 nm. XRR intensity remains constant over time and always shows a decrease when shear strain is applied for both measurements. Reaction of sample structure to force application however changes. In the 180 nm confinement measurement, a force application of 2.5 V results in a XRR decrease of 20%, whereas in the 100 nm confinement measurement a force application of 2.5 V yields only a change of 5%. Also here, an increased rigidity of the sample structure for the second measurement featuring the smaller confinement is observed. Whether the structure became more rigid due to the decreased confinement or by being fully water saturated is hard to estimate.

Application of oscillatory shear

The overview of the measurement in Fig. 13.17 shows the three oscillatory shear measurements (15 mHz, 5 V; 15 mHz, 5 V; 1 Hz, 5 V) as b, c, d, respectively. Detailed views of the measurements b and c is shown in Fig. 13.19 a and b.

The first oscillation is performed in a confinement of $d = 84$ nm. This gap distance compares to about 33 micellar layers of a hcp packed pillar structure orientated along the confinement apex. The applied triangular wave profile is reflected in the force read out. Force reaction to excitation signal (not shown) is prompt, no phase difference occurs. Starting at about -9 mN relative force, shear force oscillates from $+56$ mN to -74 mN in an amplitude of ± 65 mN. See Tab. 13.2 for parameters.

Gap distance oscillations follow the shear stress signal. Upon shear force application gap distance increases instantly. Starting at the equilibrium value of 84 nm, distance increases to a higher mean value of around 92 nm, but then decreases again towards the end to values around 85 nm. Over the course of shear force application a gap distance change of only 3 nm occurs, finishing at a value of 87 nm. Amplitude of gap distance oscillation does not change over the course of shear and is around 12 nm, which corresponds to about 13% of total gap width oscillation or three times the LC-IL layer distance.

Maximum and minimum of gap distance always occurs at zero position transition. However, a hysteresis is observed depending on shearing motion direction. When the shearing surface is moved in one direction, gap distance either runs through a maximum or through a minimum, depending on which direction the surface is moving. This points towards a structure deflected from a closely packed equilibrium position. The fact that gap distance increases upon deflection might be explained by a pretilted struc-

ture. The LC-IL domain structure can be thought of to be first disordered by shear but subsequently also reordered by shear in a more compact way. This effect is repeatedly observed. Shear force application in general can be assumed to induce a preferred orientation along the confinement apex. An angle of the pillar structure different than along the confinement apex would require a rolling motion of the pillars to release shear stress. Rolling motion is unnecessary however, when pillars slide along the long axis. This orientation is much more favored under shearing conditions as it does not require the pillars to move. Being the equilibrium structure, the hexagonal pillar structure is maintained under shear. The structure reorients along shear direction, enabling diffusion of the IL molecule within the pillar, along apex direction. As molecular diffusion is about six orders of magnitude faster (μsec) than shear induced restructuring (sec), molecular reorientation is much faster than shear influence.

XRR intensity also increases upon shear force application. An increase by 12%, from 63 to 75 percent, occurs over the course of shear force application. Shear application seems to increase the isotropic orientation of the structure. The height of gap distance oscillation ranges from 6% at the beginning to about 9% at the end. XRR intensity and gap distance oscillations are in phase. This simultaneous reaction of gap distance and XRR signal also points to a deflection of a structure within the LC. The LC hexagonal pillar structure is not destroyed by shear, but merely deflected. Maximum occurs always at the half way point of motion range, i.e. the middle of the gray area which indicates continuous motion into one direction. This observation of the same hysteresis for the XRR signal backs up the idea of a perturbation/restructuring cycle induced by shear application.

The second oscillatory shear performed about 6.5 min after the first is shown in Fig. 13.19b. A triangular wave profile with the same parameters is applied (see Tab.13.2). Force oscillations also promptly followed the excitation signal, ranging from +52 mN to -80 mN, oscillating around a mean value of -14 mN with an amplitude of ± 66 mN.

Gap distance starts at 87 nm, the same value as it stopped during the first shear. No gap distance change occurred without shear force influence. Also here, on onset of shear, gap distance increases. Gap distance always seem to increase and does not go below the starting value, unless the mean value decreases as well. Constant oscillations of about ± 5 nm are visible over the course of shearing. In contrast to the first oscillatory shear, a decrease by about 14 nm (16%) to a gap width of 73 nm occurs. A mean value of 80 nm is assumed for Fig. 13.19b.

XRR intensity oscillations follow again gap distance oscillations. It starts at 76%, the end value of the first shearing. In this second shear force application, overall intensity decreases by 6% to 70%. This goes hand in hand with the decreased gap distance. In opposition to the first shearing, here in the second shearing sample material seem to leave the gap, leading to a decrease in gap distance and intensity. This might be explained by a destruction of LC structure due to the consecutive shearing. During the first shear, the sample dissipated shear stress by reorganizing in a more isotropic structure, leading to an increase of XRR intensity. This way of shear stress dissipation is not possible anymore during the second shear force application. Subsequent shearing destructs

13 RESULTS AND DISCUSSION

Table 13.2: SFA Parameters applied in Fig. 13.17 b, c, d.

Ampl. U	Frequ. f	Force F
[V]	[mHz]	[mN]
5	15	65
5	15	66
5	2000	46

the LC structure. After termination of shearing, both gap distance and XRR signal increase again, pointing to a structural recovery in a way that the structure becomes more isotropic.

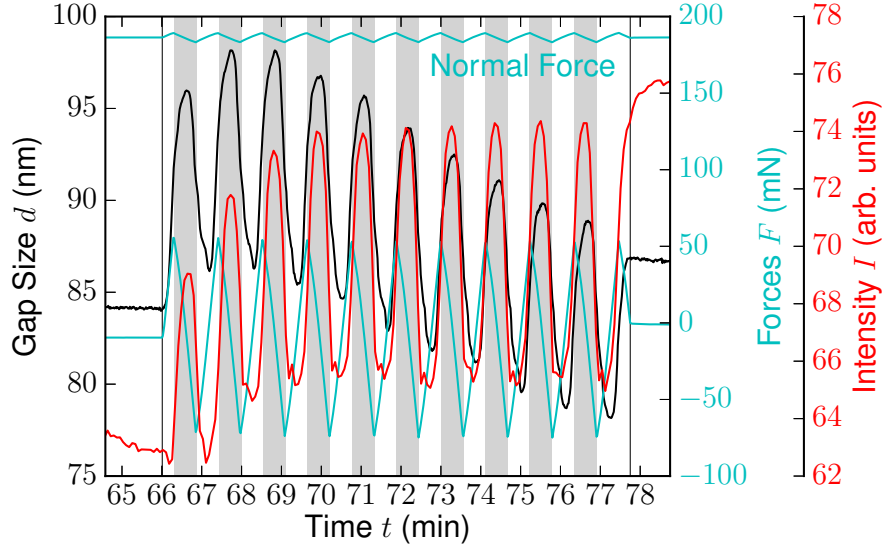
The third oscillatory shearing is shown in Fig. 13.17d, but not dealt with in a separate figure. A high oscillation frequency of $f = 2000$ mHz was applied here (see. Tab. 13.2). Oscillation frequencies that fast (two oscillations per second) were not resolved properly as recording parameters of both instruments were not set accordingly. Hence neither strain gauge force, nor XRR intensity are well resolved. Nevertheless, interesting signal behavior is observed.

Gap distance decreases rapidly and constantly under this shear regime from 74 nm to 57 nm. With 17 nm in about 9 minutes the strongest decrease (-23%) observed during shear force application. The observed drop in gap distance is obviously linked to the high shear force applied. The LC structure seems to display shear thinning as well as being destructed to a certain degree. Stopping shear, gap distance remains constant again.

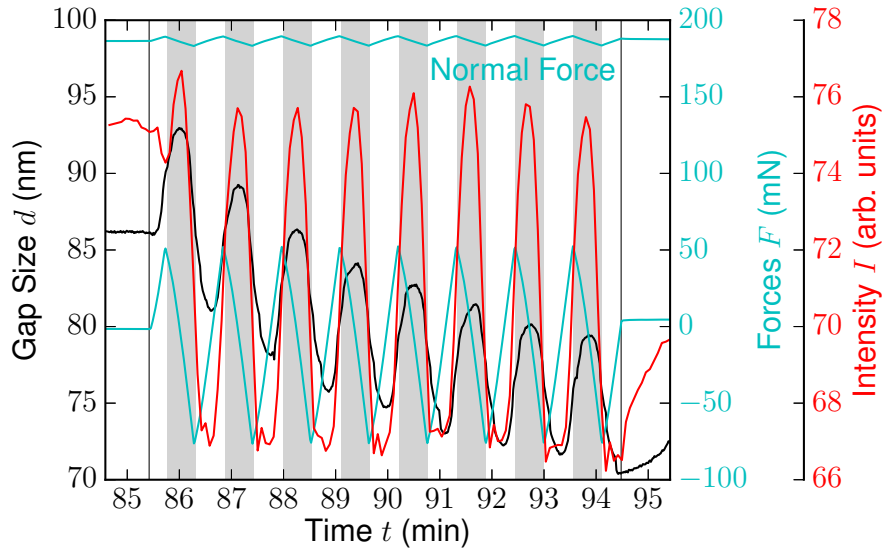
Upon shear force application intensity drops instantly by about 3%. This points to a destruction of structure, instantly occurring upon force onset. During subsequent shearing intensity only decreases slightly, but steady, by about 1%. This points to shear thinning of structure by this high shear rate, enabling material to leave the confinement gap. Stopping shear, XRR intensity recovers and rises again to a value of intensity of about 68%. A value close to the intensity before shear application. Loss of material is small, the structure recovers isotropic orientation, taking up equilibrium structure again.

The following conclusions can be drawn from oscillatory shear force application. The liquid crystalline IL structure is assumed to consist of different domains, featuring different orientations. Shear stress is released by structural reorientation of the LC domains, or squeeze out of the gap. The LC structure is not changed by the shear stress applied, the columnar structure remains the same. Upon force application gap distance and XRR intensity always instantly increase. Presumably a deflection of a pretilted structure occurs. Deflection of the structure leads to an increase of gap distance, as the structure is deflected from its optimum packing. The synchronous oscillation of XRR and gap distance also points to a tilt of structure during shear. Both signals probe the same structure. The hysteresis of the oscillations, depending on shear direction, seems to origin in structural changes of the sample. It can be assume that the structural changes do not depend upon shear direction, but on repeated perturbation by shear. A first ap-

plication of shear force leads to an increase of molecular order, the XRR signal rises in intensity. Meanwhile the gap distance remains constant. Material does not leave the gap, but domains are more isotropically ordered as a reaction towards shear. Domains orientate in the force field of shear and orientate along shear direction. When the system is already orientated, it can not release stress by orientation anymore. Now shear application leads to perturbation of the structure (XRR decrease) and squeeze out of material from the gap occurs (gap distance decrease). Upon stop of shear force application, XRR intensity and gap distance recover, but do not reach prior values. This points to a structural recovery of the sample, the mis-alignment of the structure due to shear vanishes. High shear rates however destroy the molecular order and lead to shear-thinning. An instant drop in XRR intensity shows that shear destroys molecular orientation, followed by a squeeze out of material indicated by further XRR decrease and gap distance decrease.



(a) First oscillatory shear (Fig. 13.17b).



(b) Second oscillatory shear (Fig. 13.17c).

Figure 13.19: Oscillatory shear stress of wet $[\text{C}_{10}\text{mim}]^+[\text{Cl}]^-$ in confinement: Frequency $f = 15 \text{ mHz}$, Amplitude $U = 5 \text{ V}$, shear rate at 85 nm : $\dot{\gamma} = 0.425 \text{ s}^{-1}$. Normal Force set to $F = 195 \text{ mN}$. Gap size (black); Normal Force and Shear Force (cyan); XRR intensity (red). Grey patches: continuous shearing motion in one direction. XRR intensity was to to 100% for the highest value of the scan. Relative humidity 60-62% r.h.

Part V

Summary

Chapter 14

Summary and Conclusion

The goal of this thesis was the construction and operation of an X-ray Surface Force Apparatus using a cylinder-on-flat geometry to gain new insights in the field of molecularly confined liquids. The asset of the new instrument are dynamic in-situ studies on the response of a confined liquid to an external stimulus. The sample system is brought out of equilibrium by compression/decompression or horizontal shear stress of the slit-pore. Simultaneously, molecular order dynamics are probed by X-ray scattering techniques. The structural information obtained from XRR and XRD are complemented by SFA force and distance measurements.

The capabilities of the device were demonstrated probing the smectic liquid crystal 8CB as a benchmark system. In the confinement gap the 8CB dimers display typical smectic A structure with high orientational and positional anisotropy in a stratified structure. XRR and XRD showed a sharp first peak, indicating high order perpendicular to the confining surfaces, and a second broad peak indicating low in-plane order. Applying compression/decompression cycles, the dynamic behavior of the system was resolved. Upon decompression of a $D = 1700$ nm confinement gap, anisotropy of the 8CB structure decreased, indicated by an instant drop of specular intensity and a rise of in-plane intensity. However, specular signal intensity recovers on a timescale of 20 seconds after decompression. The increase of X-ray signal points to a viscoelastic behavior of mesogens. Subsequent compression application increases specular intensity to prior values again. The alignment of 8CB liquid crystalline layers is increased by compressive stress. In a 120 nm confinement gap compression application showed a gap width decrease of one molecular layer for the first cycle, but smaller steps in subsequent cycles. In contrast to that XRR intensity did not decrease significantly. The layered structure is disturbed by stress application, but an overall change of the smectic order is not observed. Discrete smectic layers are not squeezed from the gap with each compression cycle. Structural defects on the order of misaligned mesogens seem to be induced. Under oscillatory force application it can be assumed that these defects move through the liquid crystalline structure. They are pushed out of the structure, as compression stress increases anisotropic alignment of mesogens. This effect can explain the continuous gap distance decrease at constant reflectivity intensity.

The sample system $[\text{C}_{10}\text{mim}]^+\text{Cl}^-$ gave insight into dynamics of ionic liquid crystals in confinement. Water induced structure evolution showed a transition from a mesoscopically ordered dry IL to a liquid-crystalline structure. The sixfold signal structure of very sharp reflexes indicate a stratified structure formed of domains of hexagonally close packed columns oriented along the confinement apex. High structural order is also indicated by CTRs oriented perpendicular to the confining surfaces. This pillar structure is assumed to be formed by columns of apolar IL alkyl side-chains embedded in a continuous phase of water-rich polar domains.

Step-wise shear experiments were performed in 400 nm and 100 nm confinement. Applying step-wise shear force at 400 nm confinement results in a decrease of XRR intensity, pointing to a deflection of sample structure. Whereas previous deflection force application was stored elastically in the material by deflection, for shear strain above $\sigma = 35 \text{ mN/mm}^2$ force relaxation is observed. The liquid crystalline structure shows viscoelastic creeping. When creeping is observed, no structural sample changes are observed anymore, XRR intensity stays constant. In a large gap of 400 nm creeping might be explained by defect translation throughout the structure above a threshold of shear strain. This mechanism requires neither gap distance for stress release, nor is deflection of structure necessary. An effect corroborated by the gap distance and X-ray intensity signal behavior. In a confinement of 100 nm, step-wise shear force application observed elastic structure deflection. The overall hexagonal structure is retained. In contrast to the larger confinement, here shear strain application of $\sigma = 50 \text{ mN/mm}^2$ leads to a squeeze out of discrete layers of $d = 3 \text{ nm}$ which can also be resolved by a decrease in XRR intensity. In a smaller confinement, less defects are present. Hence, the material can only release stress by discrete layer push out.

Also oscillatory shear measurements were performed in 400 and 100 nm confinement. During shear force application in 400 nm an increase of XRR intensity above a shear force of $F = 50 \text{ mN}$ indicates an increase of structural order within the IL. Higher shear forces of $F = 100 \text{ mN}$ however yield a drop of XRR intensity. Upon cease of shear force, a rise in XRR intensity is detected. Structural order recovers after perturbation. Similar to step-wise shearing, oscillatory shear force application enables restructuring. The threshold in oscillatory force was in the same regime with $\sigma = 50 \text{ mN/mm}^2$ as observed in step-wise shearing with $\sigma \geq 35 \text{ mN/mm}^2$. This points to the same mechanism of defect translation to the edge of the LC structure accounting of an increase in order. The observation of structure decrease at higher shear force however points to an inception to defects by mechanical stress. In 100 nm confinement, gap distance and XRR intensity oscillate in phase in a similar range of 12% and 13%, respectively. The LC domain structure is deflected by shear. Applying two consecutive cycles of shear with $F = 65 \pm 1 \text{ mN}$, the first application of shear force has an order inducing effect, XRR intensity rises over the course of shearing, whereas during the second cycle XRR intensity decreases. During the first cycle gap distance d remains constant, during the second cycle it decreases. Not only shear strain amplitude seems to have an influence, but also time of application. After going through a maximum of structural order, prolonged shear force application has a destructive effect and seems to induce defects.

The work presented provides novel insights into liquid (crystal) dynamics under molecular confinement. Results achieved can lead to a better understanding of structures formed by complex liquids and the resulting dynamics under mechanical stress. Contributions in several fields in which complex liquids see application might be possible. IL solid-liquid interfaces are an active area of research, as it is well known that the structure formed by ILs at the electrode interface directly influence device performance and durability [153, 248]. Thus, elucidating IL structure at an interface can contribute to a tailor made design of structures at interfaces. Based on the data obtained in this work, insight could be gained in catalysis, where IL structure formation in thin films can influence chemical reactions [16, 220, 221]. The influence of impurities such as water and resulting mechanical properties in confinement were probed in this work and can contribute to research on thin films formed in catalytic processes. The performance of shear experiments, complemented by structure elucidation by X-ray techniques on a molecular level, contributes to the field of microrheology. Fruitful contributions to this area of research [162, 282] are possible adding to fields such as technical lubrication but also effects observed in biological systems [51].

Chapter 15

Outlook

Future work can improve capabilities of the device. Using the existing device further results can be achieved by choosing the appropriate sample system.

A first approach for improvements of the device might be in redesigning the confining surface architecture and material selection. An ever applying requirement for the confining surfaces is atomic flat- and smoothness. However, the process of template-stripping always results in an amorphous glue layer below the smooth surface. Aggravating reflection measurements during the experiments performed in this thesis, this difficult surface structure might be avoided by developing deposition or etching techniques resulting in a single crystalline surface covered by an atomically smooth semi-transparent metal surface. Configuring the SFA in reflection geometry to achieve FECO distance measurement of gap width might also enable a different confining surface setup. Other promising results might be accessible by using different confining surface materials. Highly-ordered pyrolytic graphite (HOPG) might be used as an electrode material. Being electrically conductive and smooth, this material has shown first results being used as an SFA surface [180, 216]. It is often used as a model surface for researching on processes in Li-Ion batteries, where it serves as an electrode material. Shedding light on in-situ electrode processes when used in an electrochemical XSFA, this surface material promises interesting results. Using the confining surfaces as electrodes, electrochemical processes can be probed by the XSFA. Noble metal surfaces or their oxides promise insight into the process of ion adsorption when using an electrolyte as sample liquid. The template-stripped gold surface already contributes one noble metal surface.

This paves the way to further development of the XSFA into an electrochemical XSFA. Future improvements of the device can enable the application of an electric field across the confinement gap. Using the semi-transparent mirrors on both confining surfaces as electrodes, an electrochemical X-ray Surface Force Apparatus seems possible. Small metal stripes connected to the specific surfaces can provide the electric contact. A reference-electrode can enter the sample liquid from the side. Wiring to a potentiostat can be done via the feed-throughs in the sample cell. The build-in feed-throughs are already suitable for the required power supply. A comparable electrochemical Surface Force Apparatus has already been demonstrated by our collaboration partner M. Valtiner

[275]. An electrochemical XSFA can gain insight into surface structure changes under electrochemical processes such as corrosion or electroplating. Also, probing layered structures of molecules under the influence of an electric field might be possible. This time-resolved research on surface dynamics of electrodes would enable insights in the field of electrochemistry.

The already existing device without hardware changes can contribute further results when a suitable sample system is selected. Choosing the sample system for the XSFA is crucial. A well suited sample for the XSFA is characterized by an easily accessible signal in q -range, originating in a suitable real space orientation and length scale. Furthermore, an interesting liquid sample structure has to be present (liquid crystalline or other molecular ordering, layering, etc.), maybe being controlled by an external stimulus. In this thesis, humidity of the ambient helium atmosphere was used as an external stimulus to induce molecular structure change. The response of the sample structure to mechanical stress can lead to insight into structural properties.

Another external stimulus accessible by the XSFA might be light. Used as a trigger, light of suitable wavelength can be coupled into the beam path of the white light. A possible system whose structural properties can be altered by light are Azo-compounds. Azo-compounds with mesogene character can be switched by light to different conformations. This results in structure alteration (smectic/nematic/isotrope) that can be tracked by X-ray [107]. The question how mechanical stress influences the structure conversion is largely unresolved.

Also, polymer microemulsions are a possible system for dynamic XSFA measurements. Polymer microemulsions can be made of a homopolymer blend of immiscible polymers A and B, mediated by a blockcopolymer of AB which acts similar to a tenside. Under static conditions this ternary system exhibits a structure similar to the ILs probed in this work. The scattering signal generated by the mesoscopic bulk structure can be described by the Teubner-Strey model [32]. They feature a bicontinuous structure characterized by a periodicity d and a correlation length ξ . Dynamic measurements using a rheometer were successfully probed by X-ray scattering. Resolving the structural response in a molecular confinement might be possible. Influence of confinement effects on the dynamic properties could be probed. Microemulsions featuring ionic liquids have found to give good X-ray scattering signals [9], as well. This IL containing system might again be influenced by water absorption. Being mesoscopically structured, these liquid systems are promising candidates for dynamic measurements of the structural response to shear or compression.

A third interesting system are long-chain liquid alkanes like hexadecane [134]. They show pronounced layering upon molecular confinement. Measurements using AFM have been successful in detecting oscillatory force curves when a confinement regime of 5 nm and less applies. Also shear measurements of the structure have been performed in AFM measurements. On a single surface the structure is sheared by the AFM tip. Results point towards structure formation in a gap confinement of 10 to 20 nm between two surfaces.

A system comparable to liquid alkanes, 1-Dodecanol ($C_{12}H_{25}OH$), has already pro-

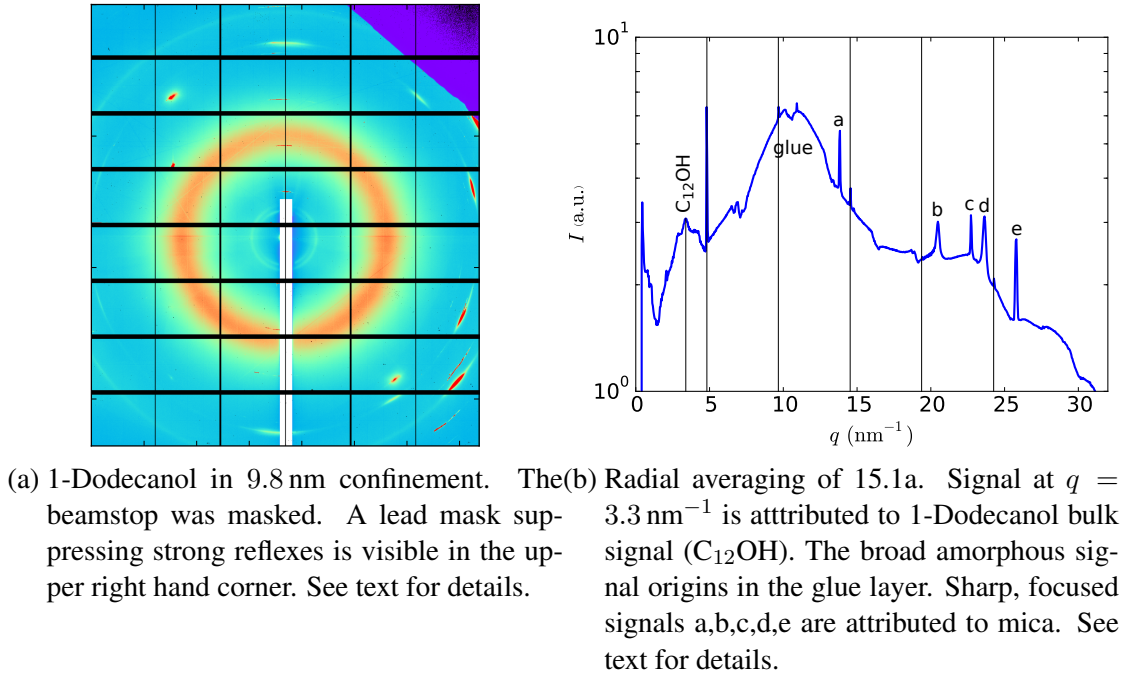


Figure 15.1: SAXS of 1-Dodecanol.

vided first results during this thesis. 1-Dodecanol has a length of $l = 1.46 \text{ nm}$ in all-trans configuration. Fig. 15.1a shows 1-Dodecanol in a confinement gap of 9.8 nm . The radial average is shown in Fig. 15.1b. Smaller confinement gaps were reached more easily for this less viscous sample. The confinement gap corresponds to about 5 molecular layers, a regime in which AFM experiments observed layering for liquid alkanes.

Besides the sample signal, several artifacts are visible. The intense uniformly distributed ring around $q = 8$ to 13 nm^{-1} is attributed to the amorphous glue. A scattering streak in horizontal direction is visible, being more pronounced on the ring. Scattering of the glue is absorbed by the confining surfaces, leading to an increased intensity in confinement gap direction where no absorptions occurs, hence this streak in horizontal direction. Intense reflexes at higher angles point to a small, highly ordered structure. The reflexes are labeled a to e in Fig. 15.1b. All these signals are sharp and focused, they do not follow confinement direction. They are attributed to the mica substrate, whose crystal structure is highly orientated, though not a single crystal.

1-Dodecanol bulk signal is visible at $q = 3.3 \text{ nm}^{-1}$. This is the most inner isotropic scattering ring marked by (C_{12}OH). This signal might origin in sample liquid before or after the confinement gap. A reflex structure in perpendicular direction to the confinement gap is visible up to the fifth order. Marked by vertical lines in the radial average its high regularity of $\Delta q = 4.82 \text{ nm}^{-1}$ is emphasized. This reciprocal length scale yields a real space length scale of about $d = 1.30 \text{ nm}$. This is just 12.5% shorter than the all-trans length of 1-Dodecanol and on a same length scale $d = 17.8 \pm 2.3 \text{ \AA}$ as observed by Ocko and coworkers [189]. There, the 1-Dodecanol film was free standing as a SAM

on a sapphire (Al_2O_3) substrate and not confined. A confinement induced freezing of 1-Dodecanol in the gap would lead to a signal as observed here: A highly periodic structure of the molecular length scale, in an orientation perpendicular to the confining surfaces. The difference of 12.5% might be explained by a tilt of the 1-Dodecanol structure in confinement. Further experiments are required to elucidate the structure formed, but the periodic signal in perpendicular direction supports the idea of a confinement induced structure. This shows that also non-liquid crystalline sample system promise to yield good results.

All in all the XSFA can form the starting point for future research in several directions. Contributions to recently developing fields of research might be gained, such as liquid crystalline dynamics, lyotropic structure dynamics or confinement induced structure dynamics. By this, contributions to a vividly developing field of interest [187] are possible. The capabilities of the device can be broadened. A solid platform to conduct further construction work was established. Nevertheless, already the existing device can yield further interesting results depending on the sample system chosen. The sample system 1-Dodecanol demonstrated that other sample systems beside liquid crystals promise interesting insights into molecular structure formation under confinement conditions.

Appendix A

Abbreviations and Acronyms

6CB	4'-n-hexyl-4-cyanobiphenyl
8CB	4'-n-octyl-4-cyanobiphenyl
AFM	Atomic Force Microscopy
ARXPS	Angle resolved X-ray Photoelectron Spectroscopy
AL	Asymmetric Lorentz
AgBe	Silverbehenic Acid
BS	Beam safety shutter
CCD camera	Charge-coupled-device camera
CTR	Crystal truncation rods
CTAB	Hexadecyltrimethylammonium Bromide
cpmU22	In-vacuum cryo-cooled undulator
CRL transfocator	Compound refractive lens transfocator
DESY	Deutsches Elektronen-Synchrotron
DHDAA	Di-hexadecyldimethylammonium Acetate
DSC	Differential Scanning Calorimetry
ESRF	The European Synchrotron Research Facility
[EA] ⁺	Ethylammonium
[FAP] ⁻	tris(pentafluoroethyl)trifluorophosphate
FS	Fast shutter
FECO	Fringes of equal chromatic order
FSDP	First Sharp Diffraction Peak
FW-line	Fisher-Widom line
FWHM	Full width at half maximum
GMSA	Generalized Mean Spherical Approximation
HEMD	High-energy micro diffraction device
HPLC	High Performance Liquid Chromatography
HOPG	Highly Oriented Pyrolytic Graphene
HWHM	Half width at half maximum
IL	Ionic Liquid

A ABBREVIATIONS AND ACRONYMS

ID-31	Insertion device 31 at the ESRF, a beamline
K-line	Kirkwood line
LC	Liquid Crystal
MD	Molecular Dynamics Simulation
MLM	Multilayer mirror
[NTf ₂] ⁻	bis(trifluoromethyl-sulfonyl)imide
[NNf ₂] ⁻	bis(nonafluorobutyl-sulfonyl)imide
OEM parts	Original equipment manufacturer parts
OMCTS	Octamethylcyclotetrasilane
OZR	Ornstein-Zernike Equation
[PA] ⁺	Propylammonium
PA	PEEK absorber
PDF	Pair Distribution Functions
PETRA III	Positron-Elektron-Tandem-Ring-Anlage III
PEEK	poly(ether) ether ketone
RDF	Radial Distribution Functions
RTIL	Room Temperature Ionic Liquid
RPM	Restricted Primitive Model
RMS	Root mean square
SAM	Self assembeled monolayer
SAS	Small Angle Scattering
SAXS	Small Angle X-ray Scattering
SANS	Small Angle Neutron Scattering
SFA	Surface Force Apparatus
SFG	Sum Frequency Generation
SLD	Scattering Length Density
SILP catalysis	Supported Ionic Liquid Phase Catalysis
SS	Slits
TEHOS	Tetrakis(2-ethlyhexoxy)silane
TTMSS	Tetrakis(trimethylsiloxo)silane
TF	Transfocator
TS	Teubner Strey
UV	Ultra violet
vdw	van der Waals
XRR	X-ray Reflectivity
XSFA	X-ray Surface Force Apparatus

Appendix B

Symbols used in equations

Elementary constants

CODATA internationally recommended values of the fundamental physical constants where taken from NIST [191].

$c = 2.9979 \cdot 10^8 \text{ ms}^{-1}$	vacuum light speed
$e = 1.6022 \cdot 10^{-19} \text{ C}$	elementary charge
$\varepsilon_0 = 8.8542 \cdot 10^{-12} \text{ Fm}^{-1}$	permittivity of free space
$\hbar = 1.0546 \cdot 10^{-34} \text{ Js}$	Planck constant $/2\pi$
$k_B = 1.3807 \cdot 10^{-23} \text{ JK}^{-1}$	Boltzmann constant
$m_e = 9.1094 \cdot 10^{-31} \text{ kg}$	electron mass
$N_A = 6.0221 \cdot 10^{23} \text{ mol}^{-1}$	Avogadro constant
$r_e = \frac{e^2}{4\pi\epsilon_0 m_e c^2} = 2.8179 \cdot 10^{-15} \text{ m}$	classical electron radius

Symbols

α	volumetric expansion coefficient
α_c	critical angle of total reflection
α_{max}	maximum angle of reflection measurements
A	amplitude
A	area
β	complex part of optical constant
b	scattering length
C	Coulomb
C_{total}	attractive forces (for example: van der Waals forces)
C_{orient}	interaction of freely rotating dipoles (Keesom interactions)
C_{ind}	interactions between induced dipoles (Debye interactions)
C_{disp}	induced dipoles in normally apolar particles (London dispersion forces)

B SYMBOLS USED IN EQUATIONS

$c(r_{\alpha,\beta})$	direct correlation between particles
D	confinement gap thickness
Δ^2	peak width (FWHM or HWHM)
δ	Dirac delta
δ	real part of optical constant
d	periodicity
d_c	length alkyl chain
ϵ	potential well depth
E	photon energy
f	atomic scattering factor
f	atomic form factor
$f'(E)$	real part of dispersion correction
$f''(E)$	imaginary part of dispersion correction
γ	correlation length
$G(r)$	oscillatory correlation function
$G(r)$	total correlation function
$g_{\alpha,\beta}$	radial distribution function (RDF)
ΔH_m	Helmholtz energy
$h(r) = g(r) - 1$	reduced pair distribution function
I_{SC}	intensity of scattered beam
I	scattered intensity
K_N	kinetic energy
$k = 2\pi/\lambda$	wave vector
K	degree Kelvin
λ'	wavelength of scattered particle
λ	wavelength of incident particle
l	length of confinement gap
μ	absorption coefficient
M	molecular mass
N	Newton
N_α	number of particles of species α
n_0	number density
$n = 1 - \delta + i\beta$	complex optical constant or refractive index
ξ	decay length
Ω	solid angle
$\omega_{\alpha,\beta}$	potential energy between particle α and β
q_α	charge of particle α
q_c	wave vector transfer at critical angle
$q = k - k'$	wave vector transfer
q_0^2	peak position
ϕ	phase factor
p	pressure
ρ	mass density

ρ_m	mass density
ρ_e	electron density
R_F	Fresnel reflectivity
rh	relative humidity
$r_{\alpha,\beta}$	interatomic distance between particle α and β
σ	root mean square (rms) roughness
$\sigma = V/d$	projected area
σ	particle distance at which inter-particle potential is zero
$d\sigma/d\Omega$	differential scattering cross section
ΔS_m	melting entropy
ΔS_f	entropy of fusion
$S(q)$	scattering amplitude
$S(q)$	liquid structure factor
$S_{TS}(q)$	structure factor Teubner Strey
Θ_0	flux of incident beam
θ	phase angle
2θ	scattering angle
T_m	melting point
t	time
$t_{Al_2O_3}$	thickness Korund substrate
t_{Au}	thickness of gold layer
t_{epoxy}	thickness of epoxy glue layer
t_{mica}	thickness of mica sheet
t_{Ag}	thickness of silver layer
$ V_N $	potential energy
V_m	molecular volume
V	confined volume
w	width of confinement gap
wt%	weight percent
$\chi_\gamma = N_\gamma/N$	direct correlation between particles
χ_j	transition coefficient of jth interface
z	number of electrons in an atom

Appendix C

Appendix

C.0.3 Small-Angle X-ray Scattering Measurements of hydrophobic ILs used at different temperatures

Corresponding Small-Angle X-ray Scattering Measurements to Fig. 8.2 of the hydrophobic Ionic Liquids used in Sec. 8.

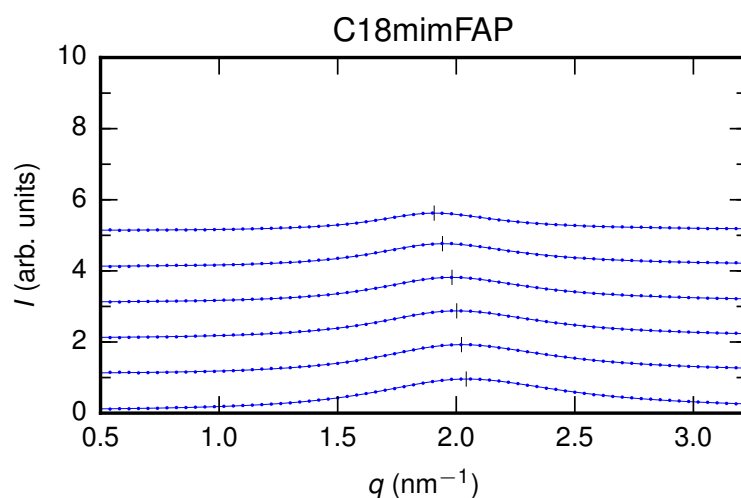


Figure C.1: Comparison of SAXS signals between 40° C and 100° C for [C₁₈C₁im]⁺[FAP]⁻. Vertical lines indicate the peak maximum q₀. Solid lines are fits to the Teubner-Strey model. Curves are vertically shifted by 1 unit.

Figure C.2: Comparison of SAXS signals between 60° C and 100° C for $[\text{C}_{18}\text{C}_1\text{im}]^+[\text{NNf}_2]^-$. Vertical lines indicate the peak maximum q_0 . Solid lines are fits to the Teubner-Strey model. Curves are vertically shifted by 1 unit.

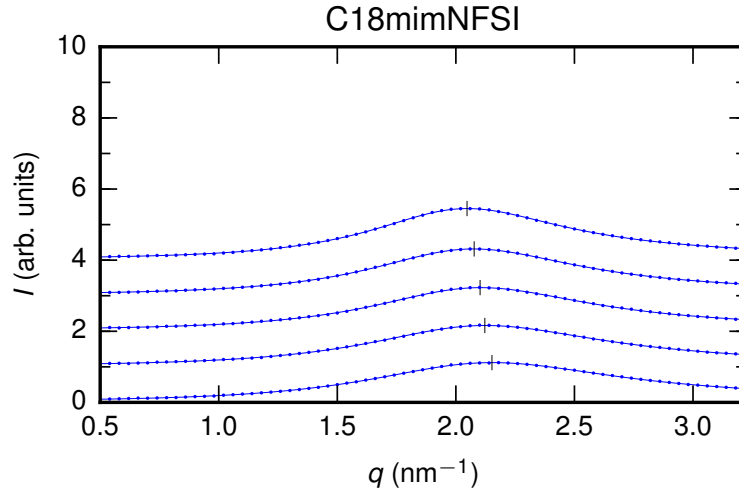
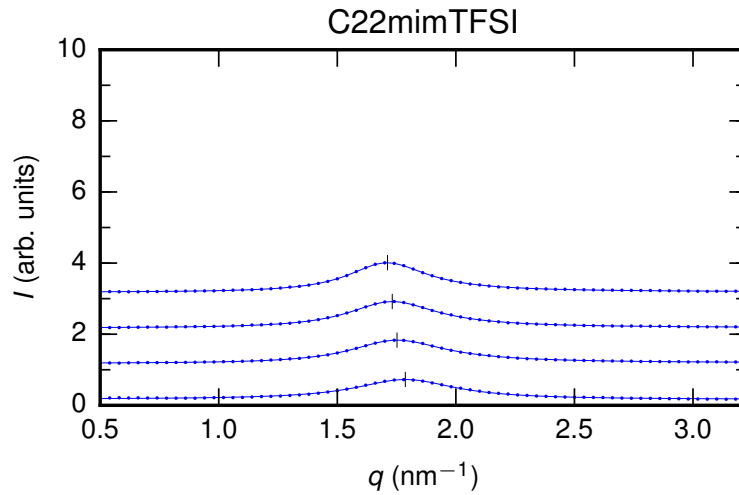


Figure C.3: Comparison of SAXS signals between 70° C and 100° C for $[\text{C}_{22}\text{C}_1\text{im}]^+[\text{NTf}_2]^-$. Vertical lines indicate the peak maximum q_0 . Solid lines are fits to the Teubner-Strey model. Curves are vertically shifted by 1 unit.



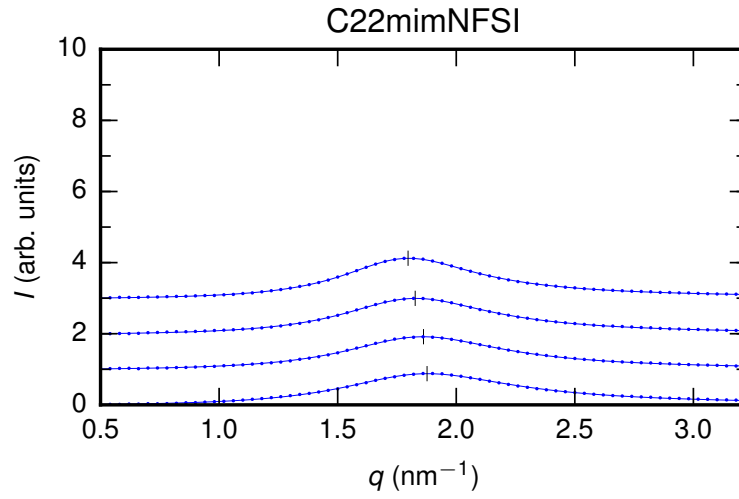
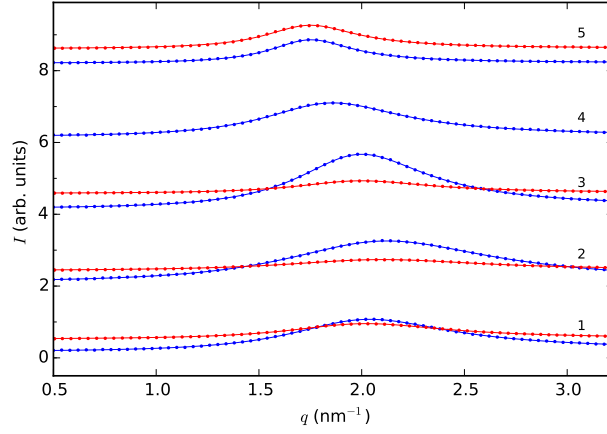


Figure C.4: Comparison of SAXS signals between 70°C and 100°C for $[\text{C}_{22}\text{C}_{1}\text{im}]^+ [\text{NNf}_2]^-$. Vertical lines indicate the peak maximum q_0 . Solid lines are fits to the Teubner-Strey model. Curves are vertically shifted by 1 unit.

C.0.4 Comparison of SAXS and SANS data at 90 degree Celsius

Figure C.5: Comparison of SAXS (blue) and SANS (red) patterns $I(q)$ of $[\text{C}_{18}\text{C}_1\text{im}]^+ [\text{FAP}]^-$ (1), $[\text{C}_{18}\text{C}_1\text{im}]^+ [\text{NNf}_2]^-$ (2), $[\text{C}_{18}\text{C}_1\text{im}]^+ [\text{NTf}_2]^-$ (3), $[\text{C}_{22}\text{C}_1\text{im}]^+ [\text{NNf}_2]^-$ (4), $[\text{C}_{22}\text{C}_1\text{im}]^+ [\text{NTf}_2]^-$ (5) at 90 degree Celsius. Solid lines are fits to the Teubner-Strey model. Curves for different ILs are vertically shifted by 2 units for clarity.



Bibliography

- [1] F. F. Abraham. The Interfacial Density Profile of a Lennard-Jones Fluid in Contact with a (100) Lennard-Jones Wall and its Relationship to Idealized Fluid/Wall Systems: A Monte Carlo Simulation. *J. Chem. Phys.*, 68(8):3713–3716, 1978.
- [2] J. Als-Nielsen and D. McMorrow. *Elements of Modern X-ray Physics*. John Wiley & Sons, 2011.
- [3] N. Anjum, M.-A. Guedeau-Boudeville, C. Stubenrauch, and A. Mourchid. Phase Behavior and Microstructure of Microemulsions Containing the Hydrophobic Ionic Liquid 1-Butyl-3-methylimidazolium Hexafluorophosphate. *J. Phys. Chem. B*, 113:239, 2009.
- [4] H. V. Annapureddy, Z. Hu, J. Xia, and C. J. Margulis. How does Water Affect the Dynamics of the Room-Temperature Ionic Liquid 1-Hexyl-3-methylimidazolium Hexafluorophosphate and the Fluorescence Spectroscopy of Coumarin-153 When Dissolved in it? *J. Phys. Chem. B*, 112(6):1770–1776, 2008.
- [5] H. V. R. Annapureddy, H. K. Kashyap, P. M. D. Biase, and C. J. Margulis. What is the Origin of the Prepeak in the X-ray Scattering of Imidazolium-Based Room-Temperature Ionic Liquids? *J. Phys. Chem. B*, 114:16838, 2010.
- [6] J. C. Araque, R. P. Daly, and C. J. Margulis. A Link Between Structure, Diffusion and Rotations of Hydrogen Bonding Tracers in Ionic Liquids. *J. Chem. Phys.*, 144(20):204504, 2016.
- [7] J. C. Araque, J. J. Hettige, and C. J. Margulis. Modern Room Temperature Ionic Liquids, a Simple Guide to Understanding Their Structure and How It May Relate to Dynamics. *J. Phys. Chem. B*, 119:12727–12740, 2015.
- [8] M. Armand, F. Endres, D. R. MacFarlane, H. Ohno, and B. Scrosati. Ionic-Liquid Materials for the Electrochemical Challenges of the Future. *Nat. Mater.*, 8(8):621–629, July 2009.
- [9] R. Atkin and G. G. Warr. Phase Behavior and Microstructure of Microemulsions with a Room-Temperature Ionic Liquid as the Polar Phase. *J. Phys. Chem. B*, 111(31):9309–9316, 2007.

BIBLIOGRAPHY

- [10] R. Atkin and G. G. Warr. Structure in Confined Room-Temperature Ionic Liquids. *J. Phys. Chem. C*, 111(13):5162–5168, 2007.
- [11] A. Balducci, R. Dugas, P. Taberna, P. Simon, D. Plee, M. Mastragostino, and S. Passerini. High Temperature Carbon-Carbon Supercapacitor using Ionic Liquid as Electrolyte. *J. Power Sources*, 165:922–927, 2007.
- [12] T. E. Balmer. *Resolving Structural and Dynamical Properties in nano-confined Fluids*. Dissertation, ETH Zürich, September 2007.
- [13] T. Becker. *Collapse Dynamics of Confined Liquid Films*. PhD thesis, University of Twente, 2005.
- [14] Q. Berrod, F. Ferdeghini, J.-M. Zanotti, P. Judeinstein, D. Lairez, V. G. Sakai, O. Czakkel, P. Fouquet, and D. Constantin. Ionic liquids: Evidence of the Viscosity Scale-Dependence. *Sci. Rep.*, 7, 2017.
- [15] B. Bhargava and M. L. Klein. Molecular Dynamics Studies of Cation Aggregation in the Room Temperature Ionic Liquid [C₁₀mim][Br] in aqueous Solution. *J. Phys. Chem. A*, 113(10):1898–1904, 2008.
- [16] K. Bica, P. Gärtner, P. J. Gritsch, A. K. Ressmann, C. Schröder, and R. Zirbs. Micellar Catalysis in aqueous–Ionic Liquid Systems. *Chem. Commun.*, 48(41):5013–5015, 2012.
- [17] J. M. Black, D. Walters, A. Labuda, G. Feng, P. C. Hillesheim, S. Dai, P. T. Cummings, S. V. Kalinin, R. Proksch, and N. Balke. Bias-dependent molecular-level Structure of Electrical Double Layer in Ionic Liquid on Graphite. *Nano Lett.*, 13(12):5954–5960, 2013.
- [18] R. Boehmer, C. Gainaru, and R. Richert. Structure and Dynamics of Monohydroxy Alcohols—milestones towards their microscopic Understanding, 100 Years after Debye. *Phys. Rep.*, 545:125–195, 2014.
- [19] P. Bonhote, A.-P. Dias, N. Papageorgiou, K. Kalyanasundaram, and M. Grätzel. Hydrophobic, highly Conductive ambient-temperature Molten Salts. *Inorg. Chem.*, 35(5):1168–1178, 1996.
- [20] I. Bou-Malham and L. Bureau. Nanoconfined Ionic Liquids: Effect of Surface Charges on Flow and Molecular Layering. *Soft Matter*, 6(17):4062–4065, 2010.
- [21] J. Bowers, C. P. Butts, P. J. Martin, M. C. Vergara-Gutierrez, and R. K. Heenan. Aggregation Behavior of Aqueous Solutions of Ionic Liquids. *Langmuir*, 20(6):2191–2198, 2004.
- [22] C. J. Bowlas, D. W. Bruce, and K. R. Seddon. Liquid-Crystalline Ionic Liquids. *Chem. Commun.*, -(14):1625–1626, 1996.

- [23] A. E. Bradley, C. Hardacre, J. D. Holbrey, S. Johnston, S. E. J. McMath, and M. Nieuwenhuizen. Small-Angle X-ray Scattering Studies of Liquid Crystalline 1-Alkyl-3-methylimidazolium Salts. *Chem. Mat.*, 14:629, 2002.
- [24] K. Breitsprecher, K. Szuttor, and C. Holm. Electrode Models for Ionic Liquid-based Capacitors. *J. Phys. Chem. C*, 119(39):22445–22451, 2015.
- [25] H.-J. Butt, B. Cappella, and M. Kappl. Force Measurements with the Atomic Force Microscope: Technique, Interpretation and Applications. *Surf. Sci. Rep.*, 59(1):1–152, 2005.
- [26] H.-J. Butt, K. Graf, and M. Kappl. *Physics and Chemistry of Interfaces*, volume 2. Wiley-VH, 2003.
- [27] S. Całus, M. Busch, A. V. Kityk, W. Piecek, and P. Huber. Chiral Phases of a Confined Cholesteric Liquid Crystal: Anchoring-dependent Helical and Smectic Self-assembly in Nanochannels. *J. Phys. Chem. C*, 120(21):11727–11738, 2016.
- [28] S. Całus, B. Jabłońska, M. Busch, D. Rau, P. Huber, and A. V. Kityk. Paranematic-to-Nematic Ordering of a Binary Mixture of Rodlike Liquid Crystals Confined in Cylindrical Nanochannels. *Phys. Rev. E*, 89(6):062501, 2014.
- [29] R. Caminiti and L. Gontrani. *The Structure of Ionic Liquids*, volume 193. Springer, 2014.
- [30] J. N. Canongia Lopes, J. Deschamps, and A. A. Pádua. Modeling Ionic Liquids Using a Systematic All-Atom Force Field. *J. Phys. Chem. B*, 108(6):2038–2047, 2004.
- [31] F. F. Canova, H. Matsubara, M. Mizukami, K. Kurihara, and A. L. Shluger. Shear Dynamics of Nanoconfined Ionic Liquids. *Phys. Chem. Chem. Phys.*, 16(18):8247–8256, 2014.
- [32] F. E. Caputo, W. R. Burghardt, K. Krishnan, F. S. Bates, and T. P. Lodge. Time-resolved Small-Angle X-ray Scattering Measurements of a Polymer Bicontinuous Microemulsion Structure Factor Under Shear. *Phys. Rev. E*, 66(4):041401, 2002.
- [33] E. W. Castner Jr, J. F. Wishart, and H. Shirota. Intermolecular Dynamics, Interactions, and Solvation in Ionic Liquids. *Acc. Chem. Res.*, 40(11):1217–1227, 2007.
- [34] T. Chemicals. *Materials Safety Data Sheet C₁₀mimCl*. TCI-Chemicals, 2017.
- [35] T. Chemicals. *Materials Safety Data Sheet C₈mimCl*. TCI-Chemicals, 2017.

BIBLIOGRAPHY

- [36] H.-W. Cheng, J.-N. Dienemann, P. Stock, C. Merola, Y.-J. Chen, and M. Valtiner. The Effect of Water and Confinement on Self-Assembly of Imidazolium Based Ionic Liquids at Mica Interfaces. *Sci. Rep.*, 6, 2016.
- [37] H.-W. Cheng, P. Stock, B. Moeremans, T. Baimpos, X. Banquy, F. U. Renner, and M. Valtiner. Characterizing the Influence of Water on Charging and Layering at Electrified Ionic-Liquid/Solid Interfaces. *Adv. Mat. int.*, 2(12), 2015.
- [38] H.-W. Cheng, H. Weiss, P. Stock, Y.-J. Chen, C. R. Reinecke, J.-N. Dienemann, M. Mezger, and M. Valtiner. The Effect of Concentration on the Interfacial and Bulk Structure of Ionic Liquids in Aqueous Solution. *Langmuir*, 2018.
- [39] J. S. Chickos, W. E. Acree, Jr., and J. F. Liebman. Estimating Solid-Liquid Phase Change Enthalpies and Entropies. *J. Phys. Chem. Ref. Data*, 28(6):1535–1673, 1999.
- [40] H. K. Christenson. Experimental Measurements of Solvation Forces in Nonpolar Liquids. *J. Chem. Phys.*, 78(11):6906–6913, 1983.
- [41] W. H. De Jeu. *Basic X-ray Scattering for Soft Matter*. Oxford University Press, 2016.
- [42] J. De Roche, C. M. Gordon, C. T. Imrie, M. D. Ingram, A. R. Kennedy, F. L. Celso, and A. Triolo. Application of Complementary Experimental Techniques to Characterization of the Phase Behavior of [C₁₆mim][PF₆] and [C₁₄mim][PF₆]. *Chem. Mat*, 15:9, 2003.
- [43] W. M. de Vos, L. L. Mears, R. M. Richardson, T. Cosgrove, R. M. Dalgliesh, and S. W. Prescott. Measuring the Structure of Thin Soft Matter Films under Confinement: a Surface-Force Type Apparatus for Neutron Reflection, Based on a Flexible Membrane Approach. *Rev. Sci. Instrum.*, 83(11):113903, 2012.
- [44] R. E. Del Sesto, T. M. McCleskey, C. Macomber, K. C. Ott, A. T. Koppisch, G. A. Baker, and A. K. Burrell. Limited Thermal Stability of Imidazolium and Pyrrolidinium Ionic Liquids. *Thermochim. Acta*, 491(1):118–120, 2009.
- [45] A. L. Demirel and S. Granick. Glasslike Transition of a Confined Simple Fluid. *Phys. Rev. Lett.*, 77(11):2261, 1996.
- [46] I. Denicolo, J. Doucet, and A. F. Craievich. X-ray Study of the Rotator Phase of Paraffins (iii): Even-numbered Paraffins C₁₈H₃₈, C₂₀H₄₂, C₂₂H₄₆, C₂₄H₅₀, and C₂₆H₅₄. *J. Chem. Phys.*, 78(3):1465–1469, 1983.
- [47] D. D. Desmarteau and M. Witz. N-fluoro-bis (trifluoromethanesulfonyl) imide. An Improved Synthesis. *J. Fluorine Chem.*, 52(1):7–12, 1991.

- [48] A. Deyko, T. Cremer, F. Rietzler, S. Perkin, L. Crowhurst, T. Welton, H.-P. Steinrueck, and F. Maier. Interfacial Behavior of Thin Ionic Liquid Films on Mica. *J. Phys. Chem. C*, 117(10):5101–5111, 2013.
- [49] M. Díaz, A. Ortiz, and I. Ortiz. Progress in the Use of Ionic Liquids as Electrolyte Membranes in Fuel Cells. *J. Membr. Sci.*, 469:379–396, 2014.
- [50] A. Doerr, M. Tolan, T. Seydel, and W. Press. The Interface Structure of Thin Liquid Hexane Films. *Physica B: Condensed Matter*, 248(1):263–268, 1998.
- [51] H. Du, C. Kim, M. Corradini, R. Ludescher, and M. Rogers. Micro-viscosity of Liquid Oil Confined in Colloidal Fat Crystal Networks. *Soft Matter*, 10(43):8652–8658, 2014.
- [52] M. J. Earle, J. M. Esperanca, M. A. Gilea, J. N. C. Lopes, L. P. Rebelo, J. W. Magee, K. R. Seddon, and J. A. Widegren. The Distillation and Volatility of Ionic Liquids. *Nature*, 439:831, 2006.
- [53] T. Egami and S. J. Billinge. *Underneath the Bragg Peaks: Structural Analysis of Complex Materials*, volume 16. Elsevier, 2003.
- [54] R. Evans and R. Leote de Carvalho. Decay of Correlations in Bulk Fluids and at Interfaces: A Density-Functional Perspective. In *ACS Symposium Series*, volume 629 of *ACS Symposium Series*, chapter 12, pages 166 – 184. ACS Publications, 1996.
- [55] T. A. Ezquerra, M. C. Garcia-Gutierrez, A. Nogales, and M. Gomez. *Applications of Synchrotron Light to Scattering and Diffraction in Materials and Life Sciences*, volume 776. Springer, 2009.
- [56] R. Feidenhans'l. Surface Structure Determination by X-ray Diffraction. *Surf. Sci. Rep.*, 10(3):105–188, 1989.
- [57] A. V. Feoktystov, H. Frielinghaus, Z. Di, S. Jaksch, V. Pipich, M.-S. Apavou, E. Babcock, R. Hanslik, R. Engels, G. Kemmerling, H. Kleines, A. Ioffe, D. Richter, and T. Brueckel. KWS-1 High-Resolution Small-Angle Neutron Scattering Instrument at JCNS: Current State. *J. Appl. Crystallogr.*, 48:61–70, 2015.
- [58] M. A. Firestone, J. A. Dzielawa, P. Zapol, L. A. Curtiss, S. Seifert, and M. L. Dietz. Lyotropic Liquid-Crystalline Gel Formation in a Room-temperature Ionic Liquid. *Langmuir*, 18(20):7258–7260, 2002.
- [59] M. A. Firestone, P. G. Rickert, S. Seifert, and M. L. Dietz. Anion Effects on Ionogel Formation in N,N'-Dialkylimidazolium-based Ionic Liquids. *Inorg. Chim. Acta*, 357:3991–3998, 2004.
- [60] M. E. Fisher and B. Wiodm. Decay of Correlations in Linear Systems. *J. Chem. Phys.*, 50(9):3756–3772, 1969.

BIBLIOGRAPHY

- [61] B. D. Fitchett and J. C. Conboy. Structure of the Room-temperature Ionic Liquid/SiO₂ Interface Studied by Sum-Frequency Vibrational Spectroscopy. *J. Phys. Chem. B*, 108(52):20255–20262, 2004.
- [62] J. Foropoulos Jr and D. D. DesMarteau. Synthesis, Properties, and Reactions of bis ((trifluoromethyl) sulfonyl) imide,(CF₃SO₂)₂ NH¹. *Inorg. Chem.*, 23(23):3720–3723, 1984.
- [63] M. Freemantle. Designer Solvents: Ionic Liquids May Boost Clean Technology Development. *Chem. Eng. News*, 76(13):32–37, 1998.
- [64] M. G. Freire, C. M. Neves, I. M. Marrucho, J. A. Coutinho, and A. M. Fernandes. Hydrolysis of Tetrafluoroborate and Hexafluorophosphate Counter Ions in Imidazolium-based Ionic Liquids. *J. Phys. Chem. A*, 114(11):3744–3749, 2009.
- [65] K. Fujii, R. Kanzaki, T. Takamuku, Y. Kameda, S. Kohara, M. Kanakubo, M. Shibayama, S. ichi Ishiguro, , and Y. Umebayashi. Experimental Evidences for Molecular Origin of Low-q Peak in Neutron/X-ray Scattering of 1-alkyl-3-methylimidazolium Bis(trifluoromethanesulfonyl)amide Ionic Liquids. *J. Chem. Phys.*, 135(24), 2011.
- [66] K. Fujii, S. Koharab, and Y. Umebayashi. Relationship between Low-q Peak and Long-range Ordering of Ionic Liquids Revealed by High-Energy X-ray Total Scattering. *Phys. Chem. Chem. Phys.*, 17:17838–17843, 2015.
- [67] Y. Gambin, G. Massiera, L. Ramos, C. Ligoure, and W. Urbach. Bounded Step Superdiffusion in an Oriented Hexagonal Phase. *Physical review letters*, 94(11):110602, 2005.
- [68] Y. Gan. Atomic and Subnanometer Resolution in ambient Conditions by Atomic Force Microscopy. *Surf. Sci. Rep.*, 64(3):99–121, 2009.
- [69] M. N. Garaga, V. Dracopoulos, U. Werner-Zwanziger, J. W. Zwanziger, M. Maréchal, M. Persson, L. Nordstierna, and A. Martinelli. A Long-Chain Protic Ionic Liquid inside Silica Nanopores: Enhanced Proton Mobility due to Efficient Self-Assembly and Decoupled Proton Transport. *Nanoscale*, 2018.
- [70] L. Garcia, L. Jacquot, E. Charlaix, and B. Cross. Nanomechanics of Ionic Liquids at Dielectric and Metallic Interfaces. *Faraday Discuss.*, 2017.
- [71] M. A. Gebbie, M. Valtiner, X. Banquy, E. T. Fox, W. A. Henderson, and J. N. Israelachvili. Ionic Liquids Behave as Dilute Electrolyte Solutions. *PNAS*, 110(24):9674–9679, 2013.
- [72] H. Gojzewski, M. Kappl, A. Ptak, and H.-J. Butt. Effect of Humidity on Nanoscale Adhesion on Self-assembled Thiol Monolayers Studied by Dynamic Force Spectroscopy. *Langmuir*, 26(3):1837–1847, 2009.

- [73] Y. Golan, A. Martin-Herranz, Y. Li, C. R. Safinya, and J. Israelachvili. Direct Observation of Shear-induced Orientational Phase Coexistence in a Lyotropic System Using a Modified X-ray Surface Forces Apparatus. *Phys. Rev. Lett.*, 86(7):1263, 2001.
- [74] Y. Golan, M. Seitz, C. Luo, A. Martin-Herranz, M. Yasa, Y. Li, C. R. Safinya, and J. Israelachvili. The X-ray Surface Forces Apparatus for Simultaneous X-ray Diffraction and Direct Normal and Lateral Force Measurements. *Rev. Sci. Instrum.*, 73(6):2486–2488, 2002.
- [75] J. W. Goodby. The Nanoscale Engineering of Nematic Liquid Crystals for Displays. *Liq. Cryst.*, 38(11-12):1363–1387, 2011.
- [76] C. M. Gordon, J. D. Holbrey, A. R. Kennedy, and K. R. Seddon. Ionic Liquid Crystals: Hexafluorophosphate Salts. *J. Mater. Chem.*, 8:2627, 1998.
- [77] S. Granick. Motions and Relaxations of Confined Liquids. *Science*, 253(5026):1374, 1991.
- [78] T. L. Greaves, D. F. Kennedy, A. Weerawardena, N. M. Tse, N. Kirby, and C. J. Drummond. Nanostructured Protic Ionic Liquids Retain Nanoscale Features in Aqueous Solution while Precursor brønsted Acids and Bases Exhibit Different Behavior. *J. Phys. Chem. B*, 115(9):2055–2066, 2011.
- [79] K. E. Gutowski, G. A. Broker, H. D. Willauer, J. G. Huddleston, R. P. Swatloski, J. D. Holbrey, and R. D. Rogers. Controlling the Aqueous Miscibility of Ionic Liquids: Aqueous Biphasic Systems of Water-miscible Ionic Liquids and Water-structuring Salts for Recycle, Metathesis, and Separations. *J. Am. Chem. Soc.*, 125(22):6632–6633, 2003.
- [80] W. Hamilton, G. Smith, N. Alcantar, J. Majewski, R. Toomey, and T. Kuhl. Determining the Density Profile of Confined Polymer Brushes with Neutron Reflectivity. *J. Polym. Sci., Part B: Polym. Phys.*, 42(17):3290–3301, 2004.
- [81] W. Han and S. Lindsay. Probing Molecular Ordering at a Liquid-solid Interface with a Magnetically Oscillated Atomic Force Microscope. *Appl. Phys. Lett.*, 72(13):1656–1658, 1998.
- [82] C. Hanke, N. Atamas, and R. Lynden-Bell. Solvation of Small Molecules in Imidazolium Ionic Liquids: A Simulation Study. *Green Chemistry*, 4(2):107–111, 2002.
- [83] C. Hanke, A. Johansson, J. Harper, and R. Lynden-Bell. Why are Aromatic Compounds More Soluble than Aliphatic Compounds in Dimethylimidazolium Ionic Liquids? A Simulation Study. *Chem. Phys. Lett.*, 374(1):85–90, 2003.

BIBLIOGRAPHY

- [84] J.-P. Hansen and I. McDonald. *Theory of Simple Liquids*. Academic Press, 3rd edition, 2006.
- [85] H. Hansen-Goos and J. Wettlaufer. Theory of Ice Premelting in Porous Media. *Phys. Rev. E*, 81(3):031604, 2010.
- [86] C. Hardacre, J. D. Holbrey, P. B. McCormac, S. J. McMath, M. Nieuwenhuyzen, and K. R. Seddon. Crystal and Liquid Crystalline Polymorphism in 1-alkyl-3-methylimidazolium Tetrachloropalladate (II) Salts. *J. Mater. Chem.*, 11(2):346–350, 2001.
- [87] C. Hardacre, J. D. Holbrey, C. L. Mullan, T. G. A. Youngs, and D. T. Bowron. Small Angle Neutron Scattering from 1-alkyl-3-methylimidazolium Hexafluorophosphate Ionic Liquids ($[C_n\text{mim}][\text{PF}_6]$, $n=4, 6$, and 8). *J. Chem. Phys.*, 133(074510-1), 2010.
- [88] R. Hayes, S. Z. El Abedin, and R. Atkin. Pronounced Structure in Confined Aprotic Room-temperature Ionic Liquids. *J. Phys. Chem. B*, 113(20):7049–7052, 2009.
- [89] R. Hayes, S. Imberti, G. G. Warr, and R. Atkin. Effect of Cation Alkyl Chain Length and Anion Type on Protic Ionic Liquid Nanostructure. *JPCC*, 118:13998–14008, 2014.
- [90] R. Hayes, G. G. Warr, and R. Atkin. At the Interface: Solvation and Designing Ionic Liquids. *Phys. Chem. Chem. Phys.*, 12(8):1709–1723, 2010.
- [91] R. Hayes, G. G. Warr, and R. Atkin. Structure and Nanostructure in Ionic Liquids. *Chem. Rev.*, 115:6357–6426, 2015.
- [92] M. Hegner, P. Wagner, and G. Semenza. Ultralarge Atomically Flat Template-stripped Au Surfaces for Scanning Probe Microscopy. *Surf. Sci.*, 291(1-2):39–46, 1993.
- [93] M. S. Hellsing, A. R. Rennie, and A. V. Hughes. Adsorption of Aerosol-OT to Sapphire: Lamellar Structures Studied with Neutrons. *Langmuir*, 27:4669, 2011.
- [94] J. J. Hettige, H. K. Kashyap, H. V. R. Annapureddy, and C. J. Margulis. Anions, the Reporters of Structure in Ionic Liquids. *J. Phys. Chem. Lett.*, 4:105–110, 2013.
- [95] M. Heuberger, M. Zäch, and N. Spencer. Density Fluctuations under Confinement: When is a Fluid not a Fluid? *Science*, 292(5518):905–908, 2001.
- [96] J. D. Holbrey and K. R. Seddon. The Phase Behaviour of 1-Alkyl-3-methylimidazolium Tetrafluoroborates; Ionic Liquids and Ionic Liquid Crystals. *Dalton Trans.*, page 2133, 1999.

-
- [97] V. Honkimäki, H. Reichert, J. Okasinski, and H. Dosch. X-ray Optics for Liquid Surface/Interface Spectrometers. *J. Synchrotron Radiat.*, 13(6):426–431, 2006.
- [98] R. Horn, D. Evans, and B. Ninham. Double-layer and Solvation Forces Measured in a Molten Salt and its Mixtures with Water. *J. Phys. Chem.*, 92(12):3531–3537, 1988.
- [99] R. G. Horn and J. N. Israelachvili. Direct Measurement of Structural Forces between two Surfaces in a Nonpolar Liquid. *J. Chem. Phys.*, 75(3):1400–1411, 1981.
- [100] M. Hoskin. Orientations of Neolithic Monuments of Brittany: (2) the Early Dolmens. *JHA*, 38(4):487–492, 2007.
- [101] P. Huber. Soft Matter in Hard Confinement: Phase Transition Thermodynamics, Structure, Texture, Diffusion and Flow in nanoporous Media. *J. Phys.: Condens. Matter*, 27(10):103102, 2015.
- [102] J. G. Huddleston, A. E. Visser, W. M. Reichert, H. D. Willauer, G. A. Broker, and R. D. Rogers. Characterization and Comparison of Hydrophilic and Hydrophobic Room Temperature Ionic Liquids Incorporating the Imidazolium Cation. *Green chemistry*, 3(4):156–164, 2001.
- [103] W. J. Huisman, J. Peters, J. Derks, H. Ficke, D. Abernathy, and J. Van Der Veen. A New X-ray Diffraction Method for Structural Investigations of Solid-liquid Interfaces. *Rev. Sci. Instrum.*, 68(11):4169–4176, 1997.
- [104] S. Idziak, I. Koltover, K. Liang, J. Israelachvili, and C. Safinya. Study of Flow in a Smectic Liquid Crystal in the X-ray Surface Forces Apparatus. *Int. J. Thermophys.*, 16(2):299–307, 1995.
- [105] S. H. Idziak, I. Koltover, J. N. Israelachvili, and C. R. Safinya. Structure in a Confined Smectic Liquid Crystal with Competing Surface and Sample Elasticities. *Phys. Rev. Lett.*, 76(9):1477, 1996.
- [106] S. H. Idziak, C. R. Safinya, R. S. Hill, K. E. Kraiser, M. Ruths, H. E. Warriner, S. Steinberg, K. S. Liang, J. N. Israelachvili, et al. The X-ray Surface Forces Apparatus: Structure of a Thin Smectic Liquid Crystal Film under Confinement. *Science*, pages 1915–1915, 1994.
- [107] T. Ikeda, O. Tsutsumi, et al. Optical Switching and Image Storage by Means of Azobenzene Liquid-crystal Films. *Science*, pages 1873–1873, 1995.
- [108] J. Israelachvili. Thin Film Studies using Multiple-beam Interferometry. *J. Colloid Interface Sci.*, 44(2):259–272, 1973.

BIBLIOGRAPHY

- [109] J. Israelachvili, Y. Min, M. Akbulut, A. Alig, G. Carver, W. Greene, K. Kristiansen, E. Meyer, N. Pesika, K. Rosenberg, and H. Zeng. Recent Advances in the Surface Forces Apparatus (SFA) Technique. *Rep. Prog. Phys.*, 73, 2010.
- [110] J. N. Israelachvili. *Intermolecular and Surface Forces*. Academic press, 2015.
- [111] J. N. Israelachvili, N. A. Alcantar, N. Maeda, T. E. Mates, and M. Ruths. Preparing Contamination-free Mica Substrates for Surface Characterization, Force Measurements, and Imaging. *Langmuir*, 20(9):3616–3622, 2004.
- [112] Y.-R. Jang, J.-M. Kim, J.-H. Lee, S.-J. Cho, G. Kim, Y.-W. Ju, S.-H. Yeon, J. Yoo, and S.-Y. Lee. Molecularly Designed, Dual-doped Mesoporous Carbon/SWCNT Nanoshields for Lithium Battery Electrode Materials. *J. Mater. Chem. A*, 4(39):14996–15005, 2016.
- [113] W. Jiang, Y. Wang, and G. A. Voth. Molecular Dynamics Simulation of Nanostructural Organization in Ionic Liquid/Water Mixtures. *J. Phys. Chem. B*, 111(18):4812–4818, 2007.
- [114] A. Jiménez, M. Bermudez, P. Iglesias, F. Carrión, and G. Martínez-Nicolás. 1-n-alkyl-3-methylimidazolium Ionic Liquids as Neat Lubricants and Lubricant Additives in Steel–Aluminium Contacts. *Wear*, 260(7):766–782, 2006.
- [115] P. B. Johnson and R.-W. Christy. Optical Constants of the Noble Metals. *Phys. Rev. B*, 6(12):4370, 1972.
- [116] J. E. Jones. On the Determination of Molecular Fields. I. From the Variation of the Viscosity of a Gas with Temperature. In *Proceedings of the Royal Society of London A: Mathematical, Physical and Engineering Sciences*, volume 106, pages 441–462. The Royal Society, 1924.
- [117] V. M. Kaganer. Crystal Truncation Rods in Kinematical and Dynamical X-ray Diffraction Theories. *Phys. Rev. B*, 75(24):245425, 2007.
- [118] A. E. Kai Schwenzfeier, Markus Valtiner. SFA-Explorer, July 2017.
- [119] E. K. Kashyap, C. S. Santos, H. V. Annapureddy, S. N. Murthy, C. J. Margulis, and E. W. J. Castner. Temperature-dependent Structure of Ionic Liquids: X-ray Scattering and Simulations. *Faraday Discuss.*, 154:133, 2012.
- [120] H. K. Kashyap, J. J. Hettige, H. V. Annapureddy, and C. J. Margulis. SAXS Anti-peaks Reveal the Length-scales of Dual Positive–Negative and Polar–Apolar Ordering in Room-temperature Ionic Liquids. *Chem. Commun.*, 48(42):5103–5105, 2012.

- [121] H. K. Kashyap, C. S. Santos, N. S. Murthy, J. J. Hettige, K. Kerr, S. Ramati, J. Gwon, M. Gohdo, S. I. Lall-Ramnarine, J. F. Wishart, et al. Structure of 1-alkyl-1-methylpyrrolidinium bis (trifluoromethylsulfonyl) amide Ionic Liquids with Linear, Branched, and Cyclic Alkyl Groups. *J. Phys. Chem. B*, 117(49):15328–15337, 2013.
- [122] J. Kieffer and D. Karkoulis. PyFAI, a Versatile Library for Azimuthal Regrouping. In *Journal of physics: conference series*, volume 425, page 202012. IOP Publishing, 2013.
- [123] A. Kienzle, S. Kurch, J. Schlöder, C. Berges, R. Ose, J. Schupp, A. Tuettenberg, H. Weiss, J. Schultze, S. Winzen, M. Schinnerer, K. Koynov, M. Mezger, N. Haass, W. Tremel, and H. Jonuleit. Dendritic Mesoporous Silica Nanoparticles for pH-Stimuli-Responsive Drug Delivery of TNF-Alpha. *Adv. Healthc. Mater.*, 2017.
- [124] J. G. Kirkwood. Statistical Mechanics of Liquid Solutions. *Chem. Rev.*, 19(3):275–307, 1936.
- [125] P. Kirsch and M. Bremer. Nematic Liquid Crystals for Active Matrix Displays: Molecular Design and Synthesis. *Angew. Chem. Int. Ed.*, 39(23):4216–4235, 2000.
- [126] M. Kittelmann, P. Rahe, and A. Kühnle. Molecular Self-Assembly on an Insulating Surface: Interplay Between Substrate Templating and Intermolecular Interactions. *J. Phys.: Condens. Matter*, 24(35):354007, 2012.
- [127] A. V. Kityk and P. Huber. Thermotropic Nematic and Smectic Order in Silica Glass Nanochannels. *Appl. Phys. Lett.*, 97(15):153124, 2010.
- [128] D. L. Klein and P. L. McEuen. Conducting Atomic Force Microscopy of Alkane Layers on Graphite. *Appl. Phys. Lett.*, 66(19):2478–2480, 1995.
- [129] J. Klein and E. Kumacheva. Confinement-Induced Phase Transitions in Simple Liquids. *Science*, 269, 1995.
- [130] E. B. Knudsen, H. O. Sørensen, J. P. Wright, G. Goret, and J. Kieffer. FabIO: Easy Access to Two-Dimensional X-ray Detector Images in Python. *J. Appl. Crystallogr.*, 46(2):537–539, 2013.
- [131] I. Koltover, S. Idziak, P. Davidson, Y. Li, C. Safinya, M. Ruths, S. Steinberg, and J. Israelachvili. Alignment of Complex Fluids Under Confinement and Flow. *J. Physique II*, 6(6):893–907, 1996.
- [132] M. Kosmulski, J. Gustafsson, and J. B. Rosenholm. Thermal Stability of Low Temperature Ionic Liquids Revisited. *Thermochim. Acta*, 412(1):47–53, 2004.

BIBLIOGRAPHY

- [133] G. Krämer, F. Hausen, and R. Bennewitz. Dynamic Shear Force Microscopy of Confined Liquids at a Gold Electrode. *Faraday Discuss.*, 2017.
- [134] M.-D. Krass, N. N. Gosvami, R. W. Carpick, M. H. Müser, and R. Bennewitz. Dynamic Shear Force Microscopy of Viscosity in Nanometer-Confined Hexadecane Layers. *J. Phys.: Condens. Matter*, 28(13):134004, 2016.
- [135] I. Krossing, J. M. Slattery, C. Daguene, P. J. Dyson, A. Oleinikova, and H. Weingärtner. Why are Ionic Liquids Liquid? A Simple Explanation Based on Lattice and Solvation Energies. *J. Am. Chem. Soc.*, 128(41):13427–13434, 2006.
- [136] T. Kuhl, G. Smith, J. Majewski, W. Hamilton, and N. Alcantar. Investigating Confined Complex Fluids with Neutron Reflectivity. *Neutron News*, 14(1):29–31, 2003.
- [137] T. L. Kuhl, G. S. Smith, J. N. Israelachvili, J. Majewski, and W. Hamilton. Neutron Confinement Cell for Investigating Complex Fluids. *Rev. Sci. Instrum.*, 72(3):1715–1720, 2001.
- [138] S. Kuhn and P. Rahe. Discriminating Short-Range from Van Der Waals Forces Using Total Force Data in Noncontact Atomic Force Microscopy. *Phys. Rev. B*, 89(23):235417, 2014.
- [139] T. Kusano, K. Fujii, K. Hashimoto, and M. Shibayama. Water-in-Ionic Liquid Microemulsion Formation in Solvent Mixture of Aprotic and Protic Imidazolium-based Ionic Liquids. *Langmuir*, 30(40):11890–11896, 2014.
- [140] T. Kusano, K. Fujii, M. Tabata, and M. Shibayama. Small-angle Neutron Scattering Study on Aggregation of 1-alkyl-3-methylimidazolium Based Ionic Liquids in Aqueous Solution. *J. Solution Chem.*, 42(10):1888–1901, 2013.
- [141] J. E. Lane and T. H. Spurling. Forces between Adsorbing Walls: Monte Carlo Calculations. *Chem. Phys. Lett.*, 67(1):107–108, 1979.
- [142] F. Lantelme, P. Turq, B. Quentrec, and J. W. Lewis. Application of the Molecular Dynamics Method to a Liquid System with Long Range Forces (molten NaCl). *Mol. Phys.*, 28(6):1537–1549, 1974.
- [143] C. Largeot, C. Portet, J. Chmiola, P.-L. Taberna, Y. Gogotsi, and P. Simon. Relation between the Ion Size and Pore Size for an Electric Double-Layer Capacitor. *J. Am. Chem. Soc.*, 130, 2008.
- [144] A. A. Lee, S. Kondrat, G. Oshanin, and A. A. Kornyshev. Charging Dynamics of Supercapacitors with Narrow Cylindrical Nanopores. *Nanotechnology*, 25, 2014.
- [145] D. R. Lee, P. Dutta, and C.-J. Yu. Observation of a Liquid-to-layered Transition in Thin Liquid Films when Surface and Interface Regions Overlap. *Phys. Rev. E*, 77(3):030601, 2008.

- [146] W. Lee, K. Schwirn, M. Steinhart, E. Pippel, R. Scholz, and U. Gösele. Structural Engineering of Nanoporous Anodic Aluminium Oxide by Pulse Anodization of Aluminium. *Nature Nanotechnology*, 3(4):234–239, 2008.
- [147] R. Leote de Carvalho and R. Evans. The Decay of Correlations in Ionic Fluids. *Mol. Phys.*, 83(4):619–654, 1994.
- [148] V. Lesch, A. Heuer, C. Holm, and J. Smiatek. Solvent Effects of 1-ethyl-3-methylimidazolium Acetate: Solvation and Dynamic Behavior of Polar and Apolar Solutes. *Phys. Chem. Chem. Phys.*, 17(13):8480–8490, 2015.
- [149] H. Li, R. J. Wood, F. Endres, and R. Atkin. Influence of Alkyl Chain Length and Anion Species on Ionic Liquid Structure at the Graphite Interface as a Function of Applied Potential. *J. Phys.: Condens. Matter*, 26(28):284115, 2014.
- [150] T. Li, F. Xu, and W. Shi. Ionic Liquid Crystals Based on 1-alkyl-3-methylimidazolium Cations and Perfluorinated Sulfonylimide Anions. *Chem. Phys. Lett.*, 628:9–15, 2015.
- [151] Y. Li, R. Beck, T. Huang, M. C. Choi, and M. Divinagracia. Scatterless Hybrid Metal–single-crystal Slit for Small-angle X-ray Scattering and High-resolution X-ray Diffraction. *J. Appl. Crystallogr.*, 41(6):1134–1139, 2008.
- [152] Y. Li, Y. Golan, A. Martin-Herranz, O. Pelletier, M. Yasa, J. Israelachivili, and C. Safinya. In Situ X-ray Diffraction Studies of a Multilayered Membrane Fluid under Confinement and Shear. *Int. J. Thermophys.*, 22(4):1175–1184, 2001.
- [153] C. Lian, K. Liu, H. Liu, and J. Wu. Impurity Effects on Charging Mechanism and Energy Storage of Nanoporous Supercapacitors. *J. Phys. Chem. C*, 2017.
- [154] M. Liley, T. A. Keller, C. Duschl, and H. Vogel. Direct Observation of Self-assembled Monolayers, Ion Complexation, and Protein Conformation at the Gold/Water Interface: An FTIR Spectroscopic Approach. *Langmuir*, 13(16):4190–4192, 1997.
- [155] B. Lindlar, A. Kogelbauer, P. J. Kooyman, and R. Prins. Synthesis of Large Pore Silica with a Narrow Pore Size Distribution. *Microporous Mesoporous Mater.*, 44:89–94, 2001.
- [156] M. Lippmann, A. Ehnes, and O. Seeck. An X-ray Setup to Investigate the Atomic Order of Confined Liquids in Slit Geometry. *Rev. Sci. Instrum.*, 85(1):015106, 2014.
- [157] W. Loose and B. J. Ackerson. Model Calculations for the Analysis of Scattering Data from Layered Structures. *J. Chem. Phys.*, 101(9):7211–7220, 1994.
- [158] J. N. A. C. Lopes and A. A. H. Padua. Nanostructural Organization in Ionic Liquids. *J. Phys. Chem. B*, 110:3330, 2006. Lop2006.

BIBLIOGRAPHY

- [159] J. N. C. Lopes, M. F. C. Gomes, and A. A. H. Padua. Nonpolar, Polar, and Associating Solutes in Ionic Liquids. *J. Phys. Chem. B Lett.*, 110(34):16816, Aug 2006.
- [160] K. R. J. Lovelock. Influence of the Ionic Liquid/Gas Surface on Ionic Liquid Chemistry. *Phys. Chem. Chem. Phys.*, 14:5071, 2012.
- [161] Q. Lu, H. Wang, C. Ye, W. Liu, and Q. Xue. Room Temperature Ionic Liquid 1-ethyl-3-hexylimidazolium-bis (trifluoromethylsulfonyl)-imide as Lubricant for Steel–Steel Contact. *Tribol. Int.*, 37(7):547–552, 2004.
- [162] G. Luengo, F.-J. Schmitt, R. Hill, and J. Israelachvili. Thin Film Rheology and Tribology of Confined Polymer Melts: Contrasts with Bulk Properties. *Macromolecules*, 30(8):2482–2494, 1997.
- [163] R. M. Lynden-Bell, M. G. Del Pópolo, T. G. Youngs, J. Kohanoff, C. G. Hanke, J. B. Harper, and C. C. Pinilla. Simulations of Ionic Liquids, Solutions, and Surfaces. *Acc. Chem. Res.*, 40(11):1138–1145, 2007.
- [164] D. R. Macfarlane, M. Forsyth, P. C. Howlett, J. M. Pringle, J. Sun, G. Annat, W. Neil, and E. I. Izgorodina. Ionic Liquids in Electrochemical Devices and Processes: Managing Interfacial Electrochemistry. *Acc. Chem. Res.*, 40, 2007.
- [165] S. Mantha and A. Yethiraj. Dynamics of Water Confined in Lyotropic Liquid Crystals: Molecular Dynamics Simulations of the Dynamic Structure Factor. *J. Chem. Phys.*, 144(8):084504, 2016.
- [166] C. J. Margulis. Computational Study of Imidazolium-based Ionic Solvents with Alkyl Substituents of Different Lengths. *Mol. Phys.*, 102(9):829–838, 2004.
- [167] J. Mars, B. Hou, H. Weiss, H. Li, O. Konovalov, S. Festersen, B. M. Murphy, U. Rütt, M. Bier, and M. Mezger. Surface Induced Smectic Order in Ionic Liquids-An X-ray Reflectivity Study of $[\text{C}_{22}\text{C}_1\text{im}]^+ [\text{NTf}_2]^-$. *Phys. Chem. Chem. Phys.*, 2017.
- [168] G. A. Martynov. *Fundamental Theory of Liquids*. Hilger, 1992.
- [169] C. Marutschke, D. Walters, J. Cleveland, I. Hermes, R. Bechstein, and A. Kühnle. Three-dimensional Hydration Layer Mapping on the (10.4) Surface of Calcite Using Amplitude Modulation Atomic Force Microscopy. *Nanotechnology*, 25(33):335703, 2014.
- [170] W. McMillan. X-ray Scattering from Liquid Crystals. I. Cholesteryl Nonanoate and Myristate. *Phys. Rev. A*, 6(3):936, 1972.
- [171] F. Meissner. Mitteilungen aus dem Institut für phys. Chemie der Universität Göttingen. Nr. 8. über den Einfluß der Zerteilung auf die Schmelztemperatur. *Z. anorg. allg. Chem.*, 110(1):169–186, 1920.

- [172] Y. B. Melnichenko. *Small-angle Scattering from Confined and Interfacial Fluids: Applications to Energy Storage and Environmental Science*. Springer, 2015.
- [173] M. Mezger. *X-ray Studies of the Density Depletion at Hydrophobic Water-Solid Interfaces*. PhD Thesis, Universität Stuttgart, 2008.
- [174] M. Mezger, B. M. Ocko, H. Reichert, and M. Deutsch. Surface Layering and Melting in an Ionic Liquid Studied by Resonant Soft X-ray Reflectivity. *PNAS*, 110(10):3733, Feb 2013.
- [175] M. Mezger, R. Roth, H. Schroeder, P. Reichert, D. Pontoni, and H. Reichert. Solid-Liquid Interfaces of Ionic Liquid Solutions-interfacial Layering and Bulk Correlations. *J. Chem. Phys.*, 142(164707-1), 2015.
- [176] M. Mezger, H. Schroeder, H. Reichert, J. S. O. Sebastian Schramm, S. Schöder, V. Honkimäki, M. Deutsch, B. M. Ocko, J. Ralston, M. Rohwerder, M. Stratmann, and H. Dosch. Molecular Layering of Fluorinated Ionic Liquids at a Charged Sapphire (0001) Surface. *Science*, 322:424, 2008.
- [177] R. Miller, J. K. Ferri, A. Javadi, J. Krägel, N. Mucic, and R. Wüstneck. Rheology of Interfacial Layers. *Colloid Polym. Sci.*, 288(9):937–950, 2010.
- [178] K. Mistry, M. Fox, and M. Priest. Lubrication of an Electroplated Nickel Matrix Silicon Carbide Coated Eutectic Aluminium-Silicon Alloy Automotive Cylinder Bore with an Ionic Liquid as a Lubricant Additive. *Proc. Inst. Mech. Eng. J*, 223(3):563–569, 2009.
- [179] H. Mo, S. Kewalramani, G. Evmenenko, K. Kim, S. N. Ehrlich, and P. Dutta. Temperature Dependence of Surface Layering in a Dielectric Liquid. *Phys. Rev. B*, 76(2):024206, 2007.
- [180] B. Moeremans, H.-W. Cheng, Q. Hu, H. F. Garces, N. P. Padture, F. U. Renner, and M. Valtiner. Lithium-ion Battery Electrolyte Mobility at Nano-confined Graphene Interfaces. *Nature Communications*, 7, 2016.
- [181] M. Moreno, F. Castiglione, A. Mele, C. Pasqui, and G. Raos. Interaction of Water with the Model Ionic Liquid [bmim][BF₄]: Molecular Dynamics Simulations and Comparison with NMR Data. *J. Phys. Chem. B*, 112(26):7826–7836, 2008.
- [182] N. Mucic, A. Javadi, N. Kovalchuk, E. Aksenenko, and R. Miller. Dynamics of Interfacial Layers - Experimental Feasibilities of Adsorption Kinetics and Dilational Rheology. *Adv. Colloid Interface Sci.*, 168(1):167–178, 2011.
- [183] B. Mukherjee, C. Peter, and K. Kremer. Dual Translocation Pathways in Smectic Liquid Crystals Facilitated by Molecular Flexibility. *Phys. Rev. E*, 88(1):010502, 2013.

BIBLIOGRAPHY

- [184] S. Nakano, M. Mizukami, N. Ohta, N. Yagi, I. Hatta, and K. Kurihara. Structural Change in Smectic Liquid Crystal Nanofilm under Molecular-Scale Confinement Measured by Synchrotron X-ray Diffraction. *Jpn. J. Appl. Phys.*, 52, 2013.
- [185] F. Nemoto, M. Kofu, and O. Yamamuro. Thermal and Structural Studies of Imidazolium-Based Ionic Liquids with and without Liquid-Crystalline Phases: The Origin of Nanostructure. *J. Phys. Chem. B*, 119:5028–5034, 2015.
- [186] A. Noda, K. Hayamizu, and M. Watanabe. Pulsed-gradient Spin-Echo ^1H and ^{19}F NMR Ionic Diffusion Coefficient, Viscosity, and Ionic Conductivity of Non-chloroaluminate Room-temperature Ionic Liquids. *J. Phys. Chem. B*, 105(20):4603–4610, 2001.
- [187] K. Nygard. Colloidal Diffusion in Confined Geometries. *Phys. Chem. Chem. Phys.*, 2017.
- [188] K. Nygård, R. Kjellander, S. Sarman, S. Chodankar, E. Perret, J. Buitenhuis, and J. Van der Veen. Anisotropic Pair Correlations and Structure Factors of Confined Hard-sphere Fluids: An Experimental and Theoretical Study. *Phys. Rev. Lett.*, 108(3):037802, 2012.
- [189] B. Ocko, H. Hlaing, P. Jepsen, S. Kewalramani, A. Tkachenko, D. Pontoni, H. Reichert, and M. Deutsch. Unifying Interfacial Self-Assembly and Surface Freezing. *Phys. Rev. Lett.*, 106(13):137801, 2011.
- [190] B. M. Ocko, X. Z. Wu, E. B. Sirota, S. K. Sinha, O. Gang, and M. Deutsch. Surface Freezing in Chain Molecules: Normal Alkanes. *Phys. Rev. E*, 55(3):3164, 1997.
- [191] N. I. of Standards and Technology. Fundamental Physical Constants, October 2017.
- [192] L. S. Ornstein. Accidental Deviations of Density and Opalescence at the Critical Point of a Single Substance. *Proc. Akad. Sci.*, 17:793, 1914.
- [193] S. O’shea and M. Welland. Atomic Force Microscopy at Solid-Liquid Interfaces. *Langmuir*, 14(15):4186–4197, 1998.
- [194] A. A. H. Padua, M. F. Costa Gomes, and J. N. A. Canongia Lopes. Molecular Solutes in Ionic Liquids: A Structural Perspective. *Acc. Chem. Res.*, 40(11):1087, Nov 2007.
- [195] J. L. Parker. Surface Force Measurements in Surfactant Systems. *Prog. Surf. Sci.*, 47(3):205–271, 1994.
- [196] L. G. Parratt. Surface Studies of Solids by Total Reflection of X-rays. *Phys. Rev.*, 95(2):359, 1954.

- [197] R. Pashley, P. McGuiggan, and B. Ninham. Effect of Pentanol Adsorption on the Forces Between Bilayers of a Cationic Surfactant. *J. Phys. Chem.*, 90(22):5841–5845, 1986.
- [198] R. Pashley, P. McGuiggan, B. Ninham, J. Brady, and D. Evans. Direct Measurements of Surface Forces Between Bilayers of Double-Chained Quaternary Ammonium Acetate and Bromide Surfactants. *J. Phys. Chem.*, 90(8):1637–1642, 1986.
- [199] J. S. Pedersen. Analysis of Small-Angle Scattering Data from Colloids and Polymer Solutions: Modeling and Least-squares Fitting. *Adv. Colloid Interface Sci.*, 70:171–210, 1997.
- [200] S. Perkin. Ionic Liquids in Confined Geometries. *Phys. Chem. Chem. Phys.*, 14(15):5052–5062, 2012.
- [201] E. Perret. *Structure of Molecular Liquids Under Nanometre Confinement*. PhD Thesis, ETH Zürich, 2010.
- [202] E. Perret, K. Nygård, D. K. Satapathy, T. Balmer, O. Bunk, M. Heuberger, and J. van der Veen. X-ray Reflectivity Reveals Equilibrium Density Profile of Molecular Liquid Under Nanometre Confinement. *EPL*, 88(3):36004, 2009.
- [203] E. Perret, K. Nygård, D. K. Satapathy, T. E. Balmer, O. Bunk, M. Heuberger, and J. F. van der Veen. Molecular Liquid Under Nanometre Confinement: Density Profiles Underlying Oscillatory Forces. *J. Phys.: Condens. Matter*, 22(23):235102, 2010.
- [204] E. Perret, K. Nygård, D. K. Satapathy, T. E. Balmer, O. Bunk, M. Heuberger, and J. F. van der Veen. X-ray Reflectivity Theory for Determining the Density Profile of a Liquid Under Nanometre Confinement. *J. Synchrotron Radiat.*, 17(4):465–472, 2010.
- [205] B. Persson and P. Ballone. Squeezing Lubrication Films: Layering Transition for Curved Solid Surfaces with Long-range Elasticity. *J. Chem. Phys.*, 112(21):9524–9542, 2000.
- [206] T. A. Petach, A. Mehta, R. Marks, B. Johnson, M. F. Toney, and D. Goldhaber-Gordon. Voltage-Controlled Interfacial Layering in an Ionic Liquid on SrTiO₃. *ACS Nano*, 10(4):4565–4569, 2016.
- [207] M. V. Petoukhov, D. Franke, A. V. Shkumatov, G. Tria, A. G. Kikhney, M. Gajda, C. Gorba, H. D. Mertens, P. V. Konarev, and D. I. Svergun. New Developments in the ATSAS Program Package for Small-Angle Scattering Data Analysis. *J. Appl. Crystallogr.*, 45(2):342–350, 2012.

BIBLIOGRAPHY

- [208] C. Pfaffenhuber, F. Hoffmann, M. Fröba, J. Popovic, and J. Maier. Soggy-sand Effects in Liquid Composite Electrolytes with Mesoporous Materials as Fillers. *J. Mater. Chem. A*, 1(40):12560–12567, 2013.
- [209] C. Pings and J. Waser. Analysis of Scattering Data for Mixtures of Amorphous Solids or Liquids. *J. Chem. Phys.*, 48(7):3016–3018, 1968.
- [210] D. Pontoni, J. Haddad, M. Di Michiel, and M. Deutsch. Self-segregated Nanostructure in Room Temperature Ionic Liquids. *Soft Matter*, 2017.
- [211] J. M. Pringle, J. Golding, K. Baranyai, C. M. Forsyth, G. B. Deacon, J. L. Scott, and D. R. MacFarlane. The Effect of Anion Fluorination in Ionic Liquids-Physical Properties of a Range of bis (methanesulfonyl) amide Salts. *New J. Chem.*, 27(10):1504–1510, 2003.
- [212] A. Rack, F. García-Moreno, T. Baumbach, and J. Banhart. Synchrotron-based Radioscopy Employing Spatio-temporal Micro-resolution for Studying Fast Phenomena in Liquid Metal Foams. *J. Synchrotron Radiat.*, 16(3):432–434, 2009.
- [213] H. Reichert, V. Honkimäki, A. Snigirev, S. Engemann, and H. Dosch. A New X-ray Transmission-Reflection Scheme for the Study of Deeply Buried Interfaces Using High-energy Microbeams. *Physica B: Condensed Matter*, 336(1):46–55, 2003.
- [214] P. Reichert. *Structure and Dynamics of Ionic Liquid/Electrode Interfaces*. PhD Thesis, Dept. Butt: Physics at Interfaces, MPI for Polymer Research, Max Planck Society, 2014.
- [215] P. Reichert, K. S. Kjær, T. B. van Driel, J. Mars, J. W. Ochsmann, D. Pontoni, M. Deutsch, M. M. Nielsen, and M. Mezger. Molecular Scale Structure and Dynamics at an Ionic Liquid/Electrode Interface. *Faraday Discuss.*, 2017.
- [216] F. U. Renner, H. Kageyama, Z. Siroma, M. Shikano, S. Schöder, Y. Gründer, and O. Sakata. Gold Model Anodes for Li-Ion Batteries: Single Crystalline Systems Studied by In Situ X-ray Diffraction. *Electrochim. Acta*, 53(21):6064–6069, 2008.
- [217] J. Restolho, A. P. Serro, J. L. Mata, and B. Saramago. Viscosity and Surface Tension of 1-ethanol-3-methylimidazolium Tetrafluoroborate and 1-methyl-3-octylimidazolium Tetrafluoroborate over a Wide Temperature Range. *J. Chem. Eng. Data*, 54(3):950–955, 2009.
- [218] W. Richtering, J. Laeuger, and R. Linemann. Shear Orientation of a Micellar Hexagonal Liquid Crystalline Phase: A Rheo and Small Angle Light Scattering Study. *Langmuir*, 10(11):4374–4379, 1994.

- [219] E. Rie. Über den Einfluss der Oberflächenspannung auf Schmelzen und Gefrieren. *Z. phys. Chem.*, 104(1):354–362, 1923.
- [220] A. Riisager, R. Fehrmann, M. Haumann, B. S. Gorle, and P. Wasserscheid. Stability and Kinetic Studies of Supported Ionic Liquid Phase Catalysts for Hydroformylation of Propene. *Ind. Eng. Chem. Res.*, 44(26):9853–9859, 2005.
- [221] A. Riisager, P. Wasserscheid, R. van Hal, and R. Fehrmann. Continuous Fixed-bed Gas-Phase Hydroformylation Using Supported Ionic Liquid-phase (SILP) Rh Catalysts. *J. Catal.*, 219:452, 2003.
- [222] I. Robinson and D. Tweet. Surface X-ray Diffraction. *Rep. Prog. Phys.*, 55(5):599, 1992.
- [223] R. D. Rogers and K. R. Seddon. Ionic-Liquids - Solvents of the Future. *Science*, 302:792, 2003.
- [224] J. B. Rollins, B. D. Fitchett, and J. C. Conboy. Structure and Orientation of the Imidazolium Cation at the Room-temperature Ionic Liquid/SiO₂ Interface Measured by Sum-Frequency Vibrational Spectroscopy. *J. Phys. Chem. B*, 111(18):4990–4999, 2007.
- [225] M. Rovere and M. Tosi. Structure and Dynamics of Molten Salts. *Rep. Prog. Phys.*, 49(9):1001, 1986.
- [226] M. Rubinstein and R. H. Colby. *Polymer Physics*. Oxford Univ. Press, 2010.
- [227] O. Russina, W. Schroer, and A. Triolo. Mesoscopic Structural and Dynamic Organization in Ionic Liquids. *Journal of Molecular Liquids*, 210:161–163, 2015.
- [228] O. Russina, A. Triolo, L. Gontrani, and R. Caminiti. Mesoscopic Structural Heterogeneities in Room-Temperature Ionic Liquids. *J. Phys. Chem. Lett.*, 3:27, 2012.
- [229] O. Russina, A. Triolo, L. Gontrani, R. Caminiti, D. Xiao, L. G. Hines Jr, R. A. Bartsch, E. L. Quitevis, N. Plechkova, and K. R. Seddon. Morphology and Intermolecular Dynamics of 1-alkyl-3-methylimidazolium bis(trifluoromethane)sulfonylamide Ionic Liquids: Structural and Dynamic Evidence of Nanoscale Segregation. *J. Phys.: Condens. Matter*, 21, 2009.
- [230] M. Ruths, S. Steinberg, and J. N. Israelachvili. Effects of Confinement and Shear on the Properties of Thin Films of Thermotropic Liquid Crystal. *Langmuir*, 12:6637–6650, 1996.
- [231] C. Safinya, E. Sirota, and R. Plano. Nematic to Smectic-A Phase Transition Under Shear Flow: A Nonequilibrium Synchrotron X-ray Study. *Phys. Rev. Lett.*, 66(15):1986, 1991.

BIBLIOGRAPHY

- [232] K. Sakai, K. Okada, A. Uka, T. Misono, T. Endo, S. Sasaki, M. Abe, and H. Sakai. Effects of Water on Solvation Layers of Imidazolium-type Room Temperature Ionic Liquids on Silica and Mica. *Langmuir*, 31(22):6085–6091, 2015.
- [233] C. S. Santos, H. V. R. Annapureddy, N. S. Murthy, H. K. Kashyap, E. W. Castner, Jr., and C. J. Margulis. Temperature-dependent Structure of Methyltributylammonium bis(trifluoromethylsulfonyl)amide: X-ray Scattering and Simulations. *J. Chem. Phys.*, 134, 2011.
- [234] M. Schoen, C. L. Rhykerd Jr, D. J. Diestler, and J. H. Cushman. Shear Forces in Molecularly Thin Films. *Science*, 245(4923):1223–1226, 1989.
- [235] C. Schröder, G. Neumayr, and O. Steinhauser. On the Collective Network of Ionic Liquid/Water Mixtures. III. Structural Analysis of Ionic Liquids on the Basis of Voronoi Decomposition. *J. Chem. Phys.*, 130(19):194503, 2009.
- [236] C. Schröder, T. Rudas, G. Neumayr, S. Benkner, and O. Steinhauser. On the Collective Network of Ionic Liquid/Water Mixtures. I. Orientational Structure. *J. Chem. Phys.*, 127(23):234503, 2007.
- [237] H. Schröder. *Molecular Ordering of Ionic Liquids at a Sapphire Hard Wall: A High Energy X-ray Reflectivity Study*. PhD Thesis, Universität Stuttgart, 2009.
- [238] L. Schulz and F. Tangherlini. Optical Constants of Silver, Gold, Copper, and Aluminum. II. The Index of Refraction n . *JOSA*, 44(5):362–368, 1954.
- [239] K. Schwirn, W. Lee, R. Hillebrand, M. Steinhart, K. Nielsch, and U. Gösele. Self-ordered Anodic Aluminum Oxide Formed by H_2SO_4 Hard Anodization. *ACS Nano*, 2(2):302–310, 2008.
- [240] F. Schwoerer, M. Trapp, M. Ballauff, R. Dahint, and R. Steitz. Surface-Active Lipid Linings under Shear Load - A Combined in-Situ Neutron Reflectivity and ATR-FTIR Study. *Langmuir*, 31(42):11539–11548, 2015.
- [241] K. R. Seddon, A. Stark, and M.-J. Torres. Clean Solvents: Alternative Media for Chemical Reactions and Processing. In *ACS Symposium Series*, volume 819, pages 34–49, 2002.
- [242] O. H. Seeck and B. Murphy. *X-ray Diffraction: Modern Experimental Techniques*. Pan Stanford, 2015.
- [243] S. Shigeto and H. Hamaguchi. Evidence for Mesoscopic Local Structures in Ionic Liquids: CARS Signal Spatial Distribution of $\text{C}_n\text{mim}[\text{PF}_6]$ ($n = 4, 6, 8$). *Chem. Phys. Lett.*, 427:329, 2006.
- [244] K. Shimizu, C. E. S. Bernardes, and J. N. C. Lopes. Structure and Aggregation in the 1-Alkyl-3-Methylimidazolium Bis(trifluoromethylsulfonyl)imide Ionic Liquid Homologous Series. *J. Phys. Chem. B*, 118:567–576, 2014.

- [245] K. Shimizu, M. F. C. Gomes, A. A. Padua, L. P. Rebelo, and J. N. C. Lopes. Three Commentaries on the Nano-segregated Structure of Ionic Liquids. *J. Mol. Struct.*, 946:70, 2010.
- [246] Sigma-Aldrich. *Materials Safety Data Sheet C₁₀mimCl*. Sigma-Aldrich, 2017.
- [247] Sigma-Aldrich. *Materials Safety Data Sheet C₈mimCl*. Sigma-Aldrich, 2017.
- [248] P. Simon and Y. Gogotsi. Materials for Electrochemical Capacitors. *Nat. Mater.*, 7(11):845–854, 2008.
- [249] D. K. Singh, S. Cha, D. Nam, H. Cheong, S.-W. Joo, and D. Kim. Raman Spectroscopic Study on Alkyl Chain Conformation in 1-Butyl-3-methylimidazolium Ionic Liquids and their aqueous Mixtures. *ChemPhysChem*, 17:3040 – 3046, 2016.
- [250] E. Sloutskin, B. M. Ocko, L. Tamam, I. Kuzmenko, T. Gog, and M. Deutsch. Surface Layering in Ionic Liquids: An X-ray Reflectivity Study. *J. Am. Chem. Soc.*, 127(21):7796–7804, 2005.
- [251] N. Smirnova and E. Safonova. Ionic Liquids as Surfactants. *Russ. J. Phys. Chem. A*, 84(10):1695–1704, 2010.
- [252] A. Snigirev, I. Snigireva, G. Vaughan, J. Wright, M. Rossat, A. Bychkov, and C. Curfs. High Energy X-ray Transfocator Based on Al Parabolic Refractive Lenses for Focusing and Collimation. *J. Phys. Conf. Ser.*, 186(1):012073, 2009.
- [253] A. A. Snigirev, B. Filseth, P. Elleaume, T. Klocke, V. Kohn, B. Lengeler, I. Snigireva, A. Souvorov, and J. Tuemmler. Refractive Lenses for High-Energy X-ray Focusing. In *Optical Science, Engineering and Instrumentation'97*, pages 164–170. International Society for Optics and Photonics, 1997.
- [254] I. K. Snook and D. Henderson. Monte Carlo Study of a Hard-Sphere Fluid Near a Hard Wall. *J. Chem. Phys.*, 68(5):2134–2139, 1978.
- [255] M. Sobota, M. Schmid, M. Happel, M. Amende, F. Maier, H.-P. Steinrück, N. Paape, P. Wasserscheid, M. Laurin, J. M. Gottfried, et al. Ionic Liquid Based Model Catalysis: Interaction of [BMIM][Tf₂N] with Pd Nanoparticles Supported on an Ordered Alumina Film. *Phys. Chem. Chem. Phys.*, 12(35):10610–10621, 2010.
- [256] B. Song, W. Walczyk, and H. Schönherr. Contact Angles of Surface Nanobubbles on Mixed Self-assembled Monolayers with Systematically Varied Macroscopic Wettability by Atomic Force Microscopy. *Langmuir*, 27(13):8223–8232, 2011.
- [257] H. Söngen, C. Marutschke, P. Spijker, E. Holmgren, I. M. Hermes, R. Bechstein, S. Klassen, J. Tracey, A. S. Foster, and A. Kuhnle. Chemical Identification at the Solid-Liquid Interface. *Langmuir*, 2016.

BIBLIOGRAPHY

- [258] D. Stamou, D. Gourdon, M. Liley, N. A. Burnham, A. Kulik, H. Vogel, and C. Duschl. Uniformly Flat Gold Surfaces: Imaging the Domain Structure of Organic Monolayers Using Scanning Force Microscopy. *Langmuir*, 13(9):2425–2428, 1997.
- [259] H.-P. Steinrueck and P. Wasserscheid. Ionic Liquids in Catalysis. *Catal. Lett.*, 145:380, 2015.
- [260] B. Struth, K. Hyun, E. Kats, T. Meins, M. Walther, M. Wilhelm, and G. Grübel. Observation of New States of Liquid Crystal 8CB Under Nonlinear Shear Conditions as Observed via a Novel and Unique Rheology/Small-Angle X-ray Scattering Combination. *Langmuir*, 27(6):2880–2887, 2011.
- [261] Y. Suzuki, H. Duran, W. Akram, M. Steinhart, G. Floudas, and H.-J. Butt. Multiple Nucleation Events and Local Dynamics of Poly (ϵ -caprolactone)(PCL) Confined to Nanoporous Alumina. *Soft Matter*, 9(38):9189–9198, 2013.
- [262] Y. Suzuki, H. Duran, M. Steinhart, H.-J. Butt, and G. Floudas. Homogeneous Crystallization and Local Dynamics of Poly (ethylene oxide)(PEO) Confined to Nanoporous Alumina. *Soft Matter*, 9(9):2621–2628, 2013.
- [263] M. Tabuchi and Y. Takeda. Atomic Scale Analysis of MOVPE Grown Heterostructures by X-ray Crystal Truncation Rod Scattering Measurement. *J. Cryst. Growth*, 298:12–17, 2007.
- [264] M. Teubner and R. Strey. Origin of the Scattering Peak in Microemulsions. *J. Chem. Phys.*, 87:3195, 1987.
- [265] J. J. Thomson. *Applications of Dynamics to Physics and Chemistry*. Macmillan, 1888.
- [266] H. Tokuda, K. Hayamizu, K. Ishii, M. A. B. H. Susan, and M. Watanabe. Physicochemical Properties and Structures of Room Temperature Ionic Liquids. 1. Variation of Anionic Species. *J. Phys. Chem. B*, 108(42):16593–16600, 2004.
- [267] H. Tokuda, K. Hayamizu, K. Ishii, M. A. B. H. Susan, and M. Watanabe. Physicochemical Properties and Structures of Room Temperature Ionic Liquids. 2. Variation of Alkyl Chain Length in Imidazolium Cation. *J. Phys. Chem. B*, 109(13):6103–6110, 2005.
- [268] K. Tomita, M. Mizukami, S. Nakano, N. Ohta, N. Yagi, and K. Kurihara. X-ray Diffraction and Resonance Shear Measurement on Nano-Confined Ionic Liquids. *Physical Chemistry Chemical Physics*, 2018.
- [269] M. Tomsic, M. Bester-Rogac, A. Jamnik, W. Kunz, D. Touraud, A. Bergmann, and O. Glatter. Nonionic Surfactant Brij 35 in Water and in Various Simple Alcohols: Structural Investigations by Small-Angle X-ray Scattering and Dynamic Light Scattering. *J. Phys. Chem. B*, 108:7021, 2004.

- [270] C. D. Tran, S. H. De Paoli Lacerda, and D. Oliveira. Absorption of Water by Room-temperature Ionic Liquids: Effect of Anions on Concentration and State of Water. *Appl. Spectrosc.*, 57(2):152–157, 2003.
- [271] A. Triolo, A. Mandanici, O. Russina, V. Rodriguez-Mora, M. Cutroni, C. Hardacre, M. Nieuwenhuyzen, H.-J. Bleif, L. Keller, and M. A. Ramos. Thermodynamics, Structure, and Dynamics in Room Temperature Ionic Liquids: The Case of 1-Butyl-3-methyl Imidazolium Hexafluorophosphate ([bmim][PF₆]). *J. Phys. Chem. B*, 110:21357, 2006.
- [272] A. Triolo, O. Russina, H.-J. Bleif, and E. Di Cola. Nanoscale Segregation in Room Temperature Ionic Liquids. *J. Phys. Chem. B*, 111(18):4641, May 2007.
- [273] S. M. Urahata and M. C. Ribeiro. Structure of Ionic Liquids of 1-alkyl-3-methylimidazolium Cations: A Systematic Computer Simulation Study. *J. Chem. Phys.*, 120(4):1855–1863, 2004.
- [274] A. Uysal, H. Zhou, G. Feng, S. S. Lee, S. Li, P. T. Cummings, P. F. Fulvio, S. Dai, J. K. McDonough, Y. Gogotsi, et al. Interfacial Ionic Liquids: Connecting Static and Dynamic Structures. *J. Phys.: Condens. Matter*, 27(3):032101, 2014.
- [275] M. Valtiner, X. Banquy, K. Kristiansen, G. W. Greene, and J. N. Israelachvili. The Electrochemical Surface Forces Apparatus: The Effect of Surface Roughness, Electrostatic Surface Potentials, and Anodic Oxide Growth on Interaction Forces, and Friction between Dissimilar Surfaces in Aqueous Solutions. *Langmuir*, 28:13080 – 13093, 2012.
- [276] J. Van Alsten and S. Granick. Molecular Tribometry of Ultrathin Liquid Films. *Phys. Rev. Lett.*, 61(22):2570, 1988.
- [277] W. van Megen and I. Snook. Solvent Structure and Solvation Forces between Solid Bodies. *J. Chem. Soc. Farad. Trans 2: Mol. Chem. Phys.*, 75:1095–1102, 1979.
- [278] W. Van Megen and I. Snook. Solvation Forces in Simple Dense Fluids. II. Effect of Chemical Potential. *J. Chem. Phys.*, 74(2):1409–1411, 1981.
- [279] P. L. Verma, P. Singh, and S. P. Gejji. Structure and Electronic Properties of Ion Pairs Accompanying Cyclic Morpholinium Cation and Alkylphosphite Anion Based Ionic Liquids. *Chem. Phys.*, 2017.
- [280] B. Vestergaard, N. Bjerrum, I. Petrushina, H. Hjuler, R. W. Berg, and M. Begtrup. Molten Triazolium Chloride Systems as New Aluminum Battery Electrolytes. *J. Electrochem. Soc.*, 140(11):3108–3113, 1993.
- [281] J. M. Vicent-Luna, J. M. Romero-Enrique, S. Calero, and J. A. Anta. Micelle Formation in Aqueous Solutions of Room Temperature Ionic Liquids: a Molecular Dynamics Study. *J. Phys. Chem. B*, 2017.

BIBLIOGRAPHY

- [282] G. Vleminckx and C. Clasen. The Dark Side of Microrheology: Non-optical Techniques. *Curr. Opin. Colloid Interface Sci.*, 19(6):503–513, 2014.
- [283] N. Vogel, J. Zieleniecki, and I. Köper. As Flat as it Gets: Ultrasmooth Surfaces from Template-stripping Procedures. *Nanoscale*, 4(13):3820–3832, 2012.
- [284] H. Wang, M. Liu, Y. Zhao, X. Xuan, Y. Zhao, and J. Wang. Hydrogen Bonding Mediated Ion Pairs of Some Aprotic Ionic Liquids and their Structural Transition in Aqueous Solution. *Science China Chemistry*, pages 1–9, 2017.
- [285] Y. Wang and G. A. Voth. Tail Aggregation and Domain Diffusion in Ionic Liquids. *J. Phys. Chem. B*, 110(37):18601–18608, 2006.
- [286] P. Wasserscheid and W. Keim. Ionic Liquids - New 'Solutions' for Transition Metal Catalysis. *Angew. Chem. Int. Ed.*, 39(21):3772–3789, 2000.
- [287] P. Wasserscheid and T. Welton. *Ionic Liquids in Synthesis*. Wiley-VCH, 2008.
- [288] Z. Wei and S. W. Prescott. Scattering Approaches to Probing Surface Layers Under Confinement. *Curr. Opin. Colloid Interface Sci.*, 20(4):253–260, 2015.
- [289] H. Weingärtner. NMR Studies of Ionic Liquids: Structure and Dynamics. *Curr. Opin. Colloid Interface Sci.*, 18(3):183–189, 2013.
- [290] H. Weiss, H.-W. Cheng, J. Mars, H. Li, C. Merola, F. U. Renner, V. Honkimäki, M. Valtiner, and M. Mezger. Molecular Scale Structure and Dynamics of a Confined Liquid Crystal studied by an X-ray Surface Force Apparatus. *in preparation*, 2017.
- [291] H. Weiss, J. Mars, H. Li, G. Kircher, O. Ivanova, A. Feoktystov, O. Soltwedel, M. Bier, and M. Mezger. Mesoscopic Correlation Functions in Heterogeneous Ionic Liquids. *J. Phys. Chem. B*, 2016.
- [292] J. S. Wilkes, J. A. Levisky, R. A. Wilson, and C. L. Hussey. Dialkylimidazolium Chloroaluminate Melts: A New Class of Room-temperature Ionic Liquids for Electrochemistry, Spectroscopy and Synthesis. *Inorg. Chem.*, 21(3):1263–1264, 1982.
- [293] S. A. Willis, G. R. Dennis, T. Stait-Gardner, G. Zheng, and W. S. Price. Determining a "diffusion-averaged" Characteristic Ratio for Aligned Lyotropic Hexagonal Phases Using PGSE NMR Self-Diffusion Measurements, Random Walk Simulations and Obstruction Models. *J. Mol. Liq.*, 236:107–116, 2017.
- [294] P. Willmott. *An Introduction to Synchrotron Radiation: Techniques and Applications*. John Wiley & Sons, 2011.
- [295] M. Wolff, B. Akgun, M. Walz, A. Magerl, and H. Zabel. Slip and Depletion in a Newtonian Liquid. *EPL*, 82(3):36001, 2008.

- [296] M. Wolff, P. Gutfreund, A. Rühm, B. Akgun, and H. Zabel. Nanoscale Discontinuities at the Boundary of Flowing Liquids: A Look into Structure. *J. Phys.: Condens. Matter*, 23(18):184102, 2011.
- [297] M. Wolff, P. Kuhns, G. Liesche, J. F. Ankner, J. F. Browning, and P. Gutfreund. Combined Neutron Reflectometry and Rheology. *J. Appl. Crystallogr.*, 46(6):1729–1733, 2013.
- [298] W. Xu and C. A. Angell. Solvent-Free Electrolytes with Aqueous Solution-Like Conductivities. *Science*, 302:422, 2003.
- [299] H. Xue, R. Verma, and M. S. Jean'ne. Review of Ionic Liquids with Fluorine-Containing Anions. *J. Fluorine Chem.*, 127(2):159–176, 2006.
- [300] E. Yakub and C. Ronchi. An Efficient Method for Computation of Long-Ranged Coulomb Forces in Computer Simulation of Ionic Fluids. *J. Chem. Phys.*, 119(22):11556–11560, 2003.
- [301] Y. Yao, T. Sakai, M. Steinhart, H.-J. Butt, and G. Floudas. Effect of Poly(ethylene oxide) Architecture on the Bulk and Confined Crystallization within Nanoporous Alumina. *Macromolecules*, 49(16):5945–5954, 2016.
- [302] J. Yarnell, M. Katz, R. G. Wenzel, and S. Koenig. Structure Factor and Radial Distribution Function for Liquid Argon at 85 K. *Phys. Rev. A*, 7(6):2130, 1973.
- [303] Y. Yasaka, C. Wakai, N. Matubayasi, and M. Nakahara. Rotational Dynamics of Water and Benzene Controlled by Anion Field in Ionic Liquids: 1-Butyl-3-methylimidazolium Chloride and Hexafluorophosphate. *J. Chem. Phys.*, 127(10):104506, 2007.
- [304] Y. Yasaka, C. Wakai, N. Matubayasi, and M. Nakahara. Slowdown of H/D Exchange Reaction Rate and Water Dynamics in Ionic Liquids: Deactivation of Solitary Water Solvated by Small Anions in 1-Butyl-3-methyl-imidazolium Chloride. *J. Phys. Chem. A*, 111(4):541–543, 2007.
- [305] C.-J. Yu, A. Richter, J. Kmetko, A. Datta, and P. Dutta. X-ray Diffraction Evidence of Ordering in a Normal Liquid Near the Solid-liquid Interface. *EPL*, 50(4):487, 2000.
- [306] C.-J. Yu, A. Richter, J. Kmetko, S. Dugan, A. Datta, and P. Dutta. Structure of Interfacial Liquids: X-ray Scattering Studies. *Phys. Rev. E*, 63(2):021205, 2001.
- [307] S. Zabler, A. Rack, F. García-Moreno, A. Ershov, T. Baumbach, and J. Banhart. Imaging Fast Processes in Liquid Metal Foams and Semi-solid Alloys Using Synchrotron Radioscopy with Spatio-temporal Micro-resolution. In *In-situ Studies with Photons, Neutrons and Electrons Scattering*, pages 149–158. Springer, 2010.

BIBLIOGRAPHY

- [308] C. A. Zell, F. Endres, and W. Freyland. Electrochemical In Situ STM Study of Phase Formation During Ag and Al Electrodeposition on Au (111) from a Room Temperature Molten Salt. *Phys. Chem. Chem. Phys.*, 1(4):697–704, 1999.
- [309] S. Zhang, J. Zhang, Y. Zhang, and Y. Deng. Nanoconfined Ionic Liquids. *Chemical Reviews*, 2016.
- [310] L. Zhao, M. Yosef, M. Steinhart, P. Göring, H. Hofmeister, U. Gösele, and S. Schlecht. Porous Silicon and Alumina as Chemically Reactive Templates for the Synthesis of Tubes and Wires of SnSe, Sn, and SnO₂. *Angew. Chem. Int. Ed.*, 45(2):311–315, 2006.
- [311] Y.-X. Zhong, J.-W. Yan, M.-G. Li, X. Zhang, D.-W. He, and B.-W. Mao. Resolving Fine Structures of the Electric Double Layer of Electrochemical Interfaces in Ionic Liquids with an AFM Tip Modification Strategy. *J. Am. Chem. Soc.*, 136(42):14682–14685, 2014.

Danksagung

[n.a. in online version]

Curriculum Vitae

[n.a. in online version]

Education

[n.a. in online version]

Publications

[n.a. in online version]

Conference Contributions

[n.a. in online version]

Poster

[n.a. in online version]